2015

Computational Studies on Bimetallic Catalysis and X-ray Absorption Spectroscopy

Sayakkarage R. G. Fernando
Louisiana State University and Agricultural and Mechanical College

COMPUTATIONAL STUDIES ON BIMETALLIC CATALYSIS AND X-RAY ABSORPTION SPECTROSCOPY

A Dissertation

Submitted to the Graduate Faculty of the
Louisiana State University and
Agricultural and Mechanical College
in partial fulfillment of the
requirements for the degree of
Doctor of Philosophy

in

The Department of Chemistry

by
Sayakkarage Ranelka Geethmi Fernando
B.S., University of Colombo, 2010
December 2015

To My Family….

To my loving parents,

for believing in me and encouraging me throughout my life….

To my beloved husband,

for his love, constant support, for always being there for me and

for being my strength.

I couldn't have done this without you…

To my loving brothers,

for their encouragement and constant support in all my endeavors….

Acknowledgements

First, I would like to thank and praise the God almighty for giving me the opportunity to pursue a Ph.D in chemistry which was one of the biggest dreams in my life.

I am truly grateful towards Prof. George Stanley for accepting me to his research group and for his immense support throughout my graduate life. I am very appreciative of all his helpful discussions, encouragement, guidance and constant support. I extend my deepest gratitude to Prof. Kenneth Lopata for giving me the opportunity to work with him. I am grateful for his constant support, guidance and all the helpful discussions. I am very grateful towards my great advisors, who were the best advisors anyone could have.

I am very thankful to my wonderful doctoral committee members; Prof. Andrew Maverick, Prof. Louis Haber, Prof. Elizabeth Webster and Prof. Ernest Mendrela. I appreciate all your time, support, guidance and helpful suggestions. I am also truly grateful to Prof. Julia Chan for all her help, guidance and encouragement.

At last but not least I am very thankful to my beloved husband, parents and my brothers. Without their support and encouragement I would not have been here. I am very thankful to my loving family for always tolerating and encouraging me constantly during my hard times, and especially to my loving husband for always being a helping hand. I am very thankful to my family for helping me to make my dream a reality and I know my father will be looking at me from heaven and will always be happy about my great achievement.

I am also very thankful to Stanley group, Lopata group and to all my friends who helped me throughout my graduate life.

Table of Contents

List of Tables

List of Figures

Abstract

Computational studies are very important to gain an insight into reaction mechanisms and in interpreting and understanding complicated experimental observations. This report contains a discussion on computational studies performed on bimetallic catalysis and on X-ray absorption spectroscopy of insulators. The viability of a bimetallic rhodium and cobalt catalysts for industrially important hydroformylation and aldehyde-water shift catalysis (AWS) is discussed. Density functional theory (DFT) studies were used for bimetallic catalysis and time-dependent DFT studies were used for excited state dynamics. These studies were performed using Gaussian 09 package and NWChem.

Hydroformylation is experimentally performed in acetone and 30% water/acetone systems and results in dicationic dirhodium complexes and monocationic dirhodium complexes respectively. DFT studies were used to determine the active catalyst and possible intermediates. Computational studies support the mechanism proposed by Prof. Stanley for hydrofomylation in acetone, but DFT studies demonstrate a different mechanism for hydroformylation in water/acetone which contains mono-bridging complexes. A detailed discussion on this is given in chapter 2.

DFT studies were used to study the AWS catalysis with the bimetallic $[rac\text{–}Rh_2(\mu\text{–}CO)_2(CO)_2(et,ph\text{-}P4)]^{2+}$ complex. These studies were performed in both vacuum and using explicit water molecules, and lower energies were obtained when explicit water molecules were used. The computations support an alternate mechanism with protonated acid intermediates different from the originally proposed mechanism. This mechanism is discussed in great detail in chapter 3.

DFT studies are also performed to study the suitability of dicobalt analogs for hydroformylation and AWS catalysis. The most suitable active catalyst and possible mechanism for hydroformylation using $Co_2(\mu\text{–}H)(\mu\text{–}CO)(CO)_3(H)(et,ph\text{-}P4)]^{2+}$(Co_2), [*rac*- and $[rac\text{-}Co_2(\mu\text{–}H)_2(CO)_4(et,ph\text{-}P4)]^{2+}$ (Co_2*) and $[rac\text{-}Co_2(\mu\text{–}CO)_2(CO)_2(H)_2(et,ph\text{-}P4)]^{2+}$ (Co_2**) are discussed in chapter 4. The capability of $[rac\text{-}Co_2(CO)_4(et,ph\text{-}P4)]^{2+}$ (Co_4*) catalyst for AWS catalysis is also discussed in chapter 4.

Chapter 5 discusses a method to generate X-ray absorption spectra of insulators using time-dependent DFT. α–Quartz was used as a model for insulators. Bulk-mimicking embedded finite cluster

models, atom-centered basis sets, tuned range-separated functionals and molecular orbital-based absorbing boundary conditions were utilized to model near and above ionization spectral features without experimental parameterization. The calculated spectra match well with the experimental results over the range of approximately 105 – 130 eV.

Chapter 1 - Introduction

1.1 Background

The discovery of Schrödinger's wave equation in 1926 initiated the first step in the field of quantum chemistry.[1-2] Schrödinger equation describes the behavior of time-evolution of the wave function of a physical system. The distribution of electrons within a molecule can be described by evaluating the Schrödinger equation:

$$\hat{H}\Psi = E\Psi$$

where $\hat{H}$ is the Hamiltonian operator that acts upon the wave function, Ψ to give the energy, E. The wave function describes the spatial position of an electron, and the Hamiltonian operator corresponds to the total energy of the system. Finding the exact solutions to Schrödinger's equation is very worthwhile, but it is virtually impossible for multi-electron systems because the complexity of the computational calculations shows an exponential growth with the number of electrons in the system.[2,3] When there is more than one electron it becomes a three-body problem where you need to include the nucleus in the calculation. Mathematically these many-body problems cannot be solved exactly and require approximations. The time-independent Schrödinger equation for multi-electron systems can be solved by the use of Born-Oppenheimer approximation.[4] This assumes that since the nucleus is much heavier than electrons, the nucleus is essentially stationary relative to the electrons; hence, the motion of nuclei and electrons can be separated. This allows solving the electronic and the nuclear part of the Schrödinger equation separately. The Schrödinger equation can also be simplified by several other approximations; namely*, ab initio* methods[5], semi-empirical[6-7] and density functional theory (DFT).[8-10]

The term "ab initio" is Latin for "from the beginning". The *ab initio* methods in quantum chemistry involve computations derived directly from theoretical concepts without the use of experimental data to parameterize variables. These methods have been widely used in the last three decades to study molecules. This discipline of computational quantum chemistry strives to determine electronic energies and wave functions of atoms, molecules and all other chemical species. In order to solve the Schrödinger equation from first principles, the molecule is considered to be a collection of positive nuclei and negative

electrons subject to Coulombic potentials without making use of any experimental data about the molecule, although one typically needs to start with a reasonable starting structure of the molecule when doing a calculation. In trying to apply *ab initio* methods to complex systems it is inevitable that approximations are used to simplify the calculations. [3, 5]

Several mathematical approximations employed in *ab initio* techniques provide solutions to many body systems. The most commonly used *ab initio* method is the Hartree Fock method which utilizes the central field approximation which neglects the Coulombic electron-electron repulsion. Another approximation in Hartree Fock calculations considers the wave function to be expressed in functional form. The exact form of the wave function is only known for a few single electron systems. The most commonly used functions are linear combinations of Slater- and Gaussian-type orbitals.[3]

Despite the advantages of the *ab initio* methods, there are several disadvantages. The *ab initio* methods are computationally expensive as well as time consuming, often limited to small and medium sized molecules since larger molecules can consume enormous amount of time.[2,3] Computational complexity for *ab initio* Hartree Fock calculations scales as N^4, where N = number of electrons in the molecule.

The semi-empirical MO method uses experimentally adjusted parameters in contrast to *ab initio* methods.[6] As a result, the calculated values via semi-empirical methods depend on the accuracy of the experimental data; thus these types of calculations often give poor results for molecules that are not similar to the ones used to adjust the parameters. The semi-empirical method also uses greater approximations of integrals and parameters, which can dramatically speed up the calculation for more complex molecules, but often with poorer results. The nature of the accuracy of the calculation depends on the optimization of the parameters and the quality of approximations.[7]

A most promising advancement in computational chemistry was the field of density functional theory. The DFT method does not solely depend on wave functions; instead the electron density of systems is also taken into consideration. The history of DFT goes back to 1927, with the discovery of Thomas–Fermi theory, which determines a method to find the electronic structure of atoms using “one-electron ground state density”.[11] This model approximates the distribution of electrons in an atom. The

atomic energy was explained using the electron density for the kinetic energy of the atom, nuclear-nuclear, and electron-electron interactions, but the exchange energy of the atom was not incorporated. An exchange energy term was later added by Dirac. The Thomas-Fermi model is not applicable for most systems as it neglects the electron correlation effect and the expression for the kinetic energy is approximate, but this model was a theoretical predecessor of DFT.

Later, the Hohenberg-Kohn (H-K) theorem proved a relationship between the electron density and the external potential.[2, 12] The first H-K theorem states for a system with interacting particles in an external potential the electron density is determined uniquely. The second H-K theorem states that the ground state energy can be achieved by minimizing the total energy via the use of electron density.

Further improvement was made on DFT by Kohn and Sham in 1965. The Kohn-Sham density functional theory (KS-DFT) uses the contribution from exchange-correlation energy instead of the kinetic energy of the energy functional, making it more computationally friendly. [2, 13,14] In KS-DFT the system of interacting particles is reduced into non-interacting particles in an effective potential. The kinetic energy of a non-interacting system is calculated using the same density as the interacting system. The exchange-correlation energy term was included into the universal functional which previously only contained the contributions of the kinetic energy, the classical Coulomb interaction and the non-classical portion.

Several approximations are made to account for the exchange-correlation energy in these types of calculations. In 1970s and 1980s the local density approximation (LDA) was used, which was derived via the application of a uniform electron gas functional to molecular systems.[13] These local approximations depend solely on electron density. In the late 1980s generalized gradient approximations (GGAs) or hydbrid functional such as; Becke-88 (B88), exchange functional, Lee-Yang-Parr (LYP) and Perdew-86 (P86) were developed.[15-19] The most commonly used modern approximation was discovered by Becke in early 1990s.[2,14] This was a hybrid functional named B3LYP because part of GGA exchange functional was replaced with Hartree-Fock exchange.[2, 20,14] This hybrid correlation functional is the most popular density functional that is used in DFT calculations as it generally results in more reliable structural and electronic data. This method has gained promising interest as it is computationally less expensive

relative to *ab initio* Hartree Fock calculations, and the use of electron density is simpler than utilizing wave functions.[14]

DFT is mostly used to study ground state properties of molecules and solids. Time-dependent density functional theory (TD-DFT) was developed to study excited state dynamics of complexes in the presence of time-dependent potentials. The groundwork for TD-DFT is the Runge-Gross theorem which is analogous to time-dependent H-K theorem. The Runge-Gross theorem states that for a given initial wave function the time-dependent potentials and their respective time-dependent densities will be different and it is used for interacting systems while the time-dependent Kohn-Sham formalism which was developed later is used for non-interacting systems.[21-22]

Linear response time-dependent density functional theory (LR-TDDFT) can be used if the system is subject to a small perturbation, i.e, if the external time-dependent potential is small, and this is very useful in studying spectroscopic properties. For systems with strong external potentials a full solution of the time-dependent Kohn-Sham equations is required.[22-23]

The application of TD-DFT is based on a suitable approximation for the time-dependent exchange-correlation potential and the most widely used approximation is the adiabatic approximation, which is valid for slowly varying time-dependent fields. Recent studies have shown that the approximation is valid even for systems exposed to high frequency fields as memory effects become negligible.[22-25]

TD-DFT is very efficient in predicting relative excitation energies, but the major drawback is its dependence on the exchange-correlation functional; hence, shifting of spectra is generally needed to match the calculated energies with the experimental results. LR-TDDFT is a very useful technique to model weak excitations (e.g., absorption spectra of molecules and materials), but this method requires computing a large number of irrelevant roots prior to obtaining core excitations, which, consequently, becomes computationally expensive and inefficient. A possible remedy for this would be the use of restricted excited window approach (REW-TDDFT) or the use of real-time time-dependent density functional theory (RT-TDDFT).[26] In REW-TDDFT the excitations will take place only from the relevant core orbital. In RT-TDDFT the wave function or the density matrix is explicitly propagated in time under

the influence of time-dependent Fock matrix.[27-28] Unlike LR-TDDFT, in RT-TDDFT the entire absorption spectrum can be obtained by only three simulations (*x*, *y*, *z* polarizations), but LR-TDDFT will still be required to assign the peaks with the corresponding transition as RT-TDDFT is incapable of producing those results.

Studying both experimental data and electronic structural calculations can help better understand the properties and behavior of molecules and their chemical reactivity. To gain a better understanding of the correlation between the molecular and electronic properties computational chemistry has been widely employed.[29,30] Computational work can be used to obtain thermochemical data, transition states of a reaction mechanism, activation barriers and band gaps.[30] Furthermore, these calculations can be employed to obtain molecular and electronic low energy structures, vibrational frequencies, and dissociation energies and many other properties.[31,32]

The determination of vibrational frequencies plays a great role in providing additional support for experimental data. Usually the calculated frequencies are calculated too high relative to the corresponding experimental frequencies. These errors result due to the use of harmonic potential energies, the lack of treatment of electron correlation effects, and inadequate basis sets.[33,34] Due to consistent disagreement of calculated frequencies with the experimental frequencies, scaling factors are usually employed.[33,34] This improves the reliability of the calculated vibrational frequencies.

Much research has been performed to determine the scaling factors for vibrational frequencies for the Hartree-Fock method as well as for DFT methods with different functionals. Scaling factors have been obtained for B3LYP functional including several diffuse and polarization functions for the 6-311G basis set. Several inorganic and organic small molecules have been utilized for the analyses.[33-36] It has been determined that a scale factor of 0.9614 is reliable for organometallic carbonyl complexes at the B3LYP/6-31G(d) level.[34] It has also been noted that the scaling factor shows a weak dependency upon the basis set for the B3LYP functional.[35,37]

Several researchers have performed studies on mechanisms of various chemical processes utilizing computational calculations. The most accepted mechanism for hydroformylation catalyzed by monometallic cobalt complexes was proposed by Heck and Breslow, but it was not thoroughly understood

until the theoretical studies performed by Folga and Ziegler.[29] Later, a more selective rhodium catalyst for hydroformylation was synthesized by Ruchremie. A more prominent study on this rhodium complex was performed by Pidun and Frenkling.[29] Several researchers carried out computational calculations on different steps of the catalytic cycle such as olefin coordination, olefin insertion, carbonyl insertion, oxidative addition of H_2 and aldehyde reductive elimination. Apart from hydroformylation, quantum calculations have also been performed on the Dotz reaction, which is also known as benzannulation, water-gas shift reaction, hydrogenation of CO_2, and hydrogenation of CO.[29] Furthermore, theoretical studies were performed on the mechanism of hydroformylation catalyzed by the heterobimetallic complex $(CO)_4Cr(\mu\text{–}PH_2)_2RhH(CO)(PH_3)$ by Hu and coworkers.[29,38] These calculations were all carried out using the DFT method, which is especially good for transition metal systems.

This research report consists of four projects which discuss about computational studies performed by bimetallic molecular catalysis and X-ray absorption spectroscopy on a solid-state material. This work is mainly focused on industrially important hydroformylation and aldehyde-water shift processes catalyzed by bimetallic rhodium and bimetallic cobalt complexes. DFT modeling studies were used to study the reaction mechanisms and to gain an insight into the reaction mechanistic. In addition to these studies, a detailed study on the development of a method to study X-ray absorption spectrum of insulators using RT-TDDFT is explained using α–quartz as a model insulator.

All bimetallic catalytic studies were performed using Gaussian 09 C.01 64-bit version.[39] The optimization and frequency analysis studies of the geometries were carried out using the hybrid B3LYP functional and various basis sets. A detailed description on the methods used is provided in each chapter. X-ray absorption studies on α–quartz was performed using the NWChem[40] real-time TD-DFT module and basis sets were selected from the EMSL Basis Set Exchange.[41]

1.2 References

1. Schrödinger, E., An Undulatory Theory of the Mechanics of Atoms and Molecules. *Physical Review* **1926,** *28* (6), 1049-1070.

2. Barden, C. J.; Schaefer, H. F., Quantum chemistry in the 21st century (Special topic article). *Pure and applied chemistry* **2000,** *72* (8), 1405-1423.

3. Friesner, R. A., Ab initio quantum chemistry: methodology and applications. *Proceedings of the National Academy of Sciences of the United States of America* **2005,** *102* (19), 6648-6653.

4. Born, M., Born-Oppenheimer Approximation. *Quantum* **1927,** *2* (2014/12), 4.

5. Parr, R. G.; Craig, D. P.; Ross, I. G., Molecular Orbital Calculations of the Lower Excited Electronic Levels of Benzene, Configuration Interaction Included. *The Journal of Chemical Physics* **1950,** *18* (12), 1561-1563.

6. Thiel, W., Semiempirical quantum-chemical methods in computational chemistry. *Theory and applications of computational chemistry: the first* **2005,** *40*, 559-580.

7. Stewart, J. J., Optimization of parameters for semiempirical methods I. Method. *Journal of Computational Chemistry* **1989,** *10* (2), 209-220.

8. Parr, R. G.; Yang, W., *Density-functional theory of atoms and molecules*. Oxford university press: 1989; Vol. 16.

9. Capelle, K., A bird's-eye view of density-functional theory. *Brazilian Journal of Physics* **2006,** *36* (4A), 1318-1343.

10. Burke, K.; Wagner, L. O., DFT in a nutshell. *International Journal of Quantum Chemistry* **2013,** *113* (2), 96-101.

11. Thomas, L. H., The calculation of atomic fields. *Mathematical Proceedings of the Cambridge Philosophical Society* **1927,** *23* (05), 542-548.

12. Hohenberg, P.; Kohn, W., Inhomogeneous Electron Gas. *Physical Review* **1964,** *136* (3B), B864-B871.

13. Kohn, W.; Sham, L. J., Self-Consistent Equations Including Exchange and Correlation Effects. *Physical Review* **1965,** *140* (4A), A1133-A1138.

14. Burke, K., Perspective on density functional theory. *The Journal of chemical physics* **2012,** *136* (15), 150901.

15. Becke, A. D., Density-functional exchange-energy approximation with correct asymptotic behavior. *Physical Review A* **1988,** *38* (6), 3098-3100.

16. Perdew, J. P.; Chevary, J. A.; Vosko, S. H.; Jackson, K. A.; Pederson, M. R.; Singh, D. J.; Fiolhais, C., Atoms, molecules, solids, and surfaces: Applications of the generalized gradient approximation for exchange and correlation. *Physical Review B* **1992,** *46* (11), 6671-6687.

17. Gill, P. M.; Johnson, B. G.; Pople, J. A.; Frisch, M. J., An investigation of the performance of a hybrid of Hartree ¡Fock and density functional theory. *International Journal of Quantum Chemistry* **1992,** *44* (S26), 319-331.

18. Gill, P. M.; Johnson, B. G.; Pople, J. A.; Frisch, M. J., The performance of the Becke—Lee—Yang—Parr (B—LYP) density functional theory with various basis sets. *Chemical Physics Letters* **1992,** *197* (4), 499-505.

19. Perdew, J. P., Density-functional approximation for the correlation energy of the inhomogeneous electron gas. *Physical Review B* **1986,** *33* (12), 8822.

20. Yanai, T.; Tew, D. P.; Handy, N. C., A new hybrid exchange–correlation functional using the Coulomb-attenuating method (CAM-B3LYP). *Chemical Physics Letters* **2004,** *393* (1–3), 51-57.

21. Runge, E.; Gross, E. K., Density-functional theory for time-dependent systems. *Physical Review Letters* **1984,** *52* (12), 997.

22. Ullrich, C. A.; Yang, Z.-h., A brief compendium of time-dependent density functional theory. *Brazilian Journal of Physics* **2014,** *44* (1), 154-188.

23. Marques, M. A.; Gross, E., Time-dependent density functional theory. *Annual Review of Physical Chemistry* **2004,** *55* (1), 427-455.

24. Maitra, N. T.; Burke, K.; Woodward, C., Memory in Time-Dependent Density Functional Theory. *Physical Review Letters* **2002,** *89* (2), 023002.

25. Baer, R., Prevalence of the adiabatic exchange-correlation potential approximation in time-dependent density functional theory. *Journal of Molecular Structure: THEOCHEM* **2009,** *914* (1–3), 19-21.

26. Lopata, K.; Van Kuiken, B. E.; Khalil, M.; Govind, N., Linear-Response and Real-Time Time-Dependent Density Functional Theory Studies of Core-Level Near-Edge X-Ray Absorption. *Journal of Chemical Theory and Computation* **2012,** *8* (9), 3284-3292.

27. Akama, T.; Nakai, H., Short-time Fourier transform analysis of real-time time-dependent Hartree–Fock and time-dependent density functional theory calculations with Gaussian basis functions. *The Journal of chemical physics* **2010,** *132* (5), 054104.

28. Yabana, K.; Bertsch, G., Time-dependent local-density approximation in real time. *Physical Review B* **1996,** *54* (7), 4484.

29. Torrent, M.; Sola, M.; Frenking, G., Theoretical studies of some transition-metal-mediated reactions of industrial and synthetic importance. *Chemical reviews* **2000,** *100* (2), 439-494.

30. Tang, D.; Zhang, Y.; Hu, C., Theoretical Study on Mechanism of Hydroformylation of Ethene Catalyzed by a Heterobimetallic Rh(I) ¡Cr Complex. *Chinese Journal of Chemistry* **2009,** *27* (1), 81-87.

31. Zhou, X.; Cui, J.; Li, Z. H.; Wang, G.; Zhou, M., Infrared photodissociation spectroscopic and theoretical study of homoleptic dinuclear chromium carbonyl cluster cations with a linear bridging carbonyl group. *The Journal of Physical Chemistry A* **2012,** *116* (50), 12349-12356.

32. Cui, J.; Xing, X.; Chi, C.; Wang, G.; Liu, Z.; Zhou, M., Infrared Photodissociation Spectra of Mass ¡Selected Homoleptic Dinuclear Palladium Carbonyl Cluster Cations in the Gas Phase. *Chinese Journal of Chemistry* **2012,** *30* (9), 2131-2137.

33. Sierraalta, A.; Martorell, G.; Ehrmann, E.; Añez, R., Improvement of scale factors for harmonic vibrational frequency calculations using new polarization functions. *International Journal of Quantum Chemistry* **2008,** *108* (6), 1036-1043.

34. Yu, L.; Srinivas, G.; Schwartz, M., Scale factors for CO vibrational frequencies in organometallic complexes. *Journal of Molecular Structure: THEOCHEM* **2003,** *625* (1), 215-220.

35. Andersson, M. P.; Uvdal, P., New scale factors for harmonic vibrational frequencies using the B3LYP density functional method with the triple-ζ basis set 6-311+G(d, p). *The Journal of Physical Chemistry A* **2005,** *109* (12), 2937-2941.

36. Merrick, J. P.; Moran, D.; Radom, L., An evaluation of harmonic vibrational frequency scale factors. *The Journal of Physical Chemistry A* **2007,** *111* (45), 11683-11700.

37. Irikura, K. K.; Johnson, R. D.; Kacker, R. N., Uncertainties in scaling factors for ab initio vibrational frequencies. *The Journal of Physical Chemistry A* **2005,** *109* (37), 8430-8437.

38. Tang, D.; Qin, S.; Su, Z.; Hu, C., Comprehensive Theoretical Study on the Mechanism of Regioselective Hydroformylation of Phosphinobutene Catalyzed by a Heterobinuclear Rhodium (I)-Chromium Complex. *Organometallics* **2007,** *26* (1), 33-47.

39. Frisch, M. J.; Trucks, G. W.; Schlegel, H. B.; Scuseria, G. E.; Robb, M. A.; Cheeseman, J. R.; Scalmani, G.; Barone, V.; Mennucci, B.; Petersson, G. A.; Nakatsuji, H.; Caricato, M.; Li, X.; Hratchian, H. P.; Izmaylov, A. F.; Bloino, J.; Zheng, G.; Sonnenberg, J. L.; Hada, M.; Ehara, M.; Toyota, K.; Fukuda, R.; Hasegawa, J.; Ishida, M.; Nakajima, T.; Honda, Y.; Kitao, O.; Nakai, H.; Vreven, T.; Montgomery Jr., J. A.; Peralta, J. E.; Ogliaro, F.; Bearpark, M. J.; Heyd, J.; Brothers, E. N.; Kudin, K. N.; Staroverov, V. N.; Kobayashi, R.; Normand, J.; Raghavachari, K.; Rendell, A. P.; Burant, J. C.; Iyengar, S. S.; Tomasi, J.; Cossi, M.; Rega, N.; Millam, N. J.; Klene, M.; Knox, J. E.; Cross, J. B.; Bakken, V.; Adamo, C.; Jaramillo, J.; Gomperts, R.; Stratmann, R. E.; Yazyev, O.; Austin, A. J.; Cammi, R.; Pomelli, C.; Ochterski, J. W.; Martin, R. L.; Morokuma, K.; Zakrzewski, V. G.; Voth, G. A.; Salvador, P.; Dannenberg, J. J.; Dapprich, S.; Daniels, A. D.; Farkas, Ö.; Foresman, J. B.; Ortiz, J. V.; Cioslowski, J.; Fox, D. J. *Gaussian 09*, Gaussian, Inc.: Wallingford, CT, USA, 2009.

40. Valiev, M.; Bylaska, E. J.; Govind, N.; Kowalski, K.; Straatsma, T. P.; Van Dam, H. J.; Wang, D.; Nieplocha, J.; Apra, E.; Windus, T. L., NWChem: a comprehensive and scalable open-source solution for large scale molecular simulations. *Computer Physics Communications* **2010,** *181* (9), 1477-1489.

41. Schuchardt, K. L.; Didier, B. T.; Elsethagen, T.; Sun, L.; Gurumoorthi, V.; Chase, J.; Li, J.; Windus, T. L., Basis set exchange: a community database for computational sciences. *Journal of chemical information and modeling* **2007,** *47* (3), 1045-1052.

Chapter 2 - Rhodium Catalyzed Hydroformylation

2.1 Introduction

The process of hydroformylation was discovered by the German industrial chemist Otto Roelen in 1938 as a result of an investigation of the cobalt catalyzed Fischer-Tropsch reactions. Hydroformylation is one of the most vital and largest industrial homogeneous catalytic processes[1] and it involves the conversion of alkenes to aldehydes using carbon monoxide and hydrogen gas (Figure 2.1). Consequently, several million tons of aldehydes are produced per year.[2] These aldehydes can be further converted into plasticizers, detergents, pharmaceuticals, agrochemicals and fragrances, making hydroformylation a very important industrial process.[2-3] The most widely used catalysts in hydroformylation contain the transition metals rhodium and cobalt. Rh is 1000 times more reactive compared to Co and it can perform catalysis at much lower temperatures and pressures.[4]

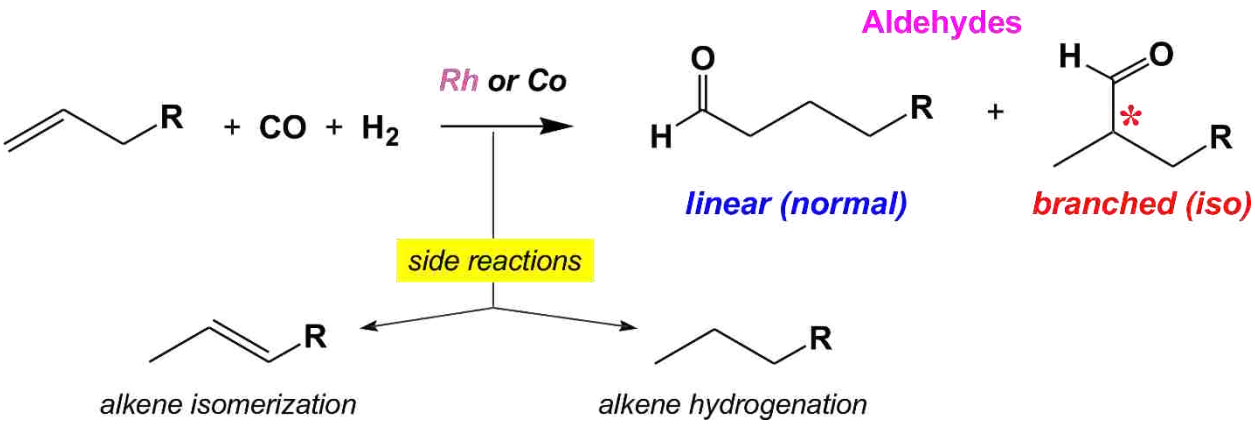

Figure 2.1. Hydroformylation.

Catalysts for hydroformylation were developed in late 1930s using cobalt(+1) carbonyl complexes, but later more efficient rhodium(+1) carbonyl complexes were synthesized. Hydroformylation was performed by BASF, ICI and Ruchremie using cobalt catalysts under high pressure (200-350 bar) and high temperature (150-180 °C).[5] The generally accepted hydroformylation mechanism catalyzed by cobalt carbonyl complexes was proposed by Heck and Breslow in 1960s (Figure 2.2) , but it was not thoroughly understood until the theoretical studies performed by Folga and Ziegler.[6,7]

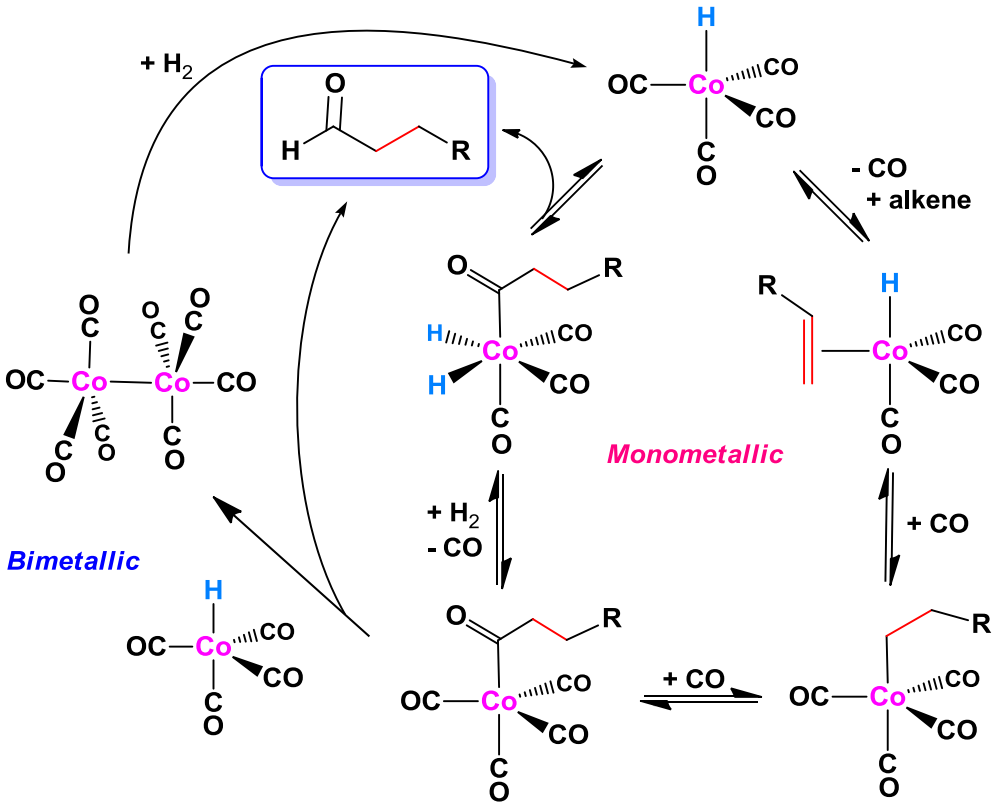

Figure 2.2. Cobalt catalyzed hydroformylation mechanism proposed by Heck and Breslow.[6]

A monometallic as well as a bimetallic pathway was proposed, but the bimetallic mechanism was not favored by Heck and Breslow. A bimetallic cobalt complex, $Co_2(CO)_8$ could be produced by the reaction of the acyl intermediate with $HCo(CO)_4$ via an intermolecular hydride transfer followed by reductive elimination of aldehyde. This has been proposed as a possibility for reactions with internal alkenes.[8] However, the monometallic pathway involving the reaction of acyl intermediate with H_2 has been found to be the dominant pathway.[9]

As the simple carbonyl complexes produced relatively low linear to branched (L:B) ratios of the aldehyde (e.g., 2:1 for $HCo(CO)_4$), phosphine-modified catalysts were developed by Shell. This was achieved by adding a trialkylphosphine ligand to $HCo(CO)_4$ complex, which improved the stability of the catalyst towards decomposition to cobalt metal and give much better L:B regioselectivities for the aldehyde (e.g., 8:1). Hydroformylation with phosphine substituted cobalt catalysts required only 50-150 bars of pressure and 180°C without decomposition of catalyst to cobalt metal.[10]

In 1965 more active and highly regioselective Rh(+1)-PPh_3 catalyst complexes for hydroformylation were reported by Osborn, Young and Wilkinson. Wilkinson's $RhCl_3(PPh_3)_3$ catalyst was initially used for hydroformylation, but later it was discovered that halides inhibited the process. Therefore, it was replaced by $HRh(CO)(PPh_3)_3$ or $Rh(acac)(CO)_2$ (acac = acetoacetonate) as the starting species. The hydroformylation mechanism catalyzed by Rh/PPh_3 complex was then proposed by Wilkinson. This mechanism included two pathways termed the associative and the dissociative pathways..[11] The associative pathway goes through a 6-coordinate Rh(+1) 20 e- complex, which has been discounted as a viable intermediate. The theoretical and experimental results support only the dissociative mechanism for hydroformylation which proceeds via a 16 e- complex (Figure 2.3).

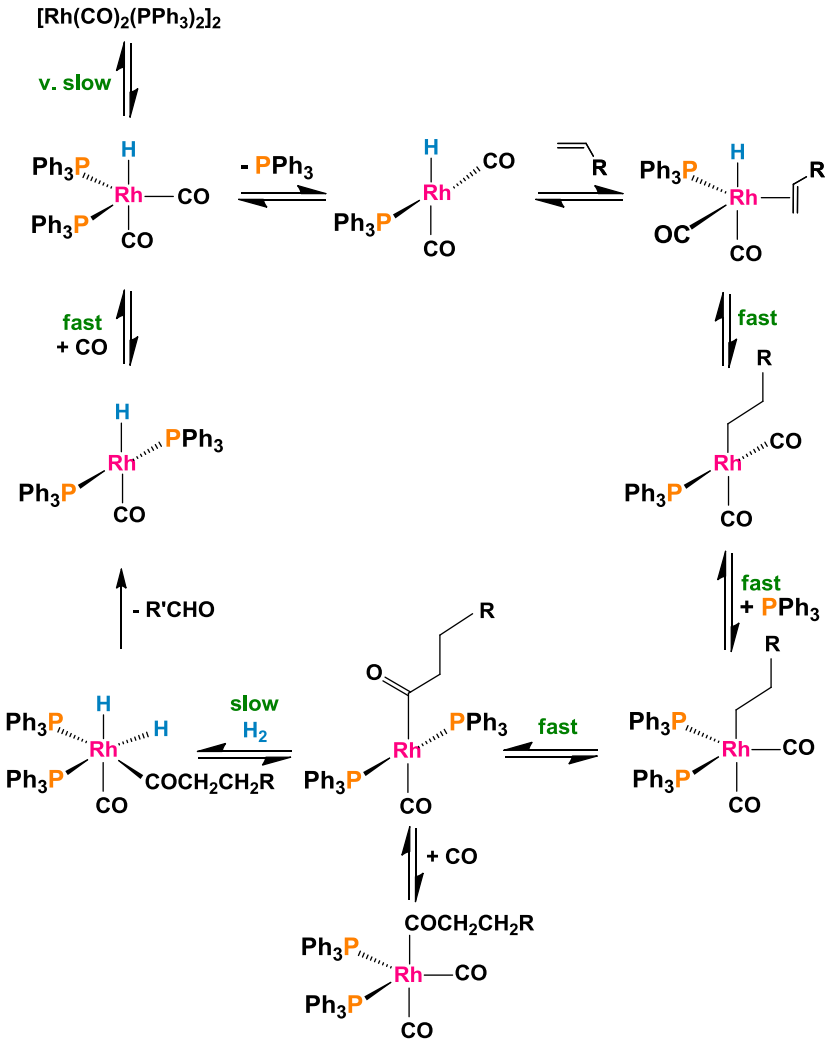

Figure 2.3. Dissociative mechanism of Rh/PPh_3 hydroformylation.[11]

Wilkinson's dissociative mechanism was analogous to the proposed mechanism by Heck and Breslow, and the dissociative mechanism shown in Figure 2.3 is the currently accepted route that most hydroformylation processes follow. Mild conditions are generallly employed for rhodium catalyzed hydroformylation process (100°C, 10 atm 1:1 H_2/CO).[12] The homogeneous low pressure oxo processes performed by Union Carbide and Celanese in mid-1970s resulted in replacement of the cobalt catalysts by rhodium catalysts due to their superior chemo- and regioselectivity.[5]

Despite the extensive use of monometallic complexes, bimetallic catalysts are very interesting due to the prospect of multi-center cooperativity, which can enhance the catalytic activity and/or selectivity. Several heterobimetallic catalysts comprised of Co/Ru, Rh/W, Rh/Mo, and Co/Pd mixed metal systems with phosphine ligands have been tested for hydroformylation, but none are more effective than monometallic catalysts.[13,14,15,16,17] Hydroformylation is now performed using mostly phosphine based rhodium catalysts as they are more active, produce more linear aldehyde, and minimize side reactions such as hydrogenation and isomerization.

A good number of quantum chemical studies on hydroformylation catalyzed by monometallic systems have been reported. Schmid et al. has performed studies on the dissociation reactions of hydroformylation catalyzed by $HRh(CO)_n(PR_3)_{4-n}$ and $HRh(CO)_n(PR_3)_{3-n}$, where n = 1-3 using *ab initio* and DFT methods. PH_3 was used as the model for the phosphine ligand.[18] *Ab initio* molecular orbital theory studies on the full catalytic cycle of hydroformylation catalyzed by $RhH(CO)_2(PH_3)_2$ was performed by Morokuma *et al*. using ethene as the model olefin and PH_3 as the model phosphine ligand.[19] Static (Gaussian) and dynamic (Car-Parrinello molecular dynamics (CPMD) simulations) studies on hydroformylation catalyzed by Rh(+1) hydrido-carbonyl complexes with modified phosphine ligands such as PF_3, PH_3, and PMe_3 were studied by Gleich et al.[20] In addition to these, several other quantum mechanical studies have been performed on hydroformylation catalyzed by monometallic complexes.[21,22,23] Very few theoretical studies have been performed on hydroformylation catalyzed by bimetallic complexes.[24]

Herein, we report computational studies on the hydroformylation cycle catalyzed by a dirhodium complex. This chapter contains computational calculations performed on the mechanism of a bimetallic

hydroformylation catalyst system proposed by Prof. George Stanley. The hydroformylation reaction is carried out in two different solvent systems, namely acetone and acetone/water, and this chapter includes a theoretical mechanistic investigation on the hydroformylation catalytic cycle in both solvent systems. The catalyst employed is a bimetallic rhodium complex. The dirhodium homogeneous catalyst system was discovered by Stanley and coworkers and is proposed to work via bimetallic cooperativity.[25,26,27] The use of a tetraphosphine ligand with both bridging and chelating groups favors the incorporation of two metal centers. The ligand, $(Et_2PCH_2CH_2)(Ph)PCH_2P(Ph)(CH_2CH_2PEt_2)$ or (et,ph-P4) exists in both *racemic* and *meso* forms (Figure 1.4).

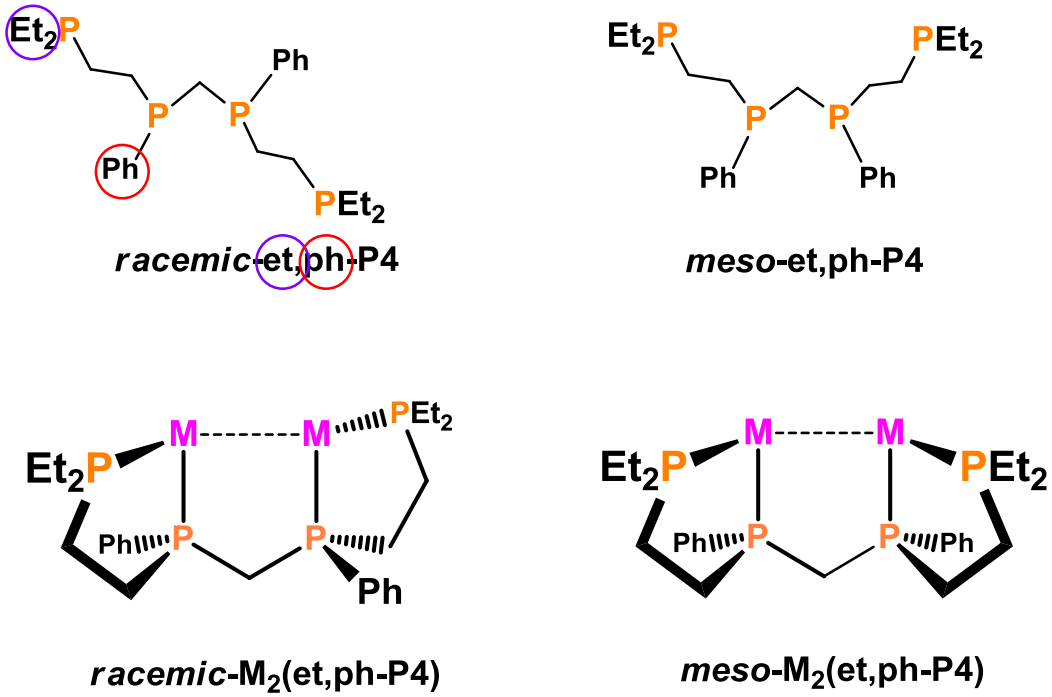

Figure 2.4. Tetraphosphine ligand *rac* and *meso*-et,ph-P4.

The hydroformylation mechanism proposed by Prof. Stanley illustrates the role of bimetallic cooperativity and is comprised of the following fundamental steps that are parallel with the monometallic hydroformylation catalysts: carbonyl group (CO) dissociation, alkene coordination, insertion of alkene into the metal-H bond, association of CO, insertion of CO, oxidative addition of H_2 and finally reductive elimination of the aldehyde.

2.2 Computational Details

All computations were performed using Gaussian 09 C.01 64-bit package.[28] The catalyst precursor employed for hydroformylation is $[Rh_2(nbd)_2(rac\text{–}et,ph\text{–}P4)](BF_4)_2$ (nbd = norbornadiene, *rac*–et,ph–P4 = $Et_2PCH_2CH_2P(Ph)CH_2P(Ph)CH_2CH_2PEt_2$). In the calculations, the ethyl and phenyl groups on the ligand were replaced with simple methyl groups to minimize computational time. Ethene was used as the model alkene substrate for the calculations. The calculations were all performed in vacuum at 298.15 K so interactions with the neighboring molecules were not considered.

Geometry optimizations were carried out using density functional theory (DFT) using Becke, three-parameter, Lee-Yang-Parr (B3LYP) functional.[29-30,30] The suitable basis set for the complexes were selected by comparing the crystal structure of $[Rh_2(CO)_5(rac\text{–}et,ph\text{–}P4)]$ with the calculated complex,**5**. (Figure 2.6a and 2.6b). The best basis sets that resulted in similar structural parameters were the all electron basis sets where the Rh centers were optimized with 3-21G and the other atoms (C, H, O and P) with 6-311G**. Vibrational analyses were performed to determine the ground states and transition states. The optimized ground states contained zero imaginary vibrational frequencies, and transition states contained a single imaginary vibrational frequency.

2.3 Results

The catalyst precursor used for hydroformylation is $[Rh_2(nbd)_2(rac\text{–}et,ph\text{–}P4)](BF_4)_2$, **1** and this is produced by reacting *rac*-et,ph-P4 with two equivalents of $[Rh(nbd)_2BF_4]$. This complex forms the dicationic dirhodium complex in an acetone solvent. The standard alkene used for the experimental studies is 1-hexene, but the results are typical for 1-alkenes. The hydroformylation activity of *racemic* and *meso* Rh_2 complexes was compared with the commercially available monometallic Rh/PPh_3 catalyst (Table 2.1). The activity of hydroformylation is considerably dependent on the concentration of PPh_3. At higher concentrations of PPh_3 the rate of catalysis decreases, while the L:B aldehyde ratio increases. A minimum PPh_3 concentration of 0.4 M (1 mM rhodium catalyst) is typically used in industry, in which case the PPh_3/Rh ratio becomes 400:1. The PPh_3 concentration used in the comparison is 0.82 M which is a middle-ground concentration used in industry.

Table 2.1. Hydroformylation activity of *racemic* and *meso* complexes compared with monometallic Rh/PPh_3 catalyst. [a] turnovers per min (# moles product / # moles catalyst); initial rate is the initial linear part of the uptake curve representing the highest catalytic rate. [b] linear to branched aldehyde product ratio based on GC and NMR analysis.

Catalyst Precursor	Initial TO/min [a]	Aldehyde l/b ratio [b]	Alkene isomerization	Alkene hydrogenation
$[Rh_2(nbd)_2$(*rac*-et,ph-P4)$](BF_4)_2$	20	28:1	2.5%	3.4%
$Rh(CO)_2(acac)$ + 0.82 M PPh_3	9	17:1	1%	0.5%
$[Rh_2(nbd)_2$(*meso*-et,ph-P4)$](BF_4)_2$	0.9	14:1	24%	10%

The results in table 2.1 demonstrate that the lowest hydroformylation activity and most side reactions are seen when the *meso* Rh catalyst is used. In contrast, a significantly higher activity and overall selectivity is seen when the *racemic* Rh catalyst is employed. The *racemic* catalyst is 22 times faster than the *meso* catalyst and results in much higher product selectivity. Even though excess phosphine ligands are required for aryl phosphine or phosphite coordinated monometallic rhodium complexes, the bimetallic complex **1** does not require any excess phosphine ligand to maintain its selectivity or stability. Indeed, excess *rac*-P4 ligand deactivates the bimetallic catalyst. In bimetallic Rh complexes the chelating ligand and strong electron donating et,ph-P4 ligand coordinates to the metal centers strongly (or so we thought), and hence excess phosphine is not required or desired.

Monometallic catalyst analogs of half our bimetallic system, $[Rh(nbd)(P_2)](BF_4)$ (P_2 = $Et_2PCH_2CH_2PEt_2$, $Et_2PCH_2CH_2PMePh$, $Et_2PCH_2CH_2PPh_2$, or $Ph_2PCH_2CH_2PPh_2$) are terrible catalysts and only give 1-2 turnovers/hr, 3:1 linear to branched aldehyde regioselectivity and 50-70% alkene isomerization and hydrogenation side reactions. It was remarkable that combining two of these poor hydroformylation catalysts with the *rac*-et,ph-P4 ligand generates a highly reactive and selective catalyst due to highly efficient bimetallic cooperativity.

During the hydroformylation process of 1-hexene, the norbornadiene groups in complex **1** are replaced by carbonyl groups, and as a result, tetracarbonyl, pentacarbonyl or hexacarbonyl complexes will be formed. This process is illustrated in Figure 2.5.

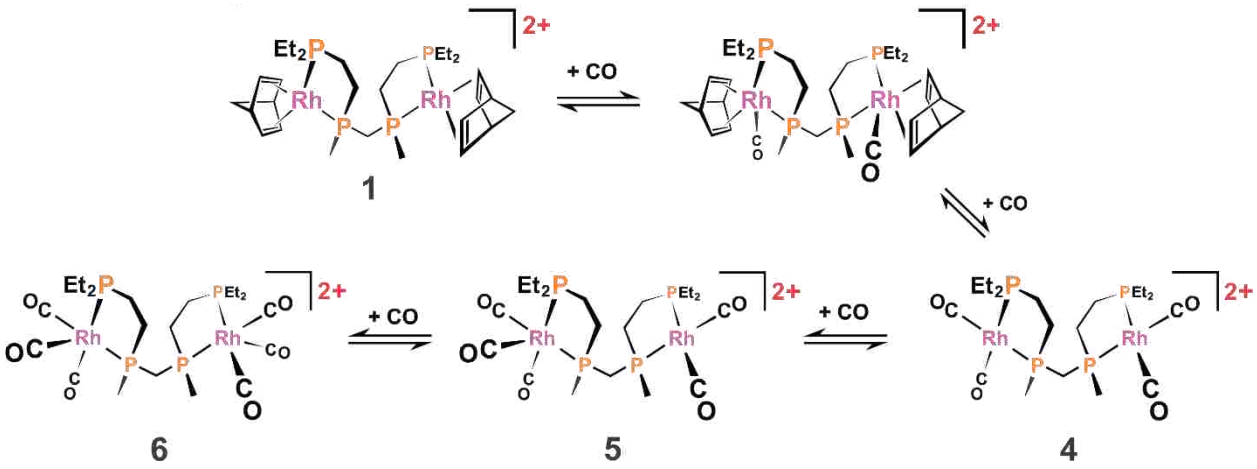

Figure 2.5. Reaction of $[Rh_2(nbd)_2(rac\text{-et,ph-P4})](BF_4)_2$ with C.

The calculations were initiated with complex **5** as it has been cyrstallographically characterized; hence, the experimental X-ray data can be compared with the calculated data (Figure 2.6). Complex **5** was optimized using several basis sets in order to determine whether one is significantly better than the others in reproducing the crystal structure. The basis sets include all electron basis sets as well as effective core potential sets for the Rh centers. The following basis sets were employed for the optimization of complex **5**.

1) Rh – 3-21G; C, H, O – 6-31G*; P – 3-21G*
2) Rh – 3-21G; C, H, O, P – 6-311G**
3) Rh – Lanl2DZ; C, H, O – 6-311G**; P – 6-31G**
4) Rh – Lanl2DZ; C, H, O, P – 6-311G**

2.3.1 Comparison of the experimental with calculated data of $[Rh_2(CO)_5(rac\text{–}meP4)]^{2+}$, 5

A detailed structural comparison of the experimental data with the calculated data of complex **5** is shown in Appendix 1. These data show a significant bond lengthening of one of the Rh–P bonds (Table 2.2).

Table 2.2. Comparison of Rh–P bond lengths of complex, 5.

	$Rh_2(CO)_5(et,ph\text{–}P4)^{2+}$ X-ray Bond Length (Å)	Rh 3–21G CHO 6–31G* P 3–21G* Bond Length (Å)	Rh Lanl2DZ CHO 6–311G** P 6–31G** Bond Length (Å)	Rh Lanl2DZ CHOP 6–311G** Bond Length (Å)	Rh 3–21G CHOP 6–311G** Bond Length (Å)
Rh1 P3	2.391	2.553	2.554	2.574	2.561
Rh1 P2	2.342	2.389	2.404	2.406	2.396
Rh47 P31	2.331	2.388	2.394	2.397	2.396
Rh47 P42	2.318	2.386	2.400	2.402	2.399

This implies that the bond lengthening of one equatorial Rh–P bond is independent from the basis set utilized. Figure 2.6 shows the DFT optimized complex **5** with its crystal structure. The two rhodium centers have different geometries; the 5-coordinate side shows distorted trigonal bipyramidal geometry with an 18 e- configuration, whereas the 4-coordinate side exhibits a square planar geometry and is 16e- with an empty orbital. Usually in trigonal bipyramidal geometry the equatorial bonds are longer than the axial bonds; hence, the equatorial Rh–P bond is longer than the axial Rh–P bond. In addition, the experimental as well as the calculated data show that Rh–CO bond distances on the square planar side are shorter than the Rh–CO bonds on the 5-coordinated side due to the presence of stronger π – back-bonding. These similarities suggest that irrespective of the basis set employed, significant bond lengthening of the one Rh–P bond is visible in all the calculated structures. Thus, the dependency of the geometry optimization upon the basis set employed is negligible.

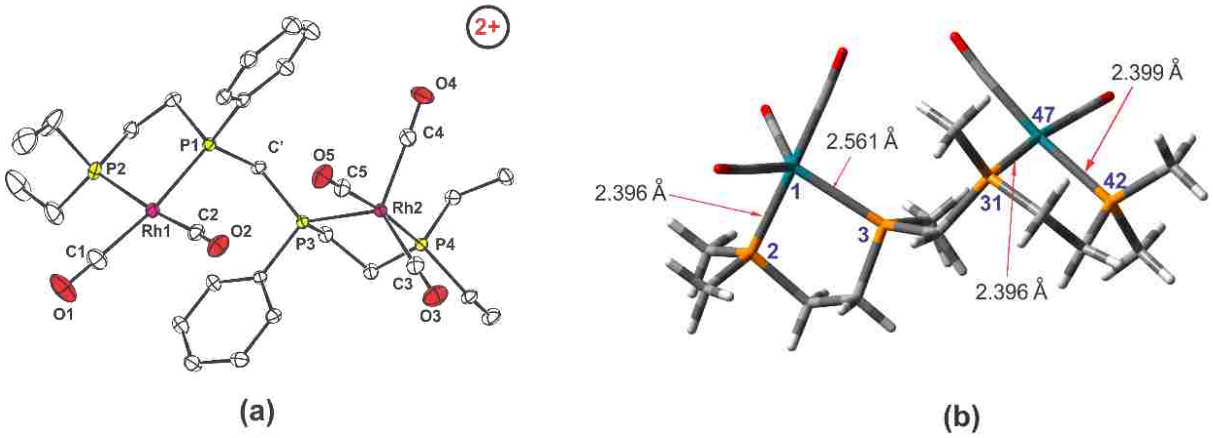

Figure 2.6. (a). ORTEP for [*rac*-$Rh_2(CO)_5$(et,ph-P4)]$^{2+}$, 5 (b). DFT calculated complex 5.

We did, however, observe what Prof. Stanley considered better energies for the various mechanistic steps in the catalytic cycle using the 6–311G** basis set on P, O, C and H atoms relative to using 3–21G* on P. Therefore, the larger 6–311G** basis set was used in all our calculations for P, O, C, and H atoms. Due to the cationic charge on the complex, it was felt that diffuse functions were not needed.

As the optimized structures were generally independent from the basis set employed, all electron basis sets were used to perform calculations on the rest of the structures of the mechanisms. All electron basis sets were employed instead of the effective core potential basis set - LanL2DZ because the bridging carbonyl complex, [*rac*–Rh_2(μ–CO)$_2$$(CO)_2$(me,me–P4)]$^{2+}$(**4***) opens up when the latter was used to optimize the Rh center. This is clearly demonstrated in Figure 2.7.

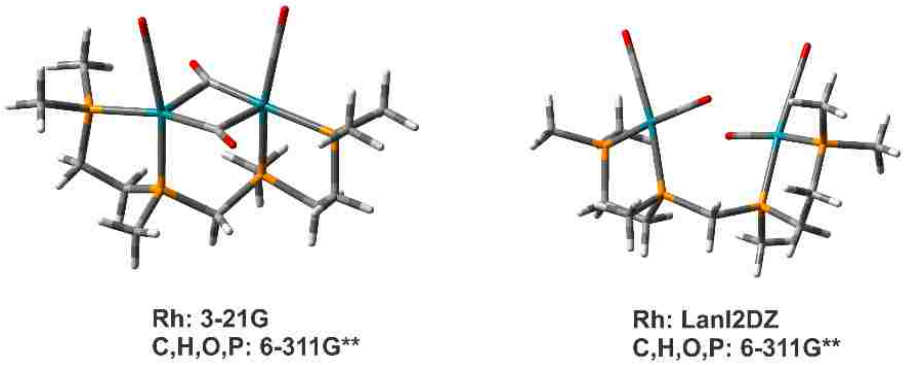

Figure 2.7. [*rac*–Rh_2(μ–CO)$_2$$(CO)_2$(me,me–P4)]2^{+}(4*) optimized using (a). 3–21G all electron basis set and (b). LanL2DZ for the Rh centers.

The experimental FT–IR data suggest the presence of bridging carbonyl complexes in the catalyst mixture, including the closed-mode version of **4***. Therefore, Rh was optimized using 3–21G basis set and C, H, O and P atoms using 6-311G** basis set.

The optimized hexacarbonyl (**6**) complex demonstrates a trigonal bipyramidal geometry at one Rh center and a square pyramidal geometry at the other. This complex, which is shown below in Figure 2.8 shows an unusually long Rh–CO bond with a distance of 2.305 Å and a bent orientation at the square pyramidal Rh center, strongly suggesting that the CO is only very weakly associated with that Rh center. The DFT calculation, therefore, supports the proposal that complex **6** does not exist. This may be due to the inductive effect between the two cationic Rh centers. This results in an electron deficiency in the metal centers disfavoring the association of a sixth CO ligand; hence, the square pyramidal geometry does not favor the coordination of a sixth CO.

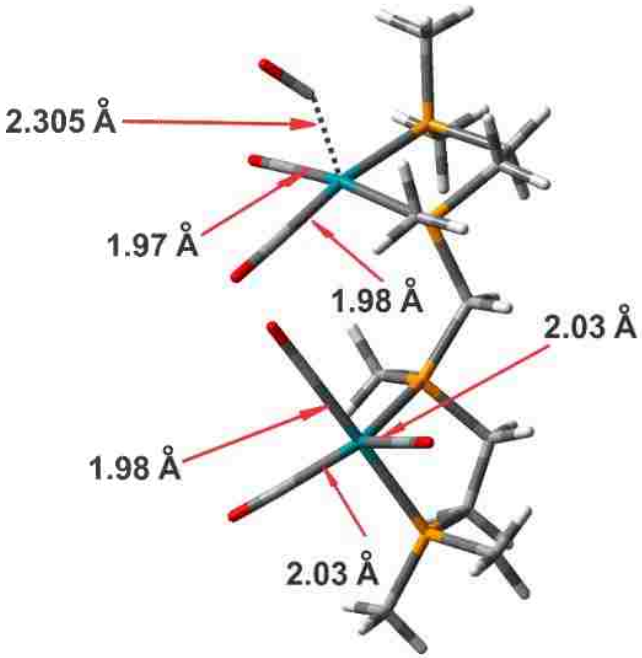

Figure 2.8. DFT optimized hexacarbonyl complex (6) with Rh–CO bond lengths.

The predicted instability of the hexacarbonyl (**6)** from the DFT calculation helps explain the FT–IR data from the reaction of the $[Rh_2(nbd)_2(rac\text{–}et,ph\text{–}P4)]^{2+}$ complex with CO in acetone. The FT–IR spectrum collected by Dr. Catherine Thomas Alexander on this reaction is shown below in Figure 2.9.

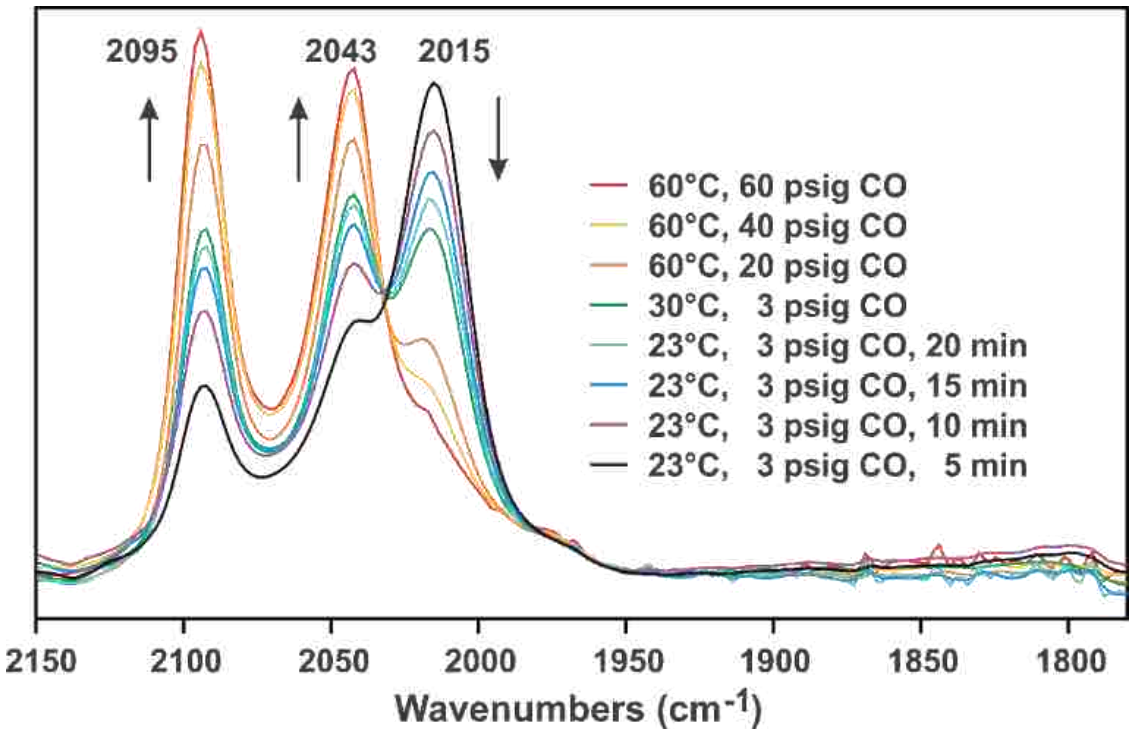

Figure 2.9. *In situ* FT–IR spectra of $[Rh_2(nbd)_2(rac\text{–}et,ph\text{–}P4)]^{2+}$ reacting with CO at various pressures and temperatures.

The single CO band at 2015 cm^{-1} forms immediately upon addition of CO to the $[Rh_2(nbd)_2(rac\text{–}et,ph\text{–}P4)]^{2+}$ complex. This represents the simple 18e- CO adduct species, $[Rh_2(CO)_2(nbd)_2(rac\text{–}et,ph\text{–}P4)]^{2+}$. But this species quickly loses the norbornadiene ligands and adds more CO ligands to form what Prof. Stanley now assigns as the pentacarbonyl species **5**. The reaction must go through the open-mode tetracarbonyl complex **4**, but it must be very reactive towards CO to form the pentacarbonyl **5** as no sign of absorbance related to **4** are visible in the series of spectra in Figure 2.9.

Due to the extremely fast timescale of IR spectroscopy, it is highly unlikely that a rapidly interconverting mixture of **5** and **6** would give such a simple spectrum with just two carbonyl bands at 2095 cm^{-1} and 2043 cm^{-1}. The DFT calculation on **5** predicts two carbonyl bands with a separation of 48 cm^{-1} compared to the experimental separation of 52 cm^{-1} (Figure 2.11). The DFT prediction that **5** does not want to coordinate a CO to form **6** supports that **5** is the main species under low to moderate pressures of CO.

This is further supported by the work performed by Kalck and coworkers.[31] The square pyramidal $[Rh(CO)_3\{(R,R)-Ph-BPE\}]^+$ ((R,R)-Ph-BPE = 1,2–bis[(R,R)–2,5–diphenylphospholano]ethane) complex synthesized by Kalck and coworkers, has a very long Rh–CO bond distance (Rh1–C5 = 2.219 Å) at the square pyramidal Rh center (Figure 2.10a). This indicates that the apical CO is very weakly coordinated to the Rh center. This is due to the cationic charge on the complex that contracts the metal d-orbitals and reduces the Rh-CO π-backbonding. This mainly affects the apical Rh-CO bond due to the presence of the filled d_z2 orbital that has a repulsive interaction with the filled CO lone pair orbital. Their DFT optimized structure of the monocationic Rh complex showed a distorted trigonal bipyramidal geometry at the Rh center. The axial Rh–CO bond had a shorter length of 1.949 Å, which is consistent with weaker coordination of the axial ligand, but not as large an effect as shown in the crystal structure.[31]

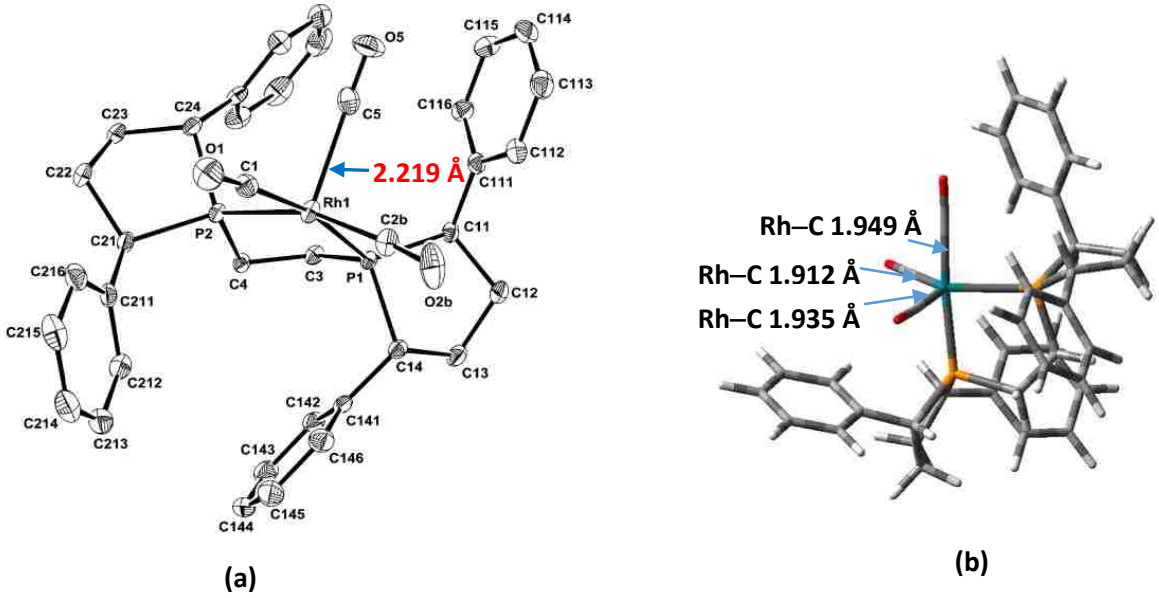

Figure 2.10. (a). Experimentally synthesized and (b). the calculated $[Rh(CO)_3(P_2)]^+$ by Kalck and coworkers with Rh–CO bond lengths.[19]

We performed DFT calculations on our dicationic hexacarbonyl complex **6** starting with trigonal bipyramidal geometries at the Rh centers. This resulted in a square pyramidal geometry at one of the Rh centers with very weak coordination of the sixth CO ligand: Rh–CO = 2.305 Å. This compares well with the long Rh-CO distance of 2.219 Å from the X-ray structure on Kalck's cationic $[Rh(CO)_3(P_2)]^+$ system.

Our dirhodium complex is dicationic, which results in an increased inductive effect and a higher electron deficiency in comparison to the monocationic complex by Kalck.[31] This may be why our calculation on **6** had one long Rh-CO bond, while Kalck's DFT calculation showed a much smaller bond increase.

Vibrational frequencies were calculated for the structures to be compared with the experimental IR data. The calculated stretching frequencies were scaled by 0.93, which was determined using experimental and calculated vibrational frequencies of dirhodium complexes. The vibrational frequencies of the pentacarbonyl (**5**) and tetracarbonyl (**4**) complexes and the experimental spectra obtained at low and high pressures are shown in Figure 2.11. These spectra demonstrate that at the experimental low and high pressures a mixture of pentacarbonyl (**5**) and tetracarbonyl (**4**) complexes exists.

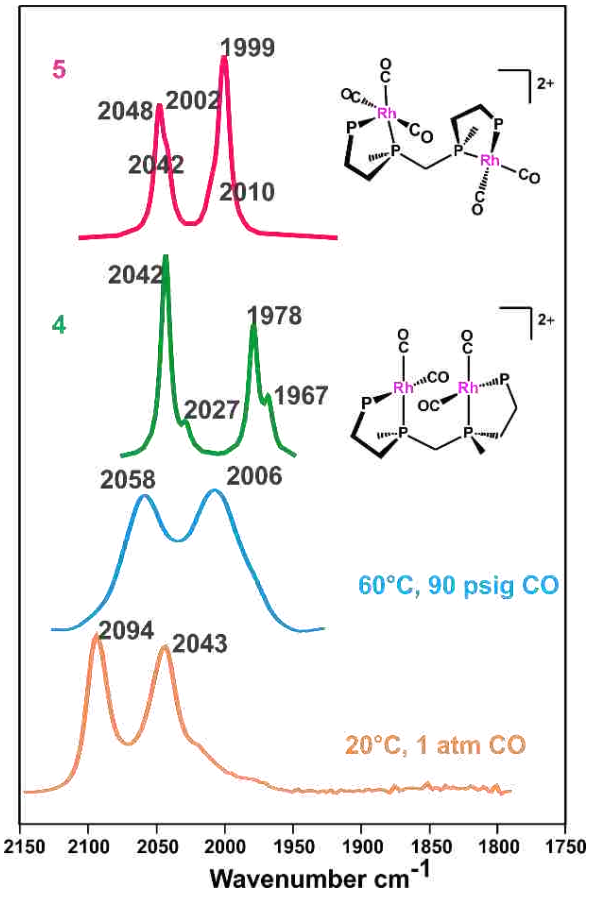

Figure 2.11. Calculated and experimental vibrational spectra of 4 and 5.

As the CO groups are further apart in the open-mode conformer of **4** the calculated CO bands are closer to being degenerate and form two distinct bands. As a fully alkylated model is used for the P4

ligand in DFT computations the CO bands will be somewhat lower in wavenumber relative to P4 ligand used in experimental work which is not quite as donating.

2.3.2 Dicationic Hydroformylation Mechanism

Prof. Stanley's proposed mechanism for hydroformylation is shown below in Figure 2.12.[32] The catalysis cycle begins with the oxidative addition of hydrogen to one of the Rh(+1) centers in the pentacarbonyl complex (**5**) forming complex **A**. Complex **A** will convert from an open mode geometry to a closed mode conformation via an intramolecular hydride transfer resulting in complex **2***, which contains a bridging hydride and a bridging carbonyl. The first bimetallic cooperativity step is demonstrated in this complex to distribute the two hydrides, so that one hydride is on each Rh center, which is optimal for hydroformylation. It is proposed that complex **2** undergoes rearrangement to form the symmetrical terminal dihydride complex **2****. Then a dissociation of the carbonyl group will occur forming a vacant site for alkene coordination. This is followed by migratory insertions and associations of carbonyl groups. The reductive elimination will produce the aldehyde ultimately regenerating the pentacarbonyl complex **5**.

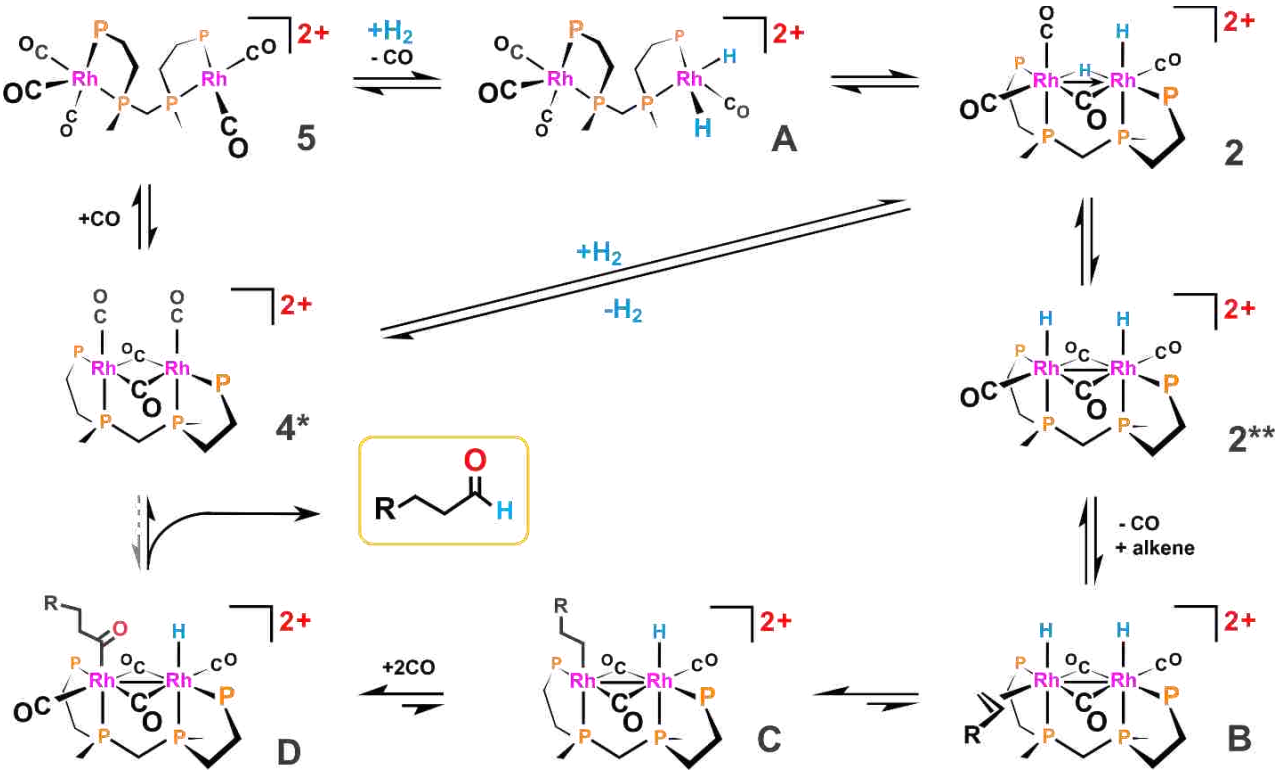

Figure 2.12. Previous proposed mechanism for hydroformylation in acetone.[32]

DFT computations show the oxidative addition of H_2 to form the open-mode dihydride, **A** is uphill by +10.7 kcal/mol. The activation barrier for this step is 10.4 kca/mol (Figure 2.13). Complex **A** then converts to a closed-mode complex (**2**, **2*** or **2****) with bridging ligands to enhance bimetallic cooperativity.

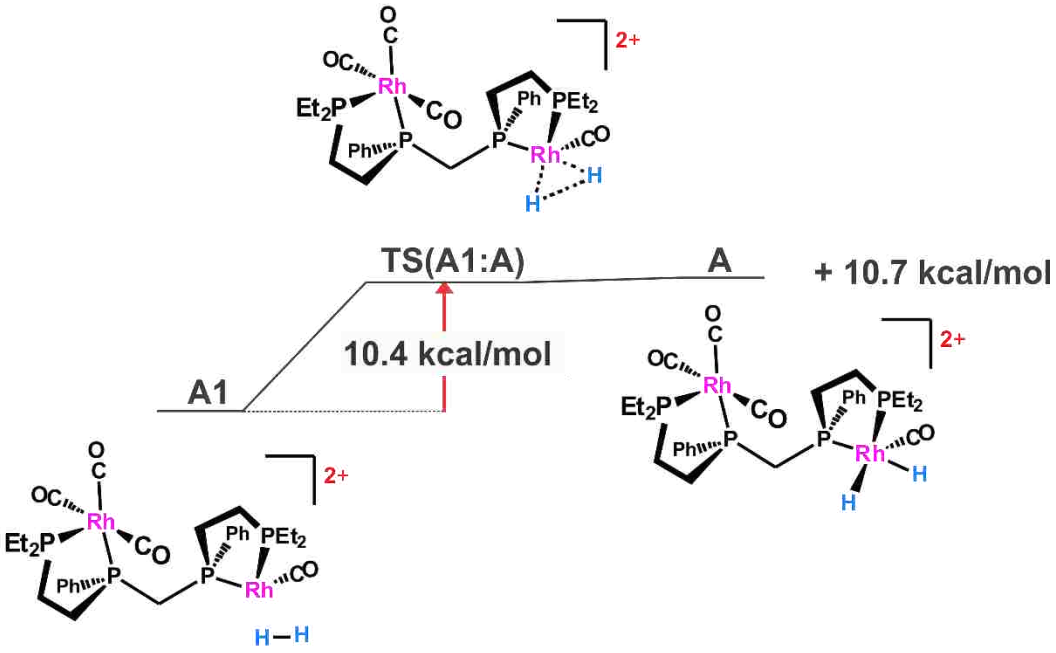

Figure 2.13. Activation barrier for H_2 oxidative addition.

Both rhodium centers in **2**** are in the +2 oxidation state, which corresponds to a d^7 electronic configuration. Based on electron-counting one would predict a Rh–Rh single covalent bond for **2**** (as drawn in the mechanism), which is supported by the DFT calculations. The terminal CO ligands are predicted to be extremely labile due to the dicationic charge on the complex that compensates for the strongly donating phosphine ligands. This will minimize the π–back-bonding and weaken the Rh-CO bonding.

The edge-sharing bioctahedral structure, however, is highly unusual for dirhodium(+2) complexes. Most Rh(+2)–Rh(+2) structures have the "lantern" D_{4h} type geometry with two axial ligands that are usually weakly coordinated (Figure 2.14). Transforming the D_{4h} type geometry to an edge-sharing bioctahedral structure should transfer the weak coordination of the axial ligands to all four of the outermost ligands. This contributes to the CO lability, but also, unfortunately, should also weaken the

coordination of the terminal phosphine ligands, which appears to be a major source of catalyst fragmentation and deactivation.

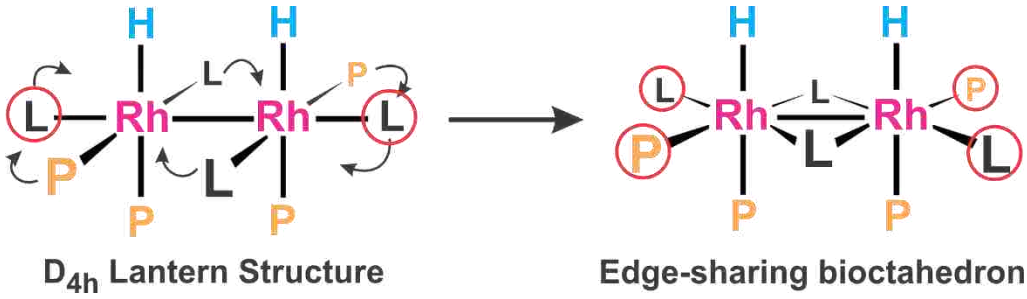

Figure 2.14. Conversion of a lantern structure to edge-sharing bioctahedral. Circled ligands have weaker bonding to the Rh centers.

One of the major considerations in analyzing the mechanism computationally is the identification of the active catalyst that reacts with the alkene. The experimental observations have confirmed that several bridging carbonyl complexes exist in the reaction mixture. *In situ* FT−IR results have shown bridging carbonyl bands with different intensities and shapes. It is been proposed that complex **2** and symmetrical complexes **2*** and/or **2**** exist in dynamic equilibrium. Due to the presence of the bridging carbonyl bands in the FT-IR spectra (1834 cm^{-1} and 1819 cm^{-1}) in acetone (Figure 2.15), Prof. Stanley for many years strongly favored the terminal dihydride complex with two bridging carbonyls, **2****. This was also tied into the common perception in the organometallic community that terminal hydrides are more reactive than bridging hydrides for doing a migratory insertion with an alkene substrate.

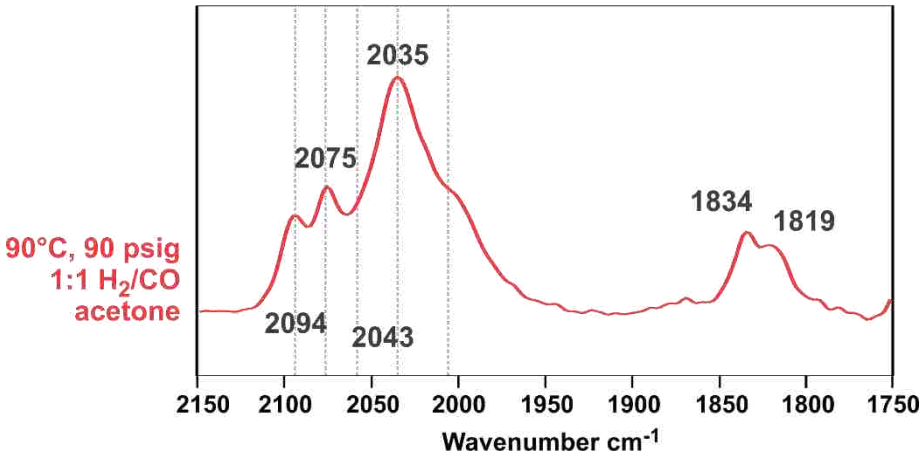

Figure 2.15. Experimental FT-IR spectrum of catalyst mixture in acetone.

The experimental ^{1}H NMR of the hydride region of the dicationic dirhodium catalyst mixture is given below in Figure 2.16.

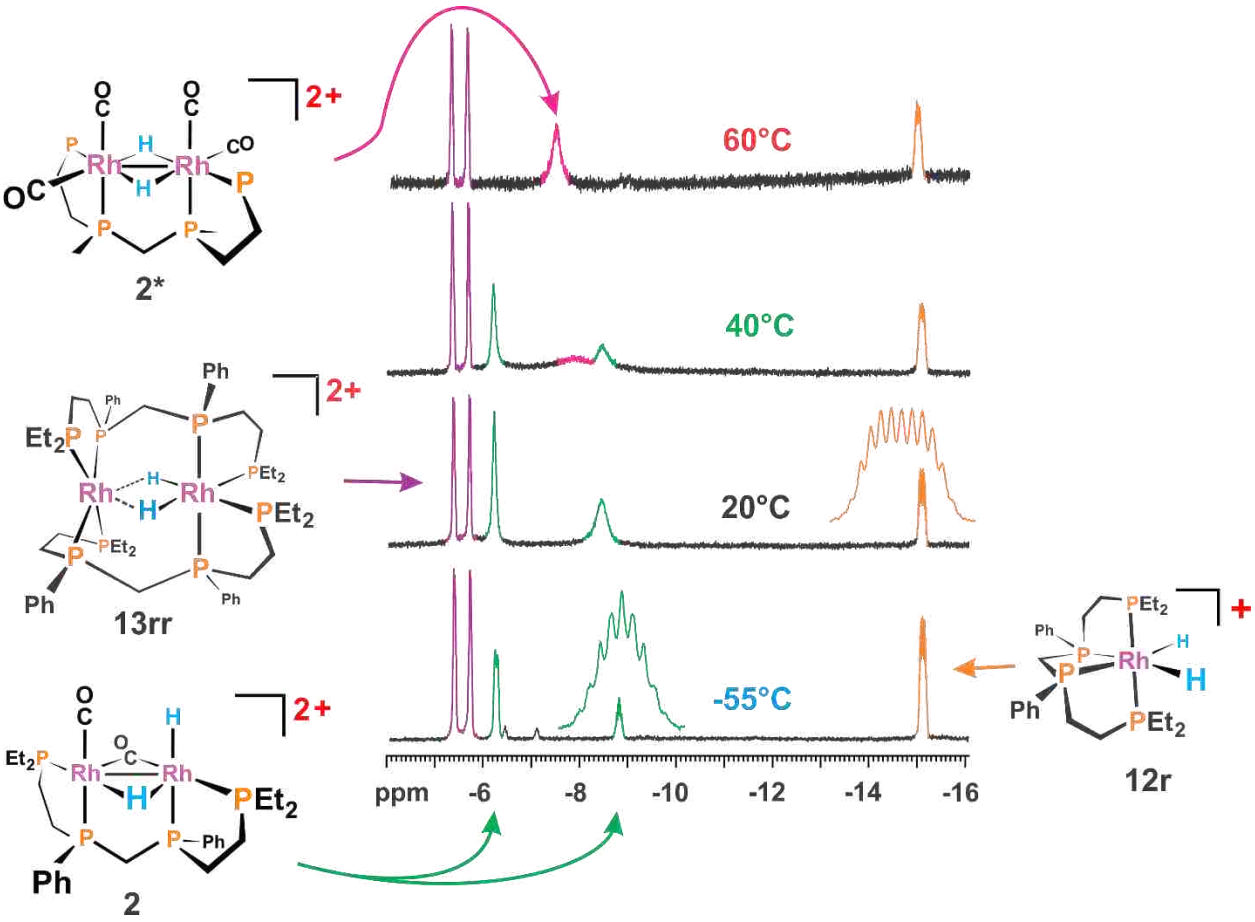

Figure 2.16. ^{1}H NMR of the hydride region of the bimetallic catalyst in acetone with updated assignments from the DFT calculations.

The peaks at –5.6 and –15.1 ppm are independent from temperature and are due to two fragmentation species: the catalytically inactive monometallic dihydride complex, $[RhH_2(\kappa^4\text{-}rac\text{-et,ph-P4})]^+$ (**12r**), and the double ligand coordinated complex $[Rh_2H_2(rac\text{-et,ph-P4})_2]^{2+}$ (**13rr**), which we believe is responsible for most of the alkene isomerization and hydrogenation side reactions. According to the experimental ^{1}H NMR, at low temperatures a pseudo-nonet pattern is observed at –8.8 ppm, which has been assigned to a bridging hydride due to the extensive coupling pattern corresponding to coupling with two spin ½ Rh centers, up to four phosphines, and the terminal hydride. The hydride resonance at –6.3 ppm is assigned to a terminal hydride and is not fully resolved at this temperature. Therefore; at –55°C,

the unsymmetrical **2** is the primary and lowest energy hydroformylation catalyst that exists in solution. As the temperature is raised the peaks at –6.3 ppm and –8.8 ppm coalesce to produce a single broad hydride resonance appointing to an exchanging symmetrical complex consistent with the bridging dihydride complex **2*,** or the terminal dihydride complex **2****.

The DFT calculations were performed on these isomeric complexes in order to find the key catalyst species that reacts with the alkene. The unsymmetrical complex **2** gives the lowest total energy resulting in a relative energy of 0.00 kcal/mol. The symmetrical bridging dihydride complex **2*** has a slightly higher energy of 0.6 kcal/mol, while the terminal dihydride complex **2**** is 12.3 kcal/mol higher than **2** (Figure 2.17). Complexes **2** and **2*** have similar energies whereas the terminal dihydride **2**** has a significantly higher energy. The experimental ^{1}H NMR spectra clearly shows the presence of unsymmetrical **2*** at low temperatures and the question remains as to the structure of the active symmetrical dihydride catalyst that forms at higher temperatures: **2*** or **2****?

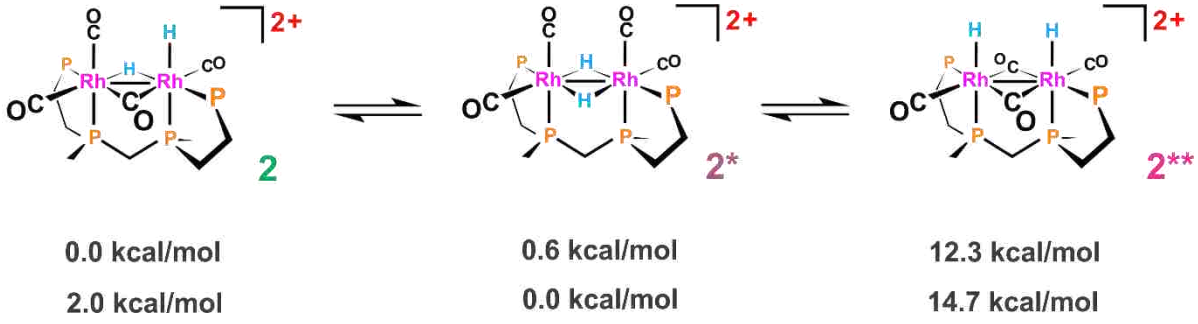

Figure 2.17. Dynamic equilibrium between 2, 2* and 2**.

Hydroformylation activity is observed at higher temperatures and at such temperatures bridging carbonyl bands are observed in the FT–IR spectrum at 1834 cm^{-1} and 1819 cm^{-1}. According to the calculated stretching frequencies, complex **2**** has a bridging carbonyl band at 1821 cm^{-1}. Even though complex **2*** does not have any bridging carbonyls, DFT data suggests some of the intermediates in the catalytic cycle of **2*** should have a bridging carbonyl with a calculated band at 1834 cm^{-1}. In order to determine the active catalyst and the correct pathway, the hydroformylation cycle was analyzed computationally utilizing both complexes **2*** and **2**** to study the activation energies for the various steps in the hydroformylation cycle.

The Rh centers are in the +2 oxidation state in **2**, **2*** and **2**** and this enables the formation of a covalent bond between the two metal centers. This is supported by DFT calculations as the Rh-Rh bond distances are 2.886 Å, 2.892 Å and, and 2.969 Å in **2**, **2*** and **2**** respectively. This results in a closer proximity between the metal centers favoring bimetallic cooperativity and intramolecular transfers between metal centers. The Rh-Rh bonding and bridging ligands minimize the geometry reorganizations about the metal centers and this enhanced steric environment favors the insertion of an alkene into M-H bond to form a linear alkyl group which in turn goes on to form the linear aldehyde product.

2.3.2.1 DFT studies on hydroformylation using complex 2** as the active catalyst

Alkene Coordination and Insertion

We started with the higher energy **2**** catalyst as the starting point because this is what Prof. Stanley has proposed for many years. Hydroformylation catalysis begins with the generation of 16-electron unsaturated catalyst species. This is achieved via a ligand dissociation from the active catalyst complex **2****, so a carbonyl group will dissociate generating a vacant site for the alkene coordination (complex **2****$^{\#}$, Figure 2.18). Even though the phosphine groups are strong electron donors, the cationic charge on the metal centers reduces the π–back-bonding to the carbonyl groups making dissociation much easier. This is a key factor in the high activity of this catalyst system. The calculations find that the CO dissociation is endothermic by 18.2 kcal/mol.

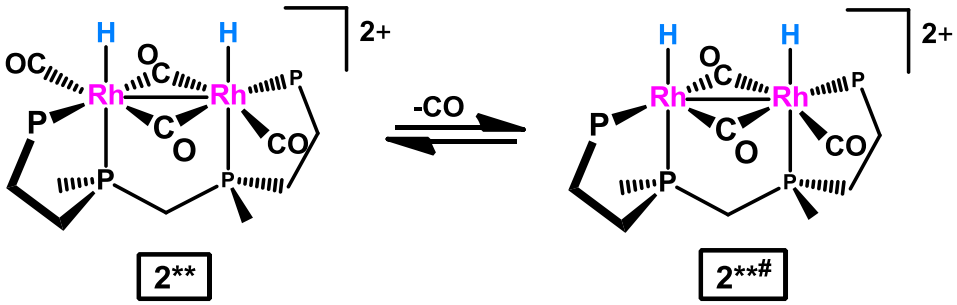

Figure 2.18. CO dissociation from complex 2**.

The alkene then coordinates to the unsaturated complex **2****$^{\#}$ in the equatorial position with C=C bond coordinated perpendicular to the plane, forming complex **B**. This coordination is downhill by 14.1

kcal/mol. The previous modeling studies on hydroformylation using monometallic Rh catalysts with phosphines and carbonyl ligands show that the olefin addition to the catalyst complex is exothermic, but these values are larger than the values obtained from our studies.[19, 33] This may be due to the different computational methods utilized or, most likely because of the dicationic charge that reduces the Rh-CO π-backbonding. The ethylene coordination to **2**#** results in lengthening of the C=C bond from 1.327 Å to 1.366 Å, consistent with donation of some of the ethylene π-bonding electron density to the Rh center.

Once the alkene coordinates it can insert into the Rh–H bond forming an alkyl group (**C1**). The transition state showing the insertion between the alkene and the hydride is shown below in Figure 2.19. The alkene rotates to the axial position while the hydride moves to the equatorial position and the methylene group of the alkene aligns with the hydride for the insertion. The neutral alkene ligand inserts into anionic hydride–Rh bond and generates an alkyl group, so an empty coordination site is created at the equatorial position where the alkene was originally coordinated. The vibrational frequency studies confirmed the generation of the transition state by producing only a single imaginary frequency and the animation shows the correct normal mode vibration for the insertion step (see Appendix 2). The calculations show that the olefin insertion is exothermic by 10.5 kcal/mol. The calculated activation barrier for the insertion of a double bond into the Rh–H bond is 23.2 kcal/mol.

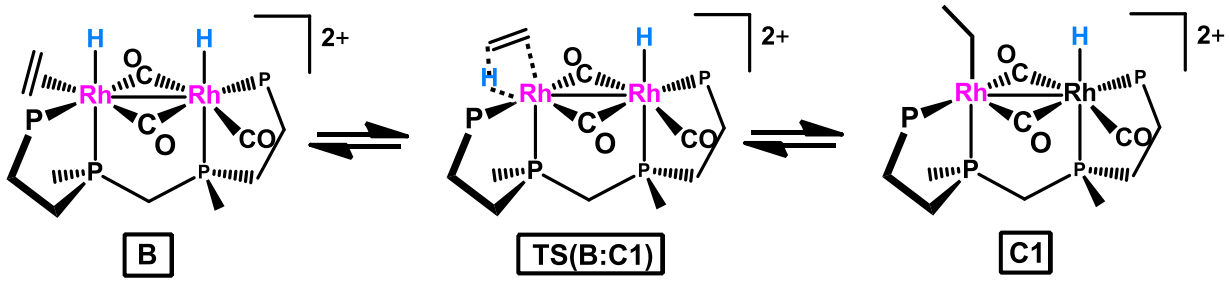

Figure 2.19. Hydride insertion.

The Rh–H bond distance in transition state geometry (**TS(B:C1**)) is longer than **B** by 0.034 Å as shown below in Figure 2.20. The C–C bond distance is elongated by only 0.024 Å in **TS(B:C1)** with respect to the ethylene adduct (**B**) C=C bond distance, but the resulting C–C single bond distance is, as expected 0.129 Å longer than the C=C double bond. The Rh–C bond of alkyl group is 0.27 Å shorter than

the Rh-C bond of ethylene adduct (**B**), which is also expected. These differences in geometries all agree well with the conversion of an alkene to alkyl group.

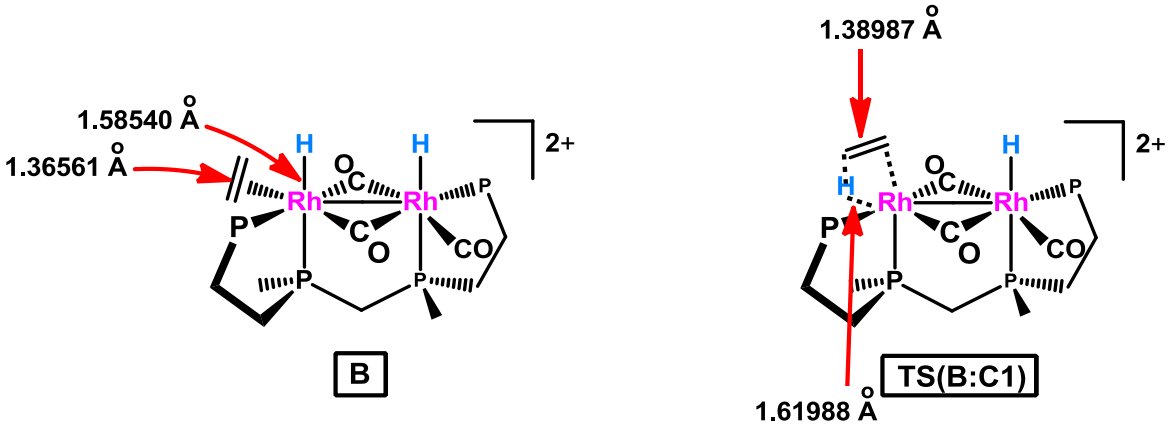

Figure 2.20. Comparison between B and TS(B:C1).

CO Addition and Insertion

The next step in the catalytic cycle is the coordination of a CO group to complex **C1** to produce an 18-electron complex **C2** (Figure 2.21). The CO addition is exothermic by 10.6 kcal/mol, consistent with the weaker Rh-ligand bonding expected for this coordination site (see Figure 2.14 and related discussion). The CO coordination increases the bond distance between Rh and the bridging CO's by 0.06 Å. The addition of CO will decrease the π-back bonding and results in lower CO stretching frequencies for **C2**. The stretching frequency of the bridging CO's was decreased by about 9 cm^{-1} in **C2,** while the terminal CO's decreased by 3 cm^{-1}.

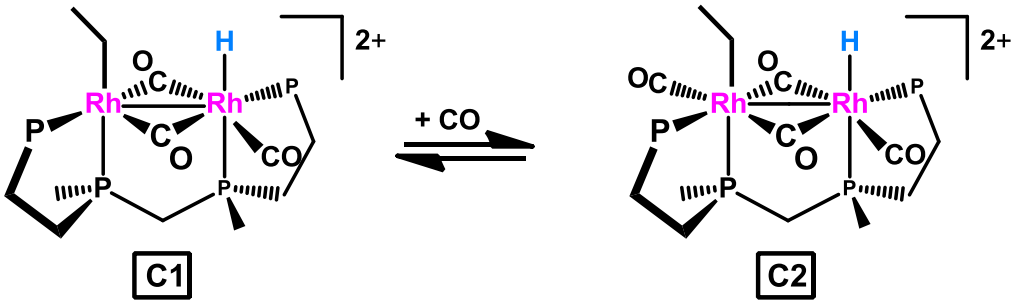

Figure 2.21. CO addition to C1.

The CO ligand in complex **C2** then undergoes a migratory insertion between the alkyl group and the carbonyl group to form complex **D1,** which results in 16- and 18-electron Rh centers. The calculations show that the CO insertion is exothermic by 3.7 kcal/mol. The calculated activation barrier for the CO insertion step is extremely small, only 0.7 kcal/mol (Figure 2.22) and the vibrational frequency studies confirm that **TS(C2:D1)** is a transition state by having a single imaginary frequency which matches with the correct vibrational mode for CO insertion (see Appendix 2). The Rh–C_{ethyl} bond in the **TS(C2:D1)** structure is 0.23 Å longer than in **C2**, while the Rh–CO bond is shortened by 0.097 Å. The CO–C_{ethyl} bond distance decreases by 0.83 Å in **TS(C2:D1)** illustrating the formation of the OC-alkyl bond in the transition state.

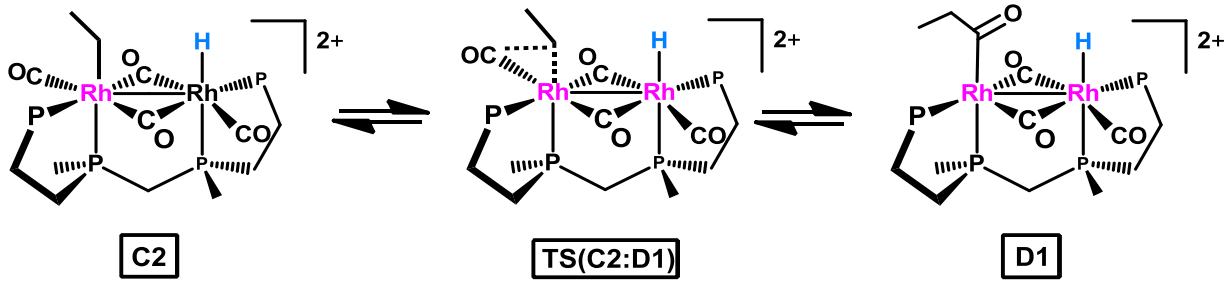

Figure 2.22. CO insertion.

A CO group will coordinate to **D1** generating the 18-electron Rh complex, **D2** (Figure. 2.23), which is exothermic by 13.2 kcal/mol.

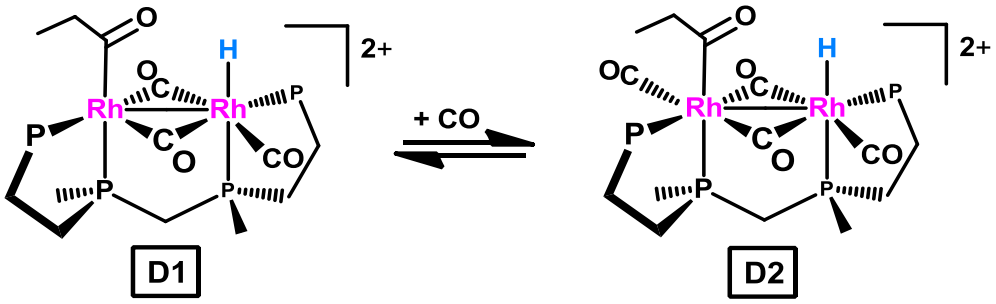

Figure 2.23. CO addition to D1.

Aldehyde Reductive Elimination

Finally, the reductive elimination of the aldehyde will take place forming complex **G**. The hydride and the acyl group in complex **D** are *cisoidal* to each other and they are separated by only 3.51 Å. These factors make the reductive elimination favorable. As shown below in Figure 2.24 the hydride ligand bends towards the acyl carbon to facilitate the elimination via a direct bimetallic reductive elimination. This step corresponds to downhill energy of –27.77 kcal/mol. This demonstrates the feasibility of a direct bimetallic reductive elimination of the aldehyde across two metal centers. The calculated activation barrier for this step is 20.9 kcal/mol. The calculations indicate that **TS(D2:G)** is a transition state by having a single imaginary frequency with the correct vibrational mode that matches with the aldehyde reductive elimination (see Appendix 2). The Rh–$C_{aldehyde}$ bond is 0.59 Å longer in **TS(D2:G)** than in **D2** and $C_{aldehyde}$–H distance, corresponding to bond formation, is decreased by 1.38 Å in the transition state. The formation of the transition state from **D2** is shown below in Figure 2.24.

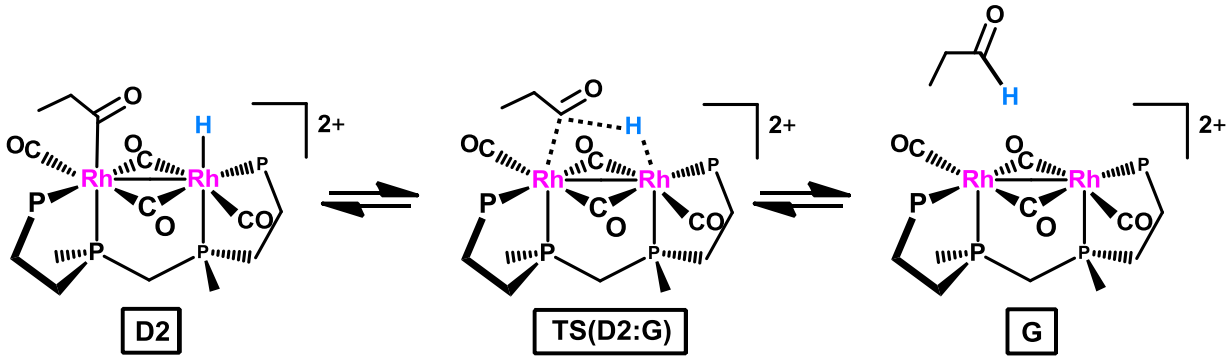

Figure 2.24. Reductive elimination of the aldehyde.

As the activation barrier for reductive elimination of the aldehyde was quite large the possibility for the rearrangement of the terminal hydride in **D2** to a bridging position was examined. DFT studies show that the rearrangement is downhill by –6.88 kcal/mol (Figure 2.25). Due to the rearrangement of the terminal hydride to the bridging position the separation between the acyl group and the hydride is lowered by 0.78 Å favoring the reductive elimination of the aldehyde.

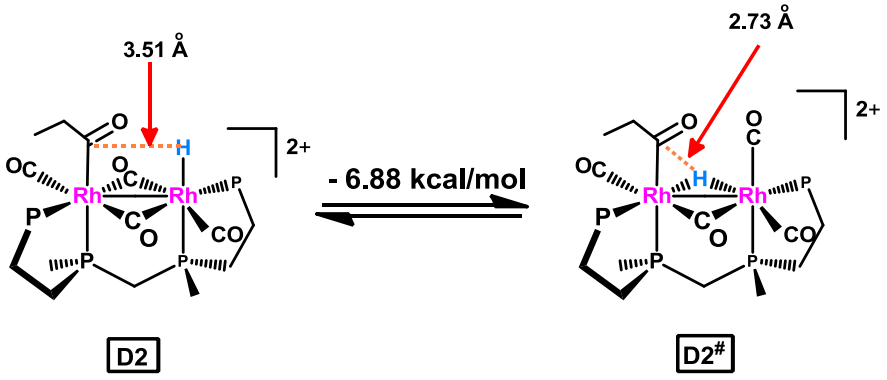

Figure 2.25. Conversion of terminal hydride in D2 to a bridging position.

The corresponding transition states for the reductive elimination with the terminal hydride and the bridging hydride are shown below in Figure 2.26. The activation barrier for the reductive elimination with the bridging hydride is 15.3 kcal/mol which is 5.6 kcal/mol lower than the terminal hydride reductive elimination and the corresponding free energy profiles for reductive elimination are shown below in Figure 2.27. In **TS(D2:G)** both the acyl group and the hydride move towards each other to facilitate the reductive elimination whereas in the bridging hydride transition state (**TS(D2$^{\#}$:G$^{\#}$)**, the bridging hydride move towards the acyl group. The distance between the acyl group C and hydride is 0.07 Å lower in **TS(D2$^{\#}$:G$^{\#}$)** than in **TS(D2:G)**. These structural orientations suggest that the reductive elimination of the aldehyde product is facilitated through the rearrangement of the terminal hydride to a bridging position.

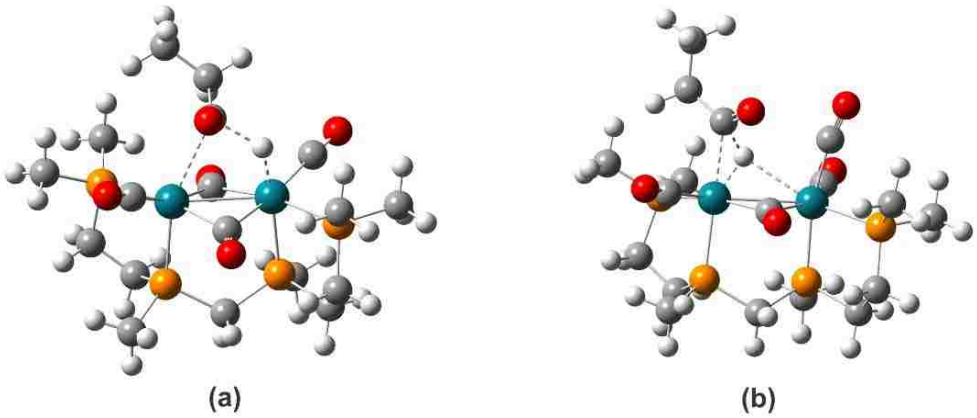

Figure 2.26 Transition states for (a) Reductive elimination from terminal hydride (TS(D2:G)) (b) Reductive elimination after rearrangement of terminal hydride to a bridging position (TS(D2#:G#)).

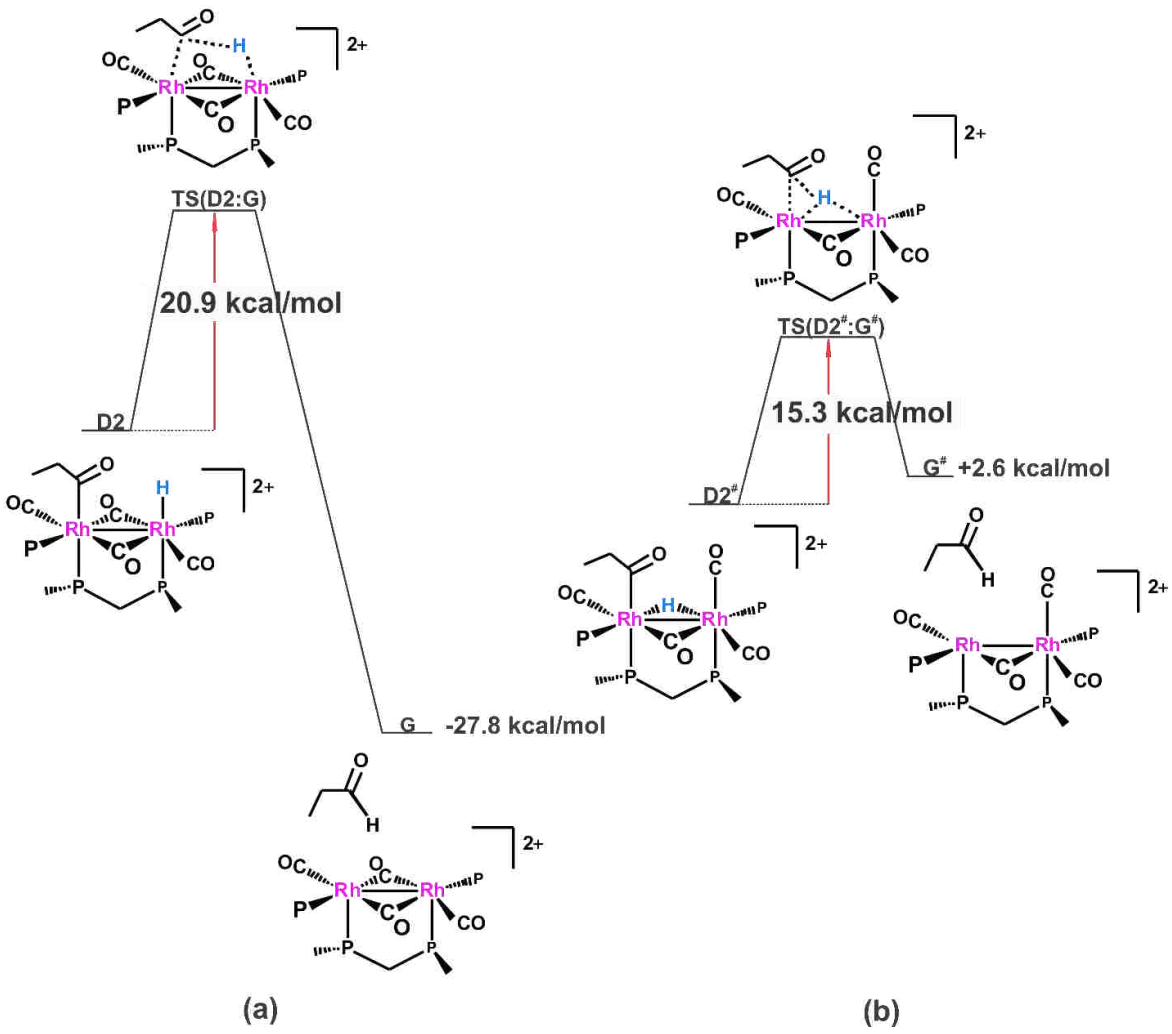

Figure 2.27. Activation barriers for (a) Reductive elimination from terminal hydride (b) Reductive elimination after rearrangement of terminal hydride to a bridging position (For clarity chelate phosphine ligand is removed).

Complex **G**$^{\#}$ will convert to a closed mode symmetric structure without bridging carbonyls (complex **4***$^{\#}$), and this step is downhill by -24.7 kcal/mol. This will then react with carbon monoxide to regenerate the open mode complex **5** (Figure 2.28) and this corresponds to an energy change of +8.8 kcal/mol.

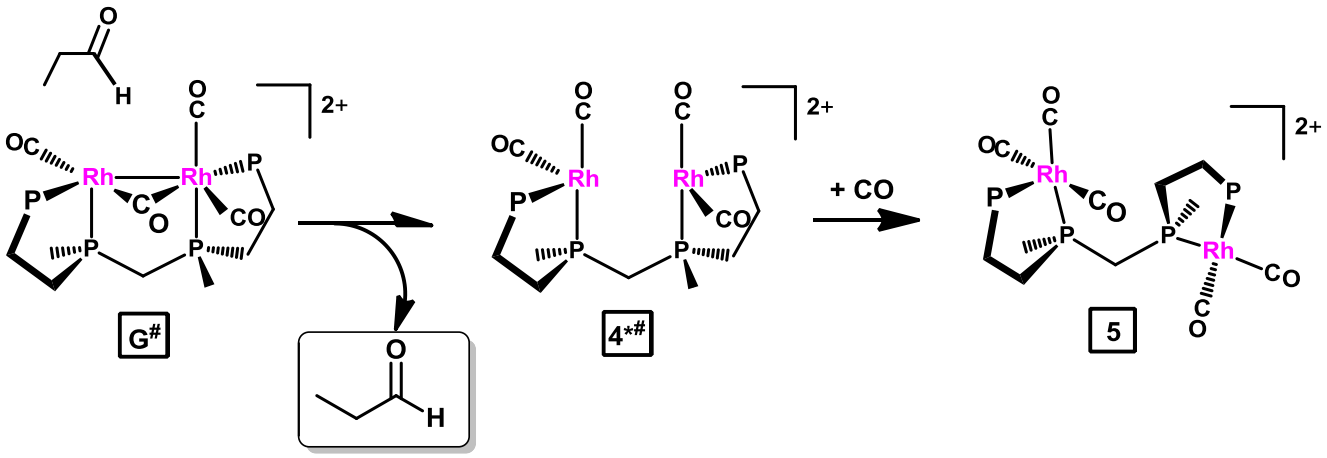

Figure 2.28. Regeneration of complex 5.

The free energy profile for hydroformylation using the dicationic terminal dihydride complex is shown in Figure 2.29.

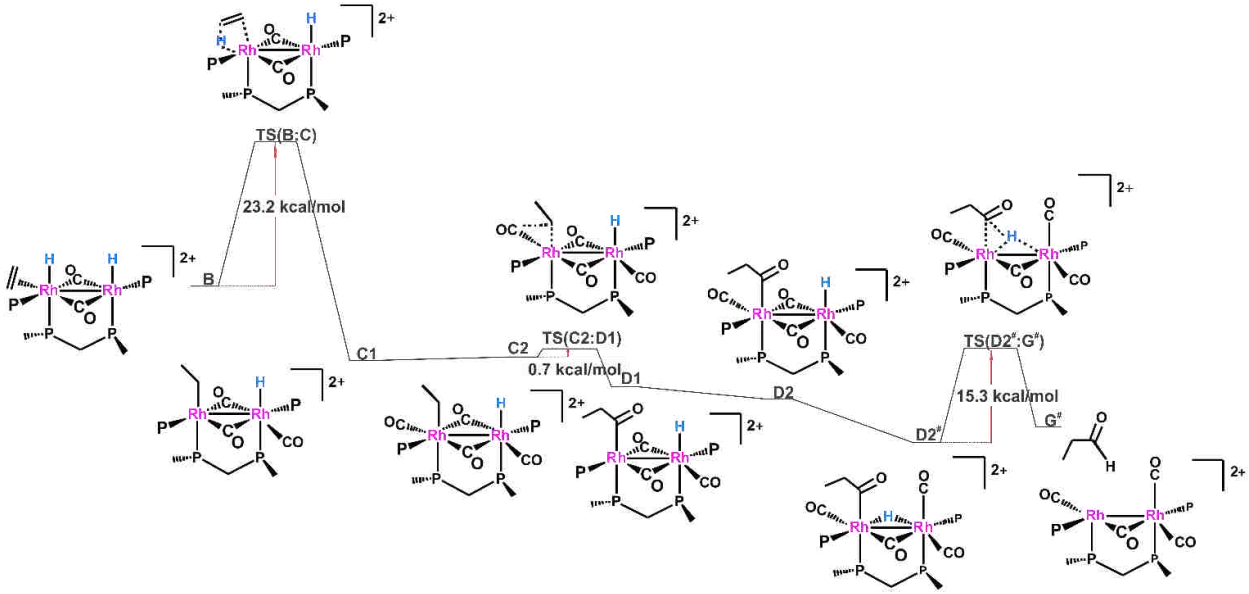

Figure 2.29. Free energy profile for hydroformylation using the dicationic terminal dihydride catalyst 2** (For clarity chelate phosphine ligand is removed).

The rate-determining step in this cycle is the migratory insertion of the alkene and hydride that take place in the beginning of the reaction sequence. The rate-limiting step in hydroformylation depends on the catalyst, the reaction conditions used, and the computational methods utilized to study the catalytic cycle. According to studies performed by other research groups, the rate limiting step when $HCo(CO)_3$ is

used at BP86 level was found to be the CO insertion step[34], whereas when $HRh(CO)_2(PH_3)_2$ was used at MP2/HF level the rate determining step was the H_2 oxidative addition step[35].

2.3.2.2 DFT studies on hydroformylation using complex 2* as the catalyst

Alkene coordination and Insertion

The DFT computational results for using the dicationic bridging dihydride species **2*** is reported in this section. The catalytic cycle begins with CO dissociation followed by alkene coordination to the vacant site on the Rh center. CO dissociation from **2*** is endothermic by 12.3 kcal/mol, which is lower by 5.9 kcal/mol relative to the dissociation from **2**** (18.2 kcal/mol). Dissociation of a CO ligand results in 0.1 Å decrease in $Rh_{unsaturated}$–P bond length of **2*** but significant changes in Rh–P bond lengths are not observed in **2****. This is likely due to the σ-*trans* effect of the bridging hydrides in **2*** that favors the dissociation of a *trans*-carbonyl group, and consequently the stronger electron donation of phosphine to the metal center resulting in a somewhat shorter Rh–P bond distance.

Alkene coordination to **2*,** on the other hand, corresponds to an uphill energy change of 6.3 kcal/mol, which is 7.9 kcal/mol higher than that for the coordination of alkene to **2****. The strong σ–σ *trans* effect of bridging hydride and phosphine ligands results in a higher electron density at the metal center of **2***, which accounts for the higher energy requirement for the alkene coordination to **2***. The π-accepting bridging carbonyl groups in complex **2**** favor coordination of an electron-donating alkene. The alkene coordinates to **2*** in the equatorial position with C=C bond perpendicular to Rh-Rh bond.

Once the alkene is coordinated, the hydride inserts into C=C bond forming an alkyl group. This generates the mono bridged hydride complex, **2*C**. The alkene remains in the equatorial position and the C atom not bonded to Rh bends towards the bridging hydride *cis* to it for the transition state **TS(2*B:2*C)** (Figure 2.30). As a single imaginary frequency was obtained corresponding to the correct vibrational mode, the presence of the transition state was confirmed (see Appendix 2). The C=C bond length is increased by 0.08 Å in **TS(2*B:2*C)** with respect to the ethylene adduct, **2*B**. C–C bond length is elongated by 0.16 Å in the alkyl group. The hydride insertion appears to be more favorable in **2*** than in **2**** as the activation barrier is only 8 kcal/mol, which is 15.2 kcal/mol less in energy than in **2****.

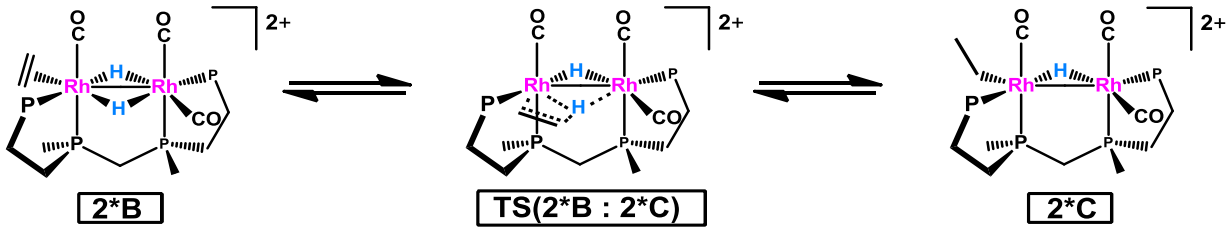

Figure 2.30. Hydride insertion.

Because the experimental IR data show two bridging carbonyl peaks the possibility of formation of a double -bridged complex was also studied. The mono bridging hydride complex was converted into a complex with a bridging hydride and a bridging carbonyl (**2*C1**) (Figure 2.31). This conversion appears to be thermodynamically feasible and corresponds to a downhill energy of –16.0 kcal.mol. This μ-CO,H dirhodium complex had a bridging carbonyl peak at 1834 cm^{-1} in the computed IR spectrum. This correlates with the experimental IR data and is another indication that **2*** is the active catalyst.

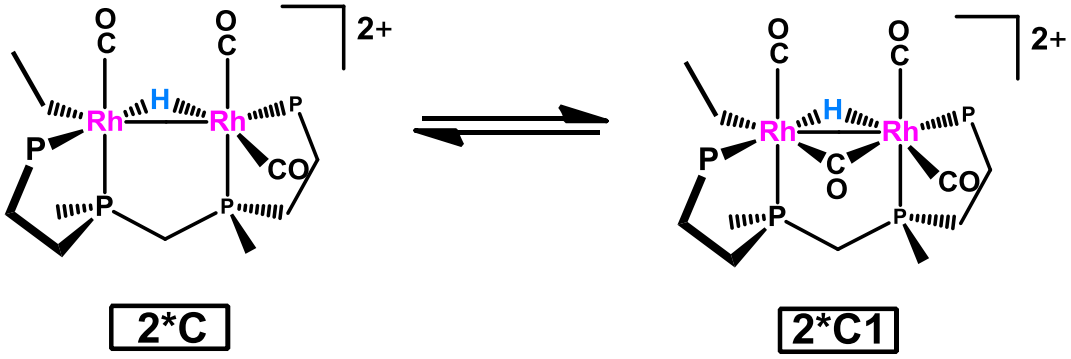

Figure 2.31. Conversion of mono bridging complex 2*C to double bridging complex 2*C1.

CO Insertion

The next step of the hydroformylation catalytic cycle is CO insertion to generate the acyl group. CO inserts into the double bridging complex (**2*C1**) forming an acyl group (**2*D**) with a small energy increase of 2.3 kcal/mol. The activation barrier for the CO insertion step is 13.2 kcal/mol. The presence of a single imaginary frequency confirmed the transition state (**TS(2*C1:2*D)**) (see Appendix 2). The alkyl group moves towards the axial carbonyl group for the CO insertion (Figure 2.32).

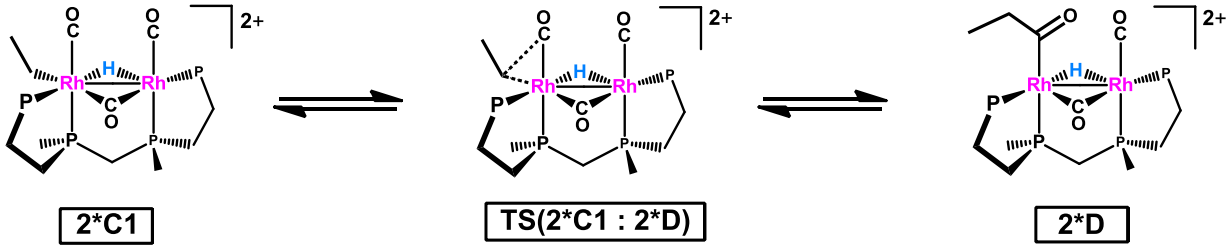

Figure 2.32. CO insertion.

Carbonyl groups will coordinate to both Rh centers to generate the 18-electron saturated complex, **2*D1** and this corresponds to a downhill energy change of –6.6 kcal/mol.

Aldehyde Reductive Elimination

Finally, aldehyde will reductively eliminate from **2*D1**. As the carbonyl group and hydride are *cisoidal* to each other, essentially on the same Rh center, and separated by only 2.67 Å, this corresponds to a small energy increase of 4.2 kcal/mol. The activation barrier for the reductive elimination of the aldehyde is 13.4 kcal/mol, which is 7.5 kcal/mol lower in energy than the reductive elimination step in **2****. The transition state (**TS(2*D1:2*E)**) was confirmed by checking for the presence of a single imaginary frequency (see Appendix 2). The bond distance between carbonyl C and bridging hydride is decreased by 1.14 Å in the transition state and Rh–C of carbonyl group is increased by 0.15 Å (Figure 2.33). These geometry differences are consistent with the transition state.

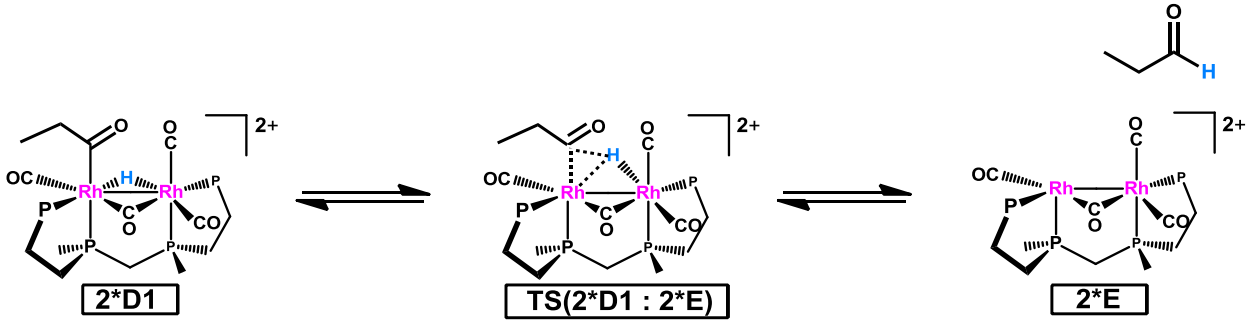

Figure 2.33. Reductive elimination of the aldehyde product.

The free energy profile for hydroformylation using **2*** as the active catalyst is shown below in Figure 2.34. The computed hydroformylation mechanism for **2**** is shown in Figure 2.35 with the

corresponding energy values. The activation barriers for the mechanism using **2*** are lower than those seen for the mechanism using **2****. The activation barrier for the hydride insertion step is 23.2 kca/mol in **2****, whereas it is only 7.97 kcal/mol in **2***. The DFT studies on **2*** does have a higher activation barrier for the CO insertion step (13.2 kcal/mol), whereas in **2**** it is essentially non-existent (0.7 kcal/mol).

I also did some calculations on the hydroformylation mechanism using asymmetric **2** for comparison. DFT calculates an activation barrier of 11.4 kcal/mol for terminal CO insertion in asymmetric **2** and a 16.2 kcal/mol barrier for a bridging CO insertion. The activation barrier for the reductive elimination for **2***, **2**** and **2** are 13.4 kcal/mol, 15.3 kcal/mol and 17.8 kcal/mol respectively. This shows that the aldehyde is more easily eliminated from **2*** than from **2** or **2****. The catalytic cycle for **2*** indicates that reductive elimination of aldehyde is the rate-limiting step, whereas in **2**** it is the hydride insertion step. Considering these facts, the energies and activation barriers, the hydroformylation catalytic cycle using **2*** as the active catalyst appears to be more feasible than using **2****.

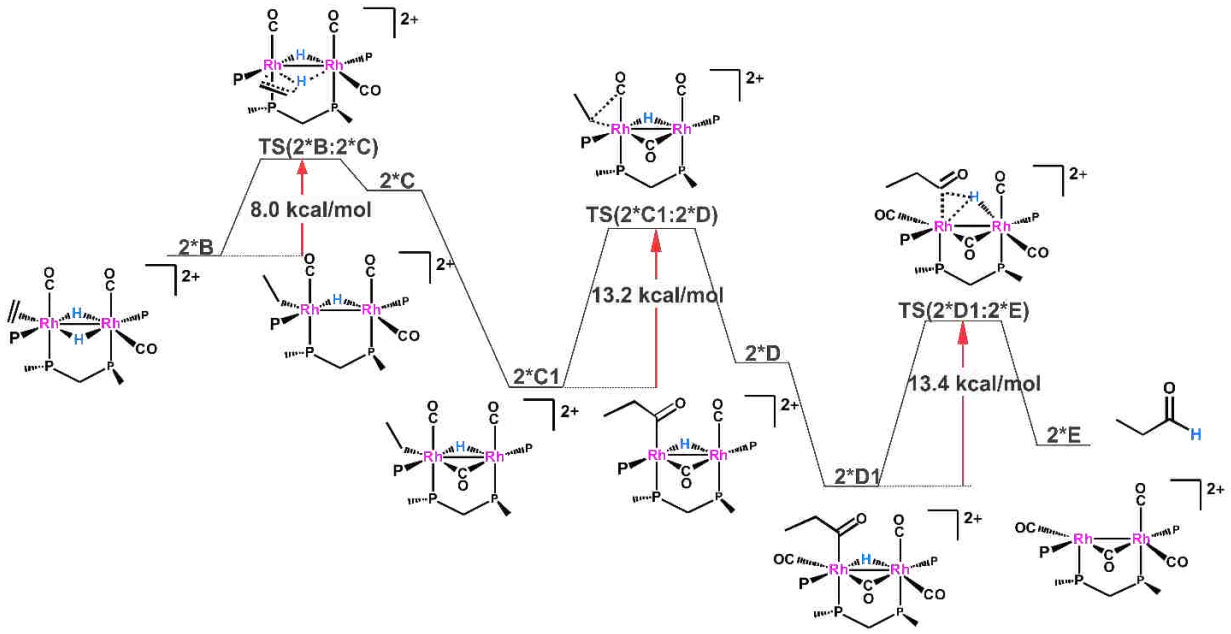

Figure 2.34. Free energy profile for hydroformylation in acetone using 2* as the active catalyst (For clarity chelate phosphine ligand is removed).

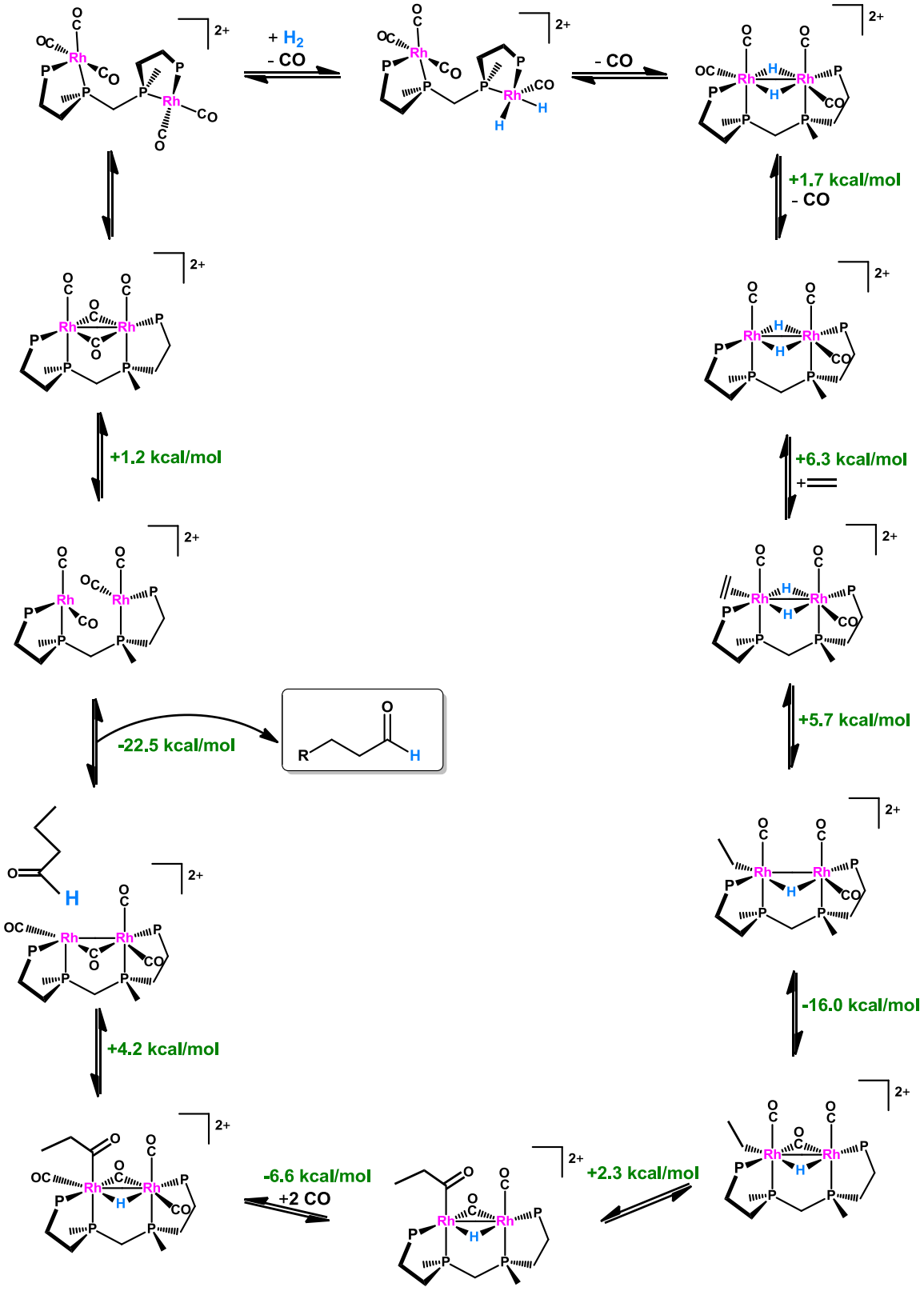

Figure 2.35. DFT computed hydroformylation catalytic cycle using 2* as the active catalyst.

2.3.3 Monocationic Bimetallic Hydroformylation

Industrial catalytic processors mostly use heterogeneous catalysts even though they are less active and selective than homogeneous catalysts. The inability to easily recover the catalyst from the reaction mixture makes homogeneous catalysts far less favorable industrially, even though they are still used for hydroformylation.[36,37] Once the Stanley group recognized that the dirhodium catalyst was dicationic they experimented with more polar solvent systems that might allow the less-polar aldehyde product to phase separate from the solvent. This would make product-catalyst separation much easier, analogous to what is done in the Shell Higher Olefin Process.[38] A 30% water/acetone mixture was found to be the best composition that did result in phase separation of the heptaldehyde product from the water-acetone solvent mixture. Unfortunately, the catalyst was more soluble in the aldehyde product phase than the water-acetone solvent phase.

A very unexpected result, however, was the large improvement in hydroformylation catalysis for our bimetallic catalyst in water-acetone from both a rate and selectivity viewpoint.[39] The stability of the dirhodium P4 catalyst system is dramatically improved in water-acetone. A common test for the stability of a Rh hydroformylation catalyst (monometallic or bimetallic) is to put the catalyst under H_2/CO at operating conditions without any alkene present. All known effective Rh-phosphine catalysts will decompose via Rh-induced phosphine cleavage reactions under these conditions within 12 hours.[40] Under our standard hydroformylation conditions (90°C, 90 psig 1:1 H_2/CO) with no alkene present $[Rh_2(nbd)_2(rac\text{-et,ph-P4})]^{2+}$ will completely deactivate within 80 mins in acetone, while in water-acetone only 10% of catalyst activity is lost after 120 mins. Somehow the addition of water to the acetone solvent dramatically stabilizes the catalyst.

The main problem with the dicationic bimetallic catalyst is it readily fragments in acetone or other non-water based polar solvents into inactive monometallic (**12r**) and double ligand coordinated bimetallic (**13rr**) complexes. This is clearly demonstrated by the *in situ* ^{31}P NMR studies that show extensive catalyst fragmentation after sitting at room temperature under 280 psig of H_2/CO for 24 hrs or longer (Figure 2.36). This same spectrum can be generated after just an hour at 60°C. Prof. Stanley was quite

surprised to see the facile fragmentation under such mild conditions, especially since the P4 ligand was specifically designed to limit this type of Rh-loss fragmentation.

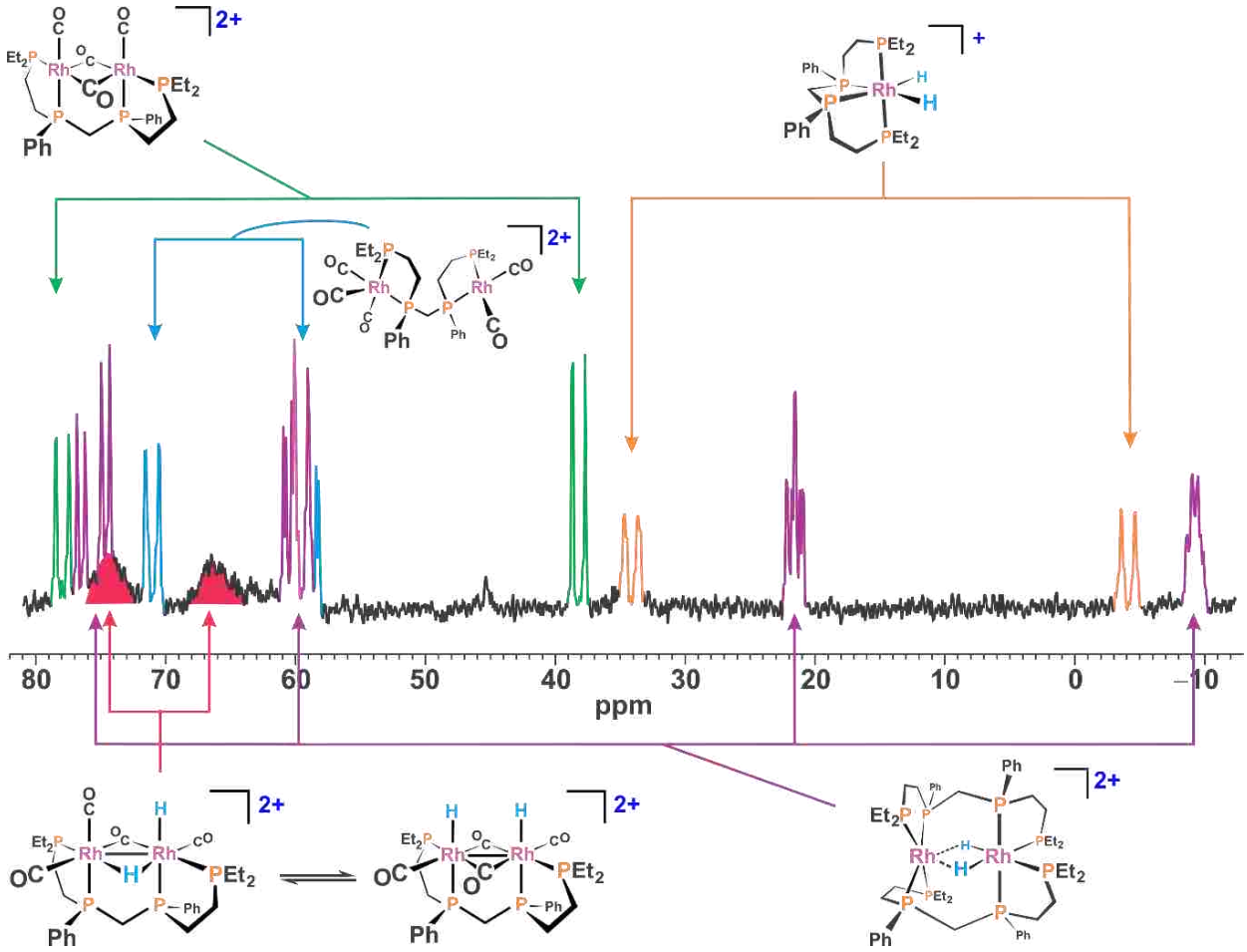

Figure 2.36. $^{31}P\{^{1}H\}$ NMR of $[Rh_2(nbd)_2(rac\text{-}P4)]^{2+}$ in Acetone, 280 psig H_2/CO, 25°C.

The proposed fragmentation pathway is shown in Figure 2.37 and centers on what we now recognize as a facile phosphine chelate arm dissociation equilibrium. Once an external phosphine is replaced by a CO ligand, the dirhodium complex is more electron-deficient, which promotes reductive elimination of H_2 to generate the closed-mode pentacarbonyl complex **F**. This doesn't have any hydrides and can't do any hydroformylation until H_2 re-adds. The one Rh center is becoming CO-saturated and is susceptible to Rh-loss to generate the monometallic κ^2-coordinated complex **G**.

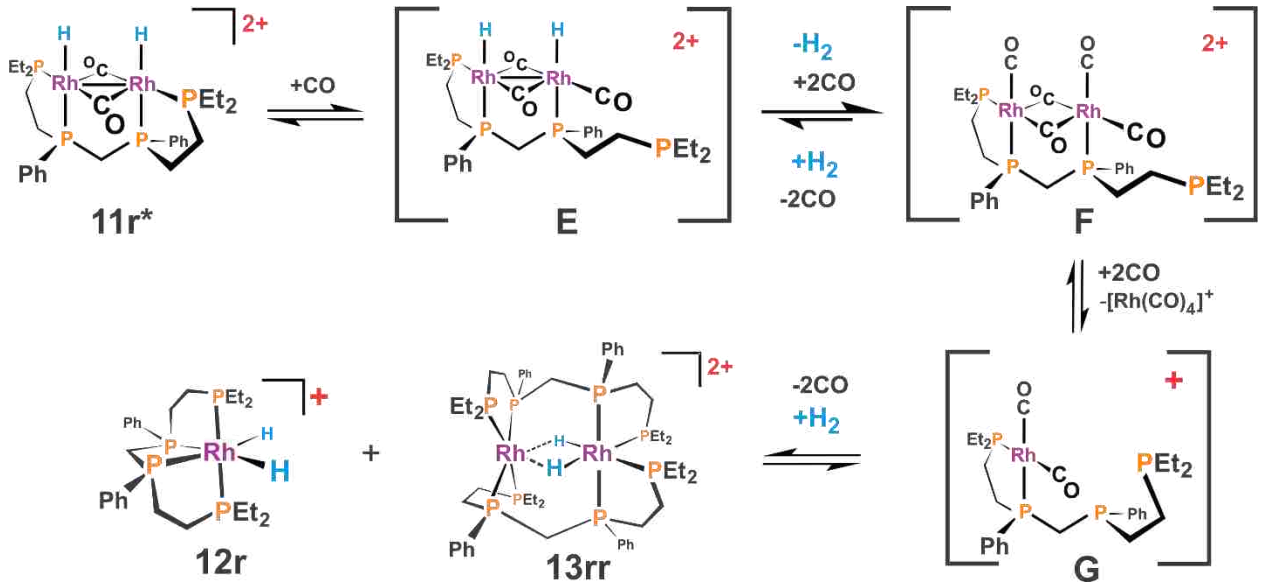

Figure 2.37. Proposed fragmentation pathway using 2** as the starting species.

The P4 ligand is flexible enough to wrap around the Rh center with oxidative addition of H_2 to form the 18e- saturated complex **12r** that is inactive for hydroformylation or other side reactions. We have strong spectroscopic evidence for this monometallic dihydride complex, which is the only hydride species that remains upon depressurization of the catalyst solution followed by purging with N_2. We have crystallographically characterized the dichloride analog, $[RhCl_2(\kappa^4\text{-}rac\text{-et,ph-P4})]^+$, which has a very similar ^{31}P NMR.[41] The double P4-ligated dirhodium complex, **13rr**, is mainly formed under our higher concentration NMR tube studies. We do not believe that this dirhodium complex is active for hydroformylation.

A variety of studies over the years performed by the Stanley group finally showed that the dicationic catalyst, now identified as $[Rh_2(\mu\text{-}H)_2(CO)_2(rac\text{-et,ph-P4})]^{2+}$, behaves as a strong acid in the presence of water. This leads to the dissociation of one of the hydrides as a proton forming monocationic monohydride dirhodium carbonyl complexes. Figure 2.38 illustrates the mechanism initially proposed by Prof. Stanley for the hydroformylation in water/acetone system catalyzed by the monocationic dirhodium catalyst system.

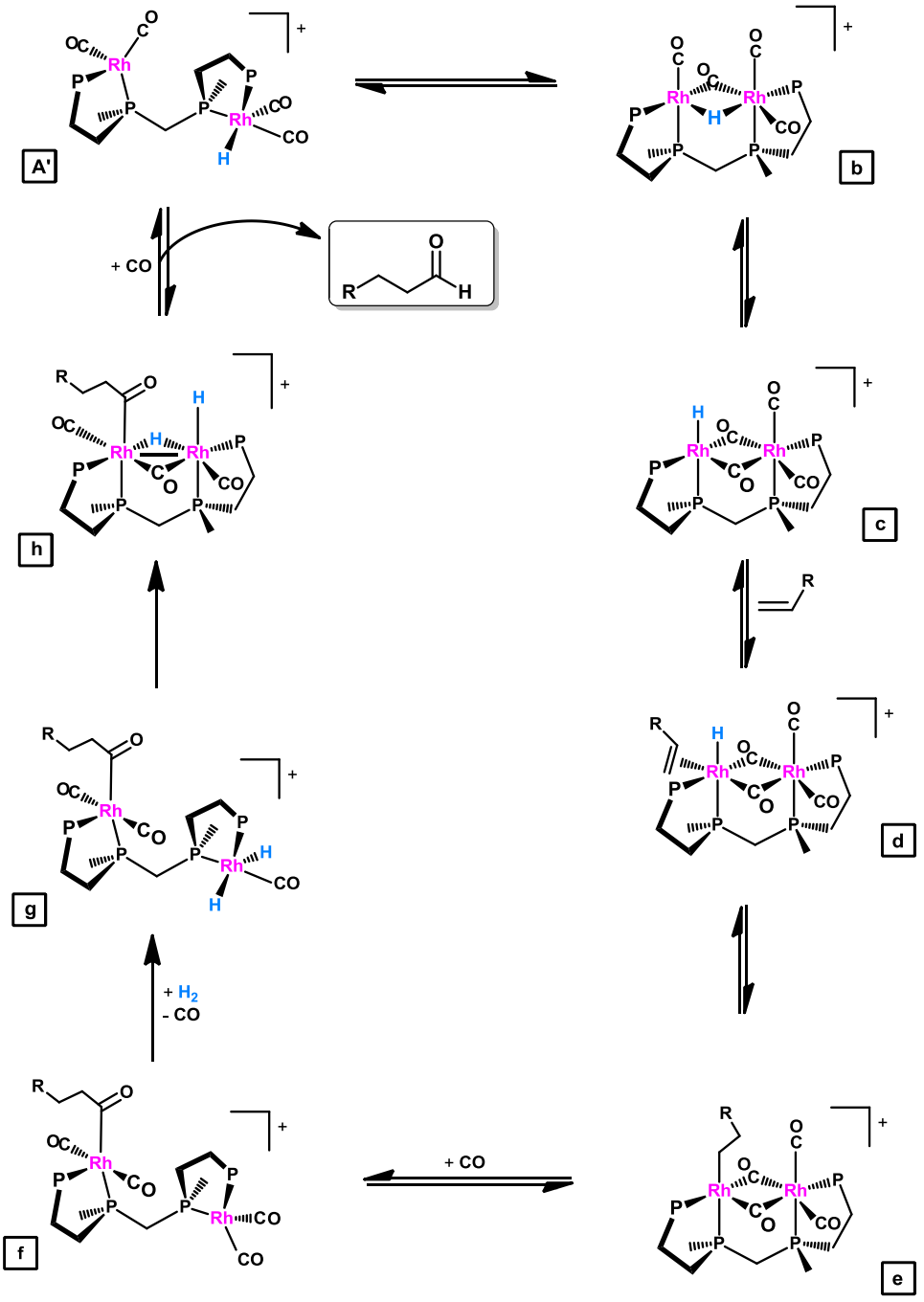

Figure 2.38. Proposed mechanism for hydroformylation in water/acetone.

Prof. Stanley initially favored the double-bridged species shown for complexes **b**, **c**, **d**, and **e** in direct analogy to the dicationic hydroformylation cycle. But the monocationic Rh_2 complexes are in the Rh(I) oxidation state, unlike most of the complexes in the dicationic cycle that are Rh(II). There are, for example, only four single atom double bridged bimetallic Rh(I) complexes with P-CH_2-P type groups:

$[Rh_2(\mu\text{–}Cl)(\mu\text{–}CO)(CO)_2(dppm)_2]^+$,[20] $[Rh_2(\mu\text{–}H)(\mu\text{–}CO)(CO)_2(dppm)_2]^+$,[21] $[Rh_2(\mu\text{–}H)_2(CO)_2(d\textit{i}Prpm)_2]$,[22] and $[Rh_2(\mu\text{–}Cl)_2(NO)_2(dppm)_2]^{2+}$.[23] The A-frame geometry with just one bridging ligand is far more common. Based on the rarity of single atom double-bridged Rh(I) structures, it was very important to perform DFT calculations to determine the most likely structures for these monocationic dirhodium complexes.

The DFT calculations demonstrated that complex **b** was a mono bridged complex with a bridging hydride (**B'**) whereas complex **c** was a mono bridged complex with a bridging carbonyl (**C'**). Based on standard electron-counting formalisms these complexes with a single hydride or CO bridge should have Rh-Rh covalent bonds, which is supported by the DFT calculations. **C'** has a DFT calculated Rh-Rh = 2.81394 Å, while **B'** has Rh-Rh = 2.94311 Å.The conversion of **A'** to **B'** is an exothermic reaction corresponding to an energy difference of -15.13 kcal/mol. The DFT calculations find **C'** to be 1.82 kcal/mol more stable than **B'**, which is consistent with the NMR data (Figure 2.39) that shows a single broad hydride resonance consistent with dynamic exchange between **C'** and **B'**.

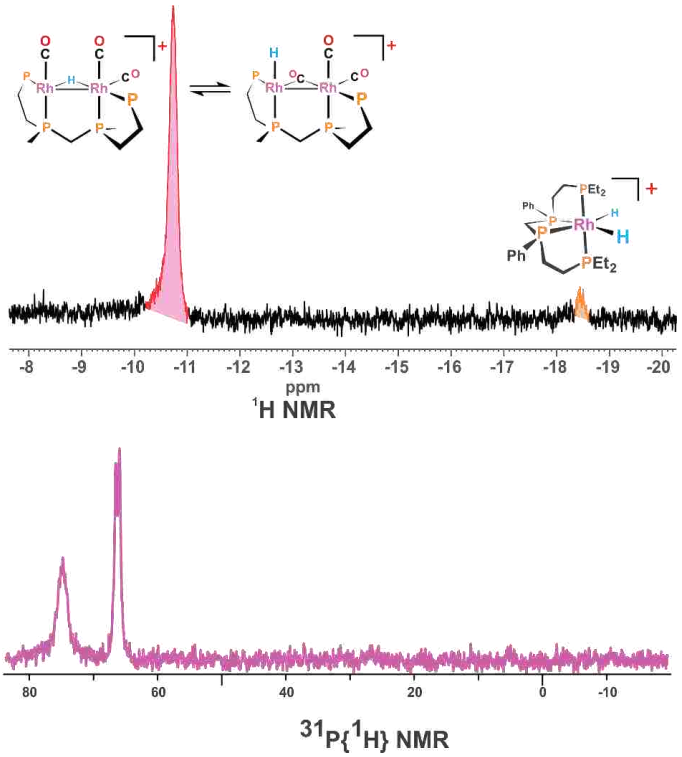

Figure 2.39. ^{1}H (top) and ^{31}P (bottom) NMR of catalyst solution after hydroformylation in 30% water/acetone.

There is a small amount of the monometallic fragmentation product present as well, but far less than seen in acetone. The ^{31}P NMR, also shown in Figure 2.39, shows broad and partially resolved NMR resonances indicating an on-average symmetrical species, once again consistent with a dynamic exchange equilibrium between **C'** and **B'**. The extremely low amount of fragmentation products in the ^{1}H and ^{31}P NMR's (compare Figures 2.36 and 2.39) is clearly indicative of the higher stability of the monocationic dirhodium catalyst species.

2.3.3.1 DFT Computed Hydroformylation Mechanism for Monocationic Dirhodium Catalyst

The key step towards proposing a mechanism is the identification of the primary catalyst species. DFT studies suggest that either complex **B'** or **C'** acts as the active catalyst in the monocationic dirhodium catalyst system. Detailed analysis of the mechanism will be helpful to determine the active catalyst more accurately. Figure 2.40 shows the new proposed catalytic cycle for the monocationic dirhodium system based on DFT computations which is quite different from the originally proposed mechanism. A detailed discussion on the computational investigation of this mechanism is given below.

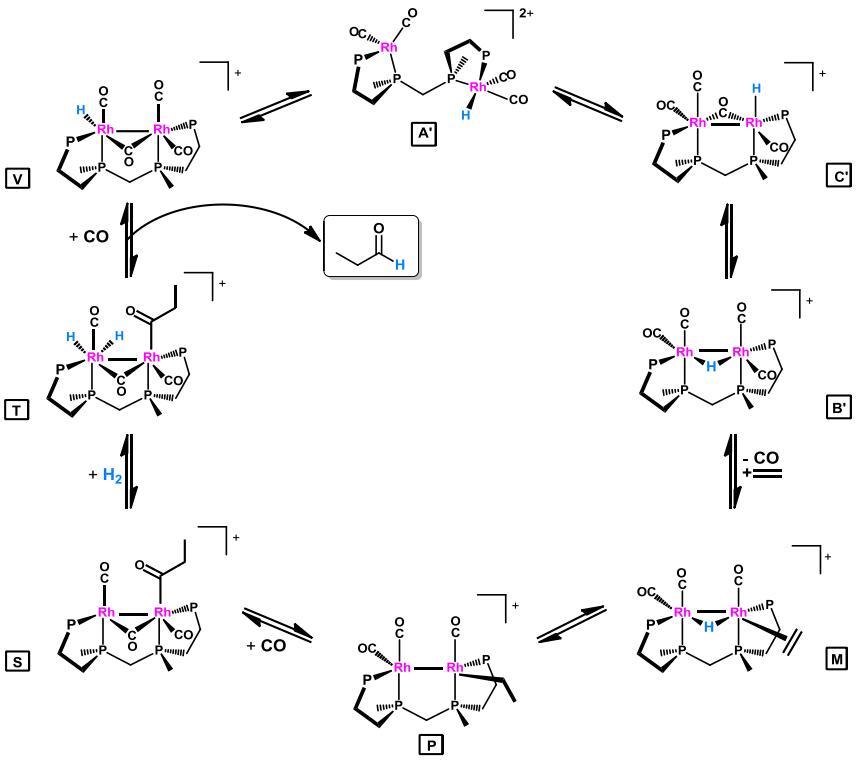

Figure 2.40. The new proposed monocationic dirhodium mechanism.

Alkene coordination and hydride insertion

The formation of the closed mode complex will be followed by the alkene coordination. After dissociating a CO ligand, the alkene can interact with either complex **B'** or **C'**. According to the DFT data, even though the terminal CO ligand dissociation energy is lower in the bridged hydride complex (**B'**) than in the terminal hydride complex (**C'**), the alkene coordination seems to be more favorable in complex **C'** than in complex **B'**. The CO ligand dissociation and alkene coordination energies are given in Figure 2.41. This figure shows that CO dissociation is highly favored in both **B'** and **C'**.

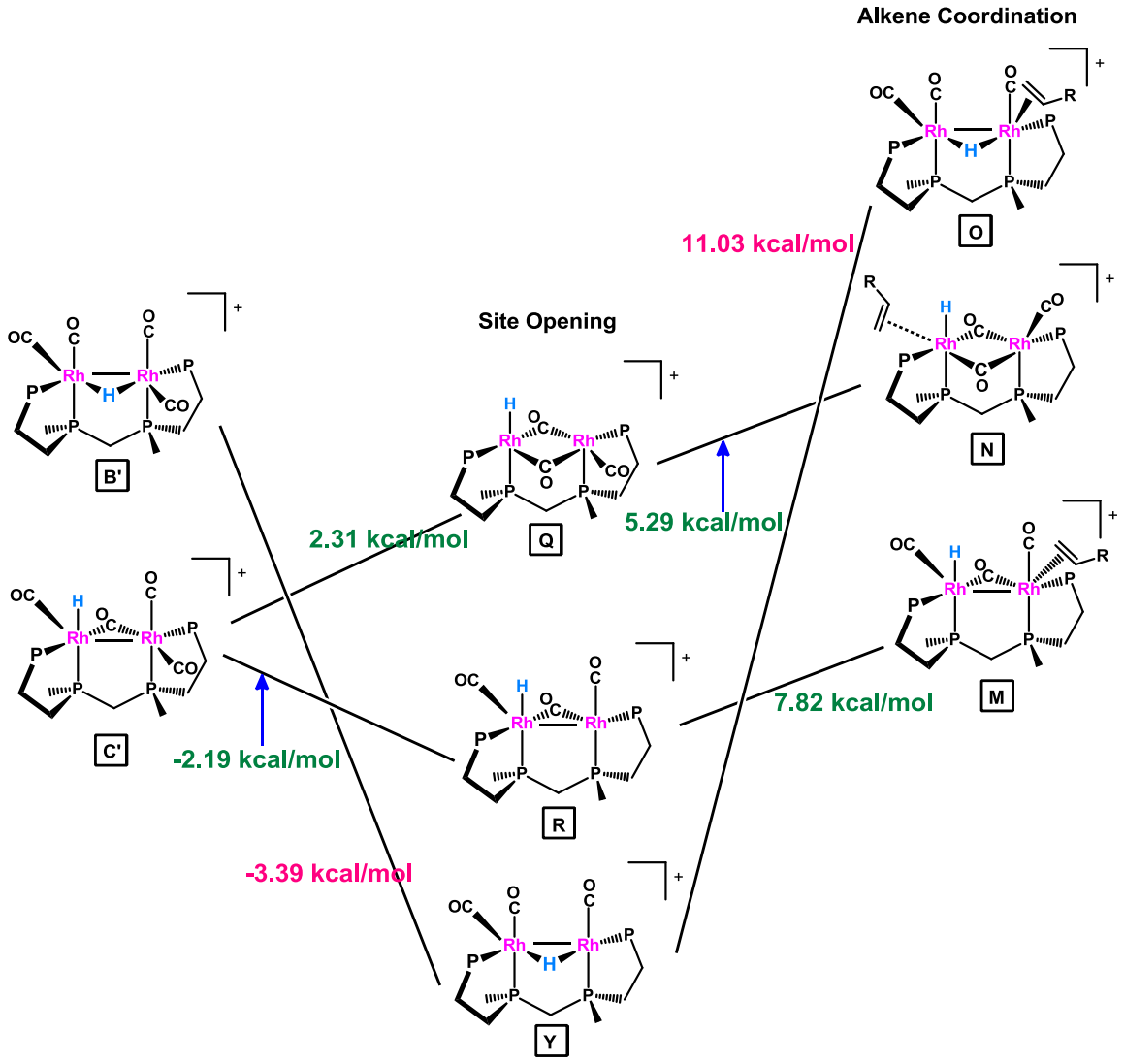

Figure 2.41. Dissociation of terminal CO and coordination of the alkene.

Figure 2.41 clearly illustrates that the dissociation of CO ligand from complex **C'** results in two complexes which are either **Q** or **R**. The CO dissociation from the neutral Rh center results in **Q** whereas the CO dissociation from the cationic Rh center results in **R**. According to the relative energies of **Q** (4.51 kcal/mol) and **R** (0.00 kcal/mol), the DFT data shows that the dissociation of a terminal CO ligand *trans* to the bridged CO results in a higher energy species. As CO dissociation is more favored from the cationic Rh center rather than from the neutral Rh center, formation of **R** is favored than **Q**.

Once the CO is dissociated, the alkene coordination to the vacant orbitals will take place. The DFT calculations illustrate that the alkene coordination does not occur to complex **Q**, as the distance between the alkene and the Rh center is 4.88 Å (**N**), whereas the coordination of alkene to **R** to form **M** does form a bond with a distance of 2.43 Å. Therefore, for species **C'**, alkene coordination would proceed through **R** to form **M**.

The alkene coordination is followed by a migratory insertion between the alkene and the hydride to form an alkyl group. The migratory insertion is favored when the two groups are *cisoidal* to each other. In the bridging hydride complex **O**, shown in Figure 2.42, the alkene and the hydride are *cis* to each other whereas in the terminal hydride complex **M** it is not. In both complexes the alkene is coordinated to the metal center in the equatorial position.

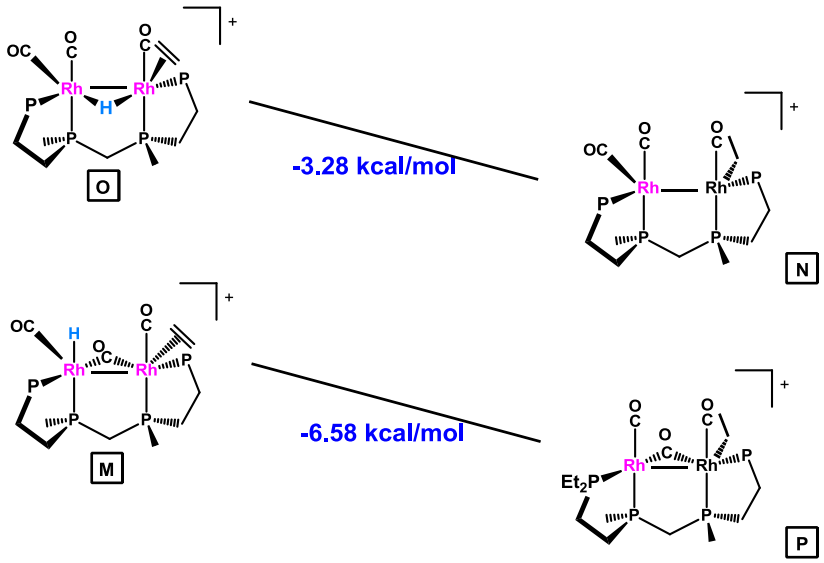

Figure 2.42. Hydride insertion step for bridged hydride complex and terminal hydride complex.

The DFT results demonstrate that hydride insertion is energetically feasible in both terminal hydride complex **M** (–6.58 kcal/mol) and in the bridged hydride complex **O** (–3.28 kcal/mol). In order to better understand the reaction pathway for the hydride insertion, transition state calculations have been performed.

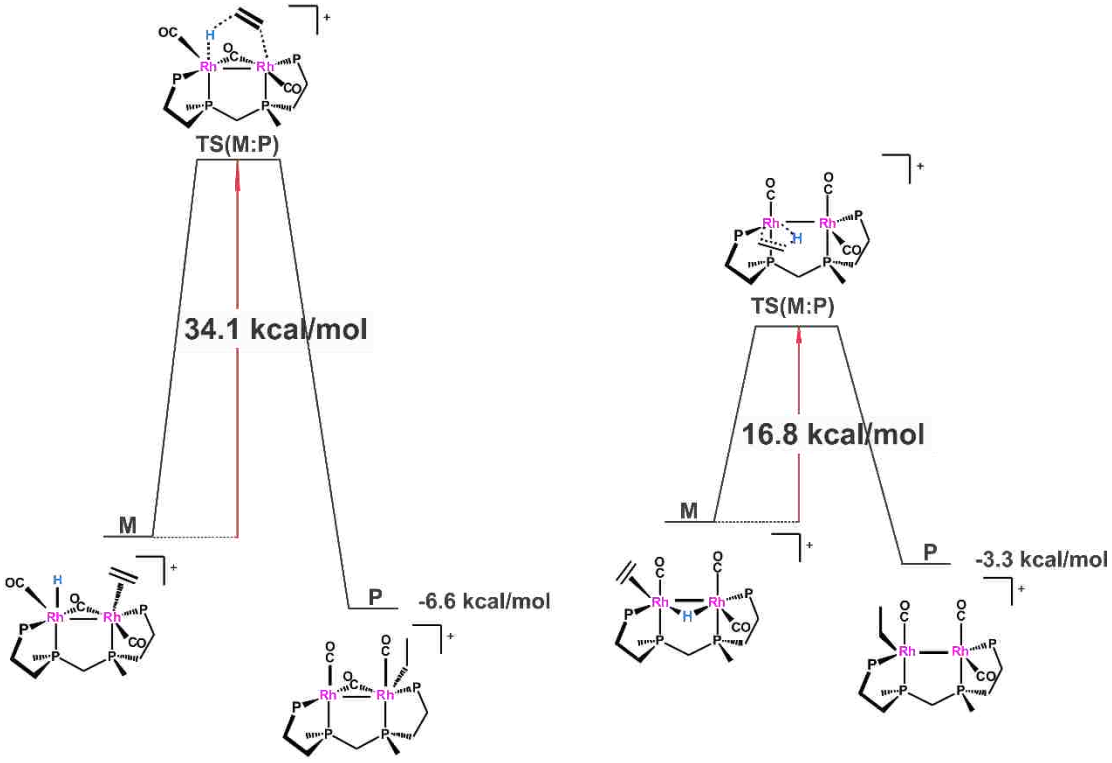

Figure 2.43. Activation barriers for (a). terminal hydride insertion (b). bridging hydride insertion.

The activation barriers for the hydride insertion step are shown above in Figure 2.43 and the DFT structures of the transition states are shown in Figure 2.44. The activation barrier for terminal hydride insertion for **M** to **P** is a rather large 34.1 kcal/mol, whereas for bridging hydride insertion for **O** to **N** it is only 16.8 kcal/mol. These activation energies clearly indicate that the alkene insertion with the bridging hydride complex **O** is the preferred pathway. Both the transition states have one imaginary frequency and they correspond to the correct vibrational mode of hydride insertion (see Appendix 2). In **TS(M:P**) the alkene has moved to the axial position, whereas in **TS(O:N)** the alkene remains at the equatorial position. The Rh-C=C bond is longer by 0.033 Å in **TS(M:P)** which suggests that the alkyl group is weakly coordinated to the metal center. The activation barriers and the structural differences clearly

indicate that the insertion of the bridging hydride is more favorable than the insertion of terminal hydride, similar to what we found for the dicationic catalyst **2*** vs **2****.

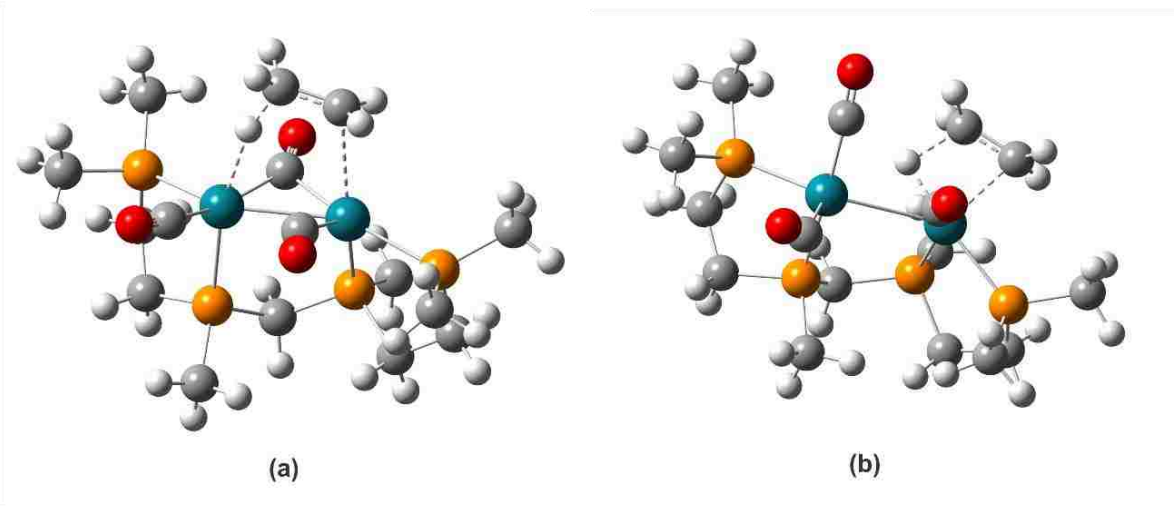

Figure 2.44. (a). Transition state of terminal hydride insertion, TS(M:P) (b). Transition state of bridging hydride insertion, TS(O:N).

As **N** is 7.8 kcal/mol higher in energy than **P**, **N** converts into the more stable product **P** after hydride insertion. The hydride insertion step is followed by migratory insertion between the alkyl group and a carbonyl group forming an acyl group. This step is predicted to be exothermic by 11.2 kcal/mol. The CO group *cis* to the alkyl group migrates to form the acyl species via the transition states **TS(P:SI)**. The DFT calculated transition state for CO insertion is shown below in Figure 2.45.

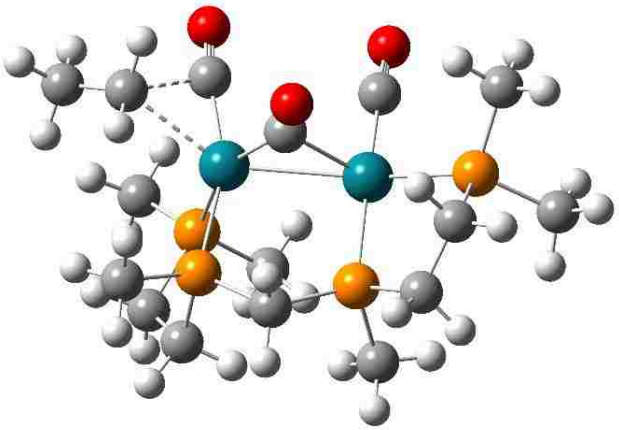

Figure 2.45. Transition state of CO insertion, TS(P:SI).

The energy barrier for the CO insertion step is 5.1 kcal/mol. The transition state contained only a single imaginary frequency (see Appendix 2). The corresponding energy value for the reaction is shown below in Figure 2.46. This will be followed by the association of a CO group. The association of CO will occur at the acyl Rh center as it is more electron rich than the cationic Rh center. The CO addition corresponds to an energy drop of -2.4 kcal/mol.

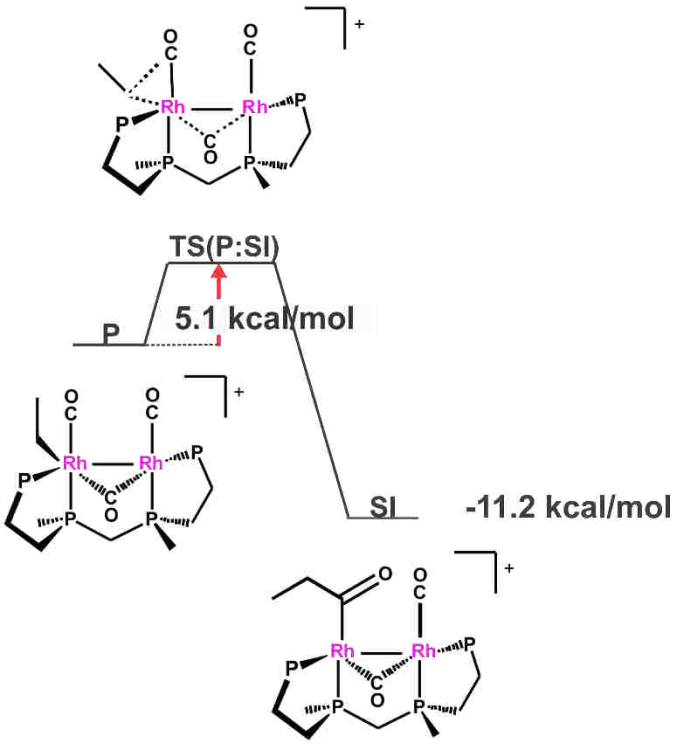

Figure 2.46. Activation barrier for terminal CO insertion.

This will then be followed by the oxidative addition of H_2 to the cationic Rh center. The oxidative addition is exothermic by only 2.2 kcal/mol and the corresponding free energy barrier is 8.7 kcal/mol. The vibrational frequency studies confirmed the presence of the transition state **TS(S:T)** by producing a single imaginary frequency (see Appendix 2). Finally, the aldehyde will reductively eliminate regenerating the catalyst complex. The DFT calculations show that the reductive elimination occurs as the acyl group and the hydride groups are in close proximity (3.5 Å) and *cisoidal* to each other. Interestingly, this step is predicted to be endothermic by 16.3 kcal/mol with an activation barrier of 21.6 kcal/mol. The transition state, **TS(T:W)** contains only one imaginary frequency (see Appendix 2). The dirhodium complex will

convert from closed mode to open mode regenerating **A'** which contains an open site that favors the continuation of the catalytic cycle. According to the activation barriers of different steps of the catalytic cycle (Figure 2.47), the reductive elimination is the rate-determining step for this catalytic pathway.

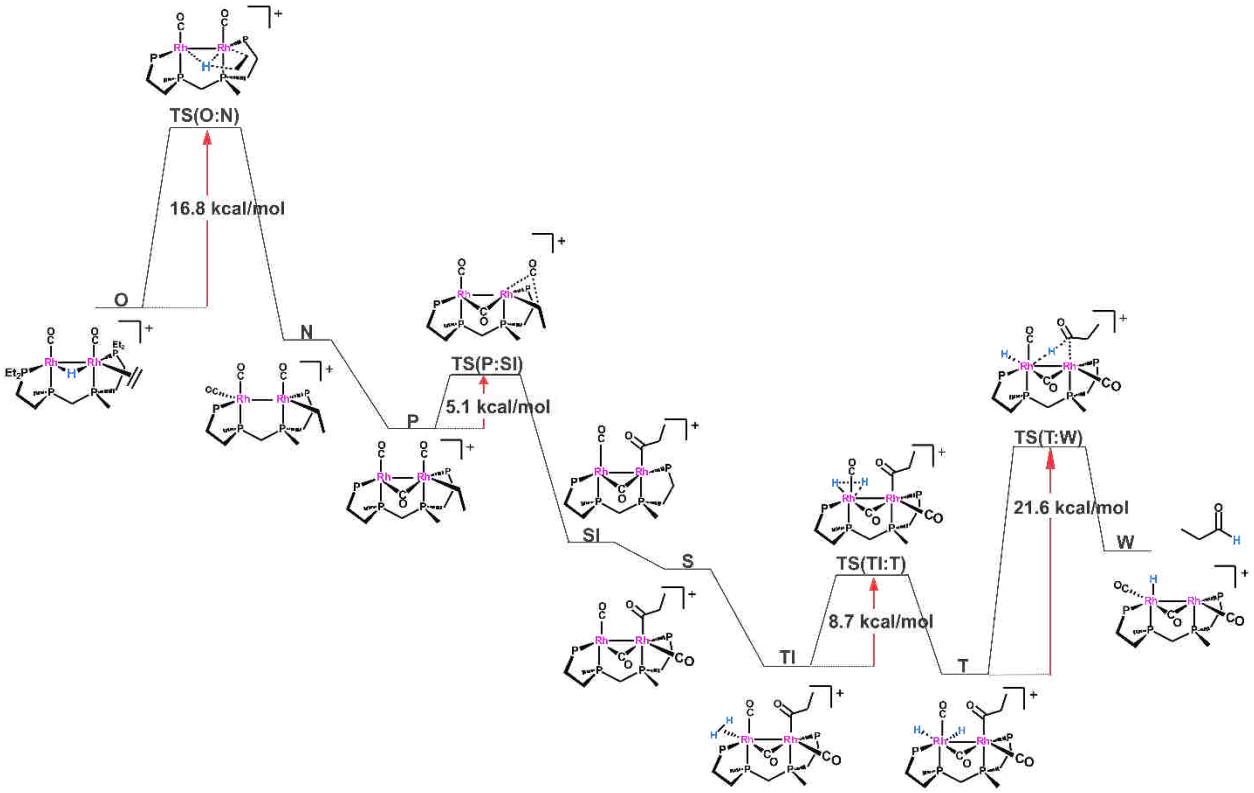

Figure 2.47. Activation barriers for hydroformylation in water/acetone (For clarity methyl groups attached to P atoms are not shown.).

2.4 Conclusions

Hydroformylation in acetone solvent system results in dicationic dihydride dirhodium complexes, whereas in 30% water/acetone solvent system monocationic monohydride dirhodium complexes are the major species. A theoretical study on dirhodium catalyzed hydroformylation mechanism was performed to determine the active catalyst for both dicationic and monocationic bimetallic species. Computational mechanistic investigations provided more reliable and energetically feasible alternatives to the initially proposed mechanisms and fit the experimental data better.

DFT studies show that dicationic dirhodium complexes result in double bridged complexes, but the monocationic dirhodium complexes primarily generate complexes bridged by one CO or one hydride

ligand, which are quite different from what Prof. Stanley originally proposed. According to DFT studies, complex **2*** is the better choice for the active dicationic catalyst in acetone due to reduced activation barriers and better agreement with the available experimental results.

The presence of two bridging IR bands in the spectra at higher temperatures and the activity dependence of these bridging bands suggested **2**** as the active catalyst, which is what Prof. Stanley believed for many years. We predict the presence of a facile phosphine-arm dissociation for all likely catalyst species **2**, **2*** and **2**** due to the presence of broad resonances in ^{31}P and ^{1}H NMR at room temperature and above. The DFT calculation had one long Rh–$P_{external}$ distance of 2.51 Å for **2** which indicates weak Rh-P bonding, consistent with phosphine arm dissociation; hence, this shows up in the IR as two separate species (Figure 2.48).

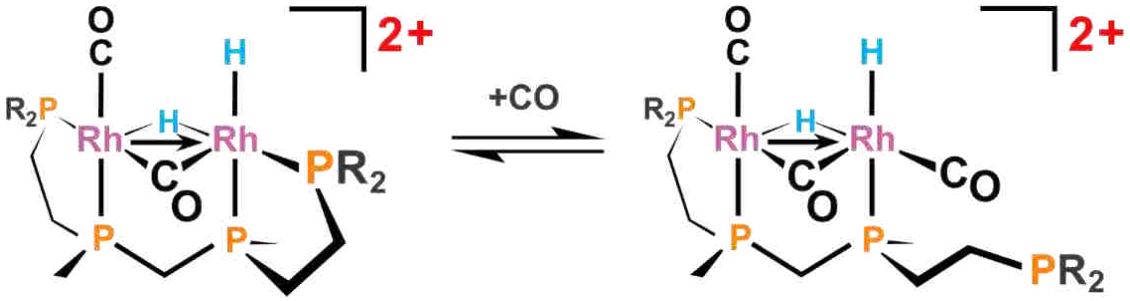

Figure 2.48. Phosphine arm-on and arm-off for 2.

DFT calculations for phosphine arm-on and arm-off for **2** give rise to bridging CO bands with different stretching frequencies (1801 cm^{-1} and 1859 cm^{-1}) and this leads to two bridging IR bands which are observed experimentally (1834 cm^{-1} and 1821 cm^{-1}) (Figure 2.15) at a temperature of 90°C and at a pressure of 90 psig where higher hydroformylation activity is observed.

The monocationic dirhodium catalyst acts as an efficient catalyst compared to the dicationic system due to improved catalyst stability that maintains more active bimetallic catalyst. The rate-limiting step for the catalytic process in both solvent systems is the aldehyde elimination step. The energy barrier for this step can be somewhat reduced by decreasing the electron density at the metal centers, which helps explain the lower activation barrier for the reductive elimination step in the dicationic catalyst. The low energy barriers calculated for the bimetallic catalyst suggest that they are more efficient than

monometallic catalysts.[19, 33] The experimental hydroformylation studies using the new somewhat more electron-deficient 1,2-phenylene-linked chelate ligand (*rac*-et,ph-P4-Ph) may increase the efficiency and stability of the catalyst through the stronger chelate effect and lower donor ability.

2.5 References

1. Cornils, B.; Herrmann, W. A.; Rasch, M., Otto Roelen, Pioneer in Industrial Homogeneous Catalysis. *Angewandte Chemie International Edition in English* **1994,** *33* (21), 2144-2163.

2. Agbossou, F.; Carpentier, J.-F.; Mortreux, A., Asymmetric Hydroformylation. *Chemical Reviews* **1995,** *95* (7), 2485-2506.

3. Whiteker, G.; Cobley, C., Applications of Rhodium-Catalyzed Hydroformylation in the Pharmaceutical, Agrochemical, and Fragrance Industries. In *Organometallics as Catalysts in the Fine Chemical Industry*, Beller, M.; Blaser, H.-U., Eds. Springer Berlin Heidelberg: 2012; Vol. 42, pp 35-46.

4. Khan, S. R.; Bhanage, B. M., Selective hydroformylation of various olefins using diphosphinite ligands. *Applied Organometallic Chemistry* **2013,** *27* (5), 313-317.

5. Pospech, J.; Fleischer, I.; Franke, R.; Buchholz, S.; Beller, M., Alternative metals for homogeneous catalyzed hydroformylation reactions. *Angewandte Chemie (International ed. in English)* **2013,** *52* (10), 2852-72.

6. Heck, R. F.; Breslow, D. S., The Reaction of Cobalt Hydrotetracarbonyl with Olefins. *Journal of the American Chemical Society* **1961,** *83* (19), 4023-4027.

7. Torrent, M.; Sola, M.; Frenking, G., Theoretical studies of some transition-metal-mediated reactions of industrial and synthetic importance. *Chemical reviews* **2000,** *100* (2), 439-494.

8. Whyman, R., In situ infrared spectral studies on the cobalt carbonyl-catalysed hydroformylation of olefins. *Journal of Organometallic Chemistry* **1974,** *66* (1), C23-C25.

9. Mirbach, M. F., On the mechanism of the Co2(CO)8 catalyzed hydroformylation of olefins in hydrocarbon solvents. A high pressure UV and IR study. *Journal of Organometallic Chemistry* **1984,** *265* (2), 205-213.

10. Slaugh, L. H.; Mullineaux, R. D., Novel Hydroformylation catalysts. *Journal of Organometallic Chemistry* **1968,** *13* (2), 469-477.

11. Osborn, J. A.; Wilkinson, G.; Young, J. F., Mild hydroformylation of olefins using rhodium catalysts. *Chemical Communications (London)* **1965,** (2), 17-17.

12. Evans, D.; Osborn, J. A.; Wilkinson, G., Hydroformylation of alkenes by use of rhodium complex catalysts. *Journal of the Chemical Society A: Inorganic, Physical, Theoretical* **1968,** (0), 3133-3142.

13. Hidai, M.; Fukuoka, A.; Koyasu, Y.; Uchida, Y., Homogeneous multimetallic catalysts: Part 6.11 For Part 5, see ref. 18. Hydroformylation and hydroesterification of olefins by homogeneous cobalt-ruthenium bimetallic catalysts. *Journal of molecular catalysis* **1986,** *35* (1), 29-37.

14. Dickson, R. S.; Bowen, J.; Campi, E. M.; Jackson, W. R.; Jonasson, C. A. M.; McGrath, F. J.; Paslow, D. J.; Polas, A.; Renton, P.; Gladiali, S., Comparison of a range of rhodium-based catalysts

for the hydroformylation of selected alkenes. *Journal of Molecular Catalysis A: Chemical* **1999,** *150* (1–2), 133-146.

15. Ishii, Y.; Hidai, M., Carbonylation reactions catalyzed by homogeneous Pd–Co bimetallic systems. *Catalysis today* **2001,** *66* (1), 53-61.

16. Rida, M. A.; Smith, A. K., A bimetallic hydroformylation catalyst: high regioselectivity through heterobimetallic cooperativity. *Journal of Molecular Catalysis A: Chemical* **2003,** *202* (1), 87-95.

17. Coutinho, K.; Dickson, R.; Fallon, G.; áRoy Jackson, W.; Simone, T.; Skelton, B.; White, A., Isolation and characterization of hydroformylation 'intermediates' from stoichiometric reactions between phosphinoalkenes and some heterobinuclear complexes. *Journal of the Chemical Society, Dalton Transactions* **1997,** (18), 3193-3200.

18. Schmid, R.; Herrmann, W. A.; Frenking, G., Coordination Chemistry and Mechanisms of Metal-Catalyzed CC-Coupling Reactions. 10. Ligand Dissociation in Rhodium-Catalyzed Hydroformylation: A Theoretical Study. *Organometallics* **1997,** *16* (4), 701-708.

19. Matsubara, T.; Koga, N.; Ding, Y.; Musaev, D. G.; Morokuma, K., Ab initio MO study of the full cycle of olefin hydroformylation catalyzed by a rhodium complex, $RhH(CO)_2(PH_3)_2$. *Organometallics* **1997,** *16* (5), 1065-1078.

20. Gleich, D.; Hutter, J., Computational Approaches to Activity in Rhodium ¡Catalysed Hydroformylation. *Chemistry-A European Journal* **2004,** *10* (10), 2435-2444.

21. Zuidema, E.; Escorihuela, L.; Eichelsheim, T.; Carbó, J. J.; Bo, C.; Kamer, P. C.; Van Leeuwen, P. W., The Rate–Determining Step in the Rhodium–Xantphos ¡Catalysed Hydroformylation of 1–Octene. *Chemistry-A European Journal* **2008,** *14* (6), 1843-1853.

22. Sparta, M.; Børve, K. J.; Jensen, V. R., Activity of rhodium-catalyzed hydroformylation: Added insight and predictions from theory. *Journal of the American Chemical Society* **2007,** *129* (27), 8487-8499.

23. Lei, M.; Wang, Z.; Du, X.; Zhang, X.; Tang, Y., Asymmetric Hydroformylation Catalyzed by $RhH(CO)_2$[(R,S)–Yanphos]: Mechanism and Origin of Enantioselectivity. *The Journal of Physical Chemistry A* **2014,** *118* (39), 8960-8970.

24. Tang, D.; Qin, S.; Su, Z.; Hu, C., Comprehensive Theoretical Study on the Mechanism of Regioselective Hydroformylation of Phosphinobutene Catalyzed by a Heterobinuclear Rhodium (I)-Chromium Complex. *Organometallics* **2007,** *26* (1), 33-47.

25. Broussard, M. E.; Juma, B.; Train, S. G.; Peng, W.-J.; Laneman, S. A.; Stanley, G. G., A bimetallic hydroformylation catalyst: high regioselectivity and reactivity through homobimetallic cooperativity. *Science* **1993,** *260* (5115), 1784-1788.

26. Matthews, R. C.; Howell, D. K.; Peng, W.-J.; Train, S. G.; Treleaven, W. D.; Stanley, G. G., Bimetallic Hydroformylation Catalysis: In Situ Characterization of a Dinuclear Rhodium(II) Dihydrido Complex with the Largest Rh–HNMR Coupling Constant. *Angewandte Chemie International Edition in English* **1996,** *35* (19), 2253-2256.

27. Peng, W.-J.; Train, S. G.; Howell, D. K.; Fronczek, F. R.; Stanley, G. G., Bimetallic hydroformylation: a zwitterionic Rh–IRhI tetraphosphine ligand-based bimetallic complex exhibiting facile CO addition and phosphine ligand rearrangement equilibrium. *Chem. Commun.* **1996,** (22), 2607-2612.

28. Frisch, M. J.; Trucks, G. W.; Schlegel, H. B.; Scuseria, G. E.; Robb, M. A.; Cheeseman, J. R.; Scalmani, G.; Barone, V.; Mennucci, B.; Petersson, G. A.; Nakatsuji, H.; Caricato, M.; Li, X.; Hratchian, H. P.; Izmaylov, A. F.; Bloino, J.; Zheng, G.; Sonnenberg, J. L.; Hada, M.; Ehara, M.; Toyota, K.; Fukuda, R.; Hasegawa, J.; Ishida, M.; Nakajima, T.; Honda, Y.; Kitao, O.; Nakai, H.; Vreven, T.; Montgomery Jr., J. A.; Peralta, J. E.; Ogliaro, F.; Bearpark, M. J.; Heyd, J.; Brothers, E. N.; Kudin, K. N.; Staroverov, V. N.; Kobayashi, R.; Normand, J.; Raghavachari, K.; Rendell, A. P.; Burant, J. C.; Iyengar, S. S.; Tomasi, J.; Cossi, M.; Rega, N.; Millam, N. J.; Klene, M.; Knox, J. E.; Cross, J. B.; Bakken, V.; Adamo, C.; Jaramillo, J.; Gomperts, R.; Stratmann, R. E.; Yazyev, O.; Austin, A. J.; Cammi, R.; Pomelli, C.; Ochterski, J. W.; Martin, R. L.; Morokuma, K.; Zakrzewski, V. G.; Voth, G. A.; Salvador, P.; Dannenberg, J. J.; Dapprich, S.; Daniels, A. D.; Farkas, Ö.; Foresman, J. B.; Ortiz, J. V.; Cioslowski, J.; Fox, D. J. *Gaussian 09*, Gaussian, Inc.: Wallingford, CT, USA, 2009.

29. Becke, A. D., Density ¡functional thermochemistry. III. The role of exact exchange. *The Journal of Chemical Physics* **1993,** *98* (7), 5648-5652.

30. Hertwig, R. H.; Koch, W., On the parameterization of the local correlation functional. What is Becke-3-LYP? *Chemical Physics Letters* **1997,** *268* (5), 345-351.

31. Crozet, D.; Gual, A.; McKay, D.; Dinoi, C.; Godard, C.; Urrutigoïty, M.; Daran, J. C.; Maron, L.; Claver, C.; Kalck, P., Interplay between Cationic and Neutral Species in the Rhodium ¡Catalyzed Hydroaminomethylation Reaction. *Chemistry-A European Journal* **2012,** *18* (23), 7128-7140.

32. Stanley, G. G., Dirhodium Tetraphosphine Catalysts. In *Multimetallic Catalysts in Organic Synthesis*, Wiley-VCH Verlag GmbH & Co. KGaA: 2005; pp 225-248.

33. Decker, S. A.; Cundari, T. R., DFT Study of the Ethylene Hydroformylation Catalytic Cycle Employing a HRh(PH3)2(CO) Model Catalyst. *Organometallics* **2001,** *20* (13), 2827-2841.

34. Ziegler, T.; Tschinke, V.; Becke, A., Theoretical study on the relative strengths of the metal-hydrogen and metal-methyl bonds in complexes of middle to late transition metals. *Journal of the American Chemical Society* **1987,** *109* (5), 1351-1358.

35. Musaev, D. G.; Morokuma, K., Potential energy surfaces of transition-metal-catalyzed chemical reactions. *Advances in Chemical Physics, Surface Properties* **1997**, 61.

36. Cole-Hamilton, D. J.; Tooze, R. P., *Catalyst separation, recovery and recycling: chemistry and process design*. Springer Science & Business Media: 2006; Vol. 30.

37. Farnetti, E.; Di Monte, R.; Kašpar, J., Homogeneous and Heterogeneous Catalysis.

38. Lutz, E., Shell higher olefins process. *Journal of Chemical Education* **1986,** *63* (3), 202.

39. Aubry, D. A.; Bridges, N. N.; Ezell, K.; Stanley, G. G., Polar phase hydroformylation: the dramatic effect of water on mono-and dirhodium catalysts. *Journal of the American Chemical Society* **2003,** *125* (37), 11180-11181.

40. Unruh, J. D.; Pearson, D., n-Propyl Alcohol. In *Kirk-Othmer Encyclopedia of Chemical Technology*, John Wiley & Sons, Inc.: 2000.

41. Hunt, C.; Fronczek, F. R.; Billodeaux, D. R.; Stanley, G. G., A Monometallic Rh(III) Tetraphosphine Complex: Reductive Activation of CH_2Cl_2 and Selective Meso to Racemic Tetraphosphine Ligand Isomerization. *Inorganic Chemistry* **2001,** *40* (20), 5192-5198.

Chapter 3 - DFT Modeling of Dirhodium Catalyzed Aldehyde-Water Shift Reaction

3.1 Introduction

Carboxylic acids have a wide variety of industrial applications. They are used in the production of pharmaceuticals, surfactants, detergents, agrochemicals, plasticizers and fragrances.[1,2] Therefore, the synthesis of carboxylic acids has become a very important industrial process. Carboxylic acids can be synthesized by a variety of transition metal catalyzed processes. One such method is the conversion of alkenes, carbon monoxide (CO) and water into carboxylic acids which is referred to as hydrocarboxylation or carbonylation (Figure 3.1).

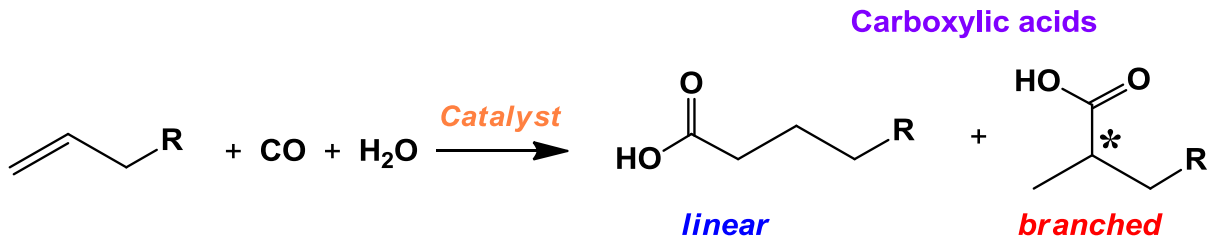

Figure 3.1. Hydrocarboxylation (or carbonylation) reaction.

Since the discovery of hydrocarboxylation by Walter Reppe in 1938, this method has been extensively used to produce carboxylic acids.[3] The first catalytic carbonylation was performed by Reppe using acetylene, CO and water to produce acrylic acid using $Ni(CO)_4$ as the catalyst.[4] Until recently acrylic acid was produced using acetylene by BASF in Ludwigshafen employing $NiBr_2$/CuI as the catalyst. This process was performed under 100 bar and 220 – 230°C.[4]

The proposed mechanism for Ni catalyzed production of acrylic acid is shown below in Figure 3.2. This involves the association of acetylene to the Ni catalyst complex followed by hydride insertion and carbonyl insertion. Finally carboxylic acid is produced by the reaction with water, which is not well understood mechanistically.

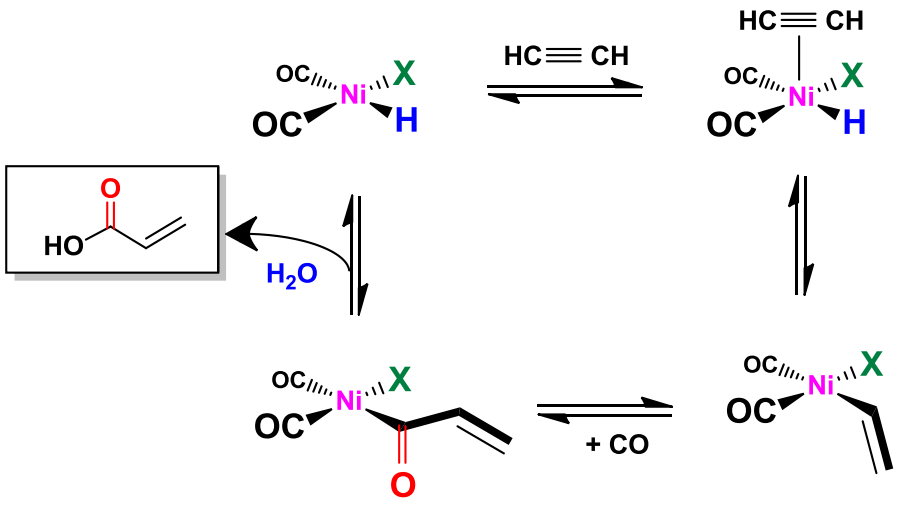

Figure 3.2. Proposed mechanism for Ni catalyzed production of acrylic acid.

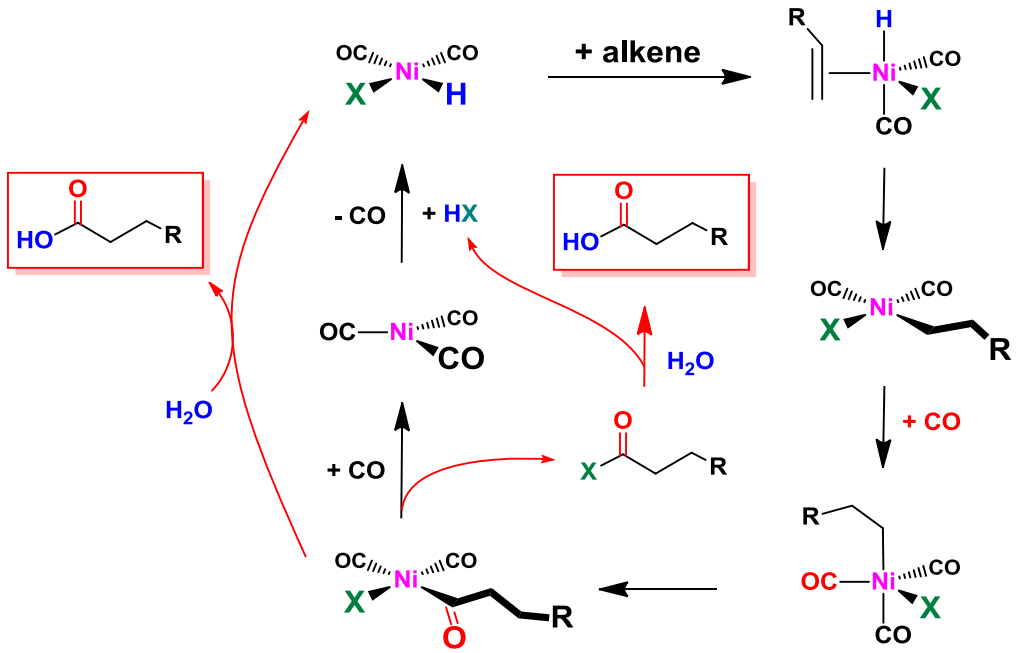

Figure 3.3. Heck's proposed mechanism for Ni catalyzed carbonylation of alkenes.[5]

More studies on carbonylation of alkenes were performed by Heck and coworkers using $Ni(CO)_4$ as a catalyst precursor. Heck's proposed mechanism for carboxylation of alkenes catalyzed by nickel carbonyl complexes is shown above in Figure 3.3.[5] The $Ni(CO)_4$ complex acts as the catalyst precursor whereas $HNiX(CO)_2$ acts as the active catalyst in this proposed carboxylation reaction. The catalyst precursor loses a carbonyl ligand and reacts with a halogen acid, HX to form the active catalyst,

halonickel dicarbonyl hydride. The alkene then coordinates to the active catalyst and the migratory insertion between the alkene and the hydride forms the alkyl. Further migratory insertion between the alkyl group and a carbonyl ligand results in the formation of an acyl group. Then the reductive elimination between the acyl group and the halide ligand produces an acyl halide which reacts with water to generate the carboxylic acid product.

In addition to carbonylation of alkenes, carboxylic acids can be synthesized from alkenes and aldehydes using an oxidant such as permanganate and hydrogen peroxide.[6] As in the Cannizzaro reaction disproportionation of an aldehyde also results in the production of carboxylic acids.[7] Rhodium catalyzed Monsanto acetic acid process[8] and Iridium catalyzed Cativa process[9] are used commercially to produce acetic acid via alcohol carbonylation. Carboxylic acid synthesis based on alcohol carbonylation is limited to methanol, and higher carbon linear aliphatic acids are mostly synthesized via hydroformylation as this process has a high selectivity to the linear products and uses less expensive syngas.[10]

Recently, the Stanley group discovered a new pathway of producing carboxylic acids using aldehydes and water. The process of producing hydrogen gas and carboxylic acids utilizing aldehyde and water is referred to as the aldehyde-water shift (AWS) catalysis (Figure 3.4a) in analogy to water-gas shift reaction, which uses carbon monoxide and water to produce carbon dioxide and hydrogen gas (Figure. 3.4b). This method can also be used to produce hydrogen gas industrially for potential use in hydrogen fuel cell. The conversion of aldehydes and water into carboxylic acids and hydrogen gas was first reported by Murahashi et al. in 1987 when they used a ruthenium catalyst to study the conversion of butanal and water into butyric acid and hydrogen gas, and octanal and water into octanoic acid and hydrogen gas.[11]

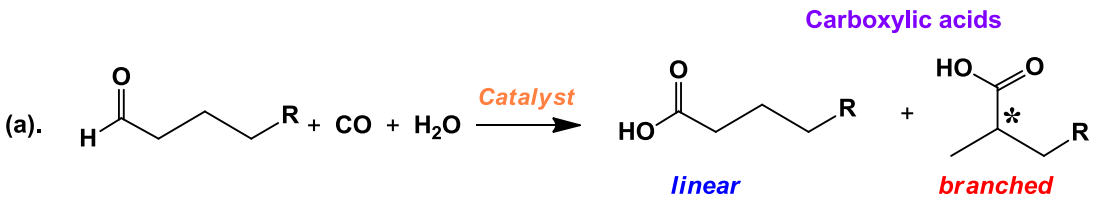

Figure 3.4. (a). Aldehyde – water shift reaction. (b).Water - gas shift reaction.

The remarkable discovery of AWS catalysis in Stanley group was quite accidental. While exploring the catalytic activity of hydroformylation in water/acetone system a leak in the reaction apparatus resulted in H_2 loss and aldehydes and carboxylic acids were observed in the GC trace of 1-hexene run under these conditions (Figure 3.5). Further studies confirmed the acid production was due to the reaction of aldehydes (produced from hydroformylation) with water.

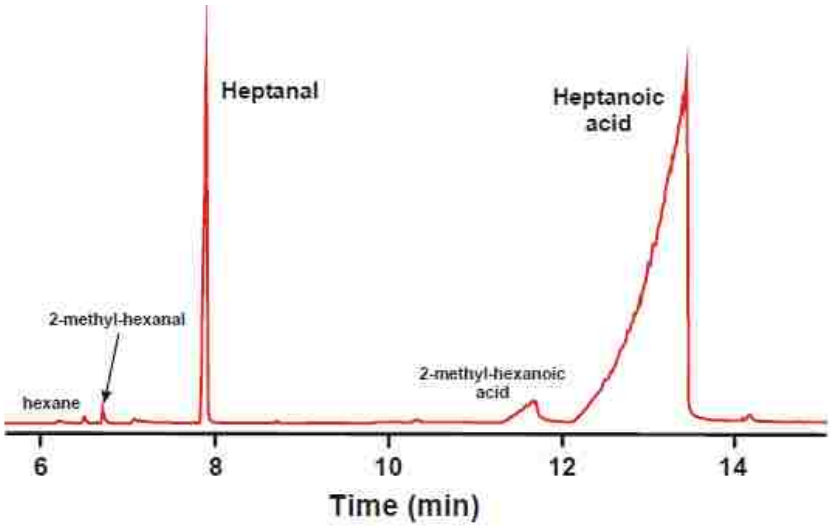

Figure 3.5. GC trace of hydroformylated 1-hexene using bimetallic Rh catalyst under H_2 depleted environment (leaky autoclave) using a water/acetone solvent mixture.

Despite the potential applications of AWS catalysis, not much work has been performed in this area. Recent studies by Heinekey and Goldberg have been performed on this process using monometallic catalyst systems based on Ir, Rh or Ru, but these reactions are slower and less selective that that seen with our bimetallic system.[12,13] This chapter discusses density functional theory (DFT) studies performed on the AWS process catalyzed by a bimetallic Rh complex, proposed to be [*rac*-$Rh_2(\mu\text{-}CO)_2(CO)_2$(et,ph-P4)]$(BF_4)_2$. Experimental work has mainly been performed on two-stage tandem catalysis: hydroformylation of alkene to produce aldehyde, followed by AWS process using our bimetallic Rh catalyst (Figure 3.6). The hydrogen gas produced during this process could be theoretically re-used for hydroformylation, but this is difficult in our batch autoclave experimental setups.

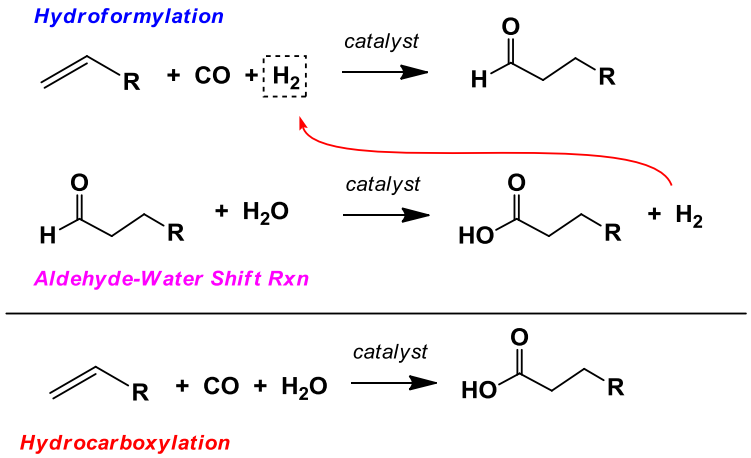

Figure 3.6. Hydrocarboxylation as a tandem reaction of hydroformylation and AWS catalysis.

DFT studies were used to determine the active catalyst, intermediates, and activation barriers in order to provide more insight into the AWS mechanism initially proposed by Prof. Stanley (Figure 3.7).

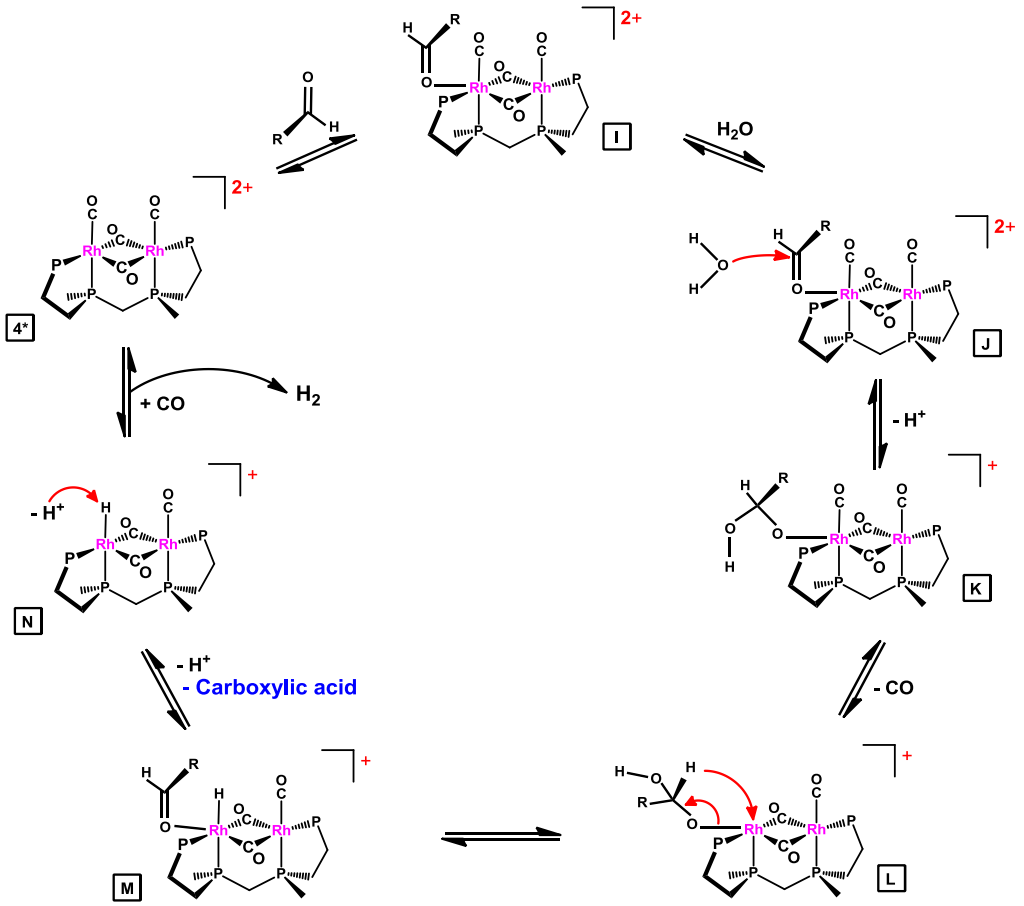

Figure 3.7. Proposed AWS mechanism.

In the proposed mechanism aldehyde coordinates to an unsaturated 16-electron Rh center (**4***). Then nucleophilic attack by water leads to a loss of a proton and activation of the aldehyde generating the monocationic complex **K**. CO dissociation from **K** generates a vacant site which facilitates the β–hydride elimination and produces a coordinated carboxylic acid complex. Reaction of a proton with the Rh-hydride produces hydrogen gas and releases carboxylic acid regenerating the dicationic complex. Coordination of a carbonyl group returns the cycle to the starting complex **4***. In addition to analyzing the proposed mechanism a more detailed mechanism from the DFT calculations is proposed.

3.2 Computational Method

All computational studies were performed using Gaussian 09 C.01 64-bit package.[14] As carboxylic acid is produced via a two-stage tandem catalysis (discussed above) the catalyst precursor used is $Rh_2(nbd)_2$(*rac*–et,ph–P4)]$(BF_4)_2$ (nbd = norbornadiene, rac–et,ph–P4 = $Et_2PCH_2CH_2P(Ph)CH_2P(Ph)CH_2CH_2PEt_2$). The ethyl and phenyl groups were replaced by methyl groups during the calculations to minimize computational time. All geometries were optimized using an all electron basis sets where Rh was optimized with 3-21G, C, H, O and P atoms using 6-311G**, and a hybrid B3LYP functional was utilized.[15] The calculations were performed in vacuum, both in the presence and absence of explicit water molecules. A better explanation for AWS catalysis is achieved with the presence of explicit water molecules. Ground state geometries and transition state geometries were determined using vibrational frequency analyses. Transition state geometries contain a single imaginary frequency whereas the optimized ground state geometries did not produce any negative frequencies.

As the AWS is not observed under normal hydroformylation conditions (1:1 H_2/CO), therefore the active catalyst should not contain any hydride ligands. The key catalyst species proposed for AWS catalysis is shown below in Figure 3.8.

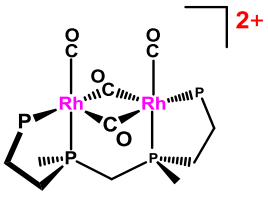

Figure 3.8. The $[Rh_2(et,ph\text{-}P4)]^{2+}$ dinuclear core proposed for aldehyde-water shift catalysis.

The tetracarbonyl complex with four carbonyl ligands and $[Rh_2(et,ph\text{-}P4)]^{2+}$ core structure generated in the hydrofomylation during the reductive elimination of the aldehyde should be the starting complex in this catalytic process. As the tetracarbonyl complex exits as open-mode and closed-mode structures, the most reliable structure should be determined. DFT studies were performed on the AWS mechanism to identify the most reliable active catalyst and consequently a plausible mechanism. DFT energies suggest that AWS catalysis is thermodynamically feasible: for propanal ΔG (298.15 K) is –6.96 kcal/mol. This is in good agreement with what Prof. Stanley has calculated from thermodynamic data using ethylene as the alkene substrate: ΔG_{rxn} = –6.8 kcals/mol. We believe that DFT calculations provided great insight into understanding the catalyst species and mechanism for our bimetallic hydroformylation systems – dicationic and monocationic. AWS catalysis should also be amenable to DFT computations.

3.3 Results

3.3.1 Determination of the Active Catalyst Species

DFT studies were performed on the open-mode (**4**) and closed-mode (**4***) tetracabonyl complexes to determine the active catalyst. As shown below in Figure 3.9, complex **4** has a square planar geometry at the Rh centers with a Rh-Rh separation of 5.7 Å. **4*** is the closed-mode isomer with the rhodium centers separated by 3.1 Å, which correlates with an edge-sharing bioctahedra with two d^8 metal centers and no covalent Rh-Rh bonding.

Figure 3.9. (a). Complex 4 (open-mode). (b). Complex 4* (closed-mode).

The lack of Rh-Rh covalent bonding in **4*** is a consequence of the filled bonding and anti-bonding Rh-Rh bonding orbitals. The bridging ligands help keep the metal centers in close proximity. The closer proximity of Rh centers in **4*** should facilitate the bimetallic cooperativity in AWS catalysis suggesting that this might be the active catalyst. DFT calculations further demonstrate that complex **4** is 4.1 kcal/mol higher in energy than **4***. These results imply that closed-mode **4*** is the more likely species compared to open-mode **4**.

In order to further probe the nature of the active catalyst, aldehyde coordination to Rh center was explored. Both **4** and **4*** contain low lying vacant orbitals to coordinate the aldehyde – the Rh $4p_z$ orbital. The coordination of acetaldehyde, propanal, and hexanal to **4** and **4*** were studied. Binding of a ligand to metal occurs as a result of the interaction between a filled ligand orbital with an empty metal orbital. These can be examined by analyzing the energy and the composition of the lowest unoccupied molecular orbital (LUMO) of metal complexes. DFT energy calculations demonstrate that the LUMO of **4** is 0.75 eV higher in energy than **4***, and this indicates that the LUMO in **4*** is a lower energy and better acceptor orbital to interact with a filled ligand lone pair (Figure 3.10).

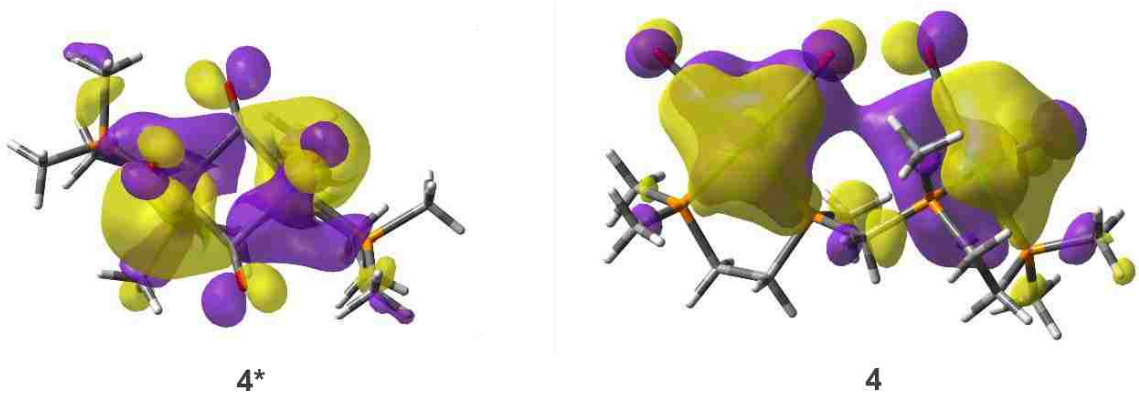

Figure 3.10. Molecular orbitals of LUMO of (a). 4* (b). 4.

In addition to the energy difference, the molecular orbital analysis of **4** and **4*** also supports that **4*** is a more suitable choice for the active catalyst than **4**. The LUMO of **4*** is comprised of an empty Rh p_z-orbital (xy-plane is defined by terminal CO and two outer phosphines) and is strongly bonded to terminal and bridging CO π^*-orbitals. This results in a strong interaction between the two Rh centers and four CO groups as opposed to the LUMO of **4** as shown in Figure 3.10. Due to the cationic charges and

CO π^* system the Rh centers in **4*** become more electron deficient producing an excellent LUMO acceptor orbital which is more prone to bind activating substrates than LUMO of **4**.

These results suggest that close-mode **4*** is a far better choice for the aldehyde-water shift catalysis than the open-mode **4**. This is supported by the experimental results. When **4** is reacted with alkene, water and CO under 90 psig pressure and 90°C temperature hardly any hydroformylation or AWS catalysis was observed. This suggests that a significant amount of water-gas shift ($CO + H_2O \rightleftharpoons CO_2 + H_2$) is not occurring under these conditions; if H_2 is produced this would facilitate hydroformylation and when H_2 is deficient this should help AWS catalysis.

The experimental results clearly show that H_2 is required to generate close-mode bridged carbonyl complexes as bridging CO bands in the IR were only observed in the presence of H_2. When the open-mode tetracarbonyl complex **4** is placed under CO it will convert to an open-mode pentacarbonyl complex **5** that does not catalyze the AWS process. The experimental results suggest that AWS catalysis initiates when the reaction mixture is initially treated with some CO and H_2. Then in the presence of a H_2 deficient environment AWS catalysis will take place, so a non-hydride complex acts as the active catalyst during this process, but not one of the open-mode carbonyl complexes. The species that agrees best with these observations is the closed-mode bridged carbonyl complex **4***.

The other key factor to consider in AWS catalysis is the concentration of alkene in the reaction mixture. As alkenes are better ligands relative to aldehydes they can bind to the metal center inhibiting the catalytic process; hence, low concentrations of alkenes and H_2 are required for aldehyde-water shift catalysis when attempting to do tandem hydroformylation and aldehyde-water shift catalysis.

3.3.2 Catalysis in Vacuum: DFT Calculations

3.3.2.1 Aldehyde Coordination to the Catalyst

The first step of the AWS catalytic process will be the binding of the aldehyde to the metal center. This was studied using acetaldehyde, propanal, and hexanal with both **4** and **4***. DFT calculations showed that the open-mode, **4** resulted in a relatively longer distances between Rh and carbonyl O atom than the

closed-mode, **4* (**see Table 3.1**)**. This further suggests that the closed-mode complex is more likely to react with the aldehyde than the open-mode complex.

Table 3.1. Bond distances (Å) between Rh and aldehyde O.

Complex	Acetaldehyde	Propanal	Hexanal
Open-mode - **4**	4.16785	4.11754	3.24157
Closed-mode – **4***	3.91386	3.20691	3.07565

According to DFT studies, when larger aldehyde substrates are coordinated to the metal center the Rh–aldehyde O distances decrease. The larger aldehydes are more electron rich than the smaller aldehydes, and this will result in a better overlap between the metal center and the aldehyde resulting in a smaller distance. The Stanley group has converted acetaldehyde to acetic acid via AWS catalysis, so that is a viable experimental substrate. Considering the computational time propanal was selected as the model aldehyde substrate for the DFT studies. Even though it was proposed initially by Prof. Stanley that aldehyde coordination occurs via the π-system, DFT calculations showed that the binding occurs via the lone pair of oxygen. Coordination of propanal to the metal center is shown below in Figure 3.11.

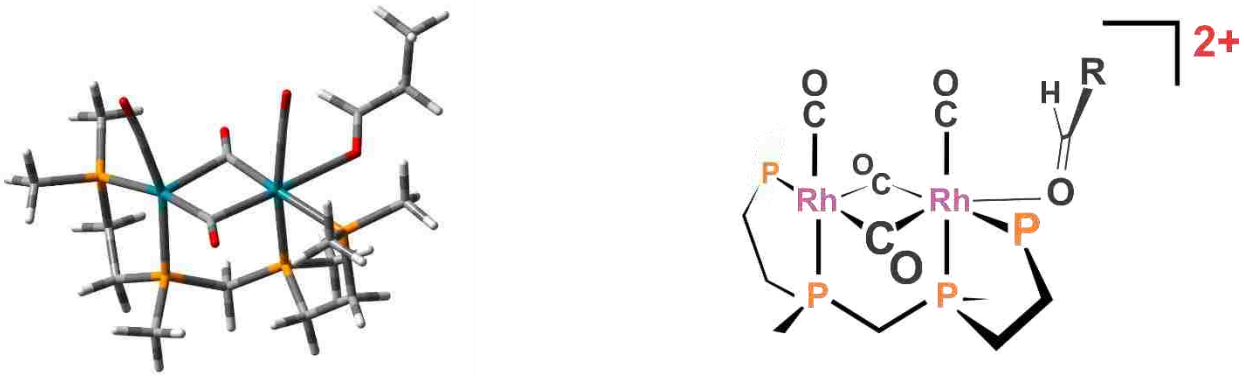

Figure 3.11. Aldehyde coordination mode to the metal center computed via DFT method.

3.3.2.2 Reaction with Water

A key step in the proposed AWS catalysis is the reaction of the coordinated aldehyde with water. Water, acting as a nucleophile, activates the aldehyde by destabilizing the C=O bond of the aldehyde. The reaction of water with propanal coordinated to **4*** can result in two intermediates; a protonated diol (**G**, see Figure 3.12 or a deprotonated diol (**G'**). DFT calculations does not support the formation of **G'** in the gas phase as it corresponds to a significantly high energy difference, whereas formation of **G** is only uphill by +6.81 kcal/mol. The activation barrier for this step in absence of a solvent medium is difficult to calculate.

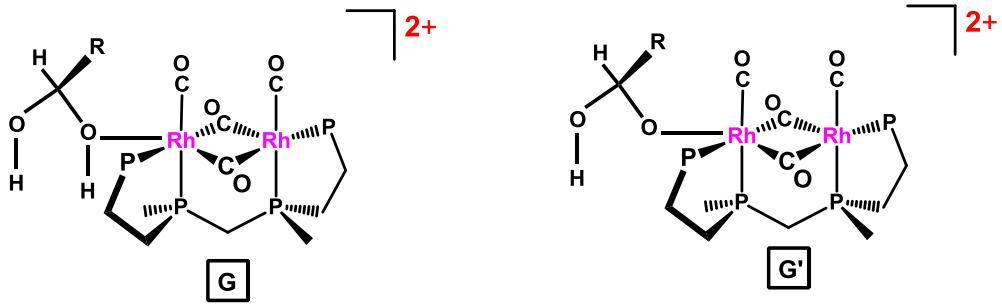

Figure 3.12. Protonated diol, G and deprotonated diol, G'.

3.3.2.3 Subsequent Catalytic Steps

A CO group dissociates from **G** forming **H** corresponding to a small energy increase of 2.4 kcal/mol. This results in the rotation of the equatorially coordinated protonated diol into an axial position, which in turn, lowers the stability of the protonated diol facilitating its conversion into a carboxylic acid. Then β-hydride elimination followed by tandem abstraction of proton in the diol results in the production of H_2 and deprotonated carboxylic acid: this step is favored by –0.7 kcal/mol. Finally, the carboxylic acid eliminates from the cycle regenerating **4*** and this is favored by –12.04 kcal/mol. The computed catalytic cycle is shown below in Figure 3.13.

The thermodynamic energy values obtained from DFT calculations indicate that except for the formation of the protonated diol (8.7 kcal/mol) and CO dissociation (2.4 kcal/mol) all the other steps in the catalytic cycle: reaction with propanal (–3.4 kcal/mol), reaction with water (–1.9 kcal/mol), β-hydride

elimination, production of H_2, and deprotonated acid (–0.7 kcal/mol), and aldehyde elimination and regeneration of **4*** (–12.04 kcal/mol) are exoergic. This results in a total free energy value of -6.96 kcal/mol**.**

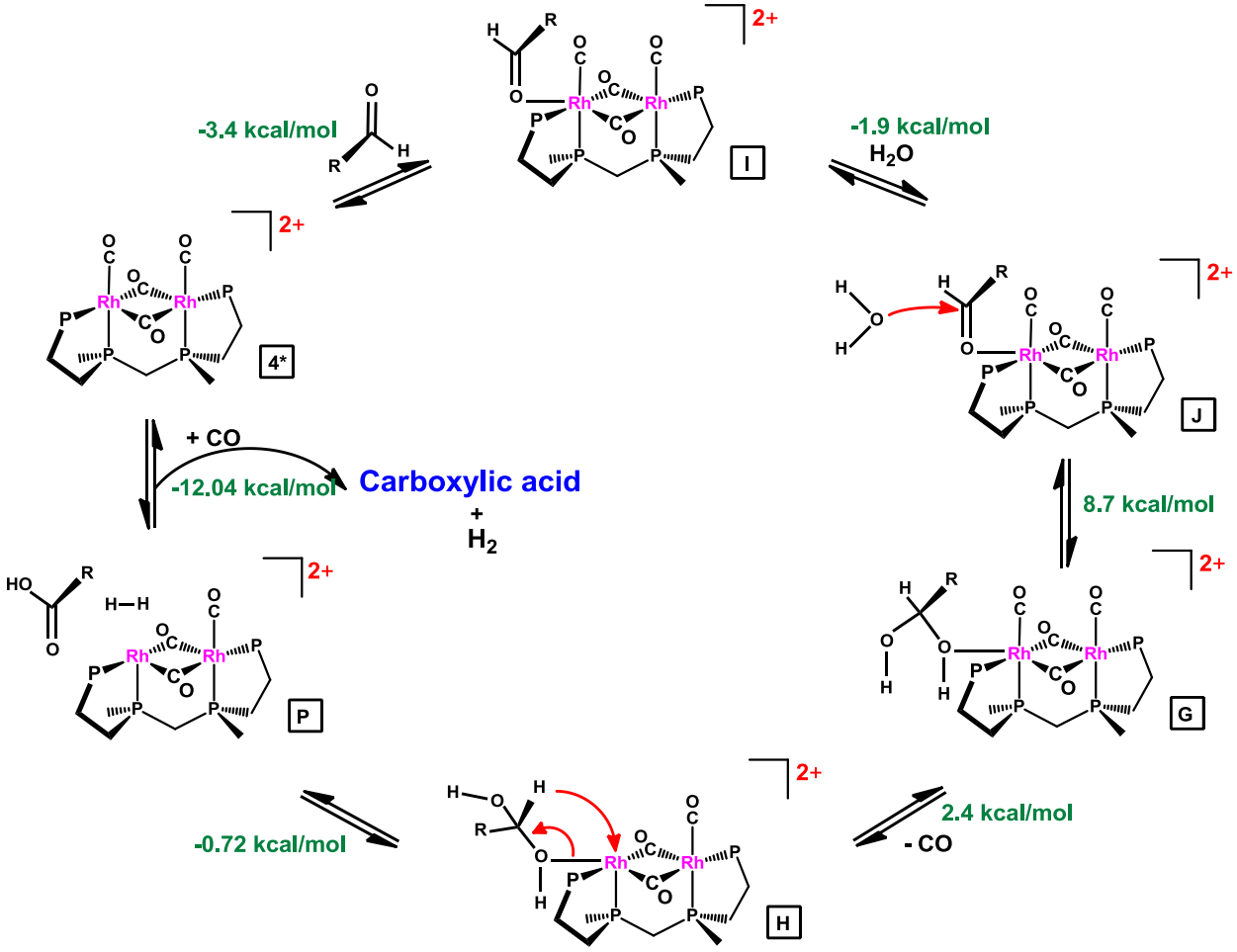

Figure 3.13. DFT computed mechanism for AWS catalysis.

3.3.3 Catalysis with Explicit Waters

3.3.3.1 Aldehyde Coordination

DFT studies were performed using four explicit water molecules to mimic the experimental conditions instead of using an implicit solvent model. Three water molecules were placed closer to the aldehyde and one water molecule was placed closer to the opposite Rh center which is not coordinated to the aldehyde. As water molecules are used explicitly they are treated as individual molecules instead of a

continuum model, so interactions between solvent and solute are modeled. If an implicit solvent model is used the solvent will be treated as a polarizable continuum, and this serves as a reaction field that interacts with the solute. The use of an implicit solvent model is computationally less time consuming, but some interactions such as hydrogen bonding with solute are difficult to model.

In the presence of explicit water molecules the separation between the metal center of **4*** and carbonyl O atom of acetaldehyde and propanal were decreased by 0.97 Å and 0.46 Å respectively. These DFT results suggest that the explicit solvent model stabilizes the reaction more so than in vacuum without waters. Coordination of propanal to the metal center in presence of water molecules corresponds to an energy drop of –7.7 kcal/mol, indicating a more favorable coordination step to start the catalysis.

3.3.3.2 Reaction with Water

The reaction of water with propanal coordinated to **4*** can result in two intermediates; a protonated diol (**K**) or a deprotonated diol (**K'**). The OH group of a water molecule in the solvent binds with the carbonyl C atom and the proton binds with the carbonyl O atom of propanal to form the protonated diol. Formation of **K** corresponds to a very small energy difference of -0.03 kcal/mol (Figure 3.14), but the activation barrier for this step is quite large at 41.7 kcal/mol, and this may be due to the use of explicit solvent molecules (Figure 3.15). DFT calculations suggest that the reaction with water is favorable in the presence of explicit solvent molecules as it corresponds to a downhill energy whereas in the absence of solvent molecules this step is uphill by +6.8 kcal/mol. This may be due to the fact that hydrogen bonding of the solvent water to the protonated diol lowers the energy change.

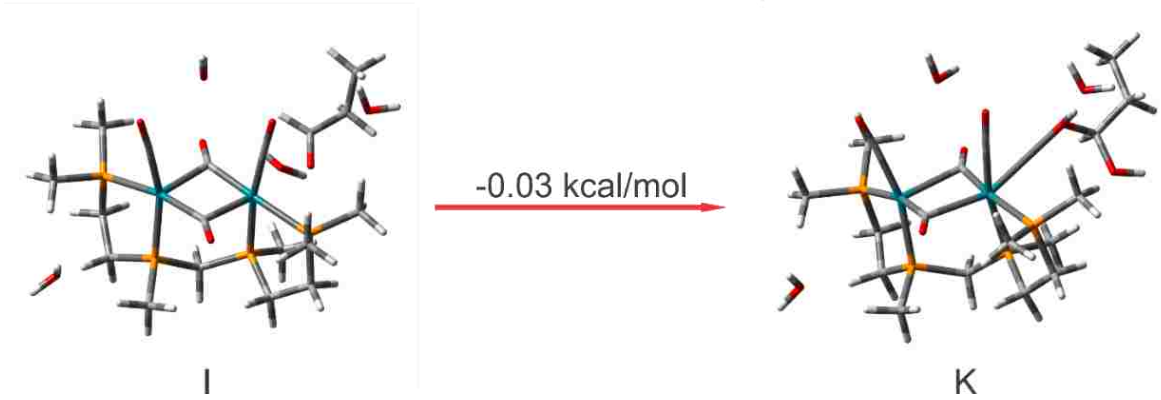

Figure 3.14. Reaction with water to produce a protonated diol.

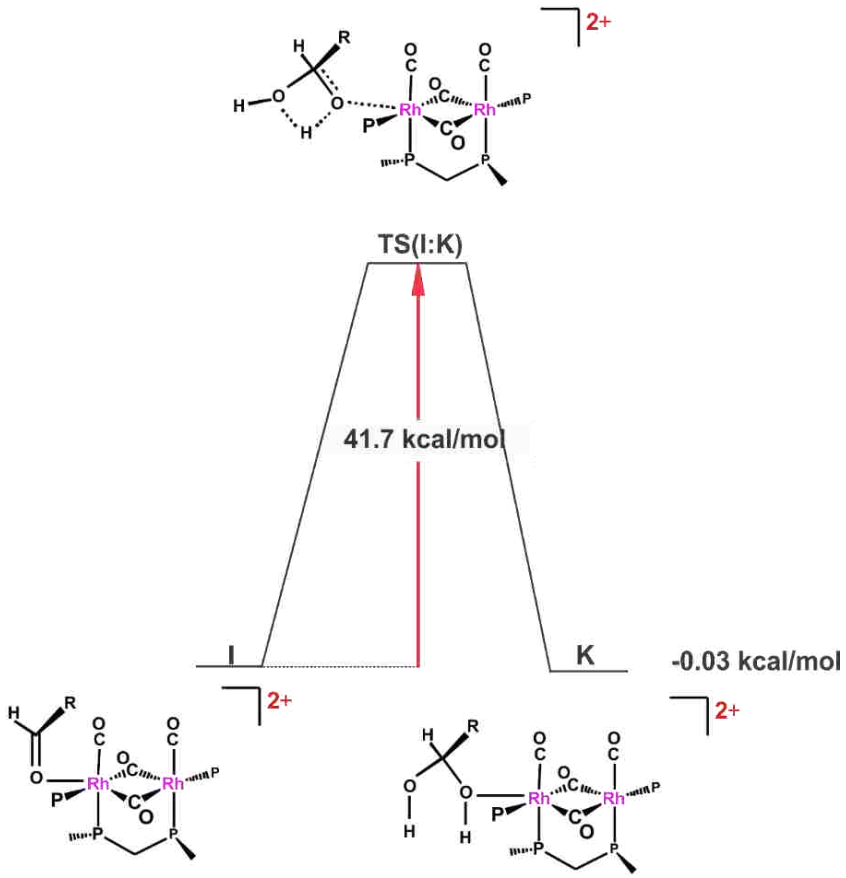

Figure 3.15. Activation barrier for the formation of the protonated diol.

The transition state in the presence of solvent molecules, **TS(I:K)** was determined via vibrational analysis and a single imaginary frequency (see Appendix 3) corresponding to the correct vibrational mode was obtained. The C=O bond of propanal was elongated by 0.14 Å in the **TS(I:K)** relative to species **I**. The distance between the carbonyl C atom and O of water decreased by 1.78 Å in the **TS(I:K)** relative to **I**, resulting in an O-H bond length of 0.96 Å in the protonated diol complex, **K**. These structural differences further determines the correct transition state.

DFT calculations indicate deprotonation is not feasible as transfer of the proton to water molecule is not observed. The distance between the proton and the closest water molecule is 1.86 Å which is significantly longer than a normal O-H bond, 0.98 Å (Figure 3.16). This may be due to low basicity of the solvent medium and lack of enough explicit water molecules to stabilize the protonated water that forms.

As a deprotonated diol is not observed at this step, reactions proceeding from the protonated diol, **K** will be discussed.

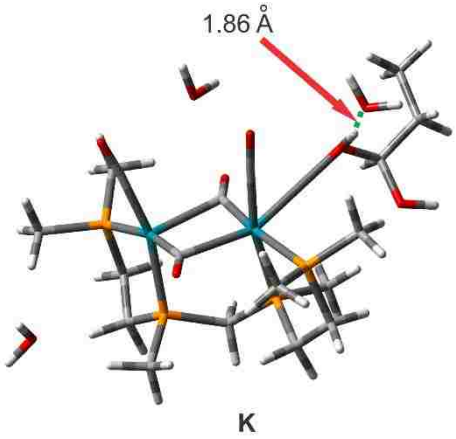

Figure 3.16. Protonated diol complex, K.

3.3.3.3 Subsequent Catalytic Steps

The axial CO group on the saturated Rh center dissociates from **K** to form **L** corresponding to an energy change of +0.7 kcal/mol. This moves the protonated diol from its equatorial position to an axial position (Figure 3.17) making the coordination less stable, which helps to initiate the β-hydride elimination to generate the protonated carboxylic acid (**M**) resulting in a +4.1 kcal/mol energy change. Transition state calculations yield a 19.4 kcal/mol activation barrier for this step.

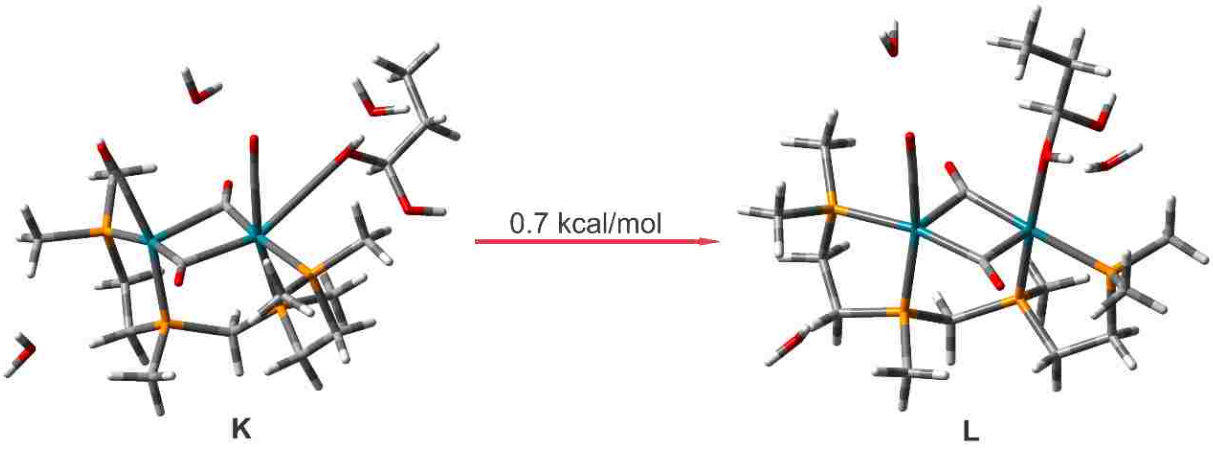

Figure 3.17. Rotation of protonated diol from equatorial position (K) to axial position (L).

In the transition state (**TS(L:M)**) the β–hydride moves to the vacant site at the Rh center generating a protonated acid, **M**. The distance between the proton of the protonated acid and the closest solvent water molecule has decreased by 0.05 Å in the transition state favoring the deprotonation of the acid. The transition state was confirmed by frequency analysis which resulted in a single imaginary frequency (see Appendix 3) . Free energy profile for β–hydride elimination is shown below in Figure 3.18.

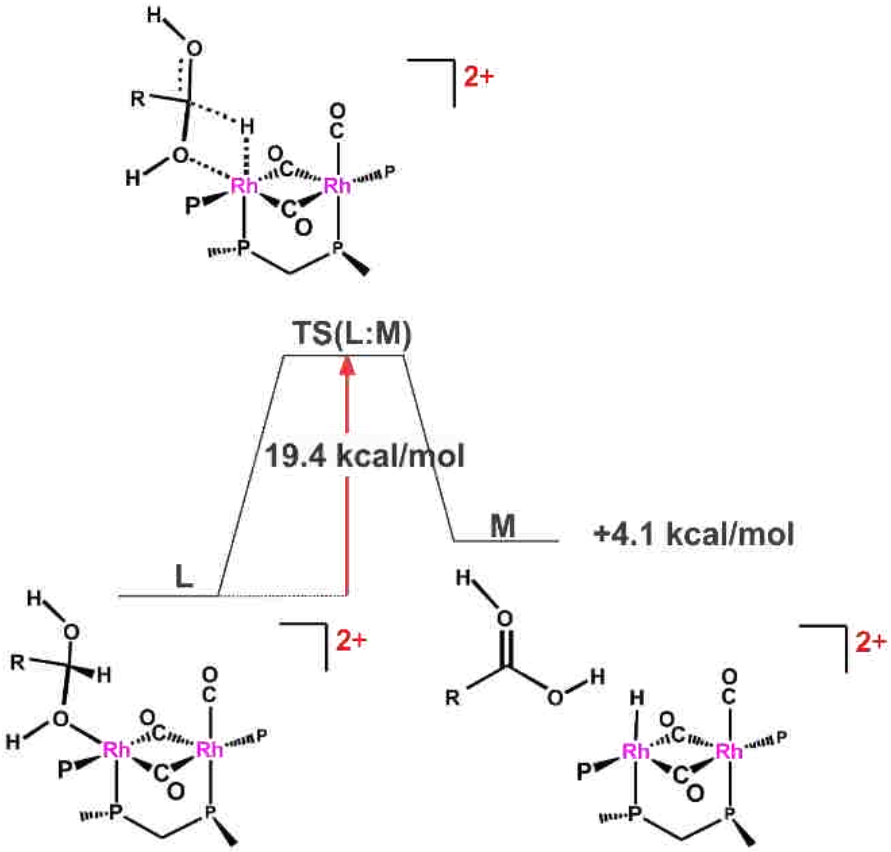

Figure 3.18. Free energy profile for β–hydride elimination.

DFT studies demonstrate that once the protonated acid is moved to axial position it is easily deprotonated due to close proximity of explicit water molecules. The proton is moved towards one of the water molecules decreasing the separation between the proton and O of water molecule by 0.81 Å, binds to the proton and releases the deprotonated carboxylic acid (Figure 3.19).

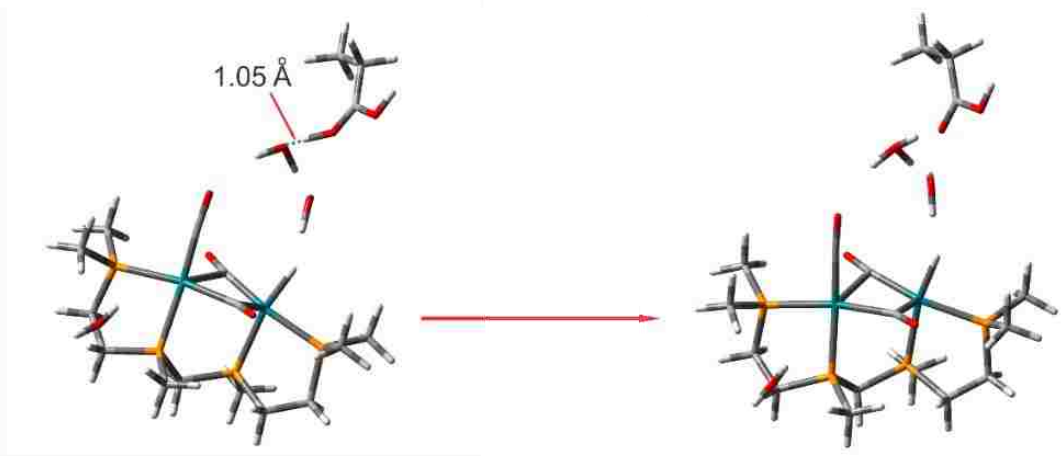

Figure 3.19. Deprotonation of carboxylic acid.

β-hydride elimination and deprotonation of the carboxylic acid are semi-concerted. This removes the unfavorable energy change for just the β-hydride elimination and formation of protonated carboxylic acid, which is a very unlikely species in water. Elimination of H_2 gas from the catalytic cycle then takes place easily. Reaction of hydride with a protonated water molecule facilitates the H_2 gas formation corresponding to a downhill energy change of –1.8 kcal/mol. DFT studies suggest elimination of H_2 is a barrier-less reaction, but it proceeds via an intermediate. The optimized intermediate for H_2 elimination is shown in Figure 3.20. The proton in the water molecule moves towards the hydride in the intermediate facilitating the elimination. This step is followed by the addition of CO which regenerates the closed-mode **4***.

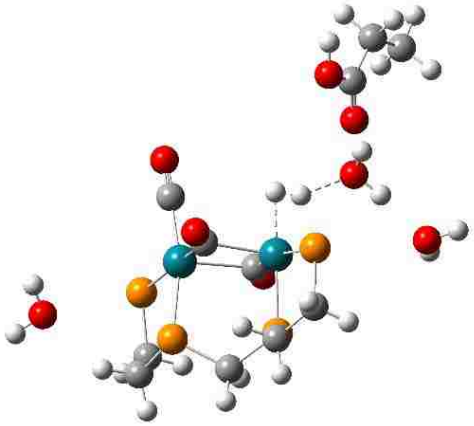

Figure 3.20. Intermediate of H2 elimination (For clarity methyl groups attached to phosphorous atoms are removed).

The thermodynamics from the DFT calculations indicate that the AWS catalysis is favorable with the bimetallic Rh catalyst, [*rac*-$Rh_2(\mu\text{-}CO)_2(CO)_2$(et,ph-P4)]$(BF4)_2$, (**4***). The coordination of propanal (–7.7 kcal/mol), reaction with water to produce protonated diol (–0.03 kcal/mol), generation of hydrogen gas (–1.8 kcal/mol), coordination of CO (–9.5 kcal/mol) and elimination of the acid and hydrogen gas to regenerate the catalyst **4*** (–5.4 kcal/mol) are all exoergic. The steps which were computed as endoergic were the CO dissociation (0.7 kcal/mol), β-hydride elimination to generate the protonated acid (4.1 kcal/mol) and deprotonation of the protonated acid (0.007 kcal/mol), but these steps correspond to small energy values. The DFT computed catalytic cycle is shown below in Figure 3.21.

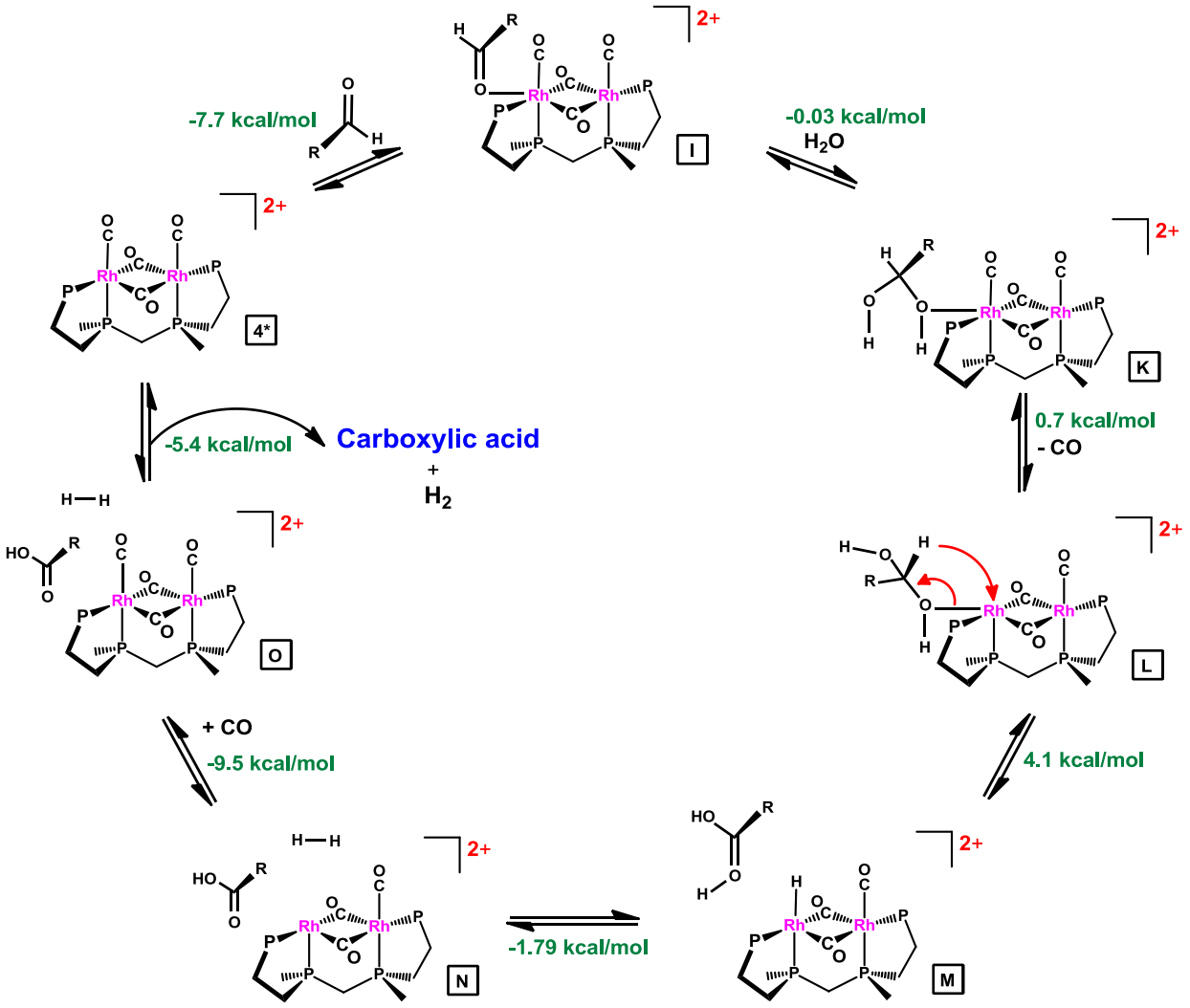

Figure 3.21. DFT computed mechanism for AWS in the presence of explicit water molecules.

The calculated total free energy values for the catalytic cycle is -19.6 kcal/mol which demonstrates that AWS catalysis in the solvent medium is very favorable in the presence of the bimetallic Rh catalyst as the energy barrier is reduced by 12.7 kcal/mol than in the gas phase. Overall, both the gas phase and solvent medium data behave similarly, but using four explicit water molecules in the calculation results in lower energy values for the reaction steps. This is not unexpected due to the importance of hydrogen-bonding to the various intermediates and the ultimate deprotonation step that almost assuredly needs solvent water. The transition state calculations suggest that the nucleophilic attack by water is the rate-determining step as the largest energy barrier was computed for this step.

3.4 Conclusions

DFT calculations were used to study the proposed bimetallic [*rac*-$Rh_2(\mu\text{–}CO)_2(CO)_2$(et,ph-P4)]$^{2+}$ catalyst for AWS process, and computations provide a more detailed mechanism with insights at several key steps. The computations indicate that closed-mode **4*** is a better choice for the active catalyst than the open-mode **4**. The originally proposed mechanism for AWS catalysis suggests the formation of a deprotonated diol during the reaction with water, but the DFT computed mechanisms point to the formation of a protonated diol at the key reaction of coordinated aldehyde with water, with deprotonation observed later in the cycle. β–hydride elimination and deprotonation of acid are semi-concerted, and due to the presence of explicit solvent molecules the protonated carboxylic acid initially produced is easily deprotonated by the solvent water. DFT studies demonstrate nucleophilic attack by water as the rate-limiting step.

According to DFT calculations AWS catalysis shows similar mechanisms in both gas phase and with explicit waters to simulate the solvent. The use of explicit water molecules creates an environment more similar to the experimental reaction conditions, and the catalytic process appears to be more feasible with the explicit water molecules with lower energies calculated. Further studies can be performed by increasing the number of water molecules and placing them at different positions, but this will become computationally time consuming unlike using an implicit solvent model.

3.5 References

1. Chappell, R. L., Fragrance materials containing cis-2-n-pentyl cyclopropane-1-carboxylic acid. Google Patents: 1975.

2. Zeikus, J. G.; Jain, M. K.; Elankovan, P., Biotechnology of succinic acid production and markets for derived industrial products. *Appl Microbiol Biotechnol* **1999,** *51* (5), 545-552.

3. Reppe, W.; Schlichting, O.; Klager, K.; Toepel, T., Cyclisierende Polymerisation von Acetylen I Über Cyclooctatetraen. *Justus Liebigs Annalen der Chemie* **1948,** *560* (1), 1-92.

4. Bertleff, W.; Roeper, M.; Sava, X., Carbonylation. In *Ullmann's Encyclopedia of Industrial Chemistry*, Wiley-VCH Verlag GmbH & Co. KGaA: 2000.

5. Heck, R. F., The Mechanism of the Allyl Halide Carboxylation Reaction Catalyzed by Nickel Carbonyl. *Journal of the American Chemical Society* **1963,** *85* (13), 2013-2014.

6. Smith, M. B.; March, J., *March's advanced organic chemistry: reactions, mechanisms, and structure*. John Wiley & Sons: 2007.

7. Cannizzaro, S., Ueber den der Benzoësäure entsprechenden Alkohol. *Justus Liebigs Annalen der Chemie* **1853,** *88* (1), 129-130.

8. Hershman, A.; Knox, W.; Paulik, F.; Roth, J., Production of carboxylic acids and esters. Google Patents: 1973.

9. Jones, J. H., The CativaTM process for the manufacture of acetic acid. *Platinum Metals Review* **2000,** *44* (3), 94-105.

10. Kiss, G., Palladium-Catalyzed Reppe Carbonylation. *Chemical Reviews* **2001,** *101* (11), 3435-3456.

11. Murahashi, S.; Naota, T.; Ito, K.; Maeda, Y.; Taki, H., Ruthenium-catalyzed oxidative transformation of alcohols and aldehydes to esters and lactones. *The Journal of Organic Chemistry* **1987,** *52* (19), 4319-4327.

12. Brewster, T. P.; Ou, W. C.; Tran, J. C.; Goldberg, K. I.; Hanson, S. K.; Cundari, T. R.; Heinekey, D. M., Iridium, Rhodium, and Ruthenium Catalysts for the “Aldehyde–Water Shift” Reaction. *ACS Catalysis* **2014,** *4* (9), 3034-3038.

13. Ou, W. C.; Cundari, T. R., DFT Modeling of the Aldehyde–Water Shift Reaction with a Cationic Cp*Ir Catalyst. *ACS Catalysis* **2015,** *5* (1), 225-232.

14. Frisch, M.J.; Trucks, G. W.; Schlegel, H. B.; Scuseria, G. E.; Robb, M. A.; Cheeseman, J. R.; Scalmani, G.; Barone, V.; Mennucci, B.; Petersson, G. A.; Nakatsuji, H.; Caricato, M.; Li, X.; Hratchian, H. P.; Izmaylov, A. F.; Bloino, J.; Zheng, G.; Sonnenberg, J. L.; Hada, M.; Ehara, M.; Toyota, K.; Fukuda, R.; Hasegawa, J.; Ishida, M.; Nakajima, T.; Honda, Y.; Kitao, O.; Nakai, H.; Vreven, T.; Montgomery Jr., J. A.; Peralta, J. E.; Ogliaro, F.; Bearpark, M. J.; Heyd, J.; Brothers, E. N.; Kudin, K. N.; Staroverov, V. N.; Kobayashi, R.; Normand, J.; Raghavachari, K.; Rendell, A. P.; Burant, J. C.; Iyengar, S. S.; Tomasi, J.; Cossi, M.; Rega, N.; Millam, N. J.; Klene, M.; Knox, J. E.; Cross, J. B.; Bakken, V.; Adamo, C.; Jaramillo, J.; Gomperts, R.; Stratmann, R. E.; Yazyev, O.; Austin, A. J.; Cammi, R.; Pomelli, C.; Ochterski, J. W.; Martin, R. L.; Morokuma, K.; Zakrzewski, V. G.; Voth, G. A.; Salvador, P.; Dannenberg, J. J.; Dapprich, S.; Daniels, A. D.; Farkas, Ö.; Foresman, J. B.; Ortiz, J. V.; Cioslowski, J.; Fox, D. J. *Gaussian 09*, Gaussian, Inc.: Wallingford, CT, USA, 2009.

15. Becke, A. D., Density ¡functional thermochemistry. III. The role of exact exchange. *The Journal of Chemical Physics* **1993,** *98* (7), 5648-5652.

Chapter 4 - DFT Studies on Bimetallic Cobalt Catalyzed Hydroformylation and Aldehyde-Water Shift Reactions

4.1 Introduction

The discovery of cobalt hydroformylation catalyst complexes by Otto Roelen in 1938 laid the ground work for the initiation of one of the most useful and important chemical industries based on homogeneous organometallic catalysts.[1] Cobalt and rhodium complexes are the most widely used commercialized catalysts for hydroformylation. Despite the higher chemo- and regioselectivity of rhodium catalysts, the use of cobalt catalysts for hydroformylation and aldehyde-water shift (AWS) catalysis is of considerable interest as they are less expensive, less toxic, and often thermally more stable.[2-5] Hence, development of modified cobalt catalysts with higher activity, good chemo- and regioselectivity is of great importance and has gained much interest industrially.

The unmodified cobalt catalyst, $HCo(CO)_4$ was the first cobalt catalyst discovered by Otto Roelen about 75 years ago that performed hydroformylation and was a major breakthrough of homogeneous catalysis. $HCo(CO)_4$-catalyzed hydroformylation is performed at temperatures ranging from 200-250 °C and H_2/CO pressures of 200-300 bar.[2,6] These conditions produce 45-55% linear aldehydes and a significant amount of aldol condensation of aldehydes.

Later, Shell Chemical discovered that modifying $HCo(CO)_4$ with phosphine ligands enhanced the catalytic activity and increased catalyst stability at lower CO pressures.[8] The incorporation of phosphine ligands increases the electron density at the metal center which consequently produces a stronger metal-CO bond leading to less fragmentation, lower catalyst activity, and enhanced hydrogenation. Phosphine-modified cobalt catalyzed hydroformylation is performed at temperatures of 160-200 °C and lower syn gas pressures of 100 bar. These conditions produce about 90% linear aldehydes or alcohols.[2,5-7]

The mechanism for hydroformylation catalyzed by $HCo(CO)_4$ was proposed by Heck and Breslow in 1960s (Figure 4.1).[9] The 18 e- saturated $HCo(CO)_4$ complex dissociates a carbonyl group to form a vacant site where an alkene can coordinate. Migratory insertion between the alkene and the hydride produces an alkyl group and further migratory insertion between the alkyl group and carbonyl group forms an acyl group. Oxidative addition of H_2 occurs, followed by reductive elimination of the aldehyde to

regenerate the catalyst. The same steps occur in the phosphine-modified cobalt catalyst system. By varying the reaction conditions and the properties of the phosphine ligand, better yields in hydroformylation can be obtained by minimizing side reactions and maximizing the desired product.

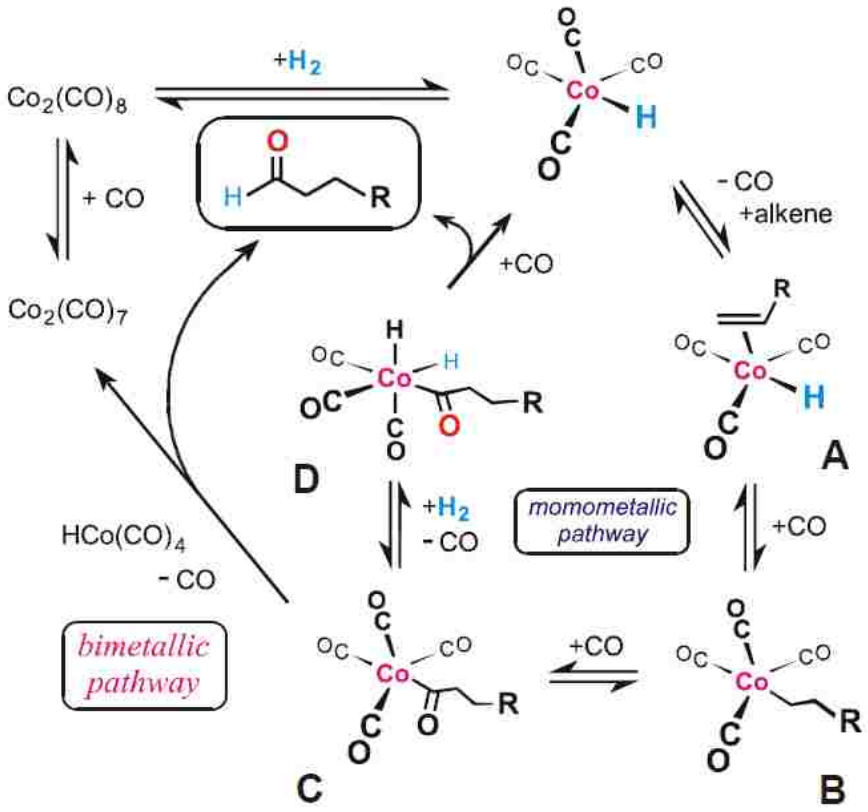

Figure 4.1. Mechanism of $HCo(CO)_4$ hydroformylation proposed by Heck and Breslow.[9]

Even though a bimetallic pathway was proposed by Heck and Breslow this was not favored (discussed in Chapter 2). This proposed bimetallic mechanism involves an intermolecular hydride transfer between $HCo(CO)_4$ and $Co(acyl)(CO)_4$ to eliminate the aldehyde product. Many proposals on polymetallic cooperativity in hydroformylation were proposed based on inter- or intramolecular hydride transfers to enhance elimination of the aldehyde product. Stoichiometric mechanistic studies performed by Bergman, Halpern, Norton and Marko have demonstrated that intermolecular hydride transfers can occur between metal-hydride and metal-acyl species to eliminate aldehyde products.[10-13]

Few studies on hydroformylation utilizing polymetallic catalysts are reported in literature. Pittman and coworkers have reported that 1-penetene could be used for hydroformylation by the intact cobalt

clusters **1** and **2** (Figure 4.2).[14] These clusters resulted in linear to branched aldehyde ratios between 1 and 5:1 (~ 2.5 being typical) at temperatures of 90-150° C and pressures of 400-1100 psig. It was observed that the addition of phosphine ligands avoided fragmentation of the cobalt clusters into $HCo(CO)_4$. An improved stability of the clusters was observed upon the addition of 2-4 equivalents of PPh_3, but this did not result in an increase in hydrogenation activity to produce alcohol products unlike monometallic $HCo(CO)_3(PR_3)$ catalysts.[15] High pressure IR studies of phosphine substituted analogs of **2** have shown that there was no observable cluster fragmentation under catalytic conditions (150° C, 600 psi), even over a two day period.[16]

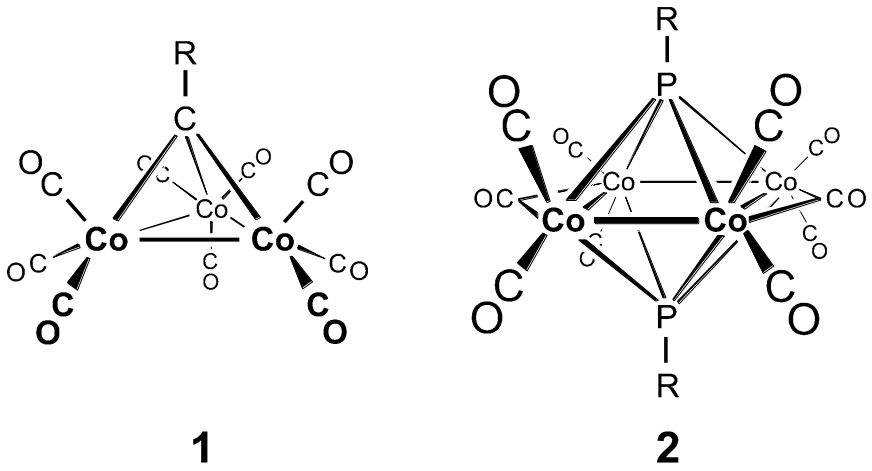

Figure 4.2. Cobalt clusters used in hydroformylation.

The use of bimetallic systems is of considerable interest due to their enhanced activity as they can form many metal-ligand bonds which may activate the substituents, metal-metal bonds that can stabilize the complex and/or the active site, and they can also be involved in multielectron transfer reactions that can be enhanced due to the presence of multiple metal centers.[17]

Use of bimetallic cobalt complexes for hydroformylation and aldehyde-water shift catalysis (AWS) will be more economical and preferable from an industrial viewpoint if the activity and selectivity can be increased over existing monometallic cobalt catalysts. Thus, exploring the chemistry behind these cobalt complexes is of great importance. Studies on the suitability of bimetallic cobalt complexes for these catalytic processes are not found in literature, nor have they been carefully studied in the Stanley group. Prof. Stanley reports that the group did study a dicobalt hydroformylation catalysts based on the et,ph-P4

ligand, but details on this are not in any of the student dissertations. Prof. Stanley's recollection is that the dicobalt system was not anywhere as fast as the dirhodium catalyst, but did show activity under very mild reaction conditions. The production of the new, and stronger coordinating et,ph-P4-Ph ligand system has rekindled interest in using the dicobalt system for hydroformylation. Ciera Gasery in our group is currently working on preparing these dicobalt complexes for experimental studies. This chapter discusses the DFT studies performed to analyze the suitability of a bimetallic cobalt complex, $[Co_2(CO)_5(rac–meP4)]^{2+}$, proposed by Prof. Stanley for hydroformylation and AWS catalysis.

4.2 Computational Method

The DFT calculations were performed using Gaussian 09 C.01 64-bit package.[18] All calculations were performed in vacuum at 298.15 K. A mixed basis set as well as a single basis set for all the atoms were used to optimize the cobalt complexes in order to find the most suitable basis set for the computational analysis. The bimetallic tetracationic cobalt complex, $[Co_2(\mu–CO)_2(CO)_2(et,ph\text{-}P4]^{4+}$, was used to determine the most suitable basis set.

Co centers were optimized with a smaller 3–21G basis set, whereas C, H, O and P atoms were optimized with 6–311G** basis set, similar to what we used for the dirhodium calculations. The Co–Co distance in the tetracationic complex was 2.4 Å. In contrast to the mixed basis set, when all the atoms were optimized with 6–311G** basis set, Co-Co distance was elongated by 0.4 Å (Figure 4.3).

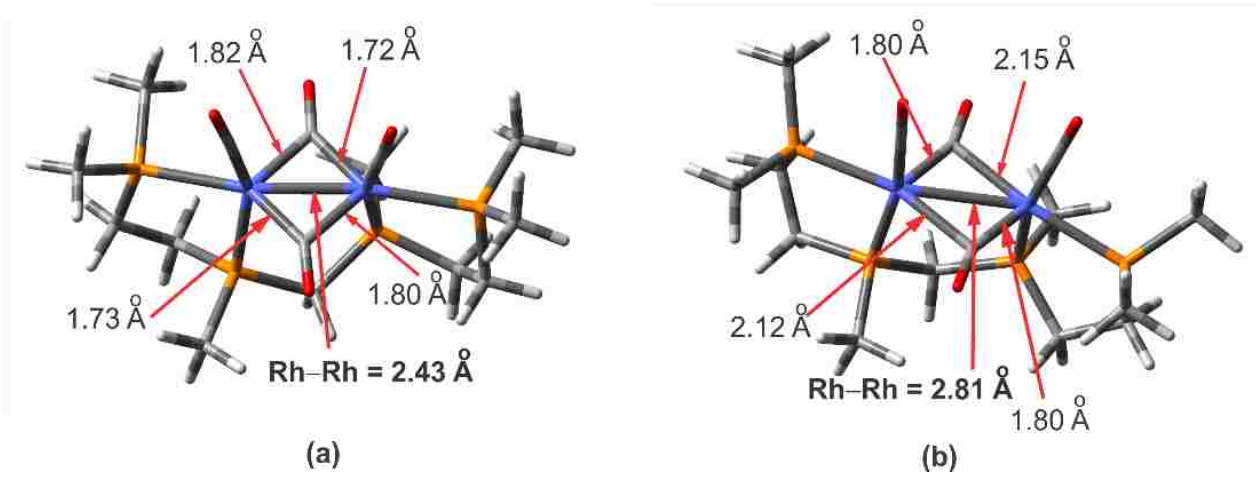

Figure 4.3. $[Co_2(\mu–CO)_2(CO)_2(et,ph\text{-}P4]^{4+}$ optimized using (a). 6–311G** basis set on all atoms. (b). 3–21G on Co and 6–311G** on C,H, O and P atoms.

The large positive charge on the cobalt tetracationic complex makes it difficult for the cobalt centers to be in close proximity and to overlap. These results suggest that the 6–311G** basis set is more suitable than the mixed basis set for the computational investigations.

The cobalt complexes were optimized using 6-311G** basis set and B3LYP hybrid functional.[19] Frequency calculations were performed to determine the ground states and transition states. The optimized ground states contained zero imaginary frequencies, whereas the transition states had a single imaginary frequency.

4.3 Results

4.3.1 Dicobalt Catalyzed Hydroformylation

DFT and experimental studies show that unlike Rh hydroformylation catalysis, the formation of saturated complexes is favored in Co hydroformylation chemistry (Figure 4.4). As cobalt metals favor higher coordination numbers unlike rhodium metals, carbonyl groups are easily bonded to the dicobalt complex to generate trigonal bipyramidal geometries at both cobalt centers. Coordination of a sixth carbonyl group to dirhodium pentacarbonyl complex is uphill by 5.6 kcal/mol with a very weakly coordinated carbonyl with a Rh-CO distance of 2.305 Å. The formation of a hexacarbonyl complex for the dicobalt complex (**Co_6**), on the other hand, is downhill by –6.4 kcal/mol with a Co-CO bond distance of 1.782 Å (for a detailed discussion on the dirhodium hexacarbonyl complex (**Rh_6**) see section 2.3.1).

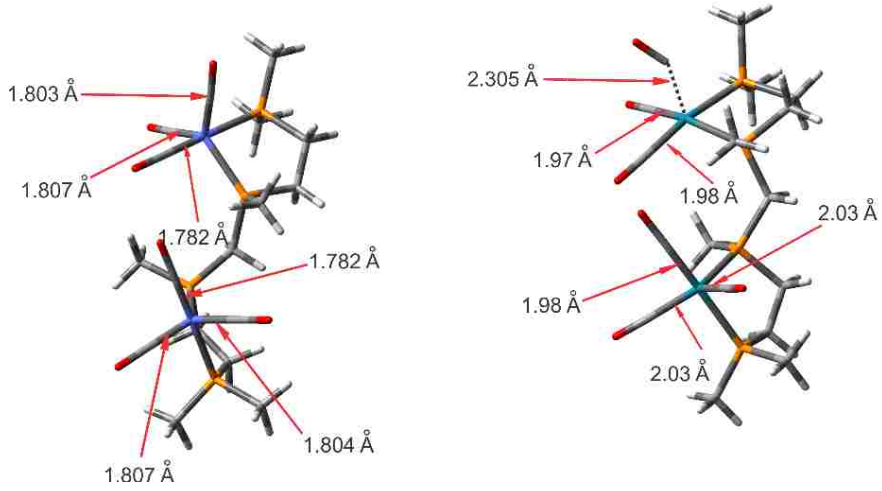

Figure 4.4. Bimetallic Co hexacarbonyl complex (Co_6) and bimetallic Rh hexacarbonyl (Rh_6) complex.

The hydroformylation catalytic cycle begins with the oxidative addition of hydrogen gas to generate a hydride complex. As both cobalt centers in the **Co_6** are saturated dissociation of a carbonyl group will take place prior to the oxidative addition. The CO dissociation will generate a pentacarbonyl complex (**Co_5**) and this reaction is favored by −6.4 kcal/mol. **Co_5** complex further dissociates a carbonyl group to generate an open mode tetracarbonyl complex (**Co_4**) and this corresponds to an energy decrease of −6.5 kcal/mol. This step will be followed by the oxidative addition of H_2 generating a dihydride open mode complex and corresponds to an energy uphill of +16.4 kcal/mo. The activation barrier for this step is 16.9 kcal/mol (Figure 4.5).

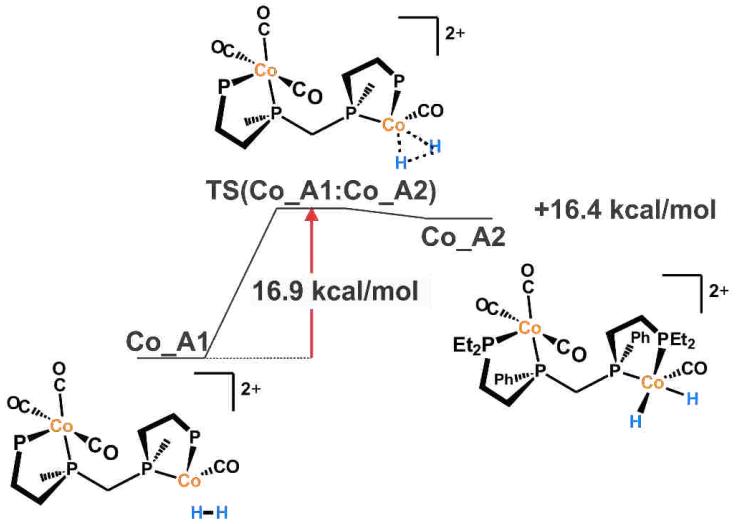

Figure 4.5. Activation barrier for oxidative addition of H_2(g).

This open-mode dihydride complex can convert into closed-mode complexes with either two terminal hydrides (**Co_2****) or two bridging hydrides (**Co_2***) or convert into an asymmetric complex with a bridging hydride and a terminal hydride (**Co_2**). The formation of **Co_2**** corresponds to an energy decrease of −12.5 kcal/mol, whereas the formation of **Co_2** and **Co_2*** correspond to energy decreases of −25.7 kcal/mol and −27.1 kcal/mol, respectively. Figure 4.6 shows the relative energies calculated for these three dihydride isomers. **Co_2**** has the highest relative energy, just as with the $[Rh_2H_2(m\text{-}CO)_2(rac\text{-}P4)]^{2+}$ analog, whereas **Co_2*** and **Co_2** have essentially the same energies within the error of DFT calculations (about 2.0 kcal/mol). These thermodynamic energy values suggest either **Co_2*** or **Co_2** should act as the active catalyst in the hydroformylation cycle due to their low relative energies.

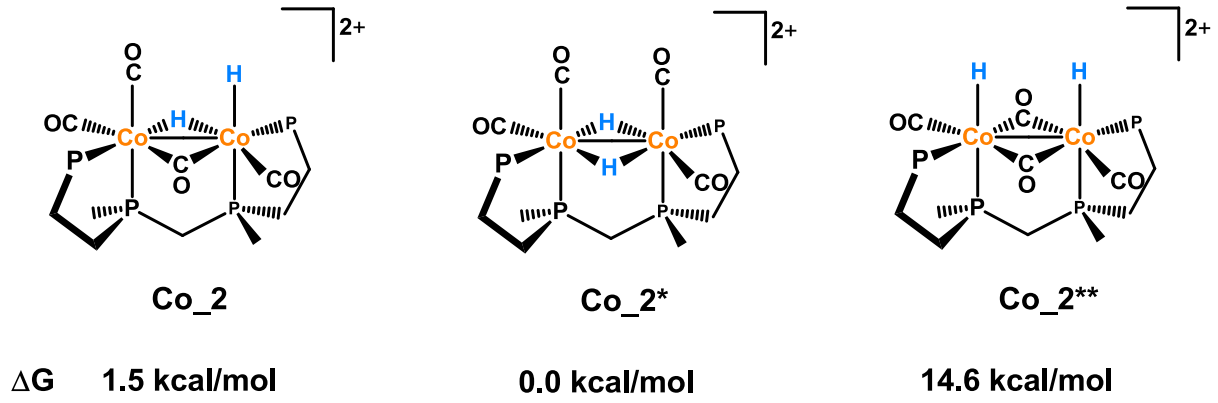

Figure 4.6. DFT relative energies for the three closed-mode dihydride isomers.

The Co–Co bond distance for the closed-mode bimetallic complexes **Co_2**, **Co_2*** and **Co_2**** are 2.663 Å, 2.783 Å and 2.658 Å and respectively, which correspond to typical Co–Co single bond lengths. This suggests that Co–Co bond formation coupled with the bridging ligands can facilitate the bimetallic cooperativity by keeping the metal centers in close proximity. The Co–Co bond distances support the assignment of a covalent single bond between the d^7 Co(+2) centers. The presence of two anionic hydrides and the dicationic charge of the complex points to Co(+2) oxidation state formalism.

The identification of the active catalyst is very important in understanding the mechanism. Hydroformylation is initiated by the generation of a 16-electron unsaturated complex from the active catalyst, and this is achieved via the dissociation of a carbonyl group which DFT calculates as an endothermic reaction. This is consistent with the much higher tendency of cobalt to prefer higher coordination numbers relative to Rh(+1) or Rh(+2). As shown below in Figure 4.7 the dissociation of a terminal CO group *trans* to bridging hydride in **Co_2** corresponds to an energy uphill of +10.4 kcal/mol (**Co_2A**), whereas dissociation of a CO group *cis* to bridging hydride results in +19.4 kcal/mol (**Co_2A'**) energy change. Dissociation of a terminal CO group from **Co_2*** corresponds to an energy change of +12.5 kcal/mol (**Co_2*A)** and dissociation of a terminal CO group from **Co_2**** corresponds to an energy uphill of +11.7 kcal/mol (**Co_2**A**),. **Co_2A** has a relative energy of 0.0 kcal/mol, and **Co_2*A** has a relative energy of +0.6 kcal/mol, whereas **Co_2A'** and **Co_2**A** have higher relative energies of +9.0 kcal/mol and +14.5 kcal/mol respectively. These DFT energies suggest the terminal CO trans to bridging hydride of **Co_2** and equatorial CO in **Co_2*** are more labile than the terminal CO cis to bridging hydride

in **Co_2**. Because CO dissociation in **Co_2**** has the highest energy, I focused the calculations on catalysis using **Co_2** and **Co_2***.

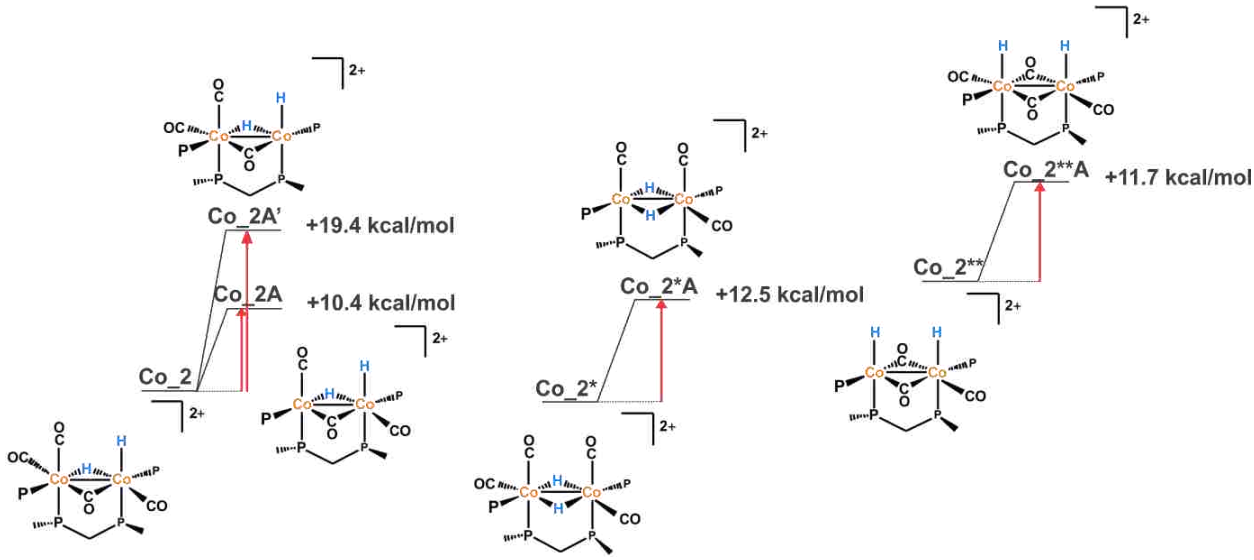

Figure 4.7. CO dissociation from Co_2, Co_2* and Co_2** (For clarity the phosphine chelate ligands are removed).

Alkene coordinates to the vacant site formed from CO dissociation to generate the 18-electron complexes, **Co_2B** and **Co_2*B**. Alkene coordination to both complexes looks good as they both correspond to downhill energies of –10.8 and –10.7 kcal/mol respectively (Figure 4.8). Alkene coordinates in the equatorial position with the C=C bond perpendicular to Co–Co bond. Hydride insertion then takes place to form the alkyl group (Figure 4.9).

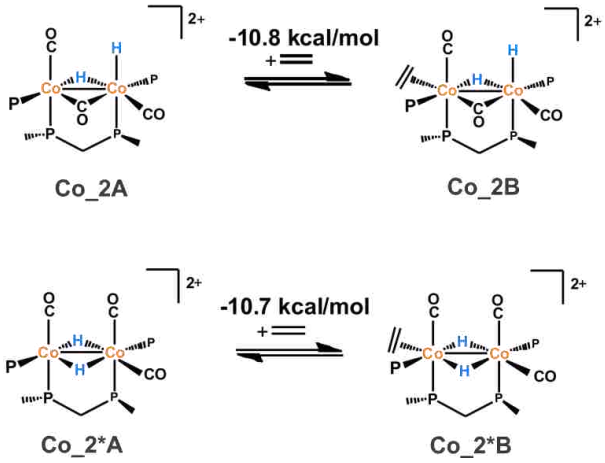

Figure 4.8. Alkene coordination in Co_2A and Co_2*A.

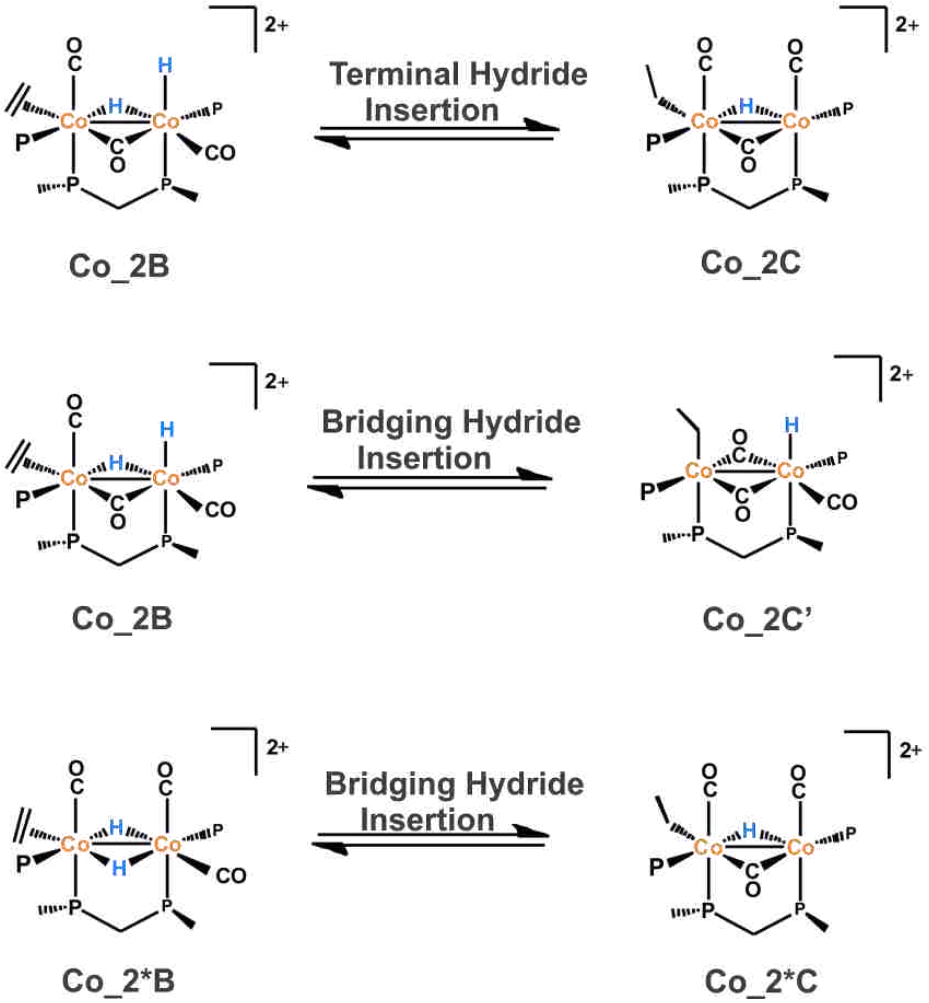

Figure 4.9. Hydride insertions in Co_2B and Co_2*B.

The activation barrier for the bridging hydride insertion in **Co_2B** is 12.1 kcal/mol. DFT, however, calculates the terminal hydride insertion in **Co_2B** and bridging hydride insertion in **Co_2*B** as barrier-less steps, in marked contrast to the Rh calculations. These energies indicate that terminal hydride insertion in **Co_2** and bridging hydride insertion in **Co_2*** are energetically the same and extremely easy.

The terminal hydride insertion in **Co_2B** occurs via an intermediate, **Co_2B**$^{\#}$ to form the alkyl, **Co_2C**. The terminal hydride moves towards the alkene and the bridging CO moves away from the alkene facilitating the hydride insertion. The corresponding intermediate, **Co_2B**$^{\#}$ for the barrier-less terminal hydride insertion step is shown below in Figure 4.10.

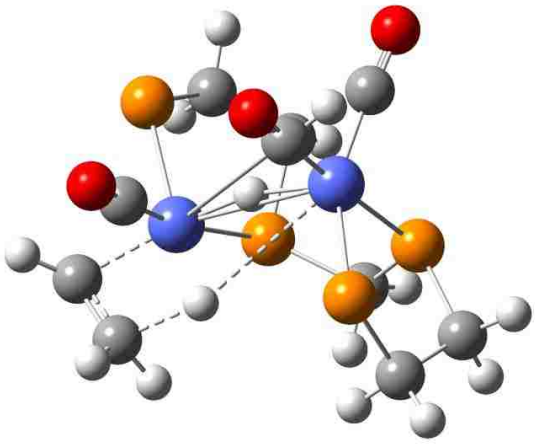

Figure 4.10. Intermediate of terminal hydride insertion in Co_2B$^{\#}$ (For clarity –CH_3 groups attached to P atoms are not shown).

The insertion of bridging hydride to **Co_2B** results in a double bridging complex with bridging carbonyls**.** The transition state (**TS(Co_2B):(Co_2C')**) has an energy of 12.1 kcals/mol and was confirmed via vibrational analysis which gave a single imaginary frequency corresponding to the correct vibrational mode (see Appendix 4). The free energy profile for the bridging hydride alkene insertion in **Co_2B** is shown below in Figure 4.11.

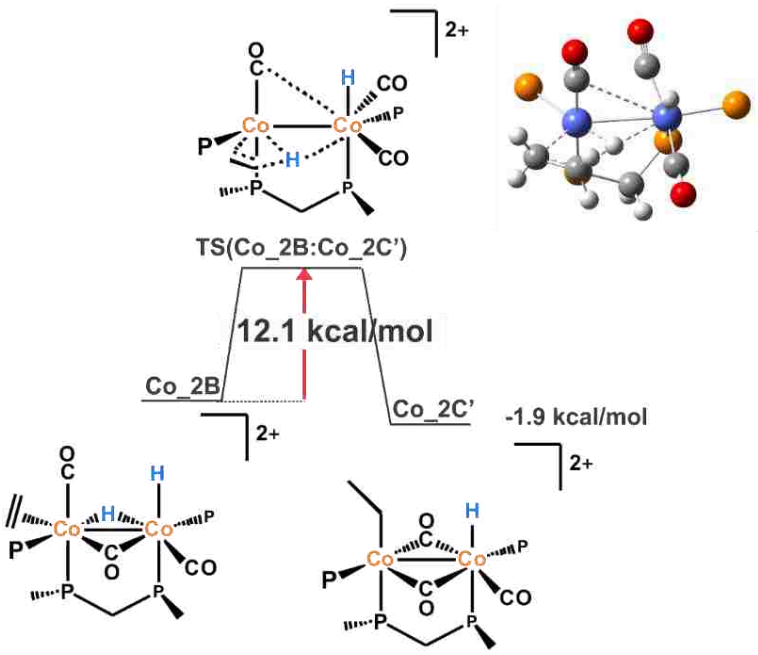

Figure 4.11. Activation barrier for bridging hydride insertion in Co_2B (For clarity P chelate ligands are removed).

The insertion of bridging hydride in **Co_2*B** generates a complex with a bridging CO and a bridging hydride, **Co_2*C**. This complex seems to be structurally similar to **Co_2C** which is formed from terminal hydride insertion, but the orientation of the alkyl groups in these two complexes appears to be different. In **Co_2C** the alkyl group is perpendicular to the Co–Co bond whereas in **Co_2*C** the alkyl group is in the plane of Co–Co bond. DFT calculates the bridging hydride insertion step in **Co_2*B** as a barrier-less step that occurs via an intermediate, **Co_2*B**$^{\#}$. The bridging hydride closer to the alkene moves towards the alkene and facilitates the insertion process. The corresponding intermediate is shown below in Figure 4.12.

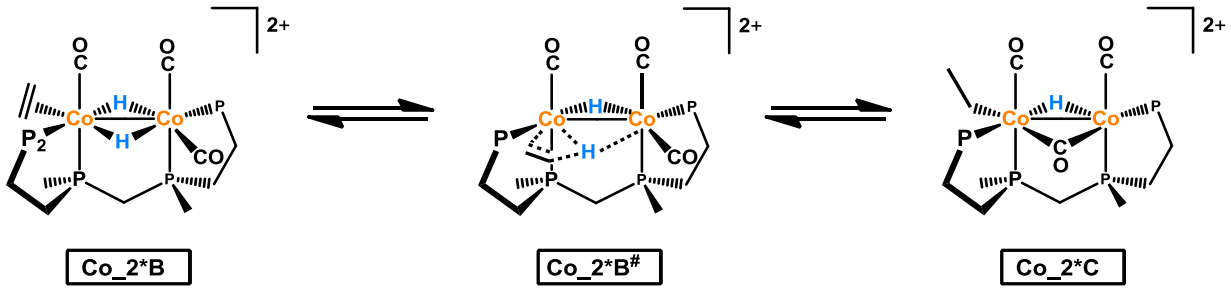

Figure 4.12. Intermediate of bridging hydride insertion of Co_2*B.

DFT calculations suggest that the most feasible pathways are either the terminal hydride insertion in **Co_2B** or the bridging hydride insertion in **Co_2*B**. A CO group then adds to the 16-electron cobalt center to generate a saturated metal center as the CO insertion from a saturated complex requires less energy compared to an unsaturated complex. In both complex **Co_2C** and **Co_2*C**, CO adds in the equatorial position. DFT energies imply that this step is quite favorable as the energy change corresponding to CO addition to **Co_2C** and **Co_2*C** is –16.7 kcal/mol (**Co_2D**), and a smaller decrease of –3.1 kcal/mol for **Co_2*D**.

Once the saturated complex is formed the migratory insertion between the CO group and alkyl takes place to generate an acyl group. DFT energies show that CO insertion is very favorable as it has a very low activation barrier (Figure 4.13). The activation barrier of terminal CO insertion to **Co_2D** is 5.9 kcal/mol, whereas for bridging CO insertion the activation barrier is only 3.9 kcal/mol. The transition states were confirmed by frequency analysis (see Appendix 4). The activation barriers depict that

bridging CO insertion is more favorable than the terminal CO insertion. In the process of terminal CO insertion (Figure 4.13a) the alkyl group moves towards the axial CO in order for the insertion to take place whereas in bridging CO insertion the bridging CO group moves towards the equatorially coordinated alkyl group and this results in a mono-bridging hydride complex (Figure 4.13b).

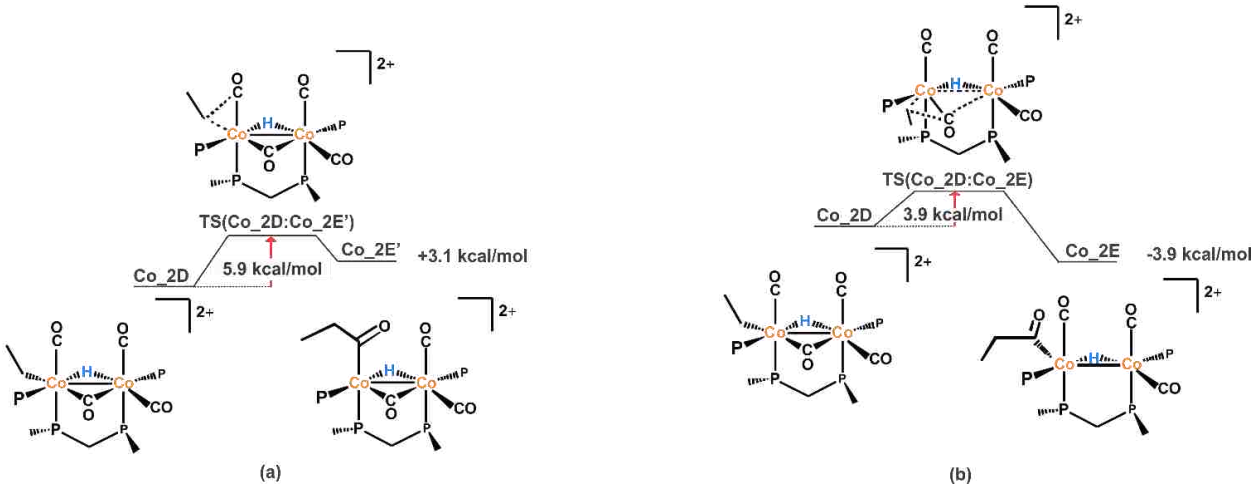

Figure 4.13. Activation barrier for (a) - terminal CO insertion and (b) - bridging CO insertion in Co_2D (For clarity P chelate ligands are removed).

DFT computations show that the activation barrier for terminal CO insertion in **Co_2*D** is 6.7 kcal/mol (–264.81 cm^{-1}) (Figure 4.14) which is greater than the barriers in **Co_2D**. The alkyl group moves towards the terminal CO favoring the CO insertion.

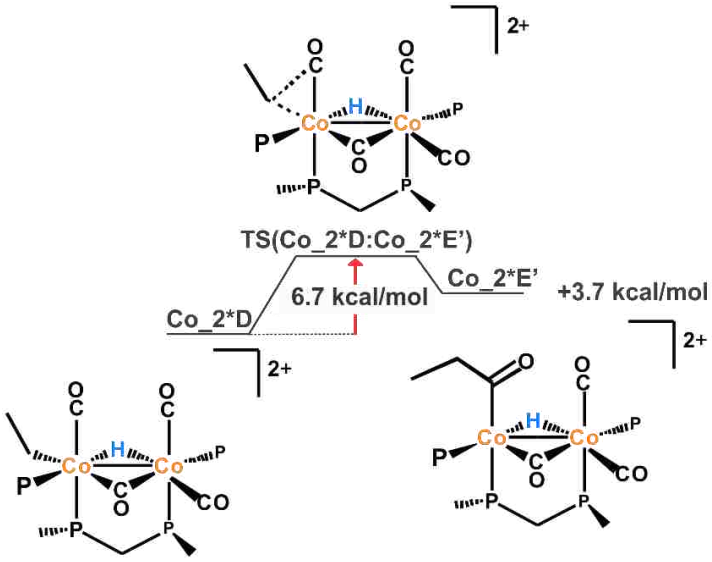

Figure 4.14. Activation barrier for terminal CO insertion in Co_2*D (For clarity P chelate ligands are removed).

Despite the slight difference in activation barriers between the terminal CO insertion in **Co_2D** and **Co_2*D** they both produce similar compounds; hence, both **Co_2E'** and **Co_2*E** show similar bond lengths, angles and atomic charges (Figure 4.15). According to DFT calculated activation barriers steps proceeding from bridging CO insertion in **Co_2D** appear to be the most favorable pathway.

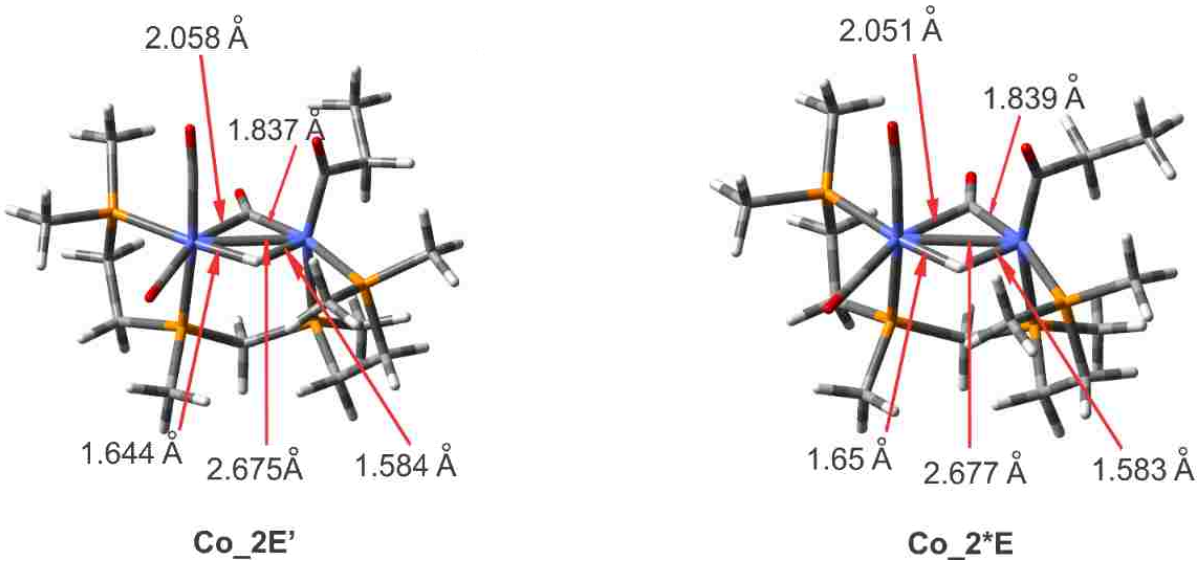

Figure 4.15. Products from terminal CO insertion in Co_2D and Co_2*D.

DFT studies show that **Co_2E** which is produced via the insertion of bridging CO in **Co_2D** results in bonding between Co centers via the μ–H (Figure 4.16). The μ–H is asymmetrically bonded to Co centers having 1.8 Å and 1.5 Å distances between the Co centers and μ–H. The cobalt with the anionic acyl has the shorter bond to the bridging hydride. This raises a question on oxidation state assignments; is there covalent bonding between the two metal centers resulting from a +2 oxidation state on each metal center, or do +3 and +1 oxidation state assignments make more sense with a dative-type Co-Co bond? The Co center that has the longer distance to the μ–H has a square planar geometry whereas the other Co center that has a slightly distorted square pyramidal geometry (Figure 4.16).

The Mulliken charge analysis suggests the Co center with the acyl group and shorter Co–μ–H bond in **Co_2E** is more positive than the Co center with two carbonyl ligands. Molecular orbital analysis studies show that π–back bonding between the Co center with the longer Co–μ–H bond and the carbonyl groups attached to it is 1.1 eV higher in energy than the back bonding between the Co center with shorter

Co–μ–H bond and the CO group attached to it. These DFT analysis studies suggest that **Co_2E** is a complex with Co centers in mixed oxidation states (+3/+1) and with a linear asymmetric Co–H–Co bond. According to DFT calculations the angle between Co–H–Co is 177.695°, which is very close to a linear angle.

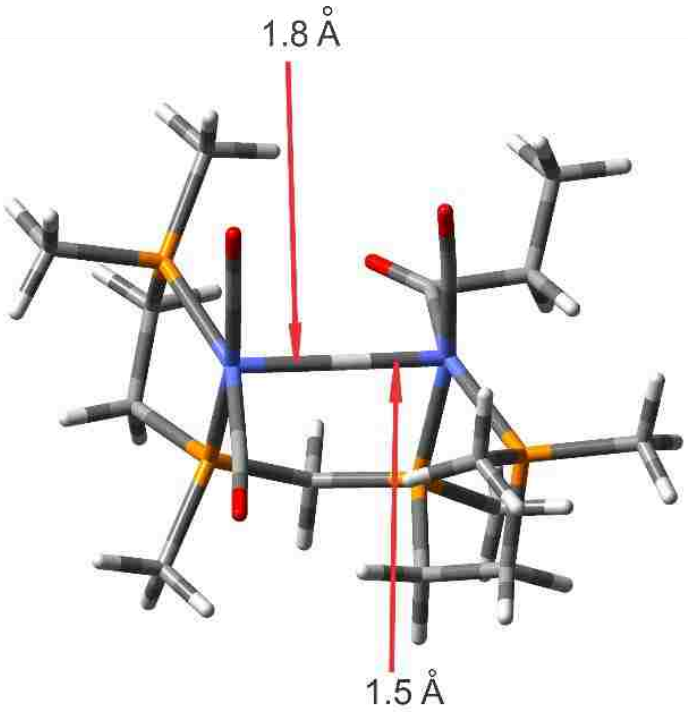

Figure 4.16. Linear Co–H–Co in Co_2E.

A very few late transition metal complexes with linear M–H-M complexes are found in literature. X-ray crystallographic data studies by Dahl and coworkers have demonstrated $[Cr_2(\mu\text{–}H)(CO)_{10}]^-$ complex to have a linear Cr–H–Cr angle, but neutron diffraction studies have revealed a bent angle of 158.9° in Cr–H–Cr. [20,21,22,23] Later, DFT studies done by Dr. Wilson suggested that a bent angle is favored between Ni–H–Ni in $Ni_2(\mu\text{–}H)(\mu\text{–}P_2)_2X_2$ ($P_2 = R_2PCH_2PR_2$, R = *i*Pr, Cy; X = Cl, Br), but the steric effects and crystal packing point to a linear angle.[24] This is the only transition metal complex found in literature with mixed oxidation states which favored a linear M–H–M angle.

Due to +3/+1 oxidation states at the Co centers in **Co_2E,** CO addition takes place at the unsaturated Co center forming **Co_2F**, and this converts the linear Co–H–Co into a bent Co–H–Co with an angle of 151.8° (Figure 4.17).

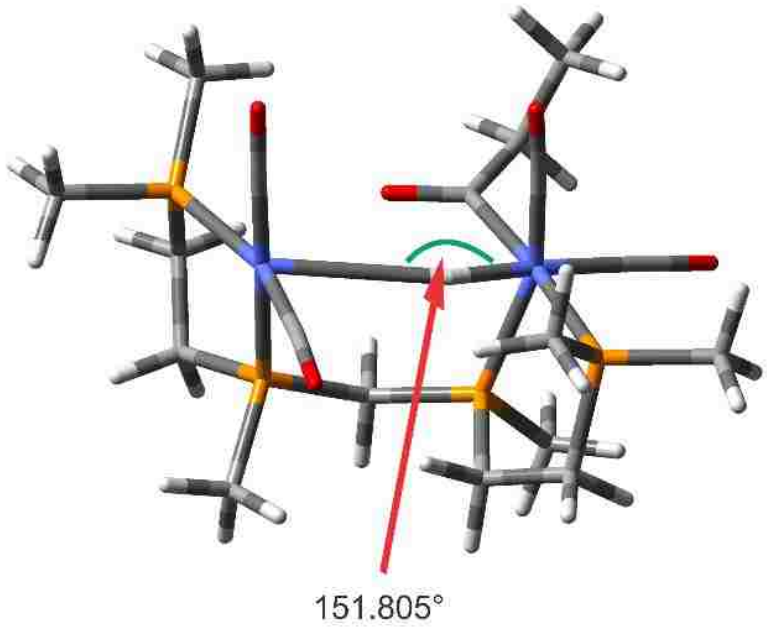

Figure 4.17. Bent Co–H–Co in Co_2*F.

The CO addition will be followed by reductive elimination between the acyl group and hydride to generate the aldehyde product. This step appears to be favorable as the carbonyl C atom and bridging hydride are *cisoidal* and separated by only 2.44 Å, and this reaction step has a considerable energy drop of –25.5 kcal/mol. Despite these generally favorable structures and energetics, the activation barrier of 42.6 kcal/mol for the reductive elimination of aldehyde obtained from DFT computations is quite large (Figure 4.18). The transition state was confirmed via frequency analysis (see Appendix 4). The bridging hydride moves towards the carbonyl O atom to facilitate the reductive elimination. The aldehyde product eliminates from the catalytic cycle regenerating the starting complex **Co_4***.

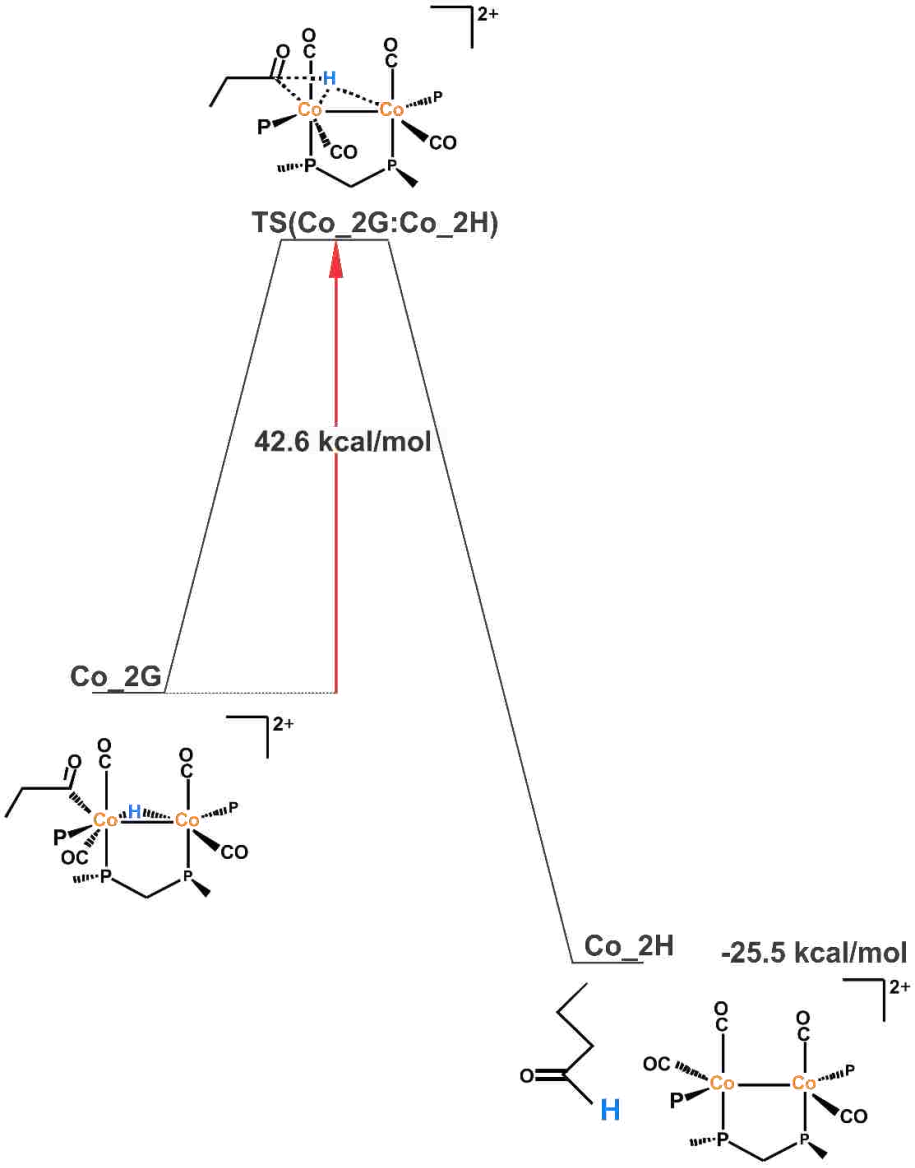

Figure 4.18. Activation barrier for reductive elimination of aldehyde.

DFT thermodynamics suggest reductive elimination of aldehyde as the rate-limiting step. According to DFT studies **Co_2** appear to be more suitable as an active catalyst than **Co_2*** and **Co_2****, but our group has not yet started experimental studies on this catalyst system. DFT computed hydroformylation mechanism catalyzed by $[Co_2(\mu\text{–}H)(\mu\text{–}CO)(H)(CO)_3(\textit{rac}\text{-et,ph-P4})]^{2+}$, **Co_2** is shown below in Figure 4.19.

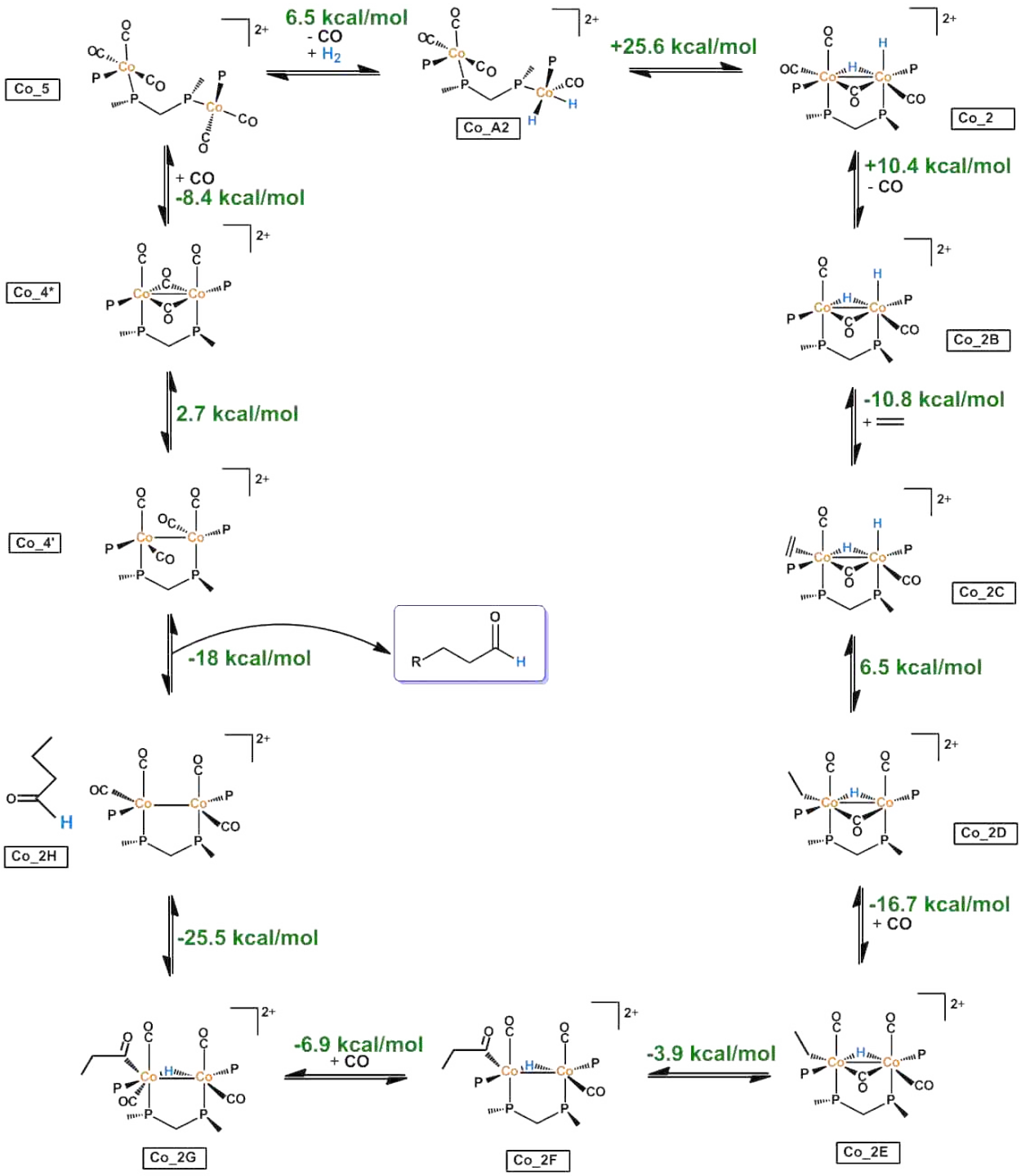

Figure 4.19. DFT computed hydroformylation mechanism catalyzed by [*rac*-$Co_2(\mu\text{–}H)(\mu\text{–}CO)(H)(CO)_3(et,ph\text{-}P4)]^{2+}$, Co_2 (For clarity P chelate ligands are removed).

4.3.2 Dicobalt Catalyzed Aldehyde-Water Shift Catalysis

In analogy to dirhodium AWS catalysis, closed-mode dicobalt tetracarbonyl complex (**Co_4***) with two bridging carbonyl ligands was used as the active catalyst for the AWS catalysis, and this contains two semi-bridging carbonyls that are more closely bonded to one of the cobalt centers, which makes the two cobalt atoms somewhat different electronically. This is supported by the different charges on the Co centers (+0.773 and +0.852), the Co-μ–CO angles, and the MOs. The angles between the Co with a low positive charge and CO are 123.2° and 120.5°, and the angles between the Co with a high positive charge and CO are 152.5° and 156.4°, which are in agreement with the unsymmetrical bridging CO ligands (Figure 4.20).

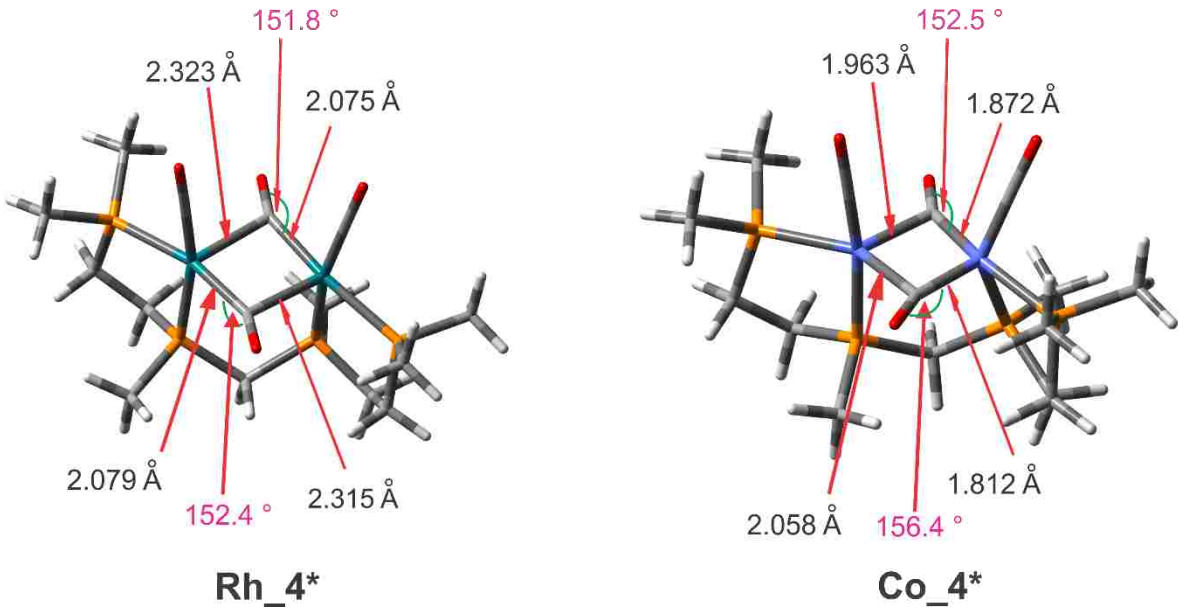

Figure 4.20. Structural comparison between closed mode Rh and Co tetracarbonyl complexes.

The highest occupied molecular orbital (HOMO) shows that electrons are donated from metal (Co/Rh) dπ orbital to unoccupied π* orbitals of the semi-bridging CO ligands (Figure 4.21). These support the presence of a semi-bridging CO ligand. In dirhodium closed mode tetracarbonyl complex (**4***) the Rh centers have approximately similar charges (+0.1 and +0.109), and unsymmetrically bridging CO ligands. The bridging CO ligands are symmetrically distributed to make both Rh centers approximately equal.

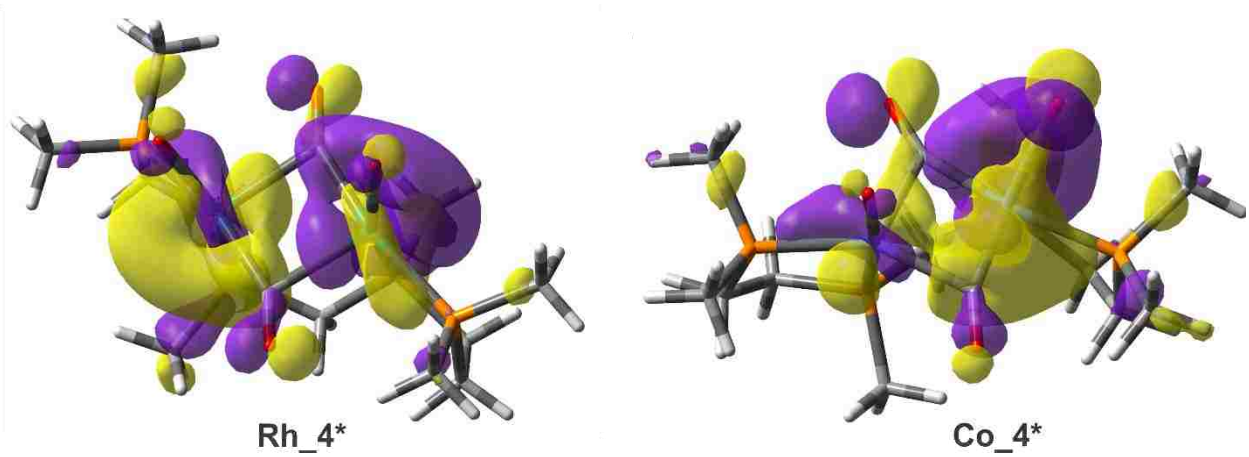

Figure 4.21. HOMO of Dicobalt closed-mode tetracarbonyl complex Co_4* and Dirhodium closed-mode tetracarbonyl complex Rh_4*.

The first step towards analyzing the AWS mechanism is the aldehyde coordination to the metal center. The HOMO of water molecule interacts with the metal LUMO. According to DFT studies the LUMO of closed mode **Co_4*** is 0.85 eV lower in energy than the LUMO of open mode tetracarbonyl Co complex, **Co_4**. This suggests that water coordinates more easily to **Co_4*** than to **Co_4**. The LUMO of **Co_4*** is shown below in Figure 4.22. Strong σ interactions are seen in **Co_4*** due to bridging CO ligands. Due to these interactions the two positively charged Co centers are coupled to each other and this result in an electron deficiency at the Co centers making the LUMO orbital a better acceptor orbital than the LUMO of open-mode **Co_4** complex.

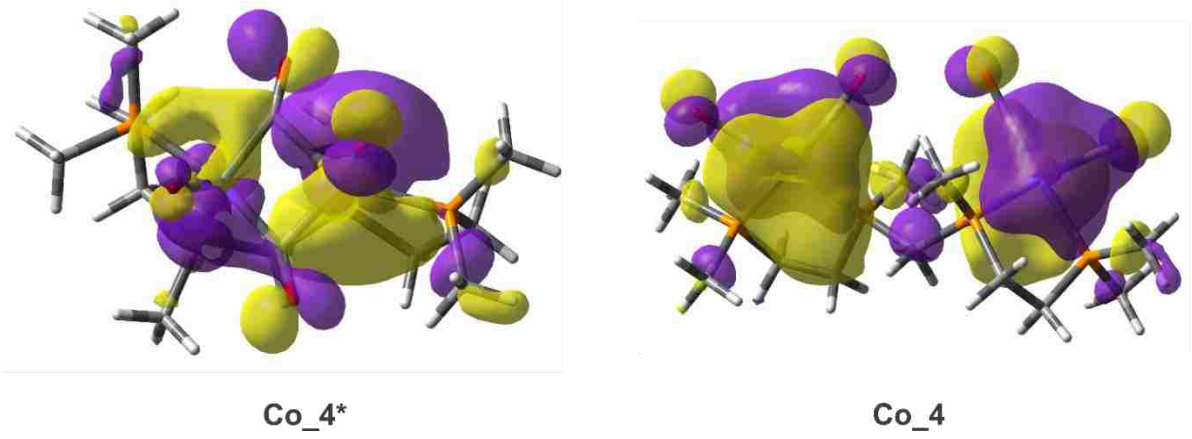

Figure 4.22. LUMO of dicobalt closed-mode Co_4* and open-mode Co_4.

DFT studies on cobalt catalyzed AWS was performed using four water molecules explicitly. Three of them were place closer to the aldehyde and one water molecule was placed closer to the opposite Co center which did not have the aldehyde coordinated.

DFT studies show that the aldehyde coordination occurs via the lone pair of the oxygen atom (Figure 4.23), just as with the rhodium calculation. The separation between the carbonyl O atoms of acetaldehyde and propanal to Co are 2.12 Å and 2.14 Å, respectively. These bond distances are shorter than those observed in the bimetallic Rh calculation (section 3.3.2.1). This is partially due to the size difference between Co and Rh centers, where the smaller Co atoms result in shorter bond distances. Experimental studies on Co complexes show a bond distance of about 2.2 Å between the Co center and carbonyl O atoms.[25-29] The smaller bond distances in Co complexes obtained from DFT studies show the presence of a stronger interaction between Co and carbonyl O atom than the interaction present between Rh and carbonyl O complexes.

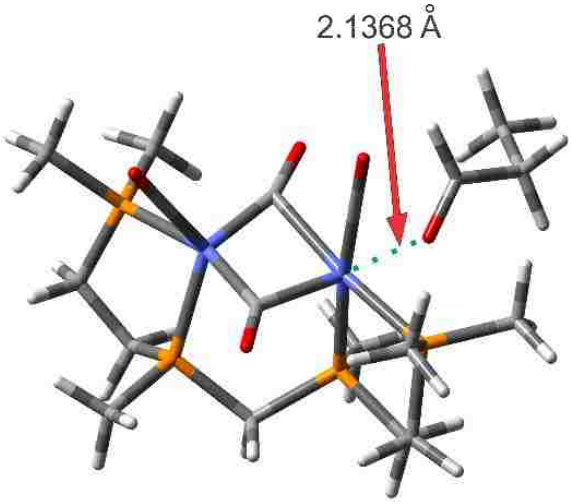

Figure 4.23. Coordination of propanal to dicobalt closed-mode 4*.

Despite the approximately similar bond distances of the two different aldehyde coordinated Co complexes, the coordination of propanal to the Co center appears to be energetically better (−14.7 kcal/mol) than coordination of acetaldehyde (+39.3 kcal/mol). Hence, we will use propanal as the model aldehyde along with a limited number of water molecules as an explicit solvent model for our AWS mechanistic computational study.

Destabilization of the carbonyl C=O bond of the aldehyde is an important aspect in AWS catalysis. This is achieved via the use of a water molecule that acts as a nucleophile. One of the water molecules that is in close proximity (2.96 Å) to the aldehyde carbonyl C atom attacks forming the protonated diol complex (**Co_K**), which corresponds to an uphill energy change of +6.8 kcal/mol. The activation barrier for the nucleophilic water attack is 33.9 kcal/mol and the transition state (**TS(Co_I:Co_K)**) was confirmed via frequency analysis. A single imaginary frequency corresponding to the correct vibrational mode was obtained (see Appendix 4). The Free energy profile for the water coordination step is shown below in Figure 4.24.

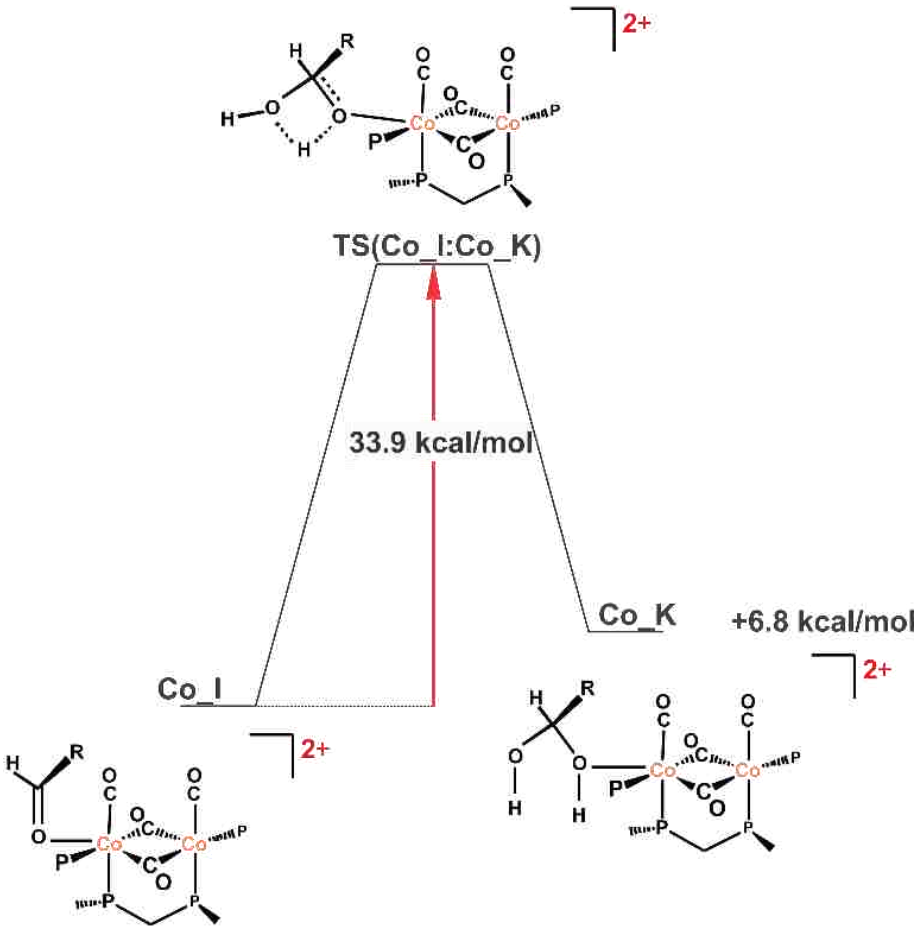

Figure 4.24. Activation barrier for water coordination. (For clarity P chelate ligands are removed).

The saturated Co center then dissociates a carbonyl group facilitating the β–hydride elimination (Figure 4.25) and this corresponds to an energy uphill of +1.6 kcal/mol. The protonated diol group moves from the equatorial position to axial position prior to β–hydride elimination.

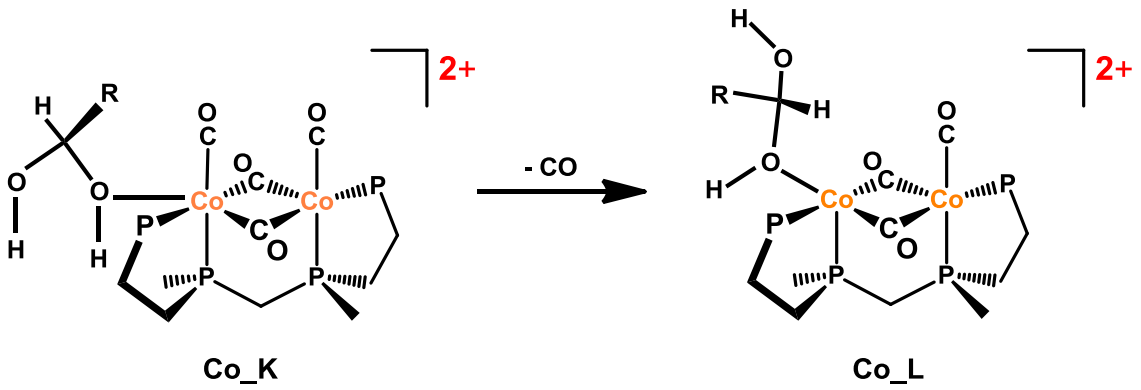

Figure 4.25. Dissociation of CO to facilitate β-hydride elimination.

The β–hydride is eliminated to the vacant orbital on the Co center and produces a protonated carboxylic acid (**Co_M**) corresponding to an uphill energy change of +5.9 kcal/mol. DFT studies calculate an activation barrier of 25.0 kcal/mol for β–hydride elimination (Figure 4.26).

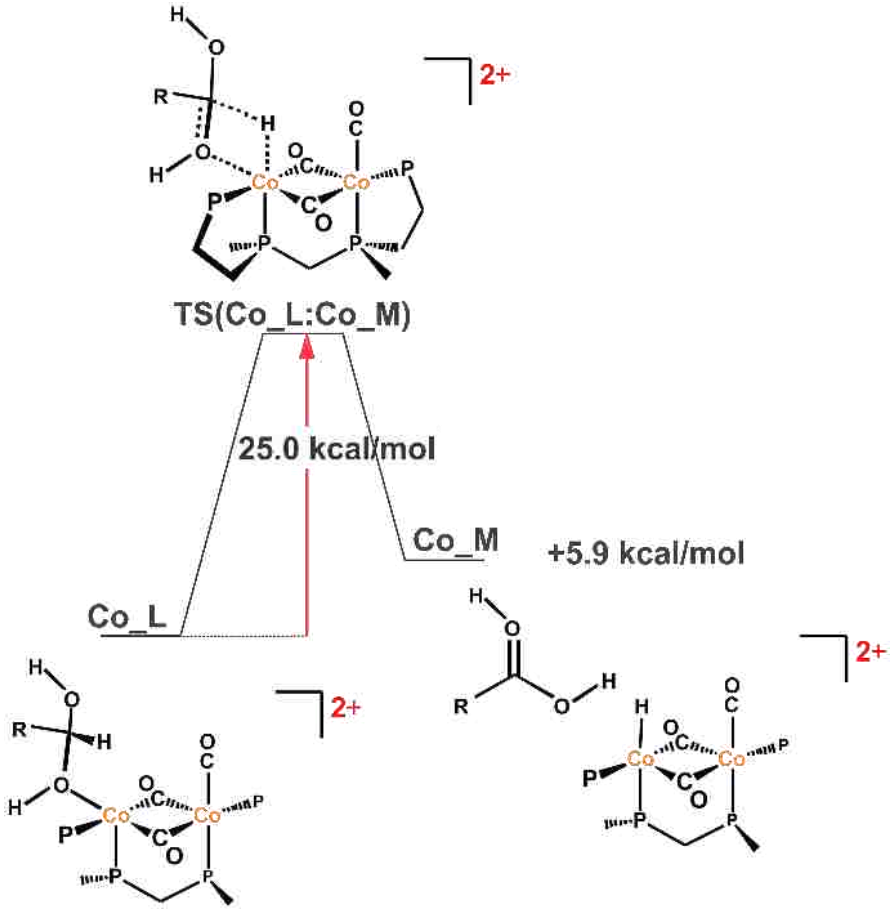

Figure 4.26. Transition state for β–hydride elimination.

The deprotonation of carboxylic acid and production of hydrogen gas is concerted and it is favorable corresponding to a downhill energy of –5.42 kcal/mol. In dirhodium catalyzed AWS catalysis the deprotonation occurs prior to generation of hydrogen gas (section 3.3.3.3). For the dicobalt AWS catalysis the deprotonation and production of hydrogen gas occur simultaneously. Transition state calculations depict that this is a barrier-less reaction, similar to that seen in dirhodium AWS catalysis. The H on the O–H group for the protonated carboxylic acid shows a partial positive charge of +0.314; hence, the hydride coordinated to Co reacts with this proton neutralizing the positive charge on the carboxylic acid (**Co_M***) to generate H_2 (Figure 4.27).

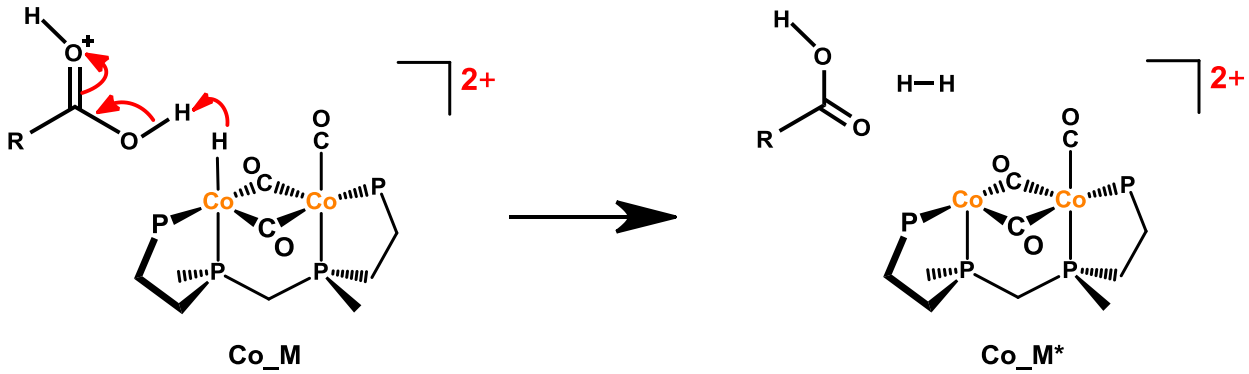

Figure 4.27. Deprotonation and H_2(g) production.

The DFT computed AWS mechanism catalyzed by dicobalt complexes is shown below in Figure 4.28, and is very similar to that calculated for the dirhodium complex. DFT thermodynamic studies suggest that AWS catalyzed by bimetallic [*rac*-$Co_2(\mu\text{-}CO)_2(CO)_2$(et,ph-P4)]$^{2+}$, (**Co_4***) is favorable. The coordination of propanal to the catalytic complex (–14.7 kcal/mol), deprotonation of protonated acid and elimination of H_2 gas (–5.4 kcal/mol) as well as CO addition to the acid and the H_2 gas eliminated complex (–12.1 kcal/mol) were all calculated to be exoergic. Reaction with water to generate the protonated diol (6.8 kcal/mol), CO dissociation from protonated diol complex (1.6 kcal/mol) and formation of protonated acid after β-hydride elimination (5.9 kcal/mol) are endoergic. These results indicate that the aldehyde-water shift catalysis is favorable with the bimetallic cobalt catalysts system as the calculated total free energy for the entire cycle is –17.9 kcal/mol.

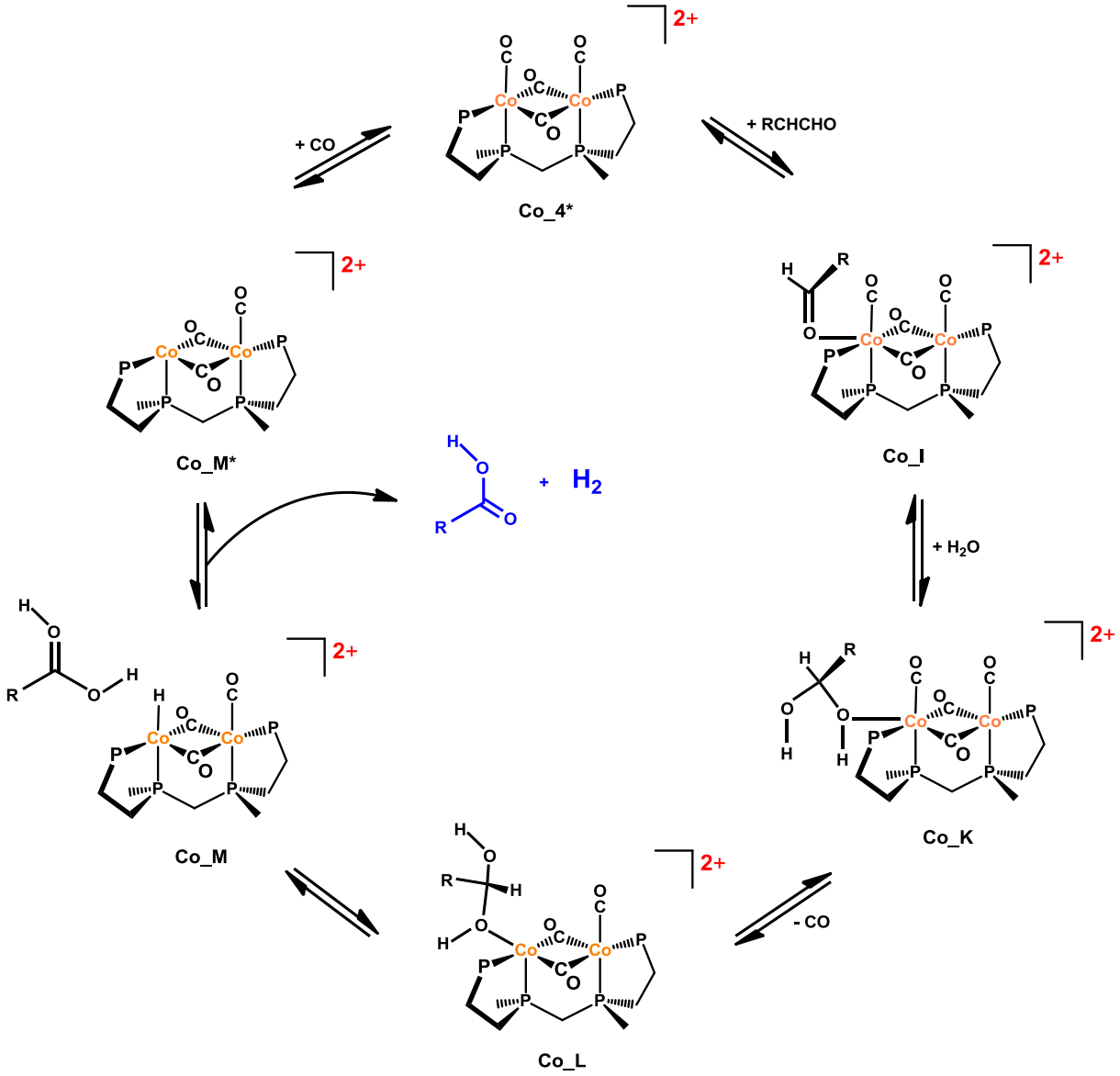

Figure 4.28. Dicobalt catalyzed AWS catalysis.

4.4 Conclusions

DFT studies suggest that either asymmetric **Co_2** or symmetric **Co_2*** are the best starting points for bimetallic cobalt catalyzed hydroformylation. The computational studies point more towards **Co_2** as the better catalyst, but due to lack of experimental results at this time we don't have any real data to compare our computational results to. Lower activation barriers are calculated for **Co_2** than for either **Co_2*** or **Co_2****. The transition state calculations for all three complexes; namely **Co_2**, **Co_2*** and **Co_2**** demonstrate the reductive elimination of the aldehyde product as the rate-determining step. If the

Co centers are more electron deficient this will reduce the energy barrier for the reductive elimination step and will facilitate the production of aldehydes. This can be achieved by incorporating electron withdrawing groups into the ligand system and DFT studies on such systems will be helpful in understanding the mechanistic.

DFT studies on AWS catalysis depict that this is a feasible process and it favors the production of carboxylic acids. The aldehyde coordinated complex is activated by the nucleophilic attack by water and this produces a protonated diol followed by β−hydride elimination which facilitates the acid production. Deprotonation of the protonated acid and production of H_2 gas are semi-concerted reactions. The elimination of H_2(g) seems to be a barrier-less reaction that proceeds via an intermediate. Transition state calculations suggest the reaction with water as the rate-determining step. DFT studies depict that the bimetallic cobalt catalyzed AWS catalysis is downhill by −17.9 kcal/mol. More studies on intrinsic reaction paths will be helpful to gain a better insight into reaction mechanistic.

4.5 References

1. Cornils, B.; Herrmann, W. A.; Rasch, M., Otto Roelen, Pioneer in Industrial Homogeneous Catalysis. *Angewandte Chemie International Edition in English* **1994,** *33* (21), 2144-2163.

2. Bungu, P. N.; Otto, S., Bicyclic phosphines as ligands for cobalt catalysed hydroformylation. Crystal structures of [Co(Phoban[3.3.1]-Q)(CO)3]2 (Q = C2H5, C5H11, C3H6NMe2, C6H11). *Dalton Transactions* **2007,** (27), 2876-2884.

3. Mika, L. T.; Orha, L.; van Driessche, E.; Garton, R.; Zih-Perényi, K.; Horváth, I. T., Water-Soluble-Phosphines-Assisted Cobalt Separation in Cobalt-Catalyzed Hydroformylation. *Organometallics* **2013,** *32* (19), 5326-5332.

4. Rush, L. E.; Pringle, P. G.; Harvey, J. N., Computational kinetics of cobalt-catalyzed alkene hydroformylation. *Angewandte Chemie (International ed. in English)* **2014,** *53* (33), 8672-6.

5. Hebrard, F.; Kalck, P., Cobalt-catalyzed hydroformylation of alkenes: generation and recycling of the carbonyl species, and catalytic cycle. *Chem Rev* **2009,** *109* (9), 4272-82.

6. Birbeck, J. M.; Haynes, A.; Adams, H.; Damoense, L.; Otto, S., Ligand Effects on Reactivity of Cobalt Acyl Complexes. *ACS Catalysis* **2012,** *2* (12), 2512-2523.

7. Pospech, J.; Fleischer, I.; Franke, R.; Buchholz, S.; Beller, M., Alternative metals for homogeneous catalyzed hydroformylation reactions. *Angewandte Chemie (International ed. in English)* **2013,** *52* (10), 2852-72.

8. Slaugh, L. H.; Mullineaux, R. D., Novel Hydroformylation catalysts. *Journal of Organometallic Chemistry* **1968,** *13* (2), 469-477.

9. Heck, R. F.; Breslow, D. S., The Reaction of Cobalt Hydrotetracarbonyl with Olefins. *Journal of the American Chemical Society* **1961,** *83* (19), 4023-4027.

10. Jones, W. D.; Huggins, J. M.; Bergman, R. G., Comparative reactivities of two isoelectronic transition-metal hydrides with transition-metal carbonyls and alkyls. *Journal of the American Chemical Society* **1981,** *103* (15), 4415-4423.

11. Nappa, M. J.; Santi, R.; Halpern, J., Mechanisms of the carbon-hydrogen bond-forming binuclear reductive elimination reactions of benzyl- and hydridomanganese carbonyls. *Organometallics* **1985,** *4* (1), 34-41.

12. Martin, B. D.; Warner, K. E.; Norton, J. R., Mechanism of the reaction of a solvated rhenium acyl complex with neutral transition-metal hydrides. Relative nucleophilicity of such hydrides. *Journal of the American Chemical Society* **1986,** *108* (1), 33-39.

13. Ungvary, F.; Marko, L., Kinetics and mechanism of ethyl formate formation from (ethoxycarbonyl)cobalt tetracarbonyl and molecular hydrogen or $HCo(CO)_4$. *Organometallics* **1983,** *2* (11), 1608-1612.

14. Ryan, R. C.; Pittman, C. U., Metal cluster catalysis. 1. Hydroformylations of 1- and 2-pentene catalyzed by two cobalt carbonyl clusters: nonacarbonyl-.mu.3-benzylidyne-tricobalt and di-.mu.2-carbonyl-di-.mu.4-phenylphosphido-octacarbonyltetracobalt. *Journal of the American Chemical Society* **1977,** *99* (6), 1986-1988.

15. Pittman, C. U.; Wilemon, G. M.; Wilson, W. D.; Ryan, R. C., Catalysis of Hydroformylation by $Co_4(CO)_{8-x}(\mu_2\text{-}CO)_2(PPh_3)\ x(\mu_4\text{-}PPh)_2$, x = 0 or 2: Clusters as Catalysts. *Angewandte Chemie International Edition in English* **1980,** *19* (6), 478-479.

16. Don, M.-J.; Richmond, M. G., In situ cluster stability studies explored by cylindrical internal reflectance (CIR) spectroscopy: 1-pentene hydroformylation using phosphine-substituted Co4(CO)8P2(μ4-PPh)2 clusters. *Journal of Molecular Catalysis* **1992,** *73* (2), 181-189.

17. Muetterties, E. L., A Coordination Chemist's View of Surface Science. *Angewandte Chemie International Edition in English* **1978,** *17* (8), 545-558.

18. Frisch, M.J.; Trucks, G. W.; Schlegel, H. B.; Scuseria, G. E.; Robb, M. A.; Cheeseman, J. R.; Scalmani, G.; Barone, V.; Mennucci, B.; Petersson, G. A.; Nakatsuji, H.; Caricato, M.; Li, X.; Hratchian, H. P.; Izmaylov, A. F.; Bloino, J.; Zheng, G.; Sonnenberg, J. L.; Hada, M.; Ehara, M.; Toyota, K.; Fukuda, R.; Hasegawa, J.; Ishida, M.; Nakajima, T.; Honda, Y.; Kitao, O.; Nakai, H.; Vreven, T.; Montgomery Jr., J. A.; Peralta, J. E.; Ogliaro, F.; Bearpark, M. J.; Heyd, J.; Brothers, E. N.; Kudin, K. N.; Staroverov, V. N.; Kobayashi, R.; Normand, J.; Raghavachari, K.; Rendell, A. P.; Burant, J. C.; Iyengar, S. S.; Tomasi, J.; Cossi, M.; Rega, N.; Millam, N. J.; Klene, M.; Knox, J. E.; Cross, J. B.; Bakken, V.; Adamo, C.; Jaramillo, J.; Gomperts, R.; Stratmann, R. E.; Yazyev, O.; Austin, A. J.; Cammi, R.; Pomelli, C.; Ochterski, J. W.; Martin, R. L.; Morokuma, K.; Zakrzewski, V. G.; Voth, G. A.; Salvador, P.; Dannenberg, J. J.; Dapprich, S.; Daniels, A. D.; Farkas, Ö.; Foresman, J. B.; Ortiz, J. V.; Cioslowski, J.; Fox, D. J. *Gaussian 09*, Gaussian, Inc.: Wallingford, CT, USA, 2009.

19. Becke, A. D., Density ¡functional thermochemistry. III. The role of exact exchange. *The Journal of Chemical Physics* **1993,** *98* (7), 5648-5652.

20. Handy, L. B.; Treichel, P. M.; Dahl, L. F.; Hayter, R. G., Structure of and Bonding in HCr2(CO)10-. The First Known Linear Electron-Deficient X-H-X Molecular System Stabilized by a Three-Center, One-Electron-Pair Bond1. *Journal of the American Chemical Society* **1966,** *88* (2), 366-367.

21. Handy, L. B.; Ruff, J. K.; Dahl, L. F., Structural characterization of the dinuclear metal carbonyl anions [M2(CO)10]2- (M = chromium, molybdenum) and [Cr2(CO)10H]-. Marked stereochemical effect of a linearly protonated metal-metal bond. *Journal of the American Chemical Society* **1970,** *92* (25), 7312-7326.

22. Roziere, J.; Williams, J. M.; Stewart, R. P.; Petersen, J. L.; Dahl, L. F., A neutron diffraction study of tetraethylammonium .mu.2-hydro-decacarbonyldichromate: a [M2(CO)10(.mu.2-H)]- monoanion with a pseudo D4h nonhydrogen geometry together with a disordered, bent symmetric metal-hydrogen-metal bond. *Journal of the American Chemical Society* **1977,** *99* (13), 4497-4499.

23. Petersen, J. L.; Brown, R. K.; Williams, J. M., Low-temperature (20 K) neutron diffraction study of [K(crypt-222)]+[Cr2(CO)10(.mu.-H)]-. Influence of the lattice environment and the K+ ion on the anion's metal carbonyl framework and the ordered chromium-hydrogen-chromium bond. *Inorganic Chemistry* **1981,** *20* (1), 158-165.

24. Wilson, Z. S.; Stanley, G. G.; Vicic, D. A., To Bend or Not to Bend: Electronic Structural Analysis of Linear versus Bent M−H−M Interactions in Dinickel Bis(dialkylphosphino)methane Complexes. *Inorganic Chemistry* **2010,** *49* (12), 5385-5392.

25. Di Vaira, M.; Stoppioni, P.; Mani, F., Synthesis, chemical properties and x-ray structure of the bis-acetone adduct [Co(Me2CO)2(TPyEA)](BPh4)2 (TPyEA = tris(1-pyrazolylethyl)amine). *Journal of Organometallic Chemistry* **1983,** *247* (1), 95-104.

26. Miler-Srenger, E.; Guglielmetti, R., Crystal and molecular structure of CoCl2(L)(1/2 acetone) where L is =[8-methoxy-3-methyl-6-nitro-2H-1-benzopyran-2-spiro-2[prime or minute]-(3-methyl-benzothiazoline)]. *Journal of the Chemical Society, Perkin Transactions 2* **1987,** (10), 1413-1418.

27. Saunders, L. N.; Pratt, M. E.; Hann, S. E.; Dawe, L. N.; Decken, A.; Kerton, F. M.; Kozak, C. M., Structural variations in the coordination chemistry of amine-bis(phenolate) cobalt(II/III) complexes. *Polyhedron* **2012,** *46* (1), 53-65.

28. Das, U. K.; Bobak, J.; Fowler, C.; Hann, S. E.; Petten, C. F.; Dawe, L. N.; Decken, A.; Kerton, F. M.; Kozak, C. M., Synthesis and structure of mono-, bi- and trimetallic amine-bis(phenolate) cobalt(ii) complexes. *Dalton Transactions* **2010,** *39* (23), 5462-5477.

29. Akita, M.; Ma, D.-q.; Hikichi, S.; Moro-oka, Y., Synthesis and crystal structures of mononuclear half-sandwich complexes of Ni and Co containing Klaui's tripodal ligand, [M{[small kappa]3-([small eta]5-C5H5)Co[P([double bond, length half m-dash]O)(OCH3)2]3}([small kappa]2-NO3)(L)] (M = Ni or Co). *Journal of the Chemical Society, Dalton Transactions* **1999,** (6), 987-996.

Chapter 5 - X-ray Absorption in Insulators with Non-Hermitian Real-Time Time-dependent Density Functional Theory

5.1 Introduction

X-ray absorption spectroscopy (XAS) is an important tool for chemistry and solid-state materials as it provides information on charge, bonding, and oxidation states of a particular atom. XAS involves the transition of a core-level electron to either bound or continuum states and is broadly characterized as pre-edge, X-ray absorption near-edge structure (XANES), and extended X-ray absorption fine structure (EXAFS).[1] Pre-edge is the region below the binding energy of the core level, whereas the near-edge region (XANES) contains features up to 50 eV above the binding energy. Photoelectrons in the XANES region have low kinetic energy and excited states in this region involve multiple scattering, which is useful for obtaining three-dimensional structural information.[1] XANES spectra are often complex and modeling these excitations is crucial for interpreting experimental results. Moreover, an accurate description of these excited states is an important first step toward understanding X-ray triggered dynamics in materials.

Several techniques have been used to model XAS. The multiple scattering approach,[2,3] which is perhaps the most widely used method for XAS, treats the photoelectron as spherical waves scattering from muffin-tin potentials. This has been widely used to study EXAFS in materials, but XANES can be challenging for these techniques as it requires experimental parametrization and can lack a rigorous treatment of the electronic structure of the material. XAS can also be calculated using first principles, such as Bethe−Salpeter equation (BSE) - based methods,[4,5] where core−hole interactions are described via a two-particle picture. BSE offers a much improved picture of the virtual states but can become extremely time consuming for large supercells, for example, in materials with defects or disorder.

Alternatively, one can use core-hole pseudopotentials in conjunction with band structure-based first-principles methods such as single-particle approximations based on density functional theory (DFT).[6] This has been used to capture XANES of lithium and fluorine *K*-edges of LiF and carbon *K*-edge of diamond[7] and the *K*-edges of silicon and oxygen in α-quartz.[6]

"This chapter 5 previously appeared as Fernando, R.G.; Balhoff, M.C.; Lopata, K. X-ray Absorption in Insulators with Non-Hermitian Real-Time Time-dependent Density Functional Theory, *J. Chem. Theory Comput.* 2015, 646-654. It is reprinted by permission of copyright [2015] American Chemical Society."

Although this method generates the XAS up to the far edge region and is suitable for weakly coordinated systems, it shows limitations in moderate and strong correlation environments. These deficiencies in the electron-electron interactions in the DFT functional can be somewhat remedied using the DFT + *U* method.[8] In addition to this, modeling transition metals and rare earths require large kinetic energy cutoffs that can result in excessive computational time. Ultrasoft pseudopotentials based on DFT methods have also been used to compute the XAS of silicon and oxygen K-edges of α-quartz and copper K-edge spectra in Cu and in La_2CuO_4.[8]

Finally, core excitations can be modeled using DFT using the Kohn-Sham approach, but this requires computing each core excited state one-by-one, which becomes computationally expensive and time consuming for materials.[9] TDDFT on the other hand can be used to generate XANES spectra from a single calculation, as discussed later. A combination of TDDFT with BSE can also offer information on a wide spectral range above the edge.[10-13]

In this paper, we develop an alternative approach to post-edge XANES using real-time time-dependent DFT (RT-TDDFT) with atom-centered basis sets. The goal is to accurately describe excitations near and above the edge of wide-gap materials without any parameterization against experiment. In many ways, this is a complementary approach to the methods discussed above but has the added bonus of easily handling doping/disorder,[14] allows for efficient use of hybrid DFT functionals, and easily translates to dynamical simulations, for example, X-ray-induced dynamics and strong-field effects.[15]

Time-dependent DFT[16] is an excellent approach for modeling these processes as it offers a good description of the electronic structure for transition metal systems and materials. A suitable choice of DFT functional yields excitations over a wide range of energies, scales to large system sizes (suitable for defect sites, surfaces, or disordered systems), and is a natural tool for modeling dynamics. For an overview of TDDFT and its myriad of applications, see the reviews by Marques and Gross,[17] Burke,[18] Casida,[19] and Ullrich.[20] Despite its wide applicability, capturing above-ionization core-level excitations can be challenging for TDDFT for two reasons: inadequacies in atom-centered basis sets and failures of

traditional exchange-correlation functionals for high energy states.[21-25] Both these issues stem from the highly diffuse Rydberg or continuum-like virtual states involved in these excitations.

These states are poorly described by atom-centered basis sets, yet grids and planewaves, which are ideal for diffuse states, can be problematic for the wave function near the core. This can be remedied somewhat through the use of excited-state core-hole pseudopotentials.[26,27] Atom centered basis sets such as Gaussian type orbitals (GTOs), however, are often preferred over planewaves due to their computational efficiency with hybrid functionals. Specifically, the Hartree-Fock wave function component is nonlocal in space and scales as N^4, which can become prohibitively expensive for planewaves that can easily have hundreds of times more functions than GTO basis sets. Local density functionals (e.g., LDAs, GGAs) are unsuitable for capturing above-ionization as they have the incorrect asymptotic form of the potential and qualitatively fail to describe the excitations. To overcome this problem, range-separated functionals such as CAM-B3LYP,[28] BNL,[29] LC-PBE,[30] LC-PBE0,[31] etc. have been developed that incorporate both long-range and short-range parts into the exchange term in the Kohn−Sham energy functional. These functionals provide robust and more successful solutions to self-repulsion that occur at long ranges. [30,32-35]

Thus, we would expect a versatile TDDFT approach to use GTOs with range-separated functionals yet also adequately describe the large spatial extent of the continuum-like states.

One way forward is to use imaginary absorbing boundary conditions (ABCs) that mimic the continuum. Typically, this is done in real space, where the potentials take the form of a slowly increasing function at the simulation box edge that removes the wave function without artificial reflections from the edge of a numerical grid.[36-38] This technique has been widely successful in modeling resonance energies and lifetimes. [39,40] Absorbing potentials have also been used with multireference configuration interaction to study resonances of metastable dianionic species,[41] resonances with coupled cluster,[42,43] and photo absorption oscillator strength of clusters and molecules,[44,45] along with computing ionization rates in atoms using TDDFT.[46]

These approaches can be inefficient for GTOs, as they require a very large number of diffuse functions to describe the ABC far from the molecule. Instead, we recently developed a phenomenological

molecular orbital (MO)-based ABC, where we impose a condition to mimic the finite lifetime of above ionization states by applying an imaginary potential to the Fock matrix in the MO basis, which is similar in spirit to complex DFT,[47] complex scaling,[48-50] and linear response complex polarizability approaches.[51] This MO-based ABC was successfully applied to UV resonance states in small gas-phase molecules.[52]

Finally, solving the time-dependent Kohn−Sham equations in time domain (i.e., real-time TDDFT[53-56]) is a natural tool for modeling XANES in materials, which requires computing spectra spanning tens of eV above the ionization edge in systems with a high density of states. Here, traditional root-based linear response TDDFT[57,58] (LR-TDDFT) requires thousands of roots, which is both inefficient and potentially creates algorithmic stability issues. RT-TDDFT, on the other hand, requires only three simulations (*x*, *y*, *z* polarized) to capture the entire absorption spectrum. RT-TDDFT has similar advantages when computing spectra in disordered solids, for example, $(Fe_{1-x}Cr_x)_2O_3$ solid solutions.[14]

One final note concerns the use of an adiabatic (local in time) approximation to the exchange-correlation functional, which is strictly valid only for slowly varying time-dependent driving fields.[59] For fields with high frequencies or strengths, the functional at a particular time is also dependent on the density at earlier times, making “memory” effects significant.[59] Recent studies, however, have shown that for a finite electron system in its ground state gradually exposed to a high frequency field these memory effects become negligible, and thus, the adiabatic approximation remains valid.[60] This picture is consistent with the results of this paper, as well as previous TDDFT studies of X-ray absorption,[61] where the computed excited states agree well with the experiment despite the use of an adiabatic functional.

TDDFT has been widely used to model XAS in a range of molecular systems such as the core excitations of Ti 1s, 2p and Cl 2p of $TiCl_4$,[62] the chlorine and sulfur *K*-edge and molybdenum *L*-edge of oxomolybdenum complexes,[63] L_3-edge of ruthenium complexes,[61,64,65] oxygen *K*-edge of water and carbon monoxide (CO), carbon *K*-edge of CO, and the carbon and flourine *K*-edges of fluorobenzenes.[61] TDDFT has also been used to compute the carbon 1s XAS of acetylene, ethylene, and benzene in gas phase and adsorbed on a Si(100) surface.[66] Sulfur *K*- and *L*-edges and the oxygen *K*-edge of SO_2 adsorbed on the MgO(100) surface[67] and sulfur *K*-edge of SO_2 adsorbed on the Ti(110) surface have also been studied using TDDFT.[68] Studies have been performed on XAS at $L_{2,3}$ edges of 3d elements (Sc, Ti,

V, Cr, Ni) of atoms and complexes using TDDFT methods.[69,70] For materials, linear response TDDFT has been applied to metal 1s and 2p edges and oxygen 1s edges of alkaline earth metal oxides using cluster models of MgO, CaO, SrO, and BaO,[71] titanium *K*- and *L*-edges and oxygen *K*-edge in rutile using finite cluster models of TiO_2,[72] vanadium and oxygen *K*-edges, and vanadium *L*-edge of V_2O_5.[73]

In this paper, we outline a real-time TDDFT approach to XAS for materials that use bulk-mimicking finite clusters, tuned range-separated functionals, and molecular orbital ABCs to capture XANES. As an illustrative example, we apply the approach to α–SiO_2 and compare with experimental spectra. Silicon dioxide (SiO_2) is an abundant material in the Earth's crust and mantle and has a wide range of technological applications including piezoelectrics, optical fibers, microelectronics, and, nanogenerators, to list only a few.[74-76]

There are several polymorphs of SiO_2, most of which are 4-fold coordinated (α–quartz, cristobalite, tridymite, and coesite), have a tetrahedral geometry around the Si atoms, and 2-fold coordination around oxygen atoms (4:2 structures). Stishovite, on the other hand, has a 6:3 coordinated rutile-type structure with an octahedral geometry around the Si atoms.[77] Among these, α–quartz is the most stable polymorph under ambient conditions, is most important industrially, and is the most well studied experimentally and theoretically.[74] Thus, we focus on α-quartz as a simple test case for near- and post-edge XANES in insulators, and we validate our results against previous computational and experimental data.

5.2 Results

In this paper, we use real-time TDDFT to model the X-ray absorption of α–quartz with a goal of capturing both near- and above-ionization XANES features without input from experiment. Atom-centered basis sets were used along with tuned range-separated functionals for a better description of high energy excitations. Absorbing boundary conditions were employed to emulate the continuum and reduce artifacts from the finite basis sets. We focus on α-quartz, but the approach is generalizable to similar materials. Schematically, the approach involves the following steps, which we discuss in the following subsections:

(1). Generate a small bulk-mimicking finite cluster of α–quartz that is capped with "siligens" tuned to ensure charge consistency of the atoms (Section 5.2.1).

(2). Tune LC-PBE0 range-separated functional to satisfy Koopmans' and ΔSCF ionization potentials; test straight line behavior of functional (Section 5.2.2).

(3). Construct a molecular orbital-based absorbing potential (Section 5.2.3).

(4). Use real-time TDDFT to compute absorption spectrum across pre-edge and XANES regions (Section 5.2.4).

5.2.1 Bulk-Mimicking Finite Cluster

The first step is to construct a finite cluster that is carved from the bulk crystal and capped to ensure charge consistency. The trigonal unit cell of α–quartz (a = 4.91239 Å and c = 5.40385 Å) obtained from the experimental crystal structure[78] was used to build a 17 Si bulk α–quartz model ($Si_{17}O_{16}$). This structure was truncated to make a smaller spherical cluster, Si_5O_{16}, centered around a silicon atom, which will eventually become the absorbing center for the XAS calculations. The dangling bonds of the spherical structure were capped with "siligens" ($\widetilde{H}$-pseudohydrogen atoms mimicking bulk Si atoms) to generate $Si_5O_{16}\widetilde{H}_{12}$. As this is a 4:2 coordinated system, hydrogens passivate this cluster without needing embedding charges. The central Si atom is are bonded to one boundary Si atom, which are in turn bonded to three boundary oxygen atoms, terminated by siligens. The finite cluster mimicking the bulk is shown below in Figure 5.1(a). The $Si_5O_{16}\widetilde{H}_{12}$ cluster geometry is shown in Appendix 5.

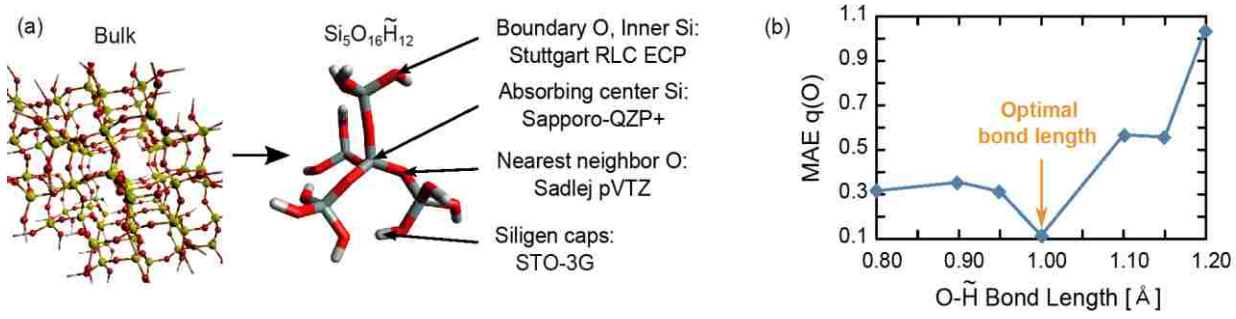

Figure 5.1. (a) Bulk-mimicking finite cluster of α–quartz with mixed basis set suitable for X-ray absorption studies. (b) Boundary O−$\widetilde{H}$ bond lengths were tuned to ensure charge consistency of the cluster.

The validity of this finite cluster depends strongly on the boundary siligen atoms, which act as a "boundary condition" for the electronic structure and dictate the charge of the cluster. One simple self-contained method for choosing the boundary atoms, which avoids tuning to the experiment, is to vary the O-$\widetilde{\mathrm{H}}$ bond length to ensure charge consistency of the atoms in the cluster.[79]

$$|q(\mathrm{Si}) = 2|q(\mathrm{O})|$$

$$4q\left(\widetilde{\mathrm{H}}\right) = q(\mathrm{Si})$$

$$q(\mathrm{O}_{\mathrm{non-bridging}}) = q(\mathrm{O}_{\mathrm{bridging}})$$

Here, for a given basis set, the O$-\widetilde{\mathrm{H}}$ bond length is tuned to minimize the error/charge inconsistencies. Mulliken population analysis is unsuitable as it is highly basis set dependent and does not consider the differences in electronegativities of atoms in molecules. Instead, the charge analysis was performed using Bader analysis, which is based on the Atoms in Molecules Theory.[80-83] This method assigns atomic "charges" (an ill-defined quality in molecules) by locating minima in the charge density and is less sensitive to basis sets than Mulliken analysis.[83,84]

In anticipation of XAS calculations, which involve transitions from the core of a single Si atom to a delocalized state, a mixed basis with 363 functions was used where the Sapporo-QZP-2012+diffuse(all)/without G functions was used for "core" Si atom and Sadlej pVTZ (Pol1) for "bridging" oxygen atoms bound to core Si, respectively, and Stuttgart RLC ECP was used for boundary Si and O atoms. STO-3G was used for H in siligen caps. This mixed basis description with absorbing center (Si) and neighbors with large polarized functions and outer atoms with a small basis set is economical but sufficient to capture the static and excited-state properties. Convergence with the basis set was checked using Dunning-type aug-cc-pV{T,Q}Z for the optical gap. Using this basis set and the PBE0[31] functional, Bader analysis[80] was performed on the small cluster, ($Si_5O_{16}\widetilde{H}_{12}$) for a series of O$-\widetilde{\mathrm{H}}$ bond lengths (0.8 to 1.2 Å) using the Bader utility from the Henkelman group.[80, 81, 83] For each fixed O$-\widetilde{\mathrm{H}}$ bond length, the cluster geometry was optimized, and the mean absolute error (MAE) for "bridging" and "boundary" oxygen atoms was determined. Figure 5.1(b) shows that the lowest MAE for oxygen atoms is achieved when O$-\widetilde{\mathrm{H}}$ bond length is 1.0 Å. Similar analysis for the Si atoms was not performed due to extreme basis set unbalance (quadruple-ζ vs ECP).

5.2.2 Tuned Range-Separated Functional

Obtaining high energy excitations using TDDFT is problematic due to the incorrect asymptotic behavior of the exchange-correlation functional.[21-25] These can be somewhat mitigated by using asymptotic correlations (e.g., LB94[22] and CS00[85,86]). Another solution, which has been very successful for high energy molecular excitations and charge transfer, is to use range-separated functionals. Here, the exchange term in the Kohn−Sham energy functional is divided into short-range and long-range parts:[28,52,87]

$$\mathrm{E_{xc}}[\rho,\{\varphi\}] = \mathrm{E_x^{DFT,short}}[\rho] + \mathrm{E_x^{HF,long}}[\{\varphi\}] + \mathrm{E_c^{DFT}}[\rho]$$

where E_{XC} is the exchange-correlation energy, E_X is the exchange energy, and E_C is the correlation energy. Here, the exchange decomposition takes the form

$$\frac{1}{r_{12}} = \frac{\alpha + \beta\mathrm{erf}(\mu r_{12})}{r_{12}} + \frac{1-[\alpha+\beta\,\mathrm{erf}(\mu r_{12})]}{r_{12}}$$

The short-range interactions use DFT exchange, and the long-range parts use Hartree Fock exchange (HF) and potentially smoothly switches from DFT to the HF exchange. α and β are dimensionless parameters that determine the HF and DFT contributions in the long/short-range region. When $r_{12} \to 0$, the functional will retain an α fraction of HF and (1 − α) fraction of DFT exchange, and as $r_{12} \to \infty$, there will be an (α + β) fraction of HF and (1 − α − β) fraction of DFT exchange. The range-separation attenuation parameter, μ, determines how rapidly the DFT exchange switches to HF.

Going further, the accuracy of the functionals for excited states has been shown to be improvable by tuning α and γ self-consistently to minimize the errors in ionization energies.[52,87] In this work, which focuses on diffuse- and above-ionization states, the range-separated functional LC-PBE0 was used to obtain the X-ray absorption spectrum of α-quartz. Similar to previous molecular studies, this functional was tuned to obtain the best parameters (α and γ), which satisfy the Koopmans' ionization potential condition ($\mathrm{IP} = -\varepsilon_{\mathrm{HOMO}}$).[52,87]

$$\begin{aligned} \mathrm{J}(\mu) &= |\mathrm{IP_{SCF}}(\mu) - \mathrm{IP_{Koopmans}}(\mu)| \\ &= |\mathrm{E_{SCF}^{cation}}(\mu) - \mathrm{E_{SCF}^{neutral}}(\mu) + \varepsilon_{\mathrm{HOMO}}^{\mathrm{neutral}}| \end{aligned}$$

J(μ) is the object function for a neutral molecule, SCF denotes the ground-state Kohn-Sham energies, and $\varepsilon_{\mathrm{HOMO}}$ is the eigenvalue of the HOMO orbital. The resulting tuned functional is denoted as LC-PBE0*.

As shown below in Figure 5.2, the lowest J(μ) for α-quartz for LC-PBE0* was achieved when α = 0.515 and γ = 0.101 au^{-1}. The calculated Koopmans' IP and Δ SCF for these values were11.2 and 11.1 eV, respectively, which results in 1.08% difference between the two energies.

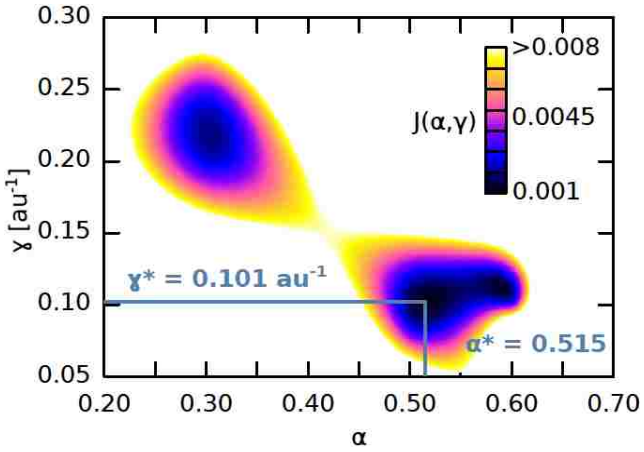

Figure 5.2. Tuning the LC-PBE0 range-separated functional.

Another important characteristic of an exchange-correlation functional is the so-called straight line behavior that measures the behavior of the energy as a function of the fractional electron number (ΔN).[87-89] For an exact functional, the energy of the atom or molecule changes linearly between adjacent integers but results in discontinuous slopes as ΔN reaches the number of electrons in the neutral molecule where the slope switches from −IP (ionization potential) to –EA (electron affinity). Although functionals can be tuned to satisfy this, we only tuned the ionization potential and simply checked the straight line behavior.

Figure 5.3 illustrates the changes in calculated energies as a function of the change in the fractional occupation number (FON) of the cluster ΔN, both for the tuned functional as well as the parent global hybrid PBE0.

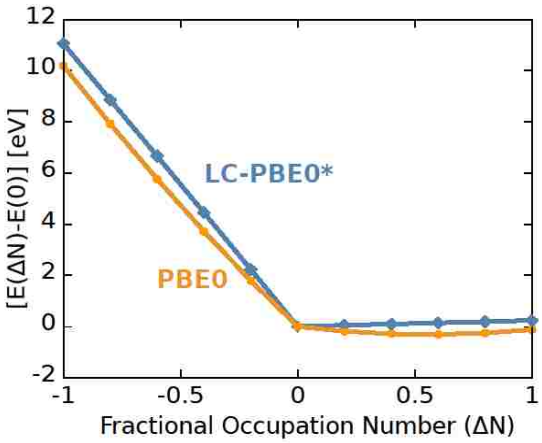

Figure 5.3. Straight line behavior for global hybrid (PBE0) and tuned range-separated functional (LC-PBE0*).

As shown in Figure 4.3, a clear derivative discontinuity is seen around the neutral molecule (ΔN = 0) for both functionals. A nearly optimal straight line is seen for the LC-PBE0* functional at the electron deficient part (ΔN < 0) as well as in the electron-rich (ΔN > 0) region, and the slope changes from – IP to – EA. In contrast to the behavior of the LC-PBE0* functional, the PBE0 functional demonstrates an incorrect convex behavior at the electron-rich part due to the delocalization errors associated with the functional. Localization errors due to non-straight line behavior result in erroneous band gaps of materials. This is often minimized by using hybrid functionals, where errors due to convex and concave parts cancel, producing more reliable band gaps.[89,90] Here, the functional, which avoids these issues, yielded an optical band gap (lowest LR-TDDFT root) of 8.4 eV in α–quartz, which agrees well with the experimental value (8.9 eV).[91] PBE0, on the other hand, significantly underestimates the band gap (6.7 eV).

5.2.3 Molecular Orbital-Based Absorbing Potential

The final ingredient for computing spectra is to construct an imaginary molecular orbital (MO) absorbing potential to remove spurious high energy peaks resulting from the finite atom-centered basis sets.[52] Although most absorbing boundary conditions take the form of a smoothly increasing potential at the simulation box edges, this approach can be problematic for

atom-centered basis sets. A simple, albeit somewhat more phenomenological, approach is to use absorbing boundary conditions directly in the MO space by applying an imaginary potential to the Fock matrix in the MO basis (prime notation).[52]

$$F'(t) = F'_0(t) + i\,\Gamma'(\mathrm{t})$$

where the imaginary potential, Γ' is obtained by projecting a diagonal damping matrix, D, on to the instantaneous MO eigenvectors of the Fock matrix, $F'_0(t)$.

$$\Gamma'(t) = C'(t)DC'^{\dagger}(t)$$

$C'(t)$ denotes the matrix in which the columns are the eigenvectors of $F'_0(t)$. D is the diagonal damping matrix with exponentially increasing damping parameters (γ) for the MOs. The damping applied to the MOs in the continuum can take virtually any form, but we use an exponential in the eigenvalues.

$$\gamma_i = \begin{cases} 0, & \tilde{\epsilon}_i \leq 0 \\ \gamma_0[\exp(\xi\tilde{\epsilon}_i) - 1], & \tilde{\epsilon}_i > 0 \end{cases}$$

Here, γ_i is the damping on the i^{th} MO; γ_0 defines the energy scale; ξ dictates the "steepness" of ABC; and $\tilde{\epsilon}_i = \epsilon_i - \epsilon_0$ is the energy of the i^{th} MO above the vacuum cutoff energy, ϵ_0. This will result in τ_i lifetime in each MO

$$\tau_i = \frac{1}{2\gamma_i}$$

This ABC is computationally inexpensive as it needs to be constructed only once due to the relatively time-independent behavior of $\Gamma'(t)$ in the limit of weak field excitations. Because this paper mainly focuses on spectroscopic data, this assumption is valid.

The vacuum energy level, ϵ_0, can be approximated by using electron affinities (EA) of the virtual orbitals. The electron affinity of each virtual orbital (EA_k) can be calculated by combining the first electron affinity EA_1 with v_k, which is the k^{th} LR-TDDFT excitation of the anion. Although approximate, this is a more accurate approximation to the EA than the raw Kohn−Sham virtual eigenvalues.

$$EA_1 = E^{anion} - E^{neutral}$$

$$EA_k \simeq EA_1 + v_{k-1,}\; k = 2,3,\ldots$$

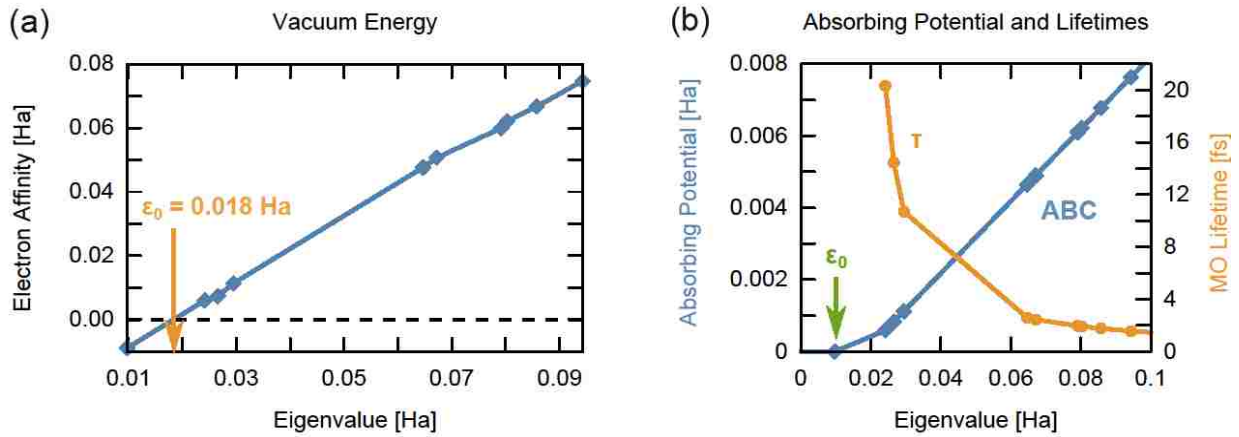

Figure 5.4. (a) Determination of vacuum energy cutoff (ϵ_0) via approximate electron affinities. (b) Absorbing boundary potential and corresponding molecular orbital lifetimes.

The eigenvalue at EA = 0 corresponds to ϵ_0 and can be obtained by interpolation of the eigenvalues (Figure 5.4(a)) which gives ϵ_0 = 0.018 Ha as the cutoff energy for the finite α–SiO_2 cluster. The imaginary potential increases exponentially with the MO eigenvalue, and the corresponding MO lifetimes decay exponentially (Figure 5.4(b)). This results in finite lifetimes in the low-lying unbound virtual orbitals (before they autoionize), while excitations to high-lying virtuals will be completely removed. For example, MO values 0.05 Ha above the cutoff energy have a lifetime of ~5 fs. As the choice of damping strength (ξ) is phenomenological, several values were tested. The results were qualitatively similar except for excess peak broadening for large values of ξ. X-ray absorption spectra with clear peaks were obtained when ξ = 0.4 Ha^{1-} for α–quartz, as this was strong enough to remove nonphysical features yet did not overbroaden peaks.

5.2.4 Absorption Spectra α–Quartz

Finally, real-time TDDFT simulations were used with this finite cluster, tuned functional, and absorbing potential. Here, three weak δ - function electric field simulations were performed (*x*, *y*, *z* polarizations) to yield the absorption spectrum spanning valence to X-ray. The computations were performed utilizing the NWChem[92] real-time TDDFT module,[93] and basis sets were selected from EMSL Basis Set Exchange.[94] All real-time simulations used a time step of Δt = 0.05 au = 0.0012 fs and were run for a total of 500 au =12 fs. This step is small enough to resolve core-level oscillations around ~100

eV. As core excitations occur at higher frequencies than the valence excitations, a smaller time step was used to obtain both valence and core oscillations in the spectrum. Convergence with Δt was checked. Each simulation used 256 2.6 GHz Xeon processors for 48 h at Louisiana State University's HPC Facility. The computed time-dependent dipole moments are shown in Figure 5.5, which clearly shows the damping effect of the $i\,\Gamma$ potential. The resulting absorption spectra were computed from the Fourier Transforms of the time-dependent dipole moments $\mu(t)$:

$$\sigma(\omega) = \frac{4\pi\omega}{3c}\, Im[f_x(\omega) + f_y(\omega) + f_z(\omega)$$

The time-dependent dipole moments were exponentially damped to accelerate the Fourier transform, $e^{(-t/\tau)}$, (τ = 75 au = 1.8 fs) and padded with 105 zeros prior to Fourier transform.

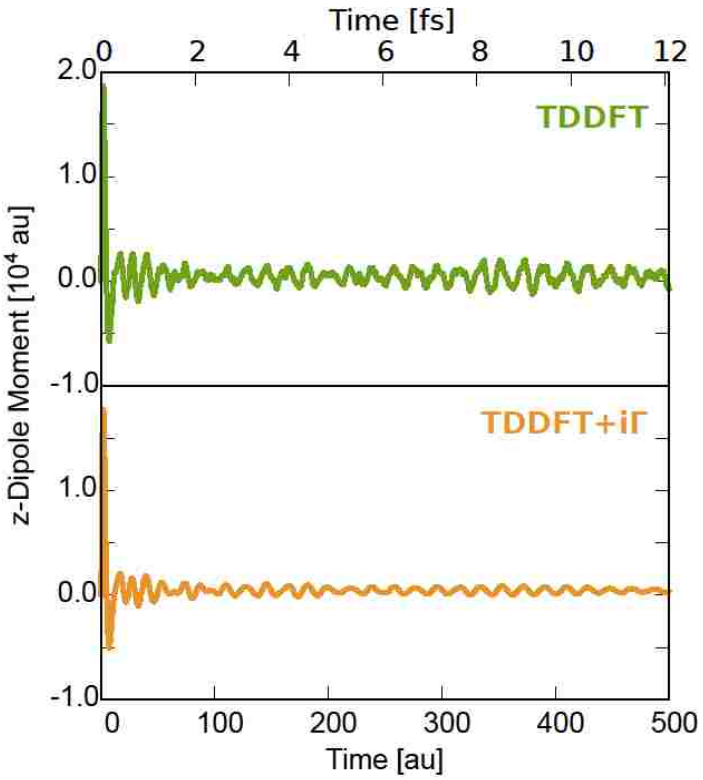

Figure 5.5. Time-dependent z-dipole moment with (orange) and without (green) absorbing potential.

The computed valence absorption spectra of α-quartz with and without the imaginary potential ($i\,\Gamma$) are shown in Figure 5.6. The experimental UV absorption spectrum was digitized from the work done by Chang et al.[95] The computed valence absorption spectrum qualitatively agrees with the

experimental spectrum[95] as well as with the density of states (DOS) of α– quartz calculated by Calabrese et al. and Binggeli et al.[74,96] Peak A at the onset (8.4 eV) of the computed spectra is the optical gap and corresponds to the transition from O 2p to antibonding counterparts of O 2s, Si 3s, and 3p. This peak is absent in the experimental data due to vanishing transition dipole for the bulk. Peak B (9.7 eV) corresponds to the transitions from O 2s and 2p orbitals to the conduction band composed of antibonding O 2s and 2p orbitals and antibonding Si 3s and 3p orbitals. The remaining low-energy calculated valence excitation energies agree fairly well with the experimental spectrum, but the oscillator strengths are significantly different. This is likely a finite cluster size effect, where transitions are artificially localized in space, have greatly overestimated MO overlaps and thus artificially large oscillator strengths. This effect is far more pronounced in the valence, where both occupied and virtual states are somewhat delocalized, and less so for the core, where the occupied state I essentially localized on one atom (Figure 5.7).

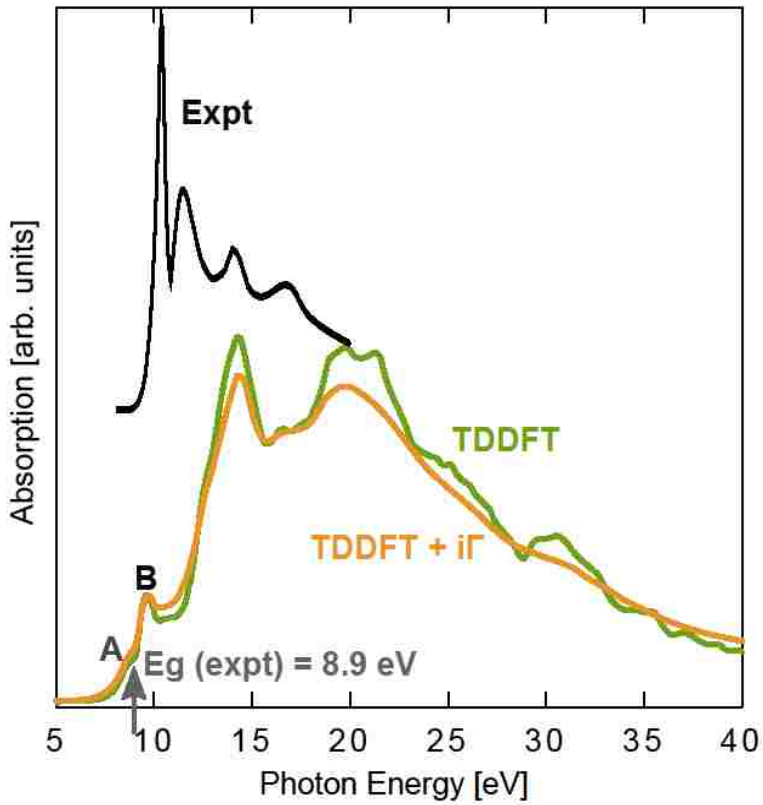

Figure 5.6. Computed UV absorption spectrum of α–quartz with (orange) and without (green) absorbing potential. The experimental spectrum (black) was digitized from the work done by Chang et al.[95] The experimental band gap is from the work done by Binggeli et al.[74] (digitized with permission from the American Physical Society).

The core absorption spectra of α-quartz obtained by RT-TDDFT computed with and without $i\,\Gamma$ are shown in Figure 5.7. Here, for clarity we subtracted the exponential continuum background from the TDDFT + $i\,\Gamma$ spectrum, and all TDDFT spectra were shifted by +1.3 eV to match the experiment. The parameters employed for ABC were ϵ_0 = 0.018 Ha and ξ = 0.4 Ha^{1-}. In order to determine the corresponding transitions, LR-TDDFT was performed using the restricted excitation window approach. The LR-TDDFT spectrum obtained for 300 roots is also shown in Figure 5.7. These spectra are compared with the experimental Si L-edge spectrum obtained by Li et al.[97]

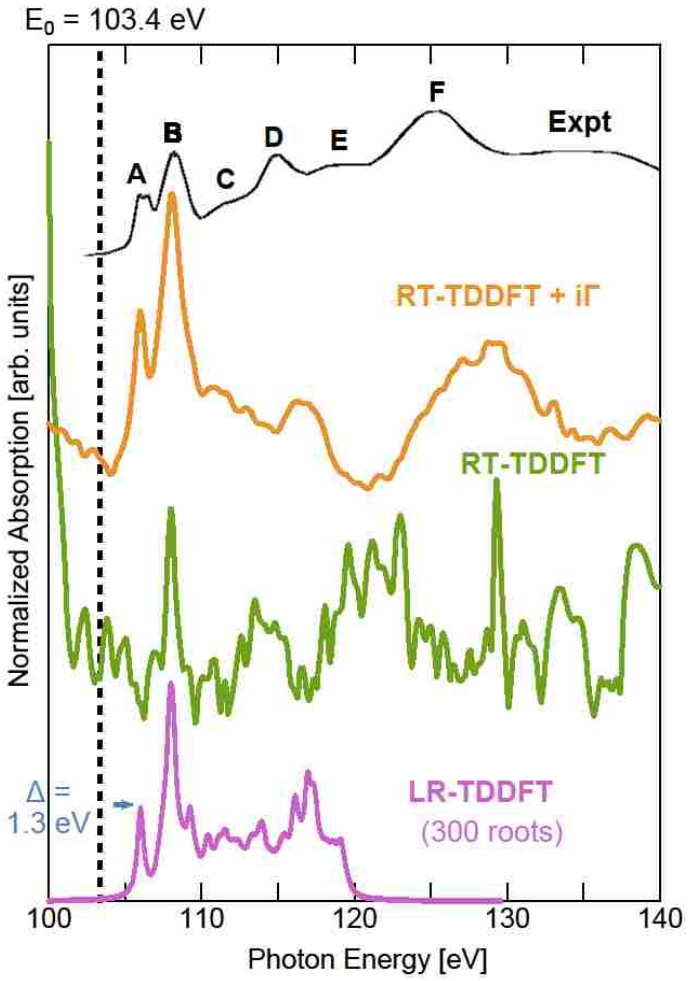

Figure 5.7. Computed real-time TDDFT X-ray absorption spectrum of α–quartz with (orange) and without (green) an absorbing potential, along with corresponding linear response TDDFT (purple). The three experimental spectra were shifted by 1.3 eV to match with the experimental spectrum (black), which was digitized from the work done by Li et al.[97] The experimental Si 2p ionization energy (103.4 eV) is shown as a dotted line (digitized with permission from the Mineralogical Society of America).

There are clear differences in the spectra obtained from the three variants of TDDFT (LR, RT, RT + $i\,\Gamma$). The RT-TDDFT without an absorbing potential is highly polluted with many nonphysical excitation, which makes interpreting this spectrum all but impossible. Adding the $i\,\Gamma$ results in a significantly better X-ray absorption spectrum, especially for the near-edge features, but the peaks corresponding to multiple scattering are shifted from experiment, likely due to finite basis effects or inadequacies in the absorbing potential. Also note, the low energy RT-TDDFT+ $i\,\Gamma$ peaks are essentially the same as the LR-TDDFT ones but differ for higher energies, mainly due to broadening from the ABC.

Finally, we discuss the origins of the various excitations. The first peak is at 105.4 eV, and as it is higher than the ionization potential of Si 2p (103.4 eV), all features in the Si *L*-edge up to 153.4 eV are near-edge features (XANES).[74] Peak A results from the transitions to antibonding Si 3s orbitals from Si 2p orbitals. The spin−orbit splitting feature ($2p_{(3/2),}2p_{(1/2)}$) seen in peak A in the experimental spectrum is not captured in our spectra as we do not include spin−orbit effects in our simulations. Peak B corresponds to the excitations of Si 2p electrons to antibonding 3p states. Even though $2p \rightarrow p$ transitions are atomically forbidden, this becomes dipole allowed due to the tetrahedral symmetry of α−quartz, that is, Laporte selection rule ($\Delta\, l = \pm 1$) is violated in this system due to its non-centrosymmetric nature. In tetrahedral symmetry, p and d orbitals transform to t_2 resulting in mixing of p and d orbitals.[98] As this will result in some d-character in p-orbitals, the $2p \rightarrow p$ transition becomes possible. Peaks C and E correspond to transitions due to multiple scattering effects where the states are not simple atomic or molecular states.[97] Peaks D and F result from the transitions to Si 3d and 3p states from Si 2p. According to the crystal field theory, in tetrahedral molecules the 3d orbitals are divided into *e* and t_2 states, where *e* states are more stable than t_2.[97,99] According to the experimental spectra obtained by Li et al., peak D corresponds to the transition to e states and peak F to t_2 states.[97]

The A and B transitions are both very well described by TDDFT, as they are relatively localized near-edge excitations. Peaks C, D, E, and F are increasingly more difficult to capture due to both finite cluster/basis effects and limitations in the exchange-correlation function for very diffuse continuum-like virtual states.

5.4 Conclusions

In summary, we have computed the near- and post-edge X-ray absorption spectrum of insulators using real-time time-dependent density functional theory (RT-TDDFT). An embedded finite cluster model of α–quartz was used as an example where the spectra were computed using atom-centered basis sets and range-separated functionals. The LC-PBE0* functional was tuned to satisfy the Koopmans' ionization potential condition to find the best tuned parameters (α and γ), and the straight-line behavior of the functional was also verified. The post-edge excitations were captured using real-time TDDFT with an imaginary absorbing potential. This results in a finite lifetime in low-lying unbound virtual orbitals and completely removes the nonphysical high-lying orbitals. The resulting Si *L*-edge spectrum was purified of spurious excitations and matches well with experimental data over the range of ~105−120 eV, i.e., approximately 15 eV above the ionization edge.

This method of computing X-ray absorption using embedded cluster models, atom-centered basis sets, tuned functionals, and absorbing boundary conditions resulted in a significantly improved spectrum over traditional TDDFT and agrees well with the experiment. Due to the difficulties in treating infinite solids with TDDFT, bulk-mimicking embedded finite cluster models are a useful tool for studying the excited-state electronic structure of materials. Embedded finite clusters with all-electron basis sets are also natural for XAS calculations and facilitate use of (tuned) hybrid DFT functionals at a more modest computational cost than planewaves or grid-based methods.

A major drawback to this approach is the choice of the molecular-orbital absorbing boundary condition, which must be picked carefully as to remove nonphysical states but not overdamp the XAS features. A more rigorous way is to use spatially dependent ABCs, but this would potentially require very large basis sets. Also, even for tuned functionals, the computed spectra are shifted from experiment by a few percent, likely due to incorrect core−hole response. Moreover, core excitations occur at higher frequencies than valence excitations, so Δt for RT-TDDFT must be sufficiently small so that it ensures the capturing of both core and valence excitations, which requires long simulation times. Finally, even though the full absorption spectrum can be obtained in just one simulation with RT-TDDFT, the transitions corresponding to the peaks cannot be easily analyzed because extracting the orbital contributions from

the time-dependent density matrix is not straightforward. Hence, LR-TDDFT is often required to assign those transitions. Despite these drawbacks, non-Hermitian real-time TDDFT offers a simple approach for near-edge XAS suitable for modeling spectroscopy and dynamics in systems ranging from organic molecules to inorganic complexes to potentially disordered solid-state materials, all without experimental parameterization.

5.5 References

1. Penner-Hahn, J. E., 2.13 - X-ray Absorption Spectroscopy. In *Comprehensive Coordination Chemistry II*, Meyer, J. A. M. J., Ed. Pergamon: Oxford, 2003; pp 159-186.

2. Fonda, L., Multiple-scattering theory of X-ray absorption: a review. *Journal of Physics: Condensed Matter* **1992,** *4* (43), 8269.

3 Ankudinov, A.; Ravel, B.; Rehr, J.; Conradson, S., Real-space multiple-scattering calculation and interpretation of x-ray-absorption near-edge structure. *Physical Review B* **1998,** *58* (12), 7565.

4. Albrecht, S.; Reining, L.; Del Sole, R.; Onida, G., Ab initio calculation of excitonic effects in the optical spectra of semiconductors. *Physical review letters* **1998,** *80* (20), 4510.

5. Shirley, E. L., Ab initio inclusion of electron-hole attraction: Application to X-Ray Absorption and Resonant Inelastic X-Ray Scattering. *Physical review letters* **1998,** *80* (4), 794.

6. Taillefumier, M.; Cabaret, D.; Flank, A.-M.; Mauri, F., X-ray absorption near-edge structure calculations with the pseudopotentials: Application to the *K* edge in diamond and a-quarts. *Physical Review B* **2002,** *66* (19), 195107.

7. Soininen, J. A.; Shirley, E. L., Scheme to calculate core hole–electron interactions in solids. *Physical Review B* **2001,** *64* (16), 165112.

8. Gougoussis, C.; Calandra, M.; Seitsonen, A. P.; Mauri, F., First-principles calculations of x-ray absorption in a scheme based on ultrasoft pseudopotentials: from α-quartz to high-T c compounds. *Physical Review B* **2009,** *80* (7), 075102.

9. Besley, N. A.; Asmuruf, F. A., Time-dependent density functional theory calculations of the spectroscopy of core electrons. *Physical Chemistry Chemical Physics* **2010,** *12* (38), 12024-12039.

10. Ankudinov, A.; Takimoto, Y.; Rehr, J., Combined Bethe-Saltpeter equations and time-dependent density-functional theory approach for x-ray absorption calculations. *Physical Review B* **2005,** *71* (16), 165110.

11. Ankudinov, A.; Nesvizhskii, A.; Rehr, J., Dynamic screening effects in x-ray absorption spectra. *Physical Review B* **2003,** *67* (11), 115120.

12. Rehr, J., Theory and calculations of X-ray spectra: XAS, XES, XRS, and NRIXS. *Radiation Physics and Chemistry* **2006,** *75* (11), 1547-1558.

13. Schwitalla, J.; Ebert, H., Electron Core-Hole Interaction in the X-Ray Absorption Spectroscopy of 3 d Transition Metals. *Physical review letters* **1998,** *80* (20), 4586.

14. Wang, Y.; Lopata, K.; Chambers, S. A.; Govind, N.; Sushko, P. V., Optical Absorption and Band Gap Reduction in $(Fe_{1-x}\ Cr_x)_2O_3$ Solid Solutions: A First-Principles Study. *The Journal of Physical Chemistry C* **2013,** *117* (48), 25504-25512.

15. Schultze, M.; Bothschafter, E. M.; Sommer, A.; Holzner, S.; Schweinberger, W.; Fiess, M.; Hofstetter, M.; Kienberger, R.; Apalkov, V.; Yakovlev, V. S., Controlling dielectrics with the electric field of light. *Nature* **2013,** *493* (7430), 75-78.

16. Runge, E.; Gross, E. K., Density-functional theory for time-dependent systems. *Physical Review Letters* **1984,** *52* (12), 997.

17. Marques, M. A.; Gross, E., Time-dependent density functional theory. *Annual Review of Physical Chemistry* **2004,** *55* (1), 427-455.

18. Burke, K.; Werschnik, J.; Gross, E., Time-dependent density functional theory: Past, present, and future. *The Journal of chemical physics* **2005,** *123* (6), 062206.

19. Casida, M. E., Time-dependent density-functional theory for molecules and molecular solids. *Journal of Molecular Structure: THEOCHEM* **2009,** *914* (1–3), 3-18.

20. Ullrich, C. A.; Yang, Z.-h., A brief compendium of time-dependent density functional theory. *Brazilian Journal of Physics* **2014,** *44* (1), 154-188.

21. Tozer, D. J.; Handy, N. C., Improving virtual Kohn–Sham orbitals and eigenvalues: Application to excitation energies and static polarizabilities. *The Journal of Chemical Physics* **1998,** *109* (23), 10180-10189.

22. van Leeuwen, R.; Baerends, E. J., Exchange-correlation potential with correct asymptotic behavior. *Physical Review A* **1994,** *49* (4), 2421-2431.

23. Dreuw, A.; Weisman, J. L.; Head-Gordon, M., Long-range charge-transfer excited states in time-dependent density functional theory require non-local exchange. *The Journal of chemical physics* **2003,** *119* (6), 2943-2946.

24. Wasserman, A.; Maitra, N. T.; Burke, K., Accurate rydberg excitations from the local density approximation. *Physical review letters* **2003,** *91* (26), 263001.

25. Autschbach, J., Charge ¡Transfer Excitations and Time ¡Dependent Density Functional Theory: Problems and Some Proposed Solutions. *ChemPhysChem* **2009,** *10* (11), 1757-1760.

26. Prendergast, D.; Galli, G., X-ray absorption spectra of water from first principles calculations. *Physical review letters* **2006,** *96* (21), 215502.

27. Uejio, J. S.; Schwartz, C. P.; Saykally, R. J.; Prendergast, D., Effects of vibrational motion on core-level spectra of prototype organic molecules. *Chemical Physics Letters* **2008,** *467* (1–3), 195-199.

28. Yanai, T.; Tew, D. P.; Handy, N. C., A new hybrid exchange–correlation functional using the Coulomb-attenuating method (CAM-B3LYP). *Chemical Physics Letters* **2004,** *393* (1–3), 51-57.

29. Baer, R.; Neuhauser, D., Density functional theory with correct long-range asymptotic behavior. *Physical review letters* **2005,** *94* (4), 043002.

30. Vydrov, O. A.; Scuseria, G. E., Assessment of a long-range corrected hybrid functional. *The Journal of chemical physics* **2006,** *125* (23), 234109.

31. Adamo, C.; Barone, V., Toward reliable density functional methods without adjustable parameters: The PBE0 model. *The Journal of chemical physics* **1999,** *110* (13), 6158-6170.

32. Iikura, H.; Tsuneda, T.; Yanai, T.; Hirao, K., A long-range correction scheme for generalized-gradient-approximation exchange functionals. *The Journal of Chemical Physics* **2001,** *115* (8), 3540-3544.

33. Tawada, Y.; Tsuneda, T.; Yanagisawa, S.; Yanai, T.; Hirao, K., A long-range-corrected time-dependent density functional theory. *The Journal of chemical physics* **2004,** *120* (18), 8425-8433.

34. Govind, N.; Valiev, M.; Jensen, L.; Kowalski, K., Excitation energies of zinc porphyrin in aqueous solution using long-range corrected time-dependent density functional theory. *The Journal of Physical Chemistry A* **2009,** *113* (21), 6041-6043.

35. Baer, R.; Livshits, E.; Salzner, U., Tuned range-separated hybrids in density functional theory. *Annual review of physical chemistry* **2010,** *61*, 85-109.

36. Kosloff, R.; Kosloff, D., Absorbing boundaries for wave propagation problems. *Journal of Computational Physics* **1986,** *63* (2), 363-376.

37. Neuhasuer, D.; Baer, M., The time ¸dependent Schrödinger equation: Application of absorbing boundary conditions. *The Journal of Chemical Physics* **1989,** *90* (8), 4351-4355.

38. Seideman, T.; Miller, W. H., Calculation of the cumulative reaction probability via a discrete variable representation with absorbing boundary conditions. *The Journal of chemical physics* **1992,** *96* (6), 4412-4422.

39. Jolicard, G.; Austin, E. J., Optical potential stabilisation method for predicting resonance levels. *Chemical physics letters* **1985,** *121* (1), 106-110.

40. Riss, U.; Meyer, H.-D., Calculation of resonance energies and widths using the complex absorbing potential method. *Journal of Physics B: Atomic, Molecular and Optical Physics* **1993,** *26* (23), 4503.

41. Sommerfeld, T.; Riss, U.; Meyer, H.-D.; Cederbaum, L., Metastable C_2^{2-} Dianion. *Physical review letters* **1997,** *79* (7), 1237.

42. Bravaya, K. B.; Zuev, D.; Epifanovsky, E.; Krylov, A. I., Complex-scaled equation-of-motion coupled-cluster method with single and double substitutions for autoionizing excited states: Theory, implementation, and examples. *The Journal of chemical physics* **2013,** *138* (12), 124106.

43. Jagau, T.-C.; Krylov, A. I., Complex Absorbing Potential Equation-of-Motion Coupled-Cluster Method Yields Smooth and Internally Consistent Potential Energy Surfaces and Lifetimes for Molecular Resonances. *The Journal of Physical Chemistry Letters* **2014,** *5* (17), 3078-3085.

44. Nakatsukasa, T.; Yabana, K., Photoabsorption spectra in the continuum of molecules and atomic clusters. *The Journal of Chemical Physics* **2001,** *114* (6), 2550-2561.

45. Yabana, K.; Nakatsukasa, T.; Iwata, J.; Bertsch, G., Real-time, real-space implementation of the linear response time-dependent density-functional theory. *Physica Status Solidi B Basic Research* **2006,** *243* (5), 1121.

46. Crawford-Uranga, A.; De Giovannini, U.; Räsänen, E.; Oliveira, M. J.; Mowbray, D. J.; Nikolopoulos, G. M.; Karamatskos, E. T.; Markellos, D.; Lambropoulos, P.; Kurth, S., Time-dependent density-functional theory of strong-field ionization of atoms by soft x rays. *Physical Review A* **2014,** *90* (3), 033412.

47. Zhou, Y.; Ernzerhof, M., Calculating the lifetimes of metastable states with complex density functional theory. *The Journal of Physical Chemistry Letters* **2012,** *3* (14), 1916-1920.

48. Reinhardt, W. P., Complex coordinates in the theory of atomic and molecular structure and dynamics. *Annual Review of Physical Chemistry* **1982,** *33* (1), 223-255.

49. Moiseyev, N., Quantum theory of resonances: calculating energies, widths and cross-sections by complex scaling. *Physics Reports* **1998,** *302* (5), 212-293.

50. Telnov, D. A.; Sosnova, K. E.; Rozenbaum, E.; Chu, S.-I., Exterior complex scaling method in time-dependent density-functional theory: Multiphoton ionization and high-order-harmonic generation of Ar atoms. *Physical Review A* **2013,** *87* (5), 053406.

51. Jensen, L.; Autschbach, J.; Schatz, G. C., Finite lifetime effects on the polarizability within time-dependent density-functional theory. *The Journal of chemical physics* **2005,** *122* (22), 224115.

52. Lopata, K.; Govind, N., Near and Above Ionization Electronic Excitations with Non-Hermitian Real-Time Time-Dependent Density Functional Theory. *Journal of Chemical Theory and Computation* **2013,** *9* (11), 4939-4946.

53. Yabana, K.; Bertsch, G., Time-dependent local-density approximation in real time. *Physical Review B* **1996,** *54* (7), 4484.

54. Yabana, K.; Bertsch, G., Time-dependent local-density approximation in real time: Application to conjugated molecules. *International journal of quantum chemistry* **1999,** *75* (1), 55-66.

55. Tsolakidis, A.; Sánchez-Portal, D.; Martin, R. M., Calculation of the optical response of atomic clusters using time-dependent density functional theory and local orbitals. *Physical Review B* **2002,** *66* (23), 235416.

56. Takimoto, Y.; Vila, F.; Rehr, J., Real-time time-dependent density functional theory approach for frequency-dependent nonlinear optical response in photonic molecules. *The Journal of chemical physics* **2007,** *127* (15), 154114.

57. Petersilka, M.; Gossmann, U.; Gross, E., Excitation energies from time-dependent density-functional theory. *Physical review letters* **1996,** *76* (8), 1212.

58. Casida, M. E., Time-dependent density functional response theory for molecules. *Recent advances in density functional methods* **1995,** *1*, 155.

59. Maitra, N. T.; Burke, K.; Woodward, C., Memory in Time-Dependent Density Functional Theory. *Physical Review Letters* **2002,** *89* (2), 023002.

60. Baer, R., Prevalence of the adiabatic exchange-correlation potential approximation in time-dependent density functional theory. *Journal of Molecular Structure: THEOCHEM* **2009,** *914* (1–3), 19-21.

61. Lopata, K.; Van Kuiken, B. E.; Khalil, M.; Govind, N., Linear-response and real-time time-dependent density functional theory studies of core-level near-edge X-ray absorption. *Journal of Chemical Theory and Computation* **2012,** *8* (9), 3284-3292.

62. Stener, M.; Fronzoni, G.; De Simone, M., Time dependent density functional theory of core electrons excitations. *Chemical physics letters* **2003,** *373* (1), 115-123.

63. Fronzoni, G.; Stener, M.; Reduce, A.; Decleva, P., Time-dependent density functional theory calculations of ligand K edge and metal L edge X-ray absorption of a series of oxomolybdenum complexes. *The Journal of Physical Chemistry A* **2004,** *108* (40), 8467-8477.

64. Van Kuiken, B. E.; Huse, N.; Cho, H.; Strader, M. L.; Lynch, M. S.; Schoenlein, R. W.; Khalil, M., Probing the electronic structure of a photoexcited solar cell dye with transient x-ray absorption spectroscopy. *The Journal of Physical Chemistry Letters* **2012,** *3* (12), 1695-1700.

65. Van Kuiken, B. E.; Valiev, M.; Daifuku, S. L.; Bannan, C.; Strader, M. L.; Cho, H.; Huse, N.; Schoenlein, R. W.; Govind, N.; Khalil, M., Simulating Ru L3-Edge X-ray Absorption Spectroscopy with Time-Dependent Density Functional Theory: Model Complexes and Electron Localization in Mixed-Valence Metal Dimers. *The Journal of Physical Chemistry A* **2013,** *117* (21), 4444-4454.

66. Besley, N. A.; Noble, A., Time-dependent density functional theory study of the X-ray absorption spectroscopy of acetylene, ethylene, and benzene on si (100). *The Journal of Physical Chemistry C* **2007,** *111* (8), 3333-3340.

67. De Francesco, R.; Stener, M.; Fronzoni, G., TDDFT calculations of NEXAFS spectra of model systems for SO2 adsorbed on the MgO (100) surface. *The Journal of Physical Chemistry C* **2007,** *111* (36), 13554-13563.

68. De Francesco, R.; Stener, M.; Fronzoni, G., S K-edge NEXAFS spectra of model systems for SO 2 on TiO 2 (110): a TDDFT simulation. *Physical Chemistry Chemical Physics* **2009,** *11* (8), 1146-1151.

69. Bunău, O.; Joly, Y., Time-dependent density functional theory applied to x-ray absorption spectroscopy. *Physical Review B* **2012,** *85* (15), 155121.

70. Bunău, O.; Joly, Y., Full potential x-ray absorption calculations using time dependent density functional theory. *Journal of Physics: Condensed Matter* **2012,** *24* (21), 215502.

71. Fronzoni, G.; De Francesco, R.; Stener, M., Time Dependent Density Functional Theory of X-Ray absorption spectroscopy of alkaline-earth oxides. *The Journal of Physical Chemistry B* **2005,** *109* (20), 10332-10340.

72. Fronzoni, G.; De Francesco, R.; Stener, M.; Causa, M., X-ray absorption spectroscopy of titanium oxide by time dependent density functional calculations. *The Journal of Physical Chemistry B* **2006,** *110* (20), 9899-9907.

73. De Francesco, R.; Stener, M.; Causa, M.; Toffoli, D.; Fronzoni, G., Time dependent density functional investigation of the near-edge absorption spectra of V_2O_5. *Physical Chemistry Chemical Physics* **2006,** *8* (37), 4300-4310.

74. Binggeli, N.; Troullier, N.; Martins, J. L.; Chelikowsky, J. R., Electronic properties of α-quartz under pressure. *Physical Review B* **1991,** *44* (10), 4771.

75. Yin, K.; Lin, H.; Cai, Q.; Zhao, Y.; Lee, S.-T.; Hu, F.; Shao, M., Silicon nanowires nanogenerator based on the piezoelectricity of alpha-quartz. *Nanoscale* **2013,** *5* (24), 12330-12334.

76. Que, R.; Shao, M.; Wang, S.; Ma, D. D. D.; Lee, S.-T., Silicon Nanowires with Permanent Electrostatic Charges for Nanogenerators. *Nano Letters* **2011,** *11* (11), 4870-4873.

77. Kasrai, M.; Fleet, M.; Bancroft, G.; Tan, K.; Chen, J., X-ray-absorption near-edge structure of alkali halides: The interatomic-distance correlation. *Physical Review B* **1991,** *43* (2), 1763.

78. Will, G.; Bellotto, M.; Parrish, W.; Hart, M., Crystal structures of quartz and magnesium germanate by profile analysis of synchrotron-radiation high-resolution powder data. *Journal of Applied Crystallography* **1988,** *21* (2), 182-191.

79. Sauer, J., Molecular models in ab initio studies of solids and surfaces: from ionic crystals and semiconductors to catalysts. *Chemical Reviews* **1989,** *89* (1), 199-255.

80. Henkelman, G.; Arnaldsson, A.; Jónsson, H., A fast and robust algorithm for Bader decomposition of charge density. *Computational Materials Science* **2006,** *36* (3), 354-360.

81. Sanville, E.; Kenny, S. D.; Smith, R.; Henkelman, G., Improved grid ¡based algorithm for Bader charge allocation. *Journal of computational chemistry* **2007,** *28* (5), 899-908.

82. Tang, D.; Qin, S.; Su, Z.; Hu, C., Comprehensive Theoretical Study on the Mechanism of Regioselective Hydroformylation of Phosphinobutene Catalyzed by a Heterobinuclear Rhodium (I)-Chromium Complex. *Organometallics* **2007,** *26* (1), 33-47.

83. Tang, W.; Sanville, E.; Henkelman, G., A grid-based Bader analysis algorithm without lattice bias. *Journal of Physics: Condensed Matter* **2009,** *21* (8), 084204.

84. Wiberg, K. B.; Rablen, P. R., Comparison of atomic charges derived via different procedures. *Journal of Computational Chemistry* **1993,** *14* (12), 1504-1518.

85. Casida, M. E.; Salahub, D. R., Asymptotic correction approach to improving approximate exchange–correlation potentials: Time-dependent density-functional theory calculations of molecular excitation spectra. *The Journal of Chemical Physics* **2000,** *113* (20), 8918-8935.

86. Hirata, S.; Zhan, C.-G.; Aprà, E.; Windus, T. L.; Dixon, D. A., A new, self-contained asymptotic correction scheme to exchange-correlation potentials for time-dependent density functional theory. *The Journal of Physical Chemistry A* **2003,** *107* (47), 10154-10158.

87. Srebro, M.; Autschbach, J., Tuned Range-Separated Time-Dependent Density Functional Theory Applied to Optical Rotation. *Journal of Chemical Theory and Computation* **2011,** *8* (1), 245-256.

88. Perdew, J. P.; Parr, R. G.; Levy, M.; Balduz, J. L., Density-Functional Theory for Fractional Particle Number: Derivative Discontinuities of the Energy. *Physical Review Letters* **1982,** *49* (23), 1691-1694.

89. Cohen, A. J.; Mori-Sanchez, P.; Yang, W., Insights into current limitations of density functional theory. *Science* **2008,** *321* (5890), 792-4.

90. Mori-Sánchez, P.; Cohen, A. J.; Yang, W., Localization and Delocalization Errors in Density Functional Theory and Implications for Band-Gap Prediction. *Physical Review Letters* **2008,** *100* (14), 146401.

91. Ruso, J. M.; Gravina, A. N.; D'Elia, N. L.; Messina, P. V., Highly efficient photoluminescence of SiO2 and Ce-SiO2 microfibres and microspheres. *Dalton Trans* **2013,** *42* (22), 7991-8000.

92. Valiev, M.; Bylaska, E. J.; Govind, N.; Kowalski, K.; Straatsma, T. P.; Van Dam, H. J.; Wang, D.; Nieplocha, J.; Apra, E.; Windus, T. L., NWChem: a comprehensive and scalable open-source solution for large scale molecular simulations. *Computer Physics Communications* **2010,** *181* (9), 1477-1489.

93. Lopata, K.; Govind, N., Modeling Fast electron dynamics with real-time time-dependent density functional theory: Application to small molecules and chromophores. *Journal of Chemical Theory and Computation* **2011,** *7* (5), 1344-1355.

94. Schuchardt, K. L.; Didier, B. T.; Elsethagen, T.; Sun, L.; Gurumoorthi, V.; Chase, J.; Li, J.; Windus, T. L., Basis set exchange: a community database for computational sciences. *Journal of chemical information and modeling* **2007,** *47* (3), 1045-1052.

95. Chang, E. K.; Rohlfing, M.; Louie, S. G., Excitons and optical properties of α-quartz. *Physical review letters* **2000,** *85* (12), 2613.

96. Calabrese, E.; Fowler, W. B., Electronic energy-band structure of α quartz. *Physical Review B* **1978,** *18* (6), 2888.

97. Li, D.; Bancroft, G.; Kasrai, M.; Fleet, M.; Secco, R.; Feng, X.; Tan, K.; Yang, B., X-ray absorption spectroscopy of silicon dioxide (SiO 2) polymorphs; the structural characterization of opal. *American Mineralogist* **1994,** *79* (7-8), 622-632.

98. Hansen, P. L.; Brydson, R.; McComb, D. W., p→ p-like transitions at the silicon L2, 3-edges of silicates. *Microscopy Microanalysis Microstructures* **1992,** *3* (2-3), 213-219.

99. Liu, Z. F.; Cutler, J. N.; Bancroft, G. M.; Tan, K. H.; Cavell, R. G.; Tse, J. S., Crystal field splittings of continuum d orbitals. A comparative study on the L2,3 edge X-ray absorption spectra of Si, P and S compounds. *Chemical Physics* **1992,** *168* (1), 133-144.

Chapter 6 - Conclusion

This work is mainly focused on DFT calculations on bimetallic homogeneous catalysis and X-ray absorption spectroscopy of insulators. DFT modeling studies on industrially useful hydroformylation and AWS reactions are performed using bimetallic rhodium and bimetallic cobalt catalysts, and TD-DFT studies are used to model X-ray absorption spectroscopy of insulators. A comparative study on bimetallic rhodium and bimetallic cobalt complexes for the hydroformylation and AWS are discussed in this chapter.

6.1 Comparison of Rh_2 and Co_2 Hydroformylation Catalysts

The bimetallic rhodium and cobalt catalyst precursors both react with carbon monoxide to form the pentacarbonyl complexes, but the dicobalt complex continues to react with excess CO to form the hexacarbonyl complex. As cobalt complexes favor higher coordination numbers, unlike rhodium(+1) complexes, the formation of the saturated hexacarbonyl cobalt complexes makes sense. The main steps in hydroformylation for both bimetallic cobalt and rhodium catalyst systems are: the oxidative addition of hydrogen gas, alkene coordination, hydride insertion into the alkene to form the alkyl group, CO insertion to form the acyl group, and reductive elimination of the aldehdyde product.

DFT modeling studies were performed on each of these steps to determine the most favorable pathway. Prior to oxidative addition of hydrogen gas CO groups will be dissociated from rhodium pentacarbonyl complex and cobalt hexacarbonyl complex. Both these complexes further dissociate the labile CO groups to form the tetracarbonyl complexes. H_2 oxidatively add to these tetracarbonyl complexes to form the open-mode dihydride complexes. The open-mode complexes then converts into closed-mode complexes to give either symmetric or unsymmetrical complexes.

The free energy change for the oxidative addition of H_2 to open-mode tetracarbonyl rhodium complex and open-mode tetracarbonyl cobalt complex +10.7 kcal/mol and +16.4 kcal/mol respectively. These energies indicate oxidative addition is more favorable in rhodium catalyzed cycle than in cobalt catalyzed cycle, which is consistent with the monometallic catalysts. The activation barrier for H_2 oxidative addition for rhodiumis 10.4 kcals/mol vs. 16.9 kcals/mol for the dicobalt catalyst, once again supporting the higher reactivity of Rh vs. Co.

DFT studies indicate that the bimetallic symmetric bridging hydride complex $[Rh_2(\mu\text{–}H)_2(CO)_4H(rac\text{–}et,ph\text{–}P4)]^{2+}$ (**2***), and unsymmetrical $[Co_2(\mu\text{–}CO)(\mu\text{–}H)(CO)_3H(rac\text{–}et,ph\text{–}P4)]^{2+}$ (**Co_2**) complexes serve as the most active species to react with alkene. A CO group dissociates to generate unsaturated complexes for the alkene coordination, which is followed by hydride insertion to form alkyl groups. The activation energy for the bridging hydride insertion is 8.0 kcal/mol for Rh. The dicobalt species with a bridging and terminal hydride has two different activation barriers: 12.1 kcal/mol for alkene and bridging hydride, while the alkene and terminal hydride is a barrier-less step. So one major difference between the Co and Rh bimetallic catalysts is the much higher reactivity of the terminal Co-H for the migratory insertion reaction with alkene.

The next major step in hydroformylation is the CO migratory insertion with the alkyl group to form the acyl group. In rhodium catalyzed hydroformylation DFT calculates the activation barrier for this step as 13.2 kcal/mol, whereas for cobalt the activation energies for terminal CO insertion and bridging CO insertion are 5.9 kcal/mol and 3.9 kcal/mol, respectively.

Finally the reductive elimination of the aldehdye takes place to regenerate the pentacarbonyl complexes. The activation energy for the reductive elimination step for rhodium is 13.4 kcal/mol, whereas in cobalt catalyzed cycle it is a high 42.6 kcal/mol.

The activation barriers show that for rhodium catalyzed hydroformylation rate-determining step is either CO insertion or reductive elimination of the aldehyde because both steps have essentially the same activation energy. The rate determining step for dicobalt catalyzed hydroformylation is the aldehyde reductive elimination. The intermediate species relative energies and activation barriers for dirhodium and dicobalt catalyzed hydroformylation are shown below in Figure 6.1. According to these observations, increasing the electron deficiency at the metal centers via incorporation of electron withdrawing groups on the P4 ligand, these barriers can be lowered.

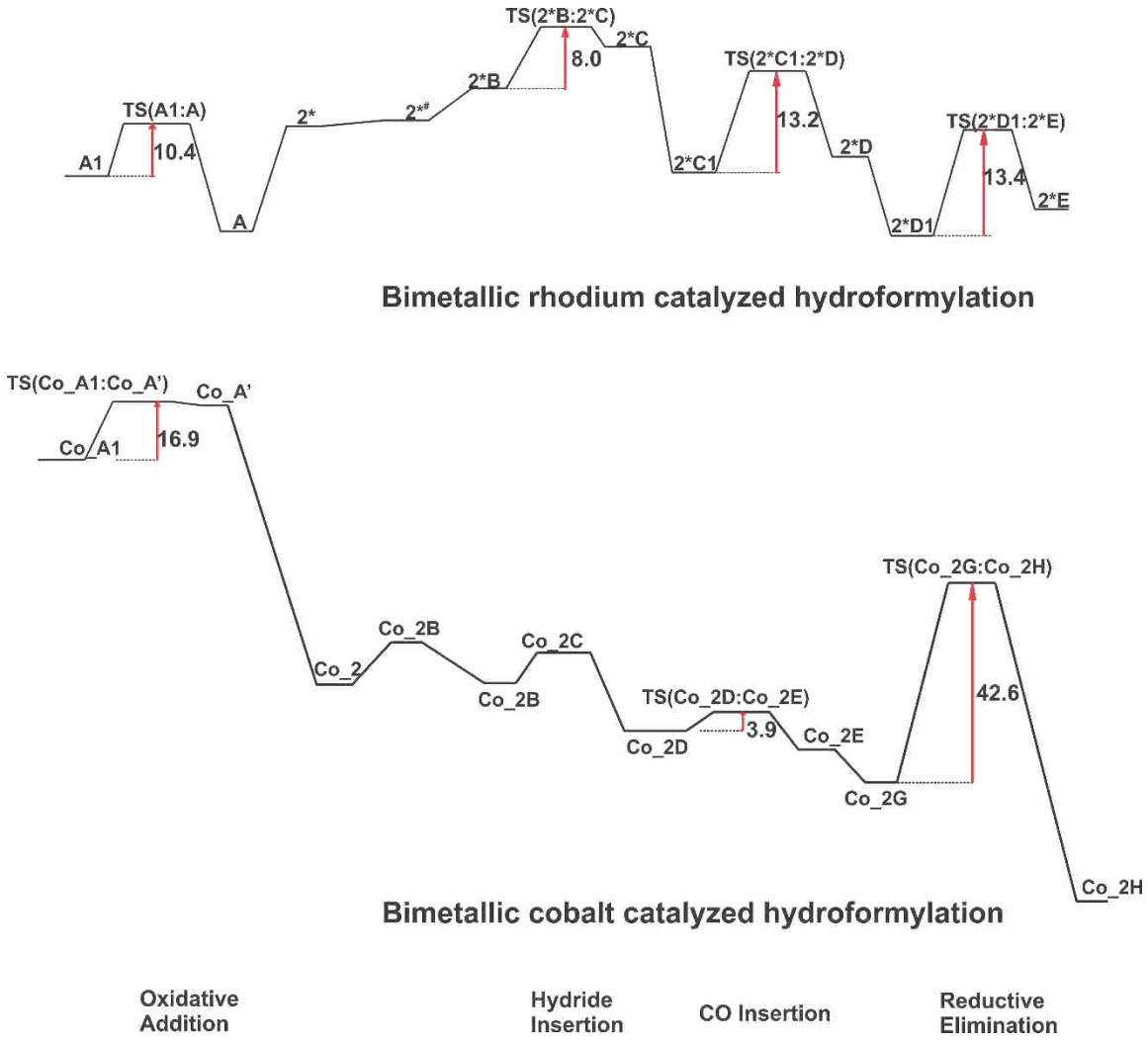

Figure 6.1. Free energy profiles for dicationic dirhodium and dicobalt catalyzed hydroformylation (Energies are shown in kcal/mol).

Even though the activation barriers for the hydride insertion step and CO insertion step are lower in cobalt catalyzed hydroformylation cycle relative to rhodium, DFT computes a larger energy barrier for the oxidative addition of H_2(g) and a significant barrier for the reductive elimination of aldehyde for the cobalt catalyzed cycle. These results suggest that the initial step and the final step of the catalytic cycle are more difficult for cobalt vs. rhodium, and indicate that the rhodium catalyzed hydroformylation is easier to do, consistent with monometallic hydroformylation.

6.2 Comparison of Rh_2 and Co_2 Aldehyde-Water Shift Catalysts

This dissertation also discusses DFT modeling of the aldehyde-water shift (AWS) reaction. The DFT studies point to an alternate mechanism that is somewhat different from Prof. Stanley's originally proposed mechanism for dirhodium catalyzed AWS. A new mechanism is proposed for dicobalt catalyzed AWS. DFT studies show that both the rhodium catalyzed and cobalt catalyzed AWS reactions in the presence of explicit water molecules are downhill by −19.6 kcal/mol and −17.9 kcal/mol. respectively.

The closed-mode tetracarbonyl complexes, **Rh_4*** and **Co_4*** formed in hydroformylation act as the active catalysts in the AWS reaction. The catalytic cycle begins with coordination of the aldehyde to one of the metal centers, followed by nucleophilic attack on the activated aldehyde by water. This results in the formation of a protonated diol. Prof. Stanley proposed that deprotonation of the diol occurred at this point, but this does not look feasible based on the DFT computations in both rhodium and cobalt systems. The energy barrier for the deprotonation of the diol reaction with an explicit water for rhodium is 41.7 kcal/mol, which is 7.8 kcal/mol higher than that seen for the cobalt catalyzed AWS. Both of these deprotonation steps do not appear to be very favorable, although the use of more than one explicit water molecule in the deprotonation step might be important and will be examined.

This step is followed by a CO dissociation to generate a vacant site for β−hydride elimination. Once the CO is dissociated the protonated diol group moves from the equatorial position to a somewhat less stable axial position, which favors β−hydride elimination and to produce a protonated carboxylic acid that dissociates. The activation barrier for this step for rhodium is 19.4 kcal/mol, while for cobalt it is 25.0 kcal/mol.

The protonated carboxylic acid readily transfers a proton to an explicit water molecule forming H_3O^+, which then reacts with the metal-hydride to produce hydrogen gas. The β-hydride elimination, formation of protonated carboxylic acid, proton-transfer to water, and H_2 loss are all semi-concerted for rhodium. However, in the dicobalt catalyzed AWS β−hydride elimination occurs prior to deprotonation of

protonated carboxylic acid. Then the deprotonation and elimination of hydrogen gas occur simultaneously.

DFT calculates the hydrogen gas production in both catalytic cycles as barrier-less steps that occur via intermediates. In both catalytic cycles the initial nucleophilic attack on the coordinated aldehyde acts as the rate-determining step. According to free energy calculations the reaction with water appears to be favorable by -0.03 kcal/mol in rhodium catalyzed AWS whereas it corresponds to an energy uphill of +6.8 kcal/mol for cobalt catalyzed AWS. The total free energy change for AWS cycles suggest that rhodium catalyzed reaction (–19.6 kcal/mol) is more favorable than the cobalt catalyzed reaction (–17.9 kcal/mol), but the lower activation energy for the rate determining aldehyde-water reaction step indicates that the dicobalt system should be faster than rhodium. The corresponding free energy profile for DFT computed rhodium catalyzed AWS and cobalt catalyzed AWS are shown below in Figure 6.2 and Figure 6.3 respectively.

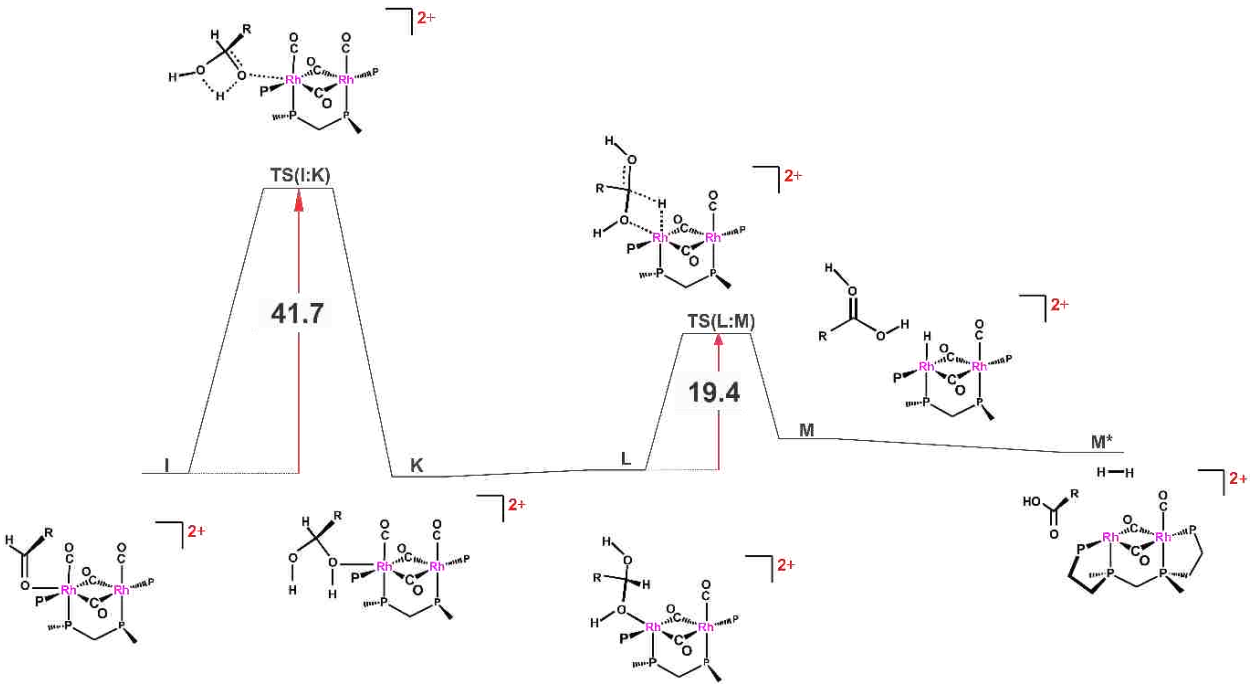

Figure 6.2. Free energy profile for dicationic rhodium catalyzed AWS reaction (for clarity P chelate ligands are not shown.). (Energies are shown in kcal/mol).

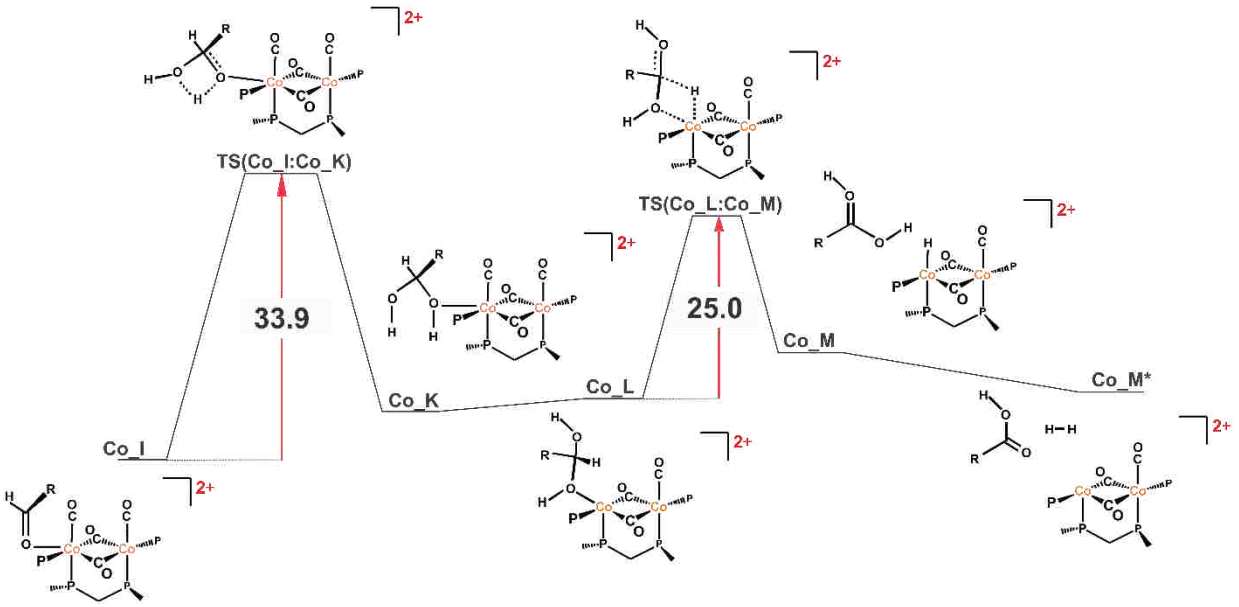

Figure 6.3. Free energy profile for dicationic cobalt catalyzed AWS reaction (for clarity P chelate ligands are not shown.). (Energies are shown in kcal/mol).

These studies were performed using only four water molecules and further studies using more water molecules will be helpful to determine whether deprotonation will be favorable via the nucleophilic attack by water. This will result in the formation of the deprotonated diol and it will undergo β–hydride elimination to generate the carboxylic acid and H_2(g).

In addition to these catalysis projects, a method was developed to calculate near and above ionization features of insulators using α–quartz as a model insulator. A finite cluster model mimicking bulk properties was generated using embedding procedure. The TD-DFT studies were performed using atom-centered basis sets and range-separated functional. As capturing excitations from core-levels to above-ionization levels is difficult for pure DFT or hybrid functional, range-separated functional were utilized. These functional fixes the incorrect behavior of exchange-correlation functional by having both short-range and long-range terms. LC-PBE0 functional was used for TD-DFT modeling studies, and functional was tuned to obtain good results that agree well with the experimental. Molecular-orbital based absorbing boundary conditions were used to remove unnecessary peaks in the spectra. Real-time TD-DFT was used to get the valence and core spectra of α–quartz and the results matched well with the experimental results.

Appendix 1 – Structural comparison of complex 5, [*rac*–$Rh_2(CO)_5$(me–P4)]$^{2+}$ optimized using different basis sets

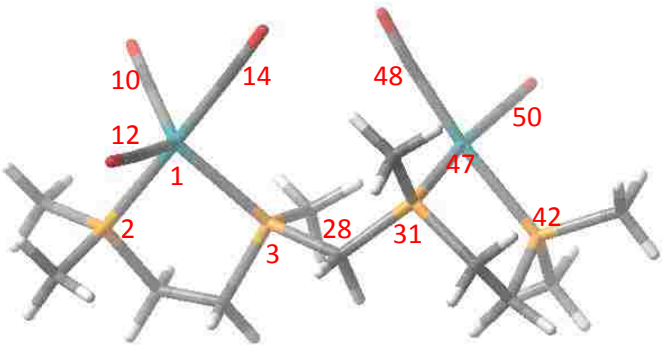

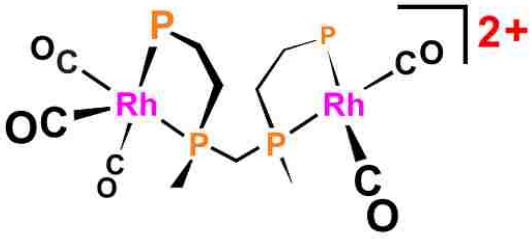

Comparison of bond lengths

	$Rh_2(CO)_5$(et,ph–P4)$^{2+}$ X-ray Bond Length (Å)	Rh 3–21G C,H,O 6–31G* P 3–21G* Bond Length (Å)	Rh Lanl2DZ C,H,O 6–311G** P 6–31G** Bond Length (Å)	Rh Lanl2DZ C,H,O,P 6–311G** Bond Length (Å)	Rh 3–21G C,H,O,P 6–311G** Bond Length (Å)
Rh1 Rh47		5.82902	6.20555	6.18364	5.87151
Rh1 P3	2.391	2.55292	2.55422	2.57405	2.56098
Rh1 P2	2.342	2.38985	2.4045	2.40633	2.39586
Rh47 P31	2.331	2.38764	2.3945	2.39723	2.3957
Rh47 P42	2.318	2.38641	2.40041	2.40233	2.39867
P3 C28		1.86469	1.87931	1.87715	1.87457
P31 C28		1.85466	1.8668	1.86385	1.86442
P2 C4		1.84213	1.85352	1.85193	1.85311
P3 C7		1.85787	1.87206	1.87086	1.86688
P31 C36		1.85217	1.86518	1.86383	1.86004
P42 C39		1.84951	1.85951	1.85846	1.85989
C4 C7		1.53486	1.53186	1.53257	1.53186
C36 C39		1.53518	1.53103	1.53138	1.53168
Rh1 C10	1.975	2.01759	1.97845	1.97566	2.03185
Rh1 C12	1.95	2.01299	1.97884	1.97556	2.02779
Rh1 C14	1.937	1.97522	1.95509	1.95647	1.98165
Rh47 C48	1.932	1.96517	1.93812	1.93812	1.97299
Rh47 C50	1.915	1.96165	1.9435	1.94314	1.97215

Comparison of bond angles

	$Rh_2(CO)_5(et,ph–P4)^{2+}$ X-ray Bond Angle (°)	Rh 3–21G C,H,O 6–31G* P 3–21G* Bond Angle (°)	Rh Lanl2DZ C,H,O 6–311G** P 6–31G** Bond Angle (°)	Rh Lanl2DZ C,H,O,P 6–311G** Bond Angle (°)	Rh 3–21G C,H,O,P 6–311G** Bond Angle (°)
C50 Rh47 C48	90.8	92.714	92.651	92.717	91.86
C50 Rh47 P42	89	89.893	89.561	89.596	90.274
C50 Rh47 P31	171.6	173.378	173.885	173.793	173.998
C48 Rh 47 P42	166.6	166.04	173.575	173.336	170.288
C48 Rh47 P31	96.5	93.906	93.401	93.431	94.112
P31 Rh47 P42	82.9	83.649	84.329	84.2	83.936
P3 C28 P31	120	120.786	124.183	123.571	121.142
C14 Rh1 C12	86.8	89.735	90.518	90.224	89.385
C14 Rh1 C10	92.6	90.764	90.405	90.424	90.511
C14 Rh1 P3	94.9	98.279	97.484	98.417	97.458
C14 Rh1 P2	174.3	177.993	178.436	177.765	178.476
C10 Rh1 C12	125.5	132.44	133.644	135.788	130.115
C12 Rh1 P3	126	116.7	116.184	115.508	116.613
C12 Rh1 P2	90	88.907	89.349	89.223	89.378
C10 Rh1 P3	108.4	110.255	109.612	108.095	112.838
C10 Rh1 P2	93.1	89.063	88.559	88.463	89.605
P2 Rh1 P3	83.2	83.653	83.971	83.774	83.894

Appendix 2 – Transition States of Rhodium Catalyzed Hydroformylation

TS(A1:A)

Frequency: –537.75 cm^{-1}

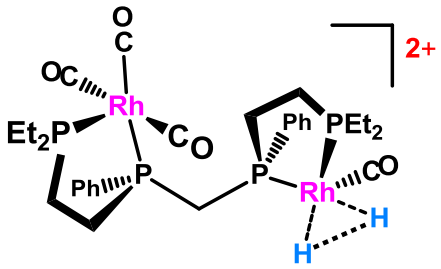

Rh	-2.6989960000	0.5871590000	0.3727810000
P	-4.1436610000	-0.8595980000	-0.8699140000
P	-0.8760210000	-0.8680530000	-0.5859630000
C	-3.0784270000	-1.7827060000	-2.0725670000
H	-3.6498590000	-2.6221100000	-2.4792850000
H	-2.8701980000	-1.1026670000	-2.9033870000
C	-1.7812350000	-2.2709640000	-1.4210150000
H	-1.1341500000	-2.7474690000	-2.1625270000
H	-1.9997200000	-3.0193170000	-0.6538400000
C	-3.2799740000	2.1368160000	-0.8072020000
O	-3.5994770000	3.0406580000	-1.4083550000
C	-3.5819240000	-0.0068210000	2.1210010000
O	-4.0662840000	-0.2771030000	3.1069660000
C	-1.4905830000	1.8028580000	1.3688490000
O	-0.8401450000	2.5204410000	1.9533300000
C	-5.4556610000	-0.0751970000	-1.8726990000
H	-5.0234290000	0.6182710000	-2.5947760000
H	-6.0227790000	-0.8416320000	-2.4062650000
H	-6.1372020000	0.4758010000	-1.2222370000
C	-5.0170510000	-2.1339050000	0.1136310000
H	-5.7248170000	-1.6533100000	0.7912690000
H	-5.5703690000	-2.8003240000	-0.5524830000
H	-4.3161450000	-2.7213970000	0.7075020000
C	0.1148430000	-0.1244130000	-1.9528370000
H	0.8455820000	0.5625410000	-1.5066130000
H	0.6374350000	-0.8932590000	-2.5276040000
H	-0.5200890000	0.4565940000	-2.6219000000
C	0.4450890000	-1.8360100000	0.3213040000
H	-0.0489360000	-2.4857950000	1.0495960000
H	0.9322990000	-2.4806050000	-0.4176280000
P	1.7976100000	-0.9140840000	1.2065810000
C	1.1569490000	-0.6048140000	2.8903490000
H	0.2956140000	0.0603980000	2.8540470000
H	0.8705930000	-1.5414420000	3.3738480000
H	1.9352680000	-0.1225380000	3.4842590000
C	3.1264400000	-2.1943540000	1.4443140000
H	3.7324840000	-1.8366030000	2.2822520000
H	2.6798370000	-3.1424890000	1.7570060000
C	3.9909920000	-2.3707660000	0.1902970000

H	3.4261790000	-2.8648750000	-0.6062220000
H	4.8510920000	-3.0097330000	0.4078670000
P	4.5695110000	-0.7318430000	-0.4826240000
C	5.1960660000	-1.1065290000	-2.1656500000
H	5.6443490000	-0.2081160000	-2.5939340000
H	5.9539460000	-1.8927790000	-2.1319420000
H	4.3787150000	-1.4252450000	-2.8144490000
Rh	2.7132200000	0.8705940000	-0.0279950000
C	3.5043240000	2.4809580000	-0.8925160000
O	3.9051750000	3.4440130000	-1.3206820000
C	6.0699060000	-0.3136080000	0.4899700000
H	6.8249310000	-1.0969190000	0.3882180000
H	6.4872650000	0.6276690000	0.1282350000
H	5.8206730000	-0.1889070000	1.5446510000
H	2.6456830000	1.6839680000	1.2665480000
H	1.4914070000	1.7897550000	0.4417730000

TS(B:C1)

Frequency: –462.78 cm^{-1}

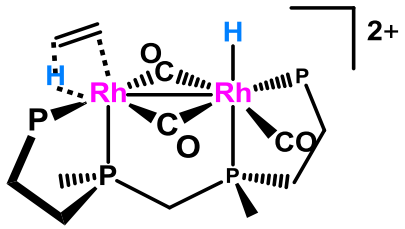

H	-1.2924690000	2.2745200000	-2.9887930000
H	3.1165060000	-0.9988930000	-2.9874560000
H	-1.2048440000	-2.3159430000	-2.8062110000
O	0.7829390000	-0.3280870000	-2.6458380000
H	4.8551960000	-0.7745770000	-2.6758050000
H	-2.9622690000	2.2293920000	-2.4205970000
C	-1.9574150000	2.5767420000	-2.1779900000
H	-1.9636960000	3.6665870000	-2.1019080000
H	-2.9734340000	-2.2889350000	-2.3341440000
H	-2.0117150000	-0.5210620000	-1.9867770000
C	3.9178140000	-1.1597390000	-2.2672470000
H	3.0191780000	1.6758060000	-1.9164150000
C	-1.9399470000	-2.3203550000	-2.0111920000
H	4.0237990000	-2.2305560000	-2.0853110000
H	-4.9519970000	-0.5770780000	-1.5750320000
H	0.6858550000	2.7719600000	-1.2885750000
C	0.5091190000	-0.4515250000	-1.5211290000
H	4.6505400000	1.7683760000	-1.2700780000
H	-4.9830410000	-2.0246950000	-0.5458960000
C	3.6208890000	1.4958430000	-1.0206740000
C	-5.0152080000	-0.9331730000	-0.5457660000
P	-1.3936760000	1.8133390000	-0.6096380000
P	3.5330650000	-0.3310600000	-0.6882850000

C	-1.6202590000	-2.8280300000	-0.7574800000
C	0.2274290000	2.6685420000	-0.3009940000
Rh	-1.3783850000	-0.5678630000	-0.4965700000
H	-0.6308700000	-3.2248530000	-0.5736980000
H	3.0822580000	3.3955590000	-0.0980950000
H	-5.9726710000	-0.6208130000	-0.1218520000
H	0.0506960000	3.6783750000	0.0806500000
H	5.8894940000	-0.4399710000	-0.1052440000
H	1.5838960000	-2.1720100000	-0.2020380000
C	3.1158480000	2.3345200000	0.1628900000
H	-2.4039550000	-3.1812030000	-0.0993980000
H	-2.7990750000	3.4454570000	0.5726450000
Rh	1.4001920000	-0.6767260000	0.3073500000
C	4.9582030000	-0.7131260000	0.3969130000
P	-3.6291280000	-0.2680700000	0.4544220000
C	-2.6150650000	2.3714460000	0.6662200000
P	1.4520580000	1.7542290000	0.7658930000
H	4.9805630000	-1.7828860000	0.6125180000
H	3.7939460000	2.2428220000	1.0166390000
H	-4.4261390000	1.8528250000	-0.4227900000
C	-3.9209800000	1.5764850000	0.5061360000
H	4.8952200000	-0.1716690000	1.3418200000
C	-0.6619840000	-0.8824370000	1.4324120000
H	-2.1770840000	2.1952040000	1.6527520000
H	-3.8735990000	-1.9429020000	2.2050560000
C	-3.9959800000	-0.8595330000	2.1519620000
C	2.1501290000	-1.4339570000	2.0653730000
H	1.4210240000	3.5862020000	2.4016150000
H	-4.6105810000	1.8089290000	1.3211320000
C	1.2677070000	2.5049230000	2.4305630000
H	-5.0270900000	-0.6110750000	2.4134560000
O	-0.8649490000	-1.0686240000	2.5450630000
H	-3.3232450000	-0.4063130000	2.8795770000
H	0.2745790000	2.2956090000	2.8319650000
H	1.9997580000	2.0623760000	3.1087650000
O	2.6579280000	-1.9613370000	2.9240960000

TS(C2:D1)

Frequency: –302.13 cm^{-1}

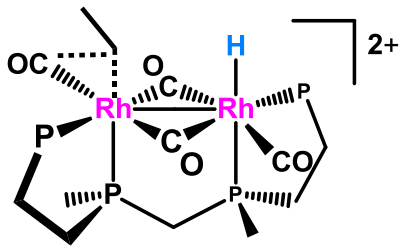

Rh	1.5069520000	-0.5323760000	0.5424320000
P	3.5929990000	-0.7762040000	-0.5703060000
P	1.7836900000	1.8878410000	0.0902280000

C	3.7937880000	0.7863070000	-1.5577040000
H	4.8210490000	0.8477960000	-1.9285210000
H	3.1454800000	0.6810810000	-2.4322030000
C	3.4360120000	2.0457770000	-0.7539140000
H	3.4570970000	2.9325520000	-1.3928930000
H	4.1668190000	2.2154050000	0.0423870000
C	3.8081400000	-2.1567620000	-1.7431210000
H	2.9824770000	-2.1860330000	-2.4531730000
H	4.7487160000	-2.0423250000	-2.2873910000
H	3.8328740000	-3.0938900000	-1.1845880000
C	5.0466260000	-0.8700720000	0.5389400000
H	4.9990910000	-1.7854110000	1.1316200000
H	5.9638910000	-0.8881110000	-0.0546530000
H	5.0830300000	-0.0182110000	1.2192010000
C	0.5482750000	2.4738030000	-1.1779550000
H	0.4862640000	3.5661090000	-1.1874930000
H	0.9291630000	2.1618940000	-2.1546160000
P	-1.1554010000	1.7354890000	-1.0653350000
C	-1.8322410000	1.9974240000	-2.7481590000
H	-1.7756090000	3.0498690000	-3.0359540000
H	-1.2700840000	1.3963820000	-3.4652580000
H	-2.8731240000	1.6736020000	-2.7847490000
C	-2.1755740000	2.7983570000	0.0561510000
H	-1.6405100000	2.8919780000	1.0050980000
H	-2.2822950000	3.8033170000	-0.3621380000
C	-3.5534630000	2.1537920000	0.2746890000
H	-4.1518870000	2.2200340000	-0.6375140000
H	-4.1045580000	2.6910630000	1.0503610000
P	-3.4712580000	0.3416110000	0.7410160000
C	-4.9973930000	-0.3596730000	0.0031710000
H	-4.9493630000	-0.3351900000	-1.0861240000
H	-5.1277800000	-1.3941960000	0.3216370000
H	-5.8651900000	0.2168000000	0.3329440000
Rh	-1.3138130000	-0.4851890000	-0.1713510000
C	-3.7921040000	0.2749650000	2.5457430000
H	-4.7724660000	0.7066460000	2.7606420000
H	-3.7855350000	-0.7637890000	2.8812900000
H	-3.0311030000	0.8202990000	3.1025070000
C	-0.4792840000	-0.0807190000	1.7164650000
O	-0.6266760000	0.2341200000	2.8092820000
C	0.5524180000	-0.8284700000	-1.2291740000
O	0.7660780000	-1.0659320000	-2.3484590000
C	1.7909140000	3.1932330000	1.3795990000
H	2.5529350000	2.9565840000	2.1246920000
H	2.0055260000	4.1761760000	0.9539240000
H	0.8270910000	3.2278690000	1.8900940000
H	1.5261270000	-2.1222180000	0.5801890000
C	2.2994080000	-0.6957060000	2.4328360000
O	2.8130060000	-0.9274320000	3.4102140000
C	-1.7018640000	-2.8861860000	-0.0899410000
C	-3.0200570000	-3.5443430000	0.2484390000
H	-1.0679750000	-2.7445360000	0.7808470000
H	-1.1227880000	-3.4046160000	-0.8507290000
H	-3.5366320000	-3.0461130000	1.0703140000
H	-3.6933660000	-3.6173100000	-0.6070080000
H	-2.8105940000	-4.5680810000	0.5800330000

C	-2.1962500000	-1.5262270000	-1.5404090000
O	-2.7989780000	-1.8556410000	-2.4572140000

TS(D2:G)

Frequency: –640.31 cm^{-1}

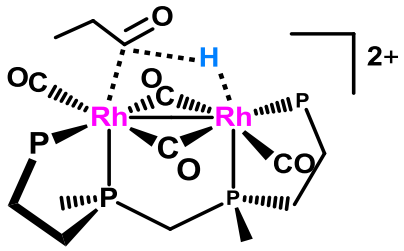

Rh	1.3825510000	0.4928750000	-0.4006870000
P	3.5332940000	0.5324750000	0.7350840000
P	1.8051670000	-1.9015710000	-0.6476510000
C	3.7911180000	-1.2344920000	1.2605130000
H	4.8267340000	-1.3684770000	1.5854860000
H	3.1588460000	-1.3902770000	2.1376010000
C	3.4524890000	-2.2422790000	0.1513870000
H	3.4843750000	-3.2667470000	0.5310710000
H	4.1870130000	-2.1858950000	-0.6574310000
C	3.7542990000	1.5335810000	2.2489220000
H	2.9565990000	1.3230800000	2.9604400000
H	4.7184670000	1.3116160000	2.7126320000
H	3.7250090000	2.5920970000	1.9850730000
C	4.9798090000	0.9507160000	-0.3132250000
H	4.9173110000	1.9943230000	-0.6276590000
H	5.9061970000	0.8131860000	0.2495440000
H	5.0140420000	0.3258450000	-1.2069670000
C	0.5388430000	-2.9668710000	0.2291460000
H	0.4699530000	-3.9212940000	-0.2997770000
H	0.9386450000	-3.1750980000	1.2249540000
P	-1.1801270000	-2.2823280000	0.5394470000
C	-1.7439050000	-3.2691250000	1.9832850000
H	-1.6662830000	-4.3424400000	1.7955100000
H	-1.1472420000	-3.0113580000	2.8602240000
H	-2.7844780000	-3.0233850000	2.2023580000
C	-2.2954160000	-2.7808360000	-0.8574510000
H	-1.7892950000	-2.5480200000	-1.7966720000
H	-2.4813180000	-3.8580410000	-0.8412020000
C	-3.6303600000	-2.0150630000	-0.7613540000
H	-4.1935500000	-2.3508270000	0.1137140000
H	-4.2493780000	-2.2402520000	-1.6335500000
P	-3.4787570000	-0.1479240000	-0.6035230000
C	-4.9669550000	0.3145870000	0.3683680000
H	-4.9107140000	-0.0920020000	1.3789770000
H	-5.0415970000	1.4013380000	0.4365290000
H	-5.8698010000	-0.0661620000	-0.1150360000
Rh	-1.2823110000	0.1795270000	0.4664740000

C	-3.8525460000	0.5108750000	-2.2771350000
H	-4.8284660000	0.1505350000	-2.6107530000
H	-3.8794480000	1.6016010000	-2.2393360000
H	-3.0938970000	0.2034050000	-2.9954920000
C	-0.4975710000	0.0272690000	-1.3939750000
O	-0.7380660000	-0.2345620000	-2.5008940000
C	0.5289240000	0.0476430000	1.4648500000
O	0.8985490000	-0.1813800000	2.5436950000
C	1.9348880000	-2.6159480000	-2.3309910000
H	2.7013050000	-2.0778340000	-2.8918210000
H	2.2048840000	-3.6737190000	-2.2910210000
H	0.9881040000	-2.5058930000	-2.8616700000
H	1.0181350000	2.0684880000	-0.0269730000
C	2.1008550000	1.1778000000	-2.2036340000
O	2.5787620000	1.6243910000	-3.1233970000
C	-2.1486750000	0.8553300000	2.1972870000
O	-2.6751430000	1.1659760000	3.1473280000
C	-0.4403450000	2.8185690000	0.3436340000
O	-0.3420230000	3.2111480000	1.4351740000
C	-0.8830580000	3.4617150000	-0.9429430000
H	-0.0480660000	4.1172330000	-1.2240030000
H	-0.9886760000	2.7066930000	-1.7172860000
C	-2.1665990000	4.2754570000	-0.7316460000
H	-2.0239700000	5.0553010000	0.0161670000
H	-2.4410240000	4.7487380000	-1.6759190000
H	-2.9942830000	3.6382210000	-0.4139530000

TS(D2$^{\#}$:G$^{\#}$)

Frequency: –870.56 cm^{-1}

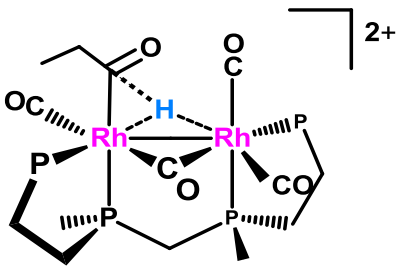

Rh	-1.4060050000	0.4462400000	0.4393290000
P	-3.6413480000	0.4491450000	-0.4516310000
P	-1.7084950000	-1.9274410000	0.3902080000
C	-3.9481010000	-1.2481110000	-1.1282700000
H	-5.0136870000	-1.3749810000	-1.3383830000
H	-3.4192360000	-1.3041180000	-2.0839540000
C	-3.4461940000	-2.3112140000	-0.1511960000
H	-3.4858420000	-3.3122680000	-0.5882950000
H	-4.0622270000	-2.3337200000	0.7521280000
C	-3.9924180000	1.5933570000	-1.8330790000
H	-3.2393750000	1.4781210000	-2.6131780000
H	-4.9803280000	1.3804250000	-2.2487850000
H	-3.9793550000	2.6248070000	-1.4773930000

C	-4.9588400000	0.7522860000	0.7854930000
H	-4.8521350000	1.7586820000	1.1944170000
H	-5.9445750000	0.6665430000	0.3212450000
H	-4.8861340000	0.0409690000	1.6093070000
C	-0.6397030000	-2.8155310000	-0.8295420000
H	-0.6960300000	-3.8978310000	-0.6770440000
H	-1.0448720000	-2.5993290000	-1.8224090000
P	1.1144430000	-2.2143090000	-0.8470580000
C	1.7677920000	-2.9100980000	-2.4159210000
H	1.5940360000	-3.9871490000	-2.4725780000
H	1.2872240000	-2.4231930000	-3.2664680000
H	2.8411420000	-2.7221820000	-2.4797970000
C	2.0179570000	-3.1346430000	0.4871120000
H	1.3860170000	-3.1563220000	1.3774470000
H	2.1873560000	-4.1708580000	0.1812350000
C	3.3392280000	-2.4204710000	0.7861150000
H	4.0210140000	-2.4996250000	-0.0656800000
H	3.8449280000	-2.8803760000	1.6394140000
P	3.0975970000	-0.6002110000	1.1095530000
C	4.8194930000	0.0373630000	1.0157210000
H	5.1659440000	0.0371600000	-0.0192490000
H	4.8735280000	1.0545650000	1.4026780000
H	5.4859070000	-0.5919930000	1.6106590000
Rh	1.3456970000	0.1618460000	-0.4617380000
C	2.7006110000	-0.4994750000	2.9025670000
H	3.4848730000	-0.9661040000	3.5032780000
H	2.6094020000	0.5467090000	3.2002430000
H	1.7500150000	-0.9922590000	3.1096700000
C	-1.5748500000	2.4442200000	0.4150190000
O	-1.8329410000	3.5403420000	0.4955970000
C	-0.4456610000	0.4323930000	-1.4904540000
O	-0.8607110000	0.4788870000	-2.5721670000
C	-1.5242930000	-2.8319980000	1.9740080000
H	-2.2612980000	-2.4567300000	2.6863390000
H	-1.6910300000	-3.9019270000	1.8287290000
H	-0.5343260000	-2.6768350000	2.4013640000
H	0.8641670000	1.2700530000	0.6810580000
C	-1.3867290000	0.4769590000	2.5844210000
O	-1.4467840000	0.5997540000	3.7053020000
C	2.5254920000	0.4860440000	-2.1900540000
O	3.0912050000	0.7166990000	-3.1395540000
C	1.5406900000	2.4257620000	-0.2124680000
O	0.7377150000	3.0701330000	-0.8047680000
C	2.8211310000	2.9610070000	0.3848420000
H	2.8536640000	2.6272410000	1.4279020000
H	3.6467260000	2.4469750000	-0.1178740000
C	2.9609970000	4.4800810000	0.2702850000
H	2.1492910000	4.9945330000	0.7865390000
H	3.9045270000	4.7952620000	0.7189350000
H	2.9541360000	4.8000290000	-0.7720480000

TS(2*B:2*C)

Frequency: –904.23 cm^{-1}

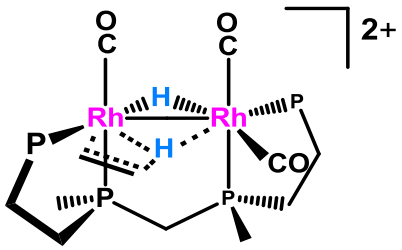

Rh	1.3972070000	-0.4807170000	0.4686270000
P	3.4483760000	-0.1700180000	-0.7412680000
P	1.4224530000	1.8816350000	0.5816090000
C	3.5887080000	1.6381710000	-1.1609460000
H	4.6282990000	1.8848960000	-1.3936950000
H	3.0091510000	1.8015120000	-2.0742110000
C	3.0662210000	2.5077820000	-0.0151390000
H	2.9946990000	3.5598770000	-0.3039700000
H	3.7396950000	2.4580650000	0.8455260000
C	3.7596720000	-1.0320270000	-2.3303910000
H	2.9653170000	-0.8071750000	-3.0432820000
H	4.7184860000	-0.7229910000	-2.7540720000
H	3.7864870000	-2.1109490000	-2.1671290000
C	4.9418000000	-0.5369230000	0.2619340000
H	4.9615670000	-1.5992190000	0.5124470000
H	5.8519260000	-0.2885150000	-0.2894770000
H	4.9198160000	0.0276210000	1.1952580000
C	0.1950020000	2.6699330000	-0.5642680000
H	0.0709750000	3.7351370000	-0.3432260000
H	0.6178050000	2.5923190000	-1.5702640000
P	-1.4505790000	1.8325160000	-0.6611620000
C	-2.1831040000	2.5947700000	-2.1618530000
H	-2.1526870000	3.6841680000	-2.0848020000
H	-1.6284610000	2.2936340000	-3.0520910000
H	-3.2210000000	2.2822240000	-2.2822510000
C	-2.4972950000	2.4534590000	0.7338380000
H	-1.9336370000	2.3264530000	1.6605690000
H	-2.7009110000	3.5208430000	0.6112430000
C	-3.7964360000	1.6397960000	0.7786360000
H	-4.4256980000	1.8649610000	-0.0864910000
H	-4.3806010000	1.8847630000	1.6692780000
P	-3.4492410000	-0.1880480000	0.7479770000
C	-4.9954790000	-0.9605450000	0.1468470000
H	-5.1770840000	-0.6725100000	-0.8894190000
H	-4.9102840000	-2.0476280000	0.1956000000
H	-5.8434480000	-0.6500170000	0.7624660000
Rh	-1.4486110000	-0.5293150000	-0.5099660000
C	-3.3076410000	-0.6912260000	2.5036270000
H	-4.2244110000	-0.4497120000	3.0465700000
H	-3.1362460000	-1.7671730000	2.5677150000
H	-2.4628070000	-0.1845990000	2.9712970000

C	1.1692510000	2.7098310000	2.1960930000
H	1.9434950000	2.3782570000	2.8902970000
H	1.2276030000	3.7959940000	2.0951450000
H	0.2026370000	2.4379630000	2.6207570000
C	1.7426490000	-0.7381910000	2.5525210000
O	2.1197790000	-1.0871950000	3.5602730000
H	-0.4076110000	-0.3708590000	0.8977260000
C	-1.5921240000	-2.4700640000	-0.1259540000
O	-1.7030140000	-3.5705030000	0.1053790000
H	0.0487320000	-0.6321590000	-1.4119250000
C	1.5430180000	-2.3955660000	0.1079960000
O	1.6580420000	-3.5057900000	-0.0962010000
C	-0.7059730000	-0.8607370000	-2.7282250000
C	-2.1226980000	-0.8832580000	-2.6294450000
H	-0.2413040000	-0.0071340000	-3.2117910000
H	-2.6948220000	-0.0385470000	-2.9868550000
H	-2.6373410000	-1.8337930000	-2.6797380000
H	-0.1922050000	-1.7988590000	-2.9115330000

TS(2*C1:2*D)

Frequency: –336.65 cm^{-1}

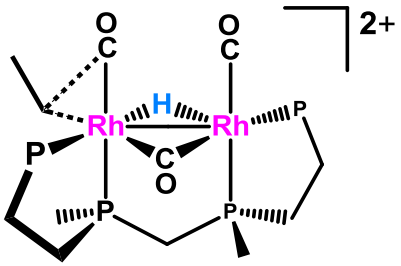

Rh	-1.4060660000	-0.3724390000	-0.6131210000
P	-3.7128380000	-0.4070900000	0.0077460000
P	-1.5779830000	1.9392300000	-0.1186490000
C	-3.9363800000	1.0665790000	1.1169240000
H	-5.0001900000	1.2320120000	1.3090170000
H	-3.4728510000	0.8054640000	2.0726380000
C	-3.2878030000	2.3197290000	0.5169970000
H	-3.2522740000	3.1362700000	1.2420780000
H	-3.8642500000	2.6812940000	-0.3389070000
C	-4.2632400000	-1.8400210000	1.0001400000
H	-3.5917360000	-1.9829030000	1.8476060000
H	-5.2797340000	-1.6782930000	1.3670860000
H	-4.2533380000	-2.7424650000	0.3863760000
C	-4.9434720000	-0.2335330000	-1.3402750000
H	-4.8990870000	-1.1107410000	-1.9885540000
H	-5.9525250000	-0.1522990000	-0.9286630000
H	-4.7318130000	0.6474540000	-1.9479690000
C	-0.3950890000	2.5630150000	1.1642250000
H	-0.3545150000	3.6559680000	1.1421380000
H	-0.8012520000	2.2681400000	2.1365320000
P	1.3068590000	1.8166640000	1.0707840000

C	2.0276000000	2.2084150000	2.7148030000
H	1.9616700000	3.2747750000	2.9417240000
H	1.5069450000	1.6436450000	3.4905390000
H	3.0788090000	1.9130820000	2.7301600000
C	2.2840320000	2.8423760000	-0.1352700000
H	1.6470830000	3.0580070000	-0.9960060000
H	2.5579960000	3.8013250000	0.3125970000
C	3.5364860000	2.0725060000	-0.5788210000
H	4.2307770000	1.9538760000	0.2582510000
H	4.0722120000	2.6219300000	-1.3579400000
P	3.1419630000	0.3588380000	-1.1947770000
C	4.7483870000	-0.5192630000	-1.1786650000
H	5.1233420000	-0.6139250000	-0.1586630000
H	4.6301890000	-1.5172930000	-1.6048340000
H	5.4825610000	0.0283950000	-1.7745530000
Rh	1.3501870000	-0.4743820000	0.1851010000
C	2.7358830000	0.5455200000	-2.9726830000
H	3.5802090000	0.9765590000	-3.5158710000
H	2.5043970000	-0.4330440000	-3.3966860000
H	1.8606340000	1.1840930000	-3.0954460000
C	-1.3673120000	3.0321880000	-1.5763080000
H	-2.1038370000	2.7627770000	-2.3354020000
H	-1.5132400000	4.0797350000	-1.3014800000
H	-0.3767410000	2.9087960000	-2.0131740000
C	-1.4181090000	-2.2697300000	-1.2550210000
O	-1.4117210000	-3.3213300000	-1.6643120000
H	0.3023670000	-0.0719740000	-1.1436800000
C	1.8495800000	-2.3196930000	-0.0683030000
O	1.9539370000	-3.3859400000	-0.4828150000
H	1.2087240000	-2.5496440000	3.0186370000
C	-0.4108880000	-0.8652380000	1.1980700000
O	-0.9314950000	-1.1636750000	2.1863600000
C	2.1745710000	-2.8545030000	2.6152120000
C	2.7434560000	-1.8404710000	1.6413910000
H	2.8666280000	-2.9465910000	3.4593500000
H	2.8485740000	-0.8543060000	2.0910400000
H	3.7049450000	-2.1230100000	1.2192540000
H	2.0718870000	-3.8444580000	2.1687920000

TS(2*D1:2*E)

Frequency: –887.54 cm^{-1}

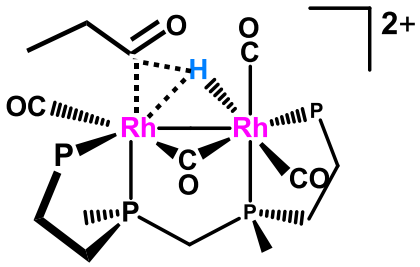

Rh	-1.4248680000	0.3919850000	0.3648040000
P	-3.6487670000	-0.0004870000	-0.4855260000
P	-1.3921970000	-2.0019520000	0.5323300000
C	-3.7777570000	-1.8044770000	-0.8946260000
H	-4.8299560000	-2.0790840000	-1.0095600000
H	-3.2996010000	-1.9463590000	-1.8681250000
C	-3.1011060000	-2.6468890000	0.1865770000
H	-3.0506600000	-3.7015530000	-0.0965290000
H	-3.6576460000	-2.5953150000	1.1267710000
C	-4.1285410000	0.8809020000	-2.0132550000
H	-3.3693850000	0.7334430000	-2.7819960000
H	-5.0892240000	0.5061520000	-2.3749080000
H	-4.2267550000	1.9491940000	-1.8129320000
C	-4.9871800000	0.3392440000	0.7196840000
H	-5.0014650000	1.4026370000	0.9655970000
H	-5.9573260000	0.0661210000	0.2969760000
H	-4.8269850000	-0.2214530000	1.6415610000
C	-0.3303450000	-2.8827520000	-0.6997030000
H	-0.2995090000	-3.9544340000	-0.4797110000
H	-0.8035260000	-2.7590120000	-1.6780940000
P	1.3656810000	-2.1481660000	-0.8412240000
C	1.9923050000	-2.8156180000	-2.4317620000
H	1.9053970000	-3.9039810000	-2.4665570000
H	1.4345290000	-2.3818460000	-3.2636690000
H	3.0426660000	-2.5414990000	-2.5485020000
C	2.4076550000	-2.9619480000	0.4651790000
H	1.7935600000	-3.0904060000	1.3583870000
H	2.7075660000	-3.9595300000	0.1325900000
C	3.6282240000	-2.0882720000	0.7781600000
H	4.3192540000	-2.0760620000	-0.0698680000
H	4.1826970000	-2.4873990000	1.6316020000
P	3.1420110000	-0.3200940000	1.1018930000
C	4.7216300000	0.5999030000	0.9797940000
H	5.1088350000	0.5528000000	-0.0392660000
H	4.5545600000	1.6431190000	1.2472430000
H	5.4622970000	0.1739230000	1.6609190000
Rh	1.3533620000	0.2326680000	-0.4859740000
C	2.7063830000	-0.2316090000	2.8809190000
H	3.5403810000	-0.5664480000	3.5022740000
H	2.4743610000	0.8053910000	3.1269400000
H	1.8306460000	-0.8450500000	3.0947370000
C	-0.9709330000	-2.7110730000	2.1686930000
H	-1.7122730000	-2.3807890000	2.8984610000
H	-0.9802010000	-3.8029980000	2.1322140000
H	0.0067460000	-2.3671550000	2.5029520000
C	-1.8328280000	2.3271580000	0.1418470000
O	-2.1799380000	3.4015630000	0.0743170000
H	0.5290700000	1.2749840000	0.5924240000
C	1.5175280000	2.4001520000	0.2746540000
O	2.1605460000	2.6291120000	1.2512830000
H	0.2173140000	4.9557820000	0.4743580000
C	-0.3940230000	0.3419350000	-1.5769700000
O	-0.8359750000	0.3215910000	-2.6494200000
C	1.0406790000	4.8554460000	-0.2352380000
C	1.1521040000	3.4269070000	-0.7778960000
H	0.8615660000	5.5460660000	-1.0607740000

H	0.2613690000	3.1137130000	-1.3232530000
H	1.9717670000	3.3643200000	-1.5054460000
H	1.9595520000	5.1538530000	0.2688540000
C	-1.5172410000	0.6303650000	2.5281870000
O	-1.6589090000	0.9289210000	3.6064980000
C	2.6018290000	0.6989770000	-2.0937820000
O	3.2376470000	0.8712970000	-3.0124120000

TS(M:P)

Frequency: –685.85 cm^{-1}

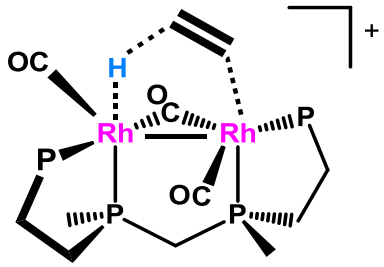

Rh	1.4473350000	-0.6391370000	0.4322940000
P	3.6186980000	0.1158450000	-0.3088560000
P	1.1431530000	1.6972820000	0.9646080000
C	3.6277630000	1.9794210000	-0.3061890000
H	4.6556960000	2.3514610000	-0.2726600000
H	3.2036070000	2.3025550000	-1.2619020000
C	2.8084130000	2.5275600000	0.8688140000
H	2.6987300000	3.6139260000	0.8076180000
H	3.3086050000	2.3075400000	1.8167570000
C	4.2897690000	-0.3292150000	-1.9600520000
H	3.5648470000	-0.0668580000	-2.7308880000
H	5.2373950000	0.1788860000	-2.1545410000
H	4.4532360000	-1.4078090000	-2.0027440000
C	4.9783010000	-0.3267060000	0.8502330000
H	5.0858050000	-1.4122600000	0.8836560000
H	5.9272270000	0.1161100000	0.5374420000
H	4.7336060000	0.0144740000	1.8572740000
C	0.1479400000	2.6628040000	-0.2765000000
H	-0.0440410000	3.6783810000	0.0831480000
H	0.7688550000	2.7408680000	-1.1736380000
P	-1.4230330000	1.8332370000	-0.8217790000
C	-1.8045220000	2.7099870000	-2.3974340000
H	-1.8011740000	3.7958430000	-2.2723020000
H	-1.0703050000	2.4306680000	-3.1550360000
H	-2.7858930000	2.3928860000	-2.7543850000
C	-2.7386100000	2.4437690000	0.3439080000
H	-2.3451080000	2.3617340000	1.3604020000
H	-2.9596560000	3.4990280000	0.1594230000
C	-3.9926130000	1.5728150000	0.1858250000
H	-4.4362530000	1.7228630000	-0.8027440000
H	-4.7531430000	1.8376920000	0.9248990000

P	-3.5574880000	-0.2392000000	0.3165020000
C	-4.9811460000	-1.0784810000	-0.4945310000
H	-4.9953500000	-0.8409380000	-1.5594150000
H	-4.8766860000	-2.1600330000	-0.3860530000
H	-5.9290160000	-0.7727320000	-0.0451600000
Rh	-1.3796630000	-0.4859010000	-0.7436060000
C	-3.8245690000	-0.6131620000	2.1015670000
H	-4.8259270000	-0.3078030000	2.4148680000
H	-3.7146110000	-1.6853490000	2.2697650000
H	-3.0721370000	-0.1101090000	2.7079000000
C	0.5038360000	2.2283310000	2.6004370000
H	1.1810530000	1.8563380000	3.3713960000
H	0.4400000000	3.3166360000	2.6709660000
H	-0.4680760000	1.7748010000	2.7855700000
C	1.9505530000	-2.4776960000	0.1617350000
O	2.2769970000	-3.5595410000	0.0135270000
C	-1.4760390000	-2.8071300000	-0.7953730000
C	-1.4040510000	-3.3429790000	0.4927670000
H	-0.7308080000	-3.1339270000	-1.5099110000
H	-0.6535900000	-4.0921980000	0.7329300000
H	-2.2862040000	-3.3653020000	1.1258000000
H	-2.4610010000	-2.6224360000	-1.2223790000
C	-0.1641130000	-1.2358080000	1.6703550000
O	-0.6195120000	-0.6960960000	2.6267070000
C	0.2294430000	-0.5531210000	-1.7913780000
O	0.9531520000	-0.5712070000	-2.6866890000
H	-0.6021380000	-2.3433040000	1.3924240000

TS(O:N)

Frequency: –898.98 cm^{-1}

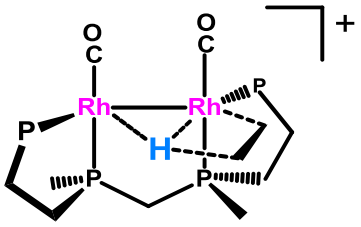

Rh	1.4376160000	-0.5432370000	0.1669180000
P	3.5251220000	0.3480910000	-0.4918340000
P	0.9711340000	1.7020260000	0.8259690000
C	3.4625310000	2.2044380000	-0.3327070000
H	4.4763710000	2.6063270000	-0.2506190000
H	3.0378020000	2.5880090000	-1.2650040000
C	2.6008130000	2.6148400000	0.8637420000
H	2.4385720000	3.6959350000	0.8893270000
H	3.0913910000	2.3379530000	1.8017950000
C	4.1531540000	0.0826560000	-2.1990190000
H	3.4055330000	0.4187950000	-2.9187680000
H	5.0873510000	0.6256020000	-2.3636050000
H	4.3315950000	-0.9814690000	-2.3627940000

C	4.9532080000	-0.1401500000	0.5619600000
H	5.1024520000	-1.2193870000	0.4952630000
H	5.8690630000	0.3662820000	0.2470420000
H	4.7437910000	0.1030450000	1.6046750000
C	-0.0423490000	2.7398180000	-0.3325370000
H	-0.2246420000	3.7495810000	0.0516730000
H	0.5431700000	2.8305920000	-1.2523190000
P	-1.5861130000	1.8111540000	-0.7897270000
C	-2.0780790000	2.6102660000	-2.3796760000
H	-2.1183350000	3.6992290000	-2.2985800000
H	-1.3664190000	2.3381060000	-3.1615830000
H	-3.0615220000	2.2415950000	-2.6784480000
C	-2.8848730000	2.4180050000	0.4063350000
H	-2.4071170000	2.5302490000	1.3820850000
H	-3.2520590000	3.4050830000	0.1113440000
C	-4.0348480000	1.4046300000	0.4936730000
H	-4.6028850000	1.3944590000	-0.4415860000
H	-4.7345070000	1.6704150000	1.2911510000
P	-3.3978170000	-0.3316290000	0.7464410000
C	-4.8505900000	-1.3820310000	0.3367340000
H	-5.0891200000	-1.2852750000	-0.7230870000
H	-4.6072000000	-2.4269310000	0.5387230000
H	-5.7239940000	-1.1022960000	0.9310810000
Rh	-1.4083420000	-0.5603320000	-0.4992450000
C	-3.2801840000	-0.5136080000	2.5744430000
H	-4.2487690000	-0.3534960000	3.0541890000
H	-2.9267250000	-1.5185150000	2.8125970000
H	-2.5581890000	0.1973420000	2.9778780000
C	0.2935750000	2.0452970000	2.4979700000
H	0.9511740000	1.5807500000	3.2344780000
H	0.2336430000	3.1186930000	2.6937850000
H	-0.6919180000	1.5964700000	2.6072080000
C	1.8423600000	-1.2661180000	2.1569210000
O	2.5165170000	-1.9408420000	2.7807930000
C	-2.3800120000	-1.4819860000	-2.3569470000
C	-1.0419070000	-1.3198470000	-2.7472800000
H	-2.7356160000	-2.4584920000	-2.0563330000
H	-0.4085920000	-2.1979800000	-2.8044470000
H	-0.7983020000	-0.5428630000	-3.4644200000
C	1.8578210000	-2.1795750000	-0.7679140000
O	2.1641410000	-3.1225810000	-1.3339800000
H	-3.1309870000	-0.7940290000	-2.7237490000
C	-0.8223590000	-2.1050770000	0.5188680000
O	-0.8024860000	-3.0880310000	1.1147800000
H	-0.1421380000	-0.6755340000	-1.6270830000

TS(P:SI)

Frequency: –267.29 cm^{-1}

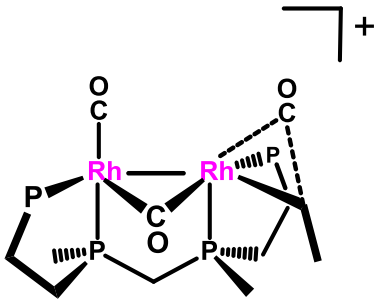

Rh	1.3546080000	-0.5230090000	0.3754580000
P	3.7224890000	-0.5507100000	0.0876770000
P	1.6128290000	1.8007670000	0.0398090000
C	3.9950300000	0.8453040000	-1.1201130000
H	5.0642300000	1.0042600000	-1.2892110000
H	3.5626710000	0.4985660000	-2.0628630000
C	3.3134410000	2.1473080000	-0.6699500000
H	3.2405510000	2.8561810000	-1.4977220000
H	3.8971410000	2.6358720000	0.1145410000
C	4.3967600000	-2.0021510000	-0.8134760000
H	3.7934110000	-2.1832210000	-1.7042630000
H	5.4364680000	-1.8364840000	-1.1067040000
H	4.3449680000	-2.8871010000	-0.1768530000
C	4.9593910000	-0.2628010000	1.4246930000
H	4.9152470000	-1.0894620000	2.1363700000
H	5.9741600000	-0.1947310000	1.0237320000
H	4.7258270000	0.6562130000	1.9646830000
C	0.3951470000	2.6407900000	-1.0815000000
H	0.4103880000	3.7274130000	-0.9582590000
H	0.7014380000	2.4110580000	-2.1065200000
P	-1.3098500000	1.9159680000	-0.8826060000
C	-2.2039700000	2.5940170000	-2.3460750000
H	-2.1096490000	3.6796210000	-2.4213080000
H	-1.8138380000	2.1361590000	-3.2572150000
H	-3.2618710000	2.3352300000	-2.2650640000
C	-2.0755760000	2.8241930000	0.5604960000
H	-1.2867620000	3.0356740000	1.2843110000
H	-2.4731510000	3.7880130000	0.2313040000
C	-3.1722190000	1.9686930000	1.2116270000
H	-4.0220960000	1.8616420000	0.5306410000
H	-3.5457590000	2.4454110000	2.1227670000
P	-2.5768240000	0.2361100000	1.5727080000
C	-4.1215310000	-0.6398870000	2.0529710000
H	-4.7974780000	-0.6962970000	1.1994780000
H	-3.8775030000	-1.6595740000	2.3571710000
H	-4.6245150000	-0.1346660000	2.8811810000
Rh	-1.3373500000	-0.4417460000	-0.3809740000
C	-1.7157190000	0.3928200000	3.1982660000
H	-2.3707550000	0.8255230000	3.9594430000
H	-1.4009850000	-0.6001010000	3.5249220000

H	-0.8208080000	1.0069800000	3.0953560000
C	1.6079030000	2.8038200000	1.5850960000
H	1.7980440000	3.8587740000	1.3728540000
H	0.6579290000	2.7096660000	2.1095860000
H	2.3912600000	2.4292780000	2.2462450000
C	1.1129370000	-2.3946960000	0.8571120000
O	0.9927490000	-3.4696180000	1.2095260000
C	-2.8932270000	-1.3753710000	-1.9946160000
C	-4.3700360000	-1.5729960000	-1.7135930000
H	-2.4591770000	-2.1772470000	-2.5885640000
H	-4.9185190000	-1.6829850000	-2.6569780000
H	-4.8057390000	-0.7192820000	-1.1886110000
H	-2.6958170000	-0.4400230000	-2.5125150000
C	-1.9490290000	-2.2514950000	-0.3337430000
O	-2.2355810000	-3.3435800000	-0.1008330000
C	0.3306810000	-0.7782570000	-1.4880410000
O	0.8390330000	-0.9845090000	-2.5121120000
H	-4.5650540000	-2.4724840000	-1.1251490000

TS(S:T)

Frequency: –1011.81 cm^{-1}

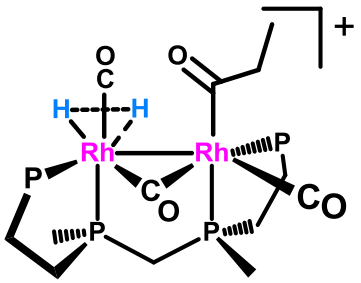

Rh	1.3288200000	0.2549740000	-0.7721210000
P	3.5636460000	0.6646330000	0.1533090000
P	1.8052150000	-1.9964380000	-0.2585080000
C	3.9029540000	-0.8208330000	1.2203930000
H	4.9557740000	-0.8492150000	1.5155280000
H	3.3105730000	-0.6842750000	2.1290090000
C	3.5080580000	-2.1138250000	0.4986910000
H	3.5519580000	-2.9754400000	1.1701670000
H	4.1967120000	-2.3178370000	-0.3258260000
C	3.9146740000	2.0944110000	1.2506540000
H	3.1837520000	2.1174920000	2.0585160000
H	4.9212950000	2.0274290000	1.6701450000
H	3.8341100000	3.0194850000	0.6764760000
C	4.9531730000	0.6979290000	-1.0527760000
H	4.8529870000	1.5791890000	-1.6891570000
H	5.9202940000	0.7361610000	-0.5450500000
H	4.9149470000	-0.1813490000	-1.6969750000
C	0.6729760000	-2.8141020000	0.9597320000
H	0.7350210000	-3.9027170000	0.8676740000
H	1.0237980000	-2.5405230000	1.9592140000

P	-1.0751550000	-2.1886170000	0.8601710000
C	-1.8727530000	-3.0701370000	2.2695100000
H	-1.7240590000	-4.1512850000	2.2193300000
H	-1.4665410000	-2.6938540000	3.2103420000
H	-2.9436830000	-2.8587590000	2.2633310000
C	-1.8178140000	-3.0090900000	-0.6396390000
H	-1.1050660000	-2.8965330000	-1.4601440000
H	-1.9542390000	-4.0806920000	-0.4653020000
C	-3.1457460000	-2.3298050000	-1.0171700000
H	-3.8818730000	-2.4626420000	-0.2182840000
H	-3.5670930000	-2.7891840000	-1.9157260000
P	-2.9177060000	-0.4890560000	-1.2542160000
C	-4.6344030000	0.1671820000	-1.1924600000
H	-5.0525620000	0.0187990000	-0.1952100000
H	-4.5940820000	1.2387490000	-1.3930570000
H	-5.2824780000	-0.3118030000	-1.9304500000
Rh	-1.3088630000	0.2698580000	0.5329700000
C	-2.4939700000	-0.3195110000	-3.0382170000
H	-3.2857340000	-0.7134480000	-3.6804350000
H	-2.3503180000	0.7409150000	-3.2519760000
H	-1.5601430000	-0.8399150000	-3.2558060000
C	1.9006920000	-3.1769650000	-1.6616100000
H	2.2147340000	-4.1659000000	-1.3196750000
H	0.9353240000	-3.2611040000	-2.1596100000
H	2.6223280000	-2.8008700000	-2.3880730000
C	1.0872370000	2.0919910000	-1.3778460000
O	1.0132680000	3.1387890000	-1.8088920000
C	-1.2870680000	3.3838830000	0.9760190000
C	-1.5167780000	4.8008060000	0.4519010000
H	-0.2452570000	3.2239650000	1.2687540000
H	-1.2350490000	5.5312220000	1.2136170000
H	-2.5649250000	4.9609280000	0.1951080000
H	-1.8646540000	3.2007440000	1.8889170000
C	-1.6747980000	2.2809450000	-0.0087780000
O	-2.1915340000	2.5258790000	-1.0635630000
C	0.4931780000	0.6375210000	1.3423150000
O	1.0365100000	0.8437480000	2.3547480000
H	-0.9243060000	4.9935500000	-0.4441840000
C	-2.4781470000	0.5346470000	2.0970770000
O	-3.1203230000	0.5947880000	3.0360960000
H	0.3648620000	-0.2676420000	-1.9876430000
H	1.5533730000	-0.1547970000	-2.3469460000

TS(T:W)

Frequency: –538.37 cm^{-1}

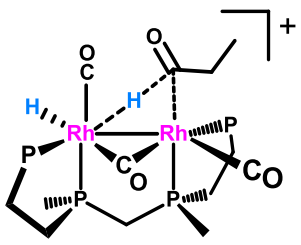

Rh	1.4809310000	0.4826450000	-0.4611870000
P	3.6645330000	-0.0984800000	0.3142820000
P	1.3126980000	-1.7950830000	-0.9747950000
C	3.8434890000	-1.9489860000	0.1888330000
H	4.9000120000	-2.2160650000	0.1001530000
H	3.4855730000	-2.3684820000	1.1336180000
C	3.0338620000	-2.4985620000	-0.9910680000
H	3.0025610000	-3.5915880000	-0.9808730000
H	3.4805230000	-2.1906830000	-1.9406700000
C	4.1836820000	0.3061610000	2.0247060000
H	3.3985140000	0.0158480000	2.7235270000
H	5.1199210000	-0.1937700000	2.2848320000
H	4.3259610000	1.3855220000	2.1069770000
C	5.0112920000	0.5656860000	-0.7424470000
H	4.9954700000	1.6563830000	-0.7066610000
H	5.9886270000	0.2130060000	-0.4042420000
H	4.8507470000	0.2620630000	-1.7778210000
C	0.4634230000	-2.8196920000	0.3240500000
H	0.3729670000	-3.8675130000	0.0212550000
H	1.0982860000	-2.7809770000	1.2132170000
P	-1.1677340000	-2.0782630000	0.8103480000
C	-1.4660450000	-2.7836590000	2.4831960000
H	-1.3540500000	-3.8704520000	2.4943330000
H	-0.7681020000	-2.3374080000	3.1939360000
H	-2.4781720000	-2.5252540000	2.8009280000
C	-2.4237140000	-2.9321500000	-0.2742410000
H	-1.9566760000	-3.1019330000	-1.2473290000
H	-2.6653740000	-3.9140690000	0.1427020000
C	-3.6802050000	-2.0657660000	-0.4351810000
H	-4.2200640000	-1.9964250000	0.5139560000
H	-4.3662390000	-2.5074130000	-1.1633260000
P	-3.2189710000	-0.3267620000	-0.9237920000
C	-4.7678080000	0.6244170000	-0.6527470000
H	-5.0095900000	0.6454200000	0.4110740000
H	-4.6109700000	1.6484760000	-0.9943410000
H	-5.6050300000	0.1893120000	-1.2040570000
Rh	-1.2694420000	0.2729530000	0.4806280000
C	-3.0971110000	-0.3758020000	-2.7598660000
H	-4.0604110000	-0.6224440000	-3.2135010000
H	-2.7754170000	0.6077270000	-3.1035690000
H	-2.3583610000	-1.1114920000	-3.0792890000
C	0.5975510000	-2.3455330000	-2.5673620000
H	0.5678840000	-3.4355080000	-2.6418030000
H	-0.4058000000	-1.9384330000	-2.6781890000
H	1.2097830000	-1.9387820000	-3.3731190000
C	1.9662680000	2.3703750000	-0.6391490000
O	2.3837730000	3.4137940000	-0.8187300000
C	-0.9237530000	3.4654400000	0.3861540000
C	-0.8194070000	4.8265200000	-0.3087300000
H	-0.0112790000	3.2024950000	0.9218800000
H	-0.6158460000	5.6066900000	0.4273750000
H	-1.7498760000	5.0698580000	-0.8220310000
H	-1.7149290000	3.4931800000	1.1450310000
C	-1.3305810000	2.3343350000	-0.5442480000
O	-2.0587080000	2.4985610000	-1.4888620000
C	0.5889440000	0.4019350000	1.4929570000

O	0.9148050000	0.3604550000	2.6149020000
H	-0.0147840000	4.8396750000	-1.0462340000
C	-2.3137780000	0.8696640000	2.1450260000
O	-2.8567380000	1.0169240000	3.1334600000
H	-0.4354770000	1.3181500000	-0.7325450000
H	1.7430350000	0.5475880000	-2.0961310000

Appendix 3 – Transition States of Rhodium Catalyzed Aldehyde-Water Shift Catalysis

TS(I:K)

Frequency: –1577.48 cm^{-1}

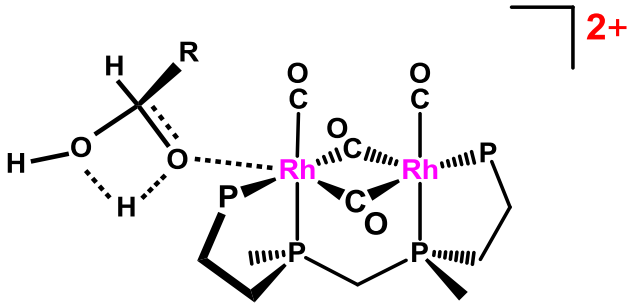

Rh	1.7857750000	0.3854210000	-0.6526000000
P	3.5962790000	1.5683550000	0.3661550000
P	2.5801060000	-1.4473930000	0.6718890000
C	4.0882810000	0.5911220000	1.8689220000
H	5.0628320000	0.9309400000	2.2306860000
H	3.3574300000	0.8240930000	2.6493390000
C	4.1178390000	-0.9114290000	1.5658070000
H	4.2618820000	-1.5020620000	2.4742110000
H	4.9375210000	-1.1491150000	0.8829120000
C	3.3653650000	3.2806620000	0.9753370000
H	2.5255540000	3.3210050000	1.6683440000
H	4.2701200000	3.6333550000	1.4760230000
H	3.1551700000	3.9387460000	0.1300790000
C	5.0959000000	1.6438360000	-0.6830370000
H	4.8871670000	2.2528340000	-1.5650570000
H	5.9231590000	2.0981690000	-0.1318180000
H	5.3780240000	0.6414980000	-1.0114530000
C	1.3699800000	-1.8827530000	2.0124310000
H	1.6270990000	-2.8407650000	2.4741070000
H	1.4674270000	-1.1091380000	2.7794420000
P	-0.4219470000	-1.8750160000	1.5307140000
C	-1.2786910000	-1.7961770000	3.1508250000
H	-1.0178810000	-2.6565440000	3.7715800000
H	-0.9887420000	-0.8807530000	3.6686790000
H	-2.3575030000	-1.7734430000	2.9969850000
C	-0.8429530000	-3.5404270000	0.8458730000
H	-0.1844900000	-3.7273800000	-0.0055190000
H	-0.6630110000	-4.3237750000	1.5874770000
C	-2.3103060000	-3.5264050000	0.3954310000
H	-2.9763430000	-3.5404870000	1.2614860000
H	-2.5380030000	-4.4168040000	-0.1948030000
P	-2.7484240000	-2.0048230000	-0.6092070000
C	-4.4597150000	-1.5968230000	-0.1178350000
H	-4.4586470000	-1.1437710000	0.8730120000
H	-4.8530970000	-0.8761820000	-0.8365230000
H	-5.0800640000	-2.4967070000	-0.1285620000
Rh	-1.1333670000	-0.2993300000	-0.0972460000
C	-2.8687140000	-2.5614500000	-2.3471500000

H	-3.5352680000	-3.4254860000	-2.4082630000
H	-3.2931910000	-1.7459080000	-2.9364080000
H	-1.8863390000	-2.8268420000	-2.7342920000
C	0.4381850000	-0.9549700000	-1.4886990000
O	0.2823170000	-1.8190870000	-2.2496910000
C	0.2356700000	1.1455370000	0.6856270000
O	0.3629950000	1.9670710000	1.4825860000
C	3.0358690000	-3.0338600000	-0.1211870000
H	3.8832970000	-2.8367840000	-0.7818340000
H	3.3250710000	-3.7775290000	0.6255920000
H	2.2086500000	-3.4179480000	-0.7186220000
C	-1.9011030000	0.9357450000	-1.4824930000
O	-2.3134340000	1.6257790000	-2.2768420000
C	1.6045870000	1.7384920000	-2.1199130000
O	1.5329580000	2.5148490000	-2.9415910000
O	-2.8973370000	0.7985270000	1.5458170000
C	-3.0938570000	2.1282620000	1.6887790000
H	-2.3280580000	2.7773500000	1.2547140000
C	-4.4971090000	2.6764120000	1.5636020000
H	-4.5378000000	3.6640930000	2.0347780000
H	-5.1854630000	2.0115280000	2.0954680000
C	-4.9116510000	2.8023160000	0.0902670000
H	-4.9207050000	1.8322190000	-0.4101930000
H	-5.9145080000	3.2261410000	0.0201990000
H	-4.2304950000	3.4642310000	-0.4509020000
O	5.6214940000	-1.6155650000	-1.6277370000
H	5.4648510000	-1.5533100000	-2.5771170000
H	6.5142770000	-1.9733130000	-1.5543960000
O	-2.6698040000	2.0870840000	3.2669710000
H	-3.4039560000	2.3023030000	3.8651030000
H	-2.6833170000	1.0096660000	2.8436920000
O	-4.8468520000	0.1093690000	-2.9608470000
H	-4.6552220000	0.9440340000	-3.4019530000
H	-5.6733180000	-0.1886070000	-3.3576690000
O	-0.9046760000	3.8479590000	-0.6727490000
H	-1.1970560000	4.3240580000	-1.4582820000
H	-0.6023900000	4.5390270000	-0.0732980000

TS(L:M)

Frequency: –419.09 cm^{-1}

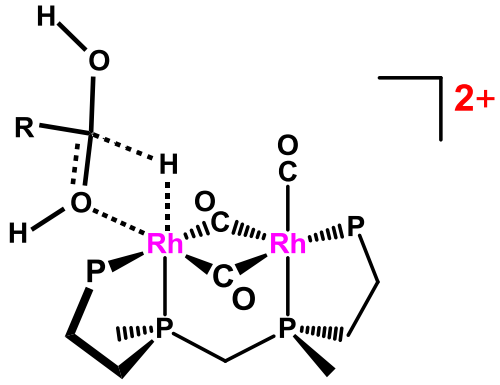

Rh	1.5278170000	-0.6207690000	0.3989490000
P	3.6292500000	-1.2305860000	-0.5584910000
P	2.4374780000	1.6057090000	0.2859920000
C	4.4117980000	0.3223840000	-1.2157540000
H	5.4749590000	0.1487470000	-1.4040500000
H	3.9443730000	0.5304890000	-2.1833220000
C	4.2122860000	1.4888000000	-0.2421630000
H	4.5512510000	2.4347650000	-0.6726070000
H	4.7725110000	1.3210480000	0.6809130000
C	3.6795390000	-2.4086350000	-1.9614960000
H	3.0220920000	-2.0659220000	-2.7603130000
H	4.6985690000	-2.5068190000	-2.3430770000
H	3.3364360000	-3.3887800000	-1.6249180000
C	4.8313290000	-1.8966180000	0.6542440000
H	4.4599520000	-2.8450030000	1.0475400000
H	5.7986710000	-2.0696040000	0.1758970000
H	4.9499540000	-1.1972400000	1.4842060000
C	1.6228080000	2.6509730000	-1.0150580000
H	1.9109920000	3.7011890000	-0.9102460000
H	1.9981250000	2.2994070000	-1.9806030000
P	-0.2236880000	2.4795500000	-1.0983950000
C	-0.6117570000	3.0859690000	-2.7903720000
H	-0.2060830000	4.0868780000	-2.9566640000
H	-0.1912350000	2.4010620000	-3.5286050000
H	-1.6924480000	3.1133410000	-2.9368220000
C	-0.9521380000	3.7530330000	0.0325280000
H	-0.5301600000	3.5906710000	1.0274540000
H	-0.6793770000	4.7637270000	-0.2841900000
C	-2.4773700000	3.5739330000	0.0650150000
H	-2.9216780000	3.9281000000	-0.8682930000
H	-2.9164410000	4.1695210000	0.8683300000
P	-2.9852030000	1.7778700000	0.2749410000
C	-4.5145760000	1.6396850000	-0.7271400000
H	-4.2852880000	1.7859340000	-1.7837380000
H	-4.9386680000	0.6439590000	-0.6018620000
H	-5.2451920000	2.3891410000	-0.4124120000
Rh	-1.1715260000	0.4059480000	-0.4271870000
C	-3.5659490000	1.6588060000	2.0102940000
H	-4.3287290000	2.4183000000	2.1991370000
H	-3.9983070000	0.6731920000	2.1894100000
H	-2.7295000000	1.8021520000	2.6939580000
C	-0.1194560000	0.1828930000	1.4106010000
O	-0.5341270000	0.5171990000	2.4420880000
C	0.2099810000	-0.7387480000	-1.4495170000
O	0.5214780000	-1.3142810000	-2.4025300000
C	2.4720620000	2.6397230000	1.7973870000
H	3.1013590000	2.1307740000	2.5302890000
H	2.8907630000	3.6268260000	1.5858920000
H	1.4692520000	2.7494140000	2.2102730000
C	1.1998270000	-2.4729850000	0.9867890000
O	1.0745740000	-3.5458830000	1.3390320000
O	-4.3291770000	-1.5606290000	0.2324570000
C	-3.3113070000	-2.0762620000	-0.4151670000
H	-2.0880520000	-0.9903620000	-0.0228620000
C	-2.5940260000	-3.2983900000	0.1227540000
H	-1.6649910000	-3.4150740000	-0.4349970000

H	-3.2385500000	-4.1388760000	-0.1704920000
C	-2.3568260000	-3.3288760000	1.6305170000
H	-3.2936300000	-3.4042560000	2.1843390000
H	-1.7585970000	-4.2032160000	1.8880540000
H	-1.8195200000	-2.4399380000	1.9687950000
O	4.7207000000	0.5309890000	3.1061750000
H	4.3146260000	0.0184800000	3.8146000000
H	5.5503960000	0.8471080000	3.4831500000
O	-3.4490980000	-1.9304060000	-1.7059540000
H	-2.7579660000	-2.4282660000	-2.2254790000
H	-4.3538390000	-1.7318960000	1.2051990000
O	-4.9816870000	-1.5795100000	2.8062620000
H	-4.5983790000	-1.7830660000	3.6663070000
H	-5.9386810000	-1.6017900000	2.9245490000
O	-1.6433260000	-3.2612680000	-3.0879330000
H	-1.9292920000	-3.9031300000	-3.7481380000
H	-0.8923960000	-2.7859930000	-3.4621340000

Appendix 4 – Transition States of Bimetallic Cobalt Catalyzed Hydroformylation and Aldehyde-Water Shift Catalysis

Bimetallic cobalt catalyzed hydroformylation

TS(Co_A1:Co_A2)

Frequency: –90.63 cm^{-1}

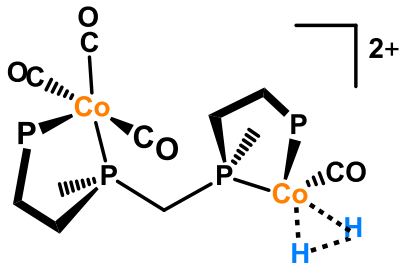

P	-4.1616980000	-0.8559210000	-0.4211020000
P	-1.0066320000	-0.7752870000	-0.5202260000
C	-3.2798110000	-1.9822680000	-1.5946230000
H	-3.8782390000	-2.8806910000	-1.7668780000
H	-3.2011600000	-1.4537460000	-2.5488460000
C	-1.8953860000	-2.3294660000	-1.0425370000
H	-1.2973670000	-2.8670210000	-1.7826040000
H	-1.9825880000	-2.9744440000	-0.1638030000
C	-3.3151740000	1.8382830000	-0.9859610000
O	-3.7868940000	2.5845390000	-1.7001540000
C	-3.2562320000	0.6171240000	1.9186650000
O	-3.6911440000	0.6098310000	2.9680470000
C	-1.3976790000	1.9253520000	0.7001320000
O	-0.6491390000	2.7207440000	1.0115510000
C	-5.6540480000	-0.2712320000	-1.3014730000
H	-5.3842000000	0.2592170000	-2.2149030000
H	-6.2863700000	-1.1248120000	-1.5551700000
H	-6.2204040000	0.4049880000	-0.6581340000
C	-4.8162000000	-1.9309350000	0.9113830000
H	-5.4402310000	-1.3434850000	1.5870380000
H	-5.4262990000	-2.7262650000	0.4773530000
H	-4.0074800000	-2.3751150000	1.4927600000
C	-0.0936650000	-0.2758920000	-2.0390030000
H	0.6339590000	0.5022540000	-1.7928330000
H	0.4232180000	-1.1310180000	-2.4811300000
H	-0.7890360000	0.1371340000	-2.7707770000
C	0.3386780000	-1.5340860000	0.5373990000
H	-0.1476930000	-1.9829940000	1.4085310000
H	0.7614740000	-2.3524060000	-0.0547910000
P	1.7884250000	-0.5468120000	1.1673360000
C	1.2463710000	0.1941720000	2.7520770000
H	0.4879160000	0.9563400000	2.5851180000
H	0.8581680000	-0.5748130000	3.4236500000
H	2.1030350000	0.6760620000	3.2273100000

C	3.0133360000	-1.8612880000	1.6576550000
H	3.6071640000	-1.4317940000	2.4701250000
H	2.5013960000	-2.7361490000	2.0658010000
C	3.9146050000	-2.2329380000	0.4717280000
H	3.3658070000	-2.8254910000	-0.2670440000
H	4.7601280000	-2.8427150000	0.8003030000
P	4.5286440000	-0.7072970000	-0.4019070000
C	5.2436420000	-1.3068220000	-1.9737050000
H	5.7188670000	-0.4761460000	-2.4985330000
H	5.9919810000	-2.0797660000	-1.7863180000
H	4.4585250000	-1.7146020000	-2.6123140000
C	3.3907040000	2.4253990000	-0.6294110000
O	3.7367080000	3.4980240000	-0.7776330000
C	5.9510190000	-0.1095580000	0.5910260000
H	6.7094530000	-0.8918390000	0.6710540000
H	6.3921820000	0.7624900000	0.1049160000
H	5.6326940000	0.1841640000	1.5924250000
Co	-2.6150050000	0.7067380000	0.2325750000
Co	2.8474050000	0.8209030000	-0.3879750000
H	1.6535240000	1.6874970000	-0.2169790000
H	3.2784780000	0.9484540000	-1.7556470000

TS(Co_2B:Co_2C')

Frequency: –837.01 cm^{-1}

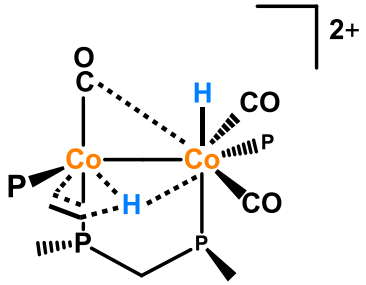

(For clarity P chelate ligands are removed.)

P	-3.5744530000	-0.5818630000	-0.1980490000
P	-1.3331080000	1.4216270000	-0.8030520000
C	-4.0794140000	1.2089170000	-0.1807740000
H	-5.0773000000	1.3260800000	-0.6107830000
H	-4.1546580000	1.4787090000	0.8758310000
C	-3.0638740000	2.1269510000	-0.8927750000
H	-3.0867020000	3.1309860000	-0.4644250000
H	-3.3082020000	2.2303430000	-1.9516670000
C	-4.6999470000	-1.4295340000	0.9636990000
H	-4.5475450000	-1.0641750000	1.9800150000
H	-5.7399660000	-1.2629800000	0.6737800000
H	-4.4949500000	-2.5014090000	0.9457550000
C	-4.0056570000	-1.2516960000	-1.8462420000
H	-3.7408980000	-2.3097300000	-1.8928350000

H	-5.0795750000	-1.1514980000	-2.0200430000
H	-3.4705790000	-0.7300150000	-2.6403950000
C	-0.1747870000	2.6291240000	-0.0253530000
H	-0.0433260000	3.5401200000	-0.6164470000
H	-0.5997580000	2.9118920000	0.9422600000
P	1.4664780000	1.8129260000	0.3261710000
C	2.1545740000	2.8912170000	1.6467670000
H	2.0580900000	3.9393580000	1.3555690000
H	1.6284470000	2.7420690000	2.5903950000
H	3.2123650000	2.6751870000	1.8026590000
C	2.5469540000	2.1683910000	-1.1418090000
H	1.9466800000	2.0885770000	-2.0496640000
H	2.9177760000	3.1950780000	-1.0917100000
C	3.6989520000	1.1572610000	-1.1645410000
H	4.4014670000	1.3483080000	-0.3485520000
H	4.2664490000	1.2214040000	-2.0963440000
P	3.0544820000	-0.5693460000	-0.9321820000
C	4.5311470000	-1.5622770000	-0.4971710000
H	4.9329020000	-1.2432430000	0.4648320000
H	4.2705100000	-2.6204250000	-0.4349370000
H	5.3005830000	-1.4407220000	-1.2629370000
C	2.6136430000	-1.1587620000	-2.6141770000
H	3.5026180000	-1.1647290000	-3.2488610000
H	2.2132230000	-2.1722450000	-2.5611740000
H	1.8579960000	-0.5211290000	-3.0729360000
C	-1.7600780000	0.1113460000	1.9923430000
O	-2.0326580000	0.4263390000	3.0518390000
C	-0.8218400000	1.3564740000	-2.5641460000
H	-1.5183820000	0.7332370000	-3.1266930000
H	-0.8252960000	2.3571080000	-3.0029030000
H	0.1700010000	0.9208150000	-2.6668270000
H	-1.5524250000	-1.8057200000	1.0332140000
C	-0.7214600000	-1.4872450000	-0.9569440000
O	-0.4806280000	-2.1577740000	-1.8518130000
H	0.2185620000	-0.3359280000	1.6044760000
C	1.4091700000	-2.2639130000	0.6765270000
O	1.4403200000	-3.3973360000	0.7048050000
Co	1.4371550000	-0.4713620000	0.6618700000
Co	-1.3991230000	-0.5095680000	0.3542010000
C	2.6413850000	-0.4304180000	2.3305260000
C	1.3051580000	-0.3497280000	2.7841710000
H	3.1773640000	-1.3646520000	2.4486310000
H	0.8616330000	-1.2203300000	3.2558660000
H	0.9444720000	0.5885600000	3.1906270000
H	3.2707400000	0.4495660000	2.3697310000

TS(Co_2D:Co_2E')

Frequency: –270.57 cm^{-1}

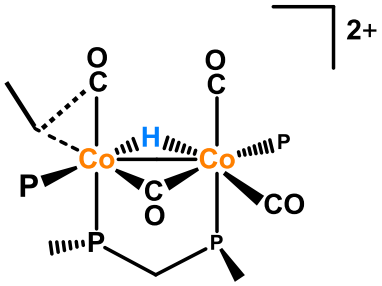

(For clarity P chelate ligands are removed.)

P	-3.3118190000	0.6865740000	-0.1995280000
P	-1.5131190000	-1.8659250000	-0.2513890000
C	-3.6146890000	-0.5492040000	-1.5433750000
H	-4.6723760000	-0.5426070000	-1.8195080000
H	-3.0461330000	-0.2097920000	-2.4119940000
C	-3.1696680000	-1.9435270000	-1.0943780000
H	-3.1243180000	-2.6426390000	-1.9328260000
H	-3.8711940000	-2.3654050000	-0.3695110000
C	-3.6335170000	2.3186660000	-0.9573370000
H	-2.8832200000	2.5289990000	-1.7195620000
H	-4.6232010000	2.3180130000	-1.4198090000
H	-3.6058150000	3.1021640000	-0.1983330000
C	-4.6472770000	0.4494560000	1.0328430000
H	-4.5401600000	1.1804790000	1.8370060000
H	-5.6240940000	0.5896570000	0.5642050000
H	-4.6022430000	-0.5483610000	1.4717270000
C	-0.2541640000	-2.3158590000	-1.5350060000
H	-0.2036380000	-3.4032210000	-1.6355980000
H	-0.5972420000	-1.9096580000	-2.4903960000
P	1.4177100000	-1.5777870000	-1.2237800000
C	2.3085650000	-1.8416660000	-2.8052140000
H	2.2788020000	-2.8917700000	-3.1021850000
H	1.8565060000	-1.2342190000	-3.5917850000
H	3.3512230000	-1.5379620000	-2.6932370000
C	2.2568060000	-2.6831750000	0.0076840000
H	1.5329910000	-2.9254930000	0.7895000000
H	2.5640730000	-3.6243220000	-0.4554780000
C	3.4585360000	-1.9420380000	0.6111900000
H	4.2578280000	-1.8379170000	-0.1282070000
H	3.8790710000	-2.4963760000	1.4537000000
P	2.9853170000	-0.2204860000	1.1527120000
C	4.5710930000	0.6973470000	1.1938280000
H	4.9998110000	0.7655060000	0.1931200000
H	4.4084560000	1.7065450000	1.5766510000
H	5.2830270000	0.1874170000	1.8465450000
C	2.5151130000	-0.3699750000	2.9198970000
H	3.3511300000	-0.7558540000	3.5071250000

H	2.2406010000	0.6135710000	3.3065290000
H	1.6600900000	-1.0372430000	3.0357930000
C	-0.2845660000	0.7819020000	-1.1522910000
O	-0.7737610000	1.0644920000	-2.1775070000
C	-1.5316330000	-3.2866270000	0.9091170000
H	-2.3304180000	-3.1563620000	1.6410560000
H	-1.7105490000	-4.2148360000	0.3616960000
H	-0.5877800000	-3.3722650000	1.4480360000
C	-1.1384330000	1.9540940000	1.1763450000
O	-1.1278080000	3.0187270000	1.5578230000
H	0.3632070000	-0.0347490000	0.9278260000
C	1.7104310000	2.1733420000	0.0817570000
O	1.8328670000	3.2120410000	0.5770620000
Co	1.3076470000	0.5016570000	-0.2709280000
Co	-1.2120450000	0.2399030000	0.6272190000
C	1.9764600000	2.9867100000	-2.4688370000
C	2.5301700000	1.8720250000	-1.5928580000
H	0.9819300000	2.7577710000	-2.8527000000
H	2.5897580000	0.9361250000	-2.1454360000
H	3.5279500000	2.0926060000	-1.2170170000
H	1.9414910000	3.9386340000	-1.9376620000
H	2.6382450000	3.1148370000	-3.3305330000
C	-1.4753510000	-0.3996700000	2.3479180000
O	-1.6067560000	-0.7777390000	3.4068030000

TS(Co_2D:Co_2E)

Frequency: –274.71 cm^{-1}

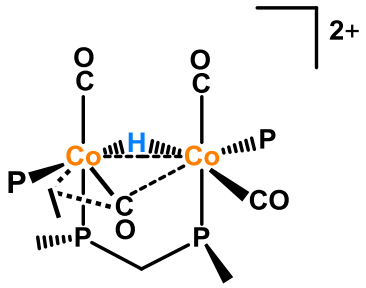

(For clarity P chelate ligands are removed.)

P	-2.9766670000	1.1832960000	-0.0816410000
P	-1.8821130000	-1.5946860000	-0.8771180000
C	-3.2508960000	0.6241640000	-1.8285750000
H	-4.1774770000	1.0530550000	-2.2180160000
H	-2.4312550000	1.0243100000	-2.4316840000
C	-3.2877410000	-0.9061640000	-1.8751810000
H	-3.2538010000	-1.2881570000	-2.8985950000
H	-4.2056370000	-1.2896160000	-1.4205620000
C	-2.6104710000	2.9740590000	-0.1949170000
H	-1.7074060000	3.1402560000	-0.7814720000
H	-3.4418380000	3.4959600000	-0.6740700000

H	-2.4718010000	3.3913540000	0.8040190000
C	-4.6279570000	1.0949700000	0.7149820000
H	-4.5701570000	1.4936240000	1.7294800000
H	-5.3541710000	1.6799290000	0.1460650000
H	-4.9666560000	0.0601060000	0.7806880000
C	-0.4565030000	-1.6168390000	-2.0802520000
H	-0.4346050000	-2.5742270000	-2.6092430000
H	-0.6484080000	-0.8420850000	-2.8276080000
P	1.2197450000	-1.2454600000	-1.3994860000
C	2.3031540000	-1.4202080000	-2.8683860000
H	2.2180480000	-2.4278370000	-3.2812000000
H	2.0204300000	-0.7024040000	-3.6400200000
H	3.3433440000	-1.2387080000	-2.5956550000
C	1.7226770000	-2.6371120000	-0.2883630000
H	0.9232240000	-2.8072580000	0.4349550000
H	1.8486380000	-3.5551690000	-0.8683290000
C	3.0218390000	-2.2464070000	0.4295710000
H	3.8677970000	-2.2683910000	-0.2624040000
H	3.2517110000	-2.9503090000	1.2327550000
P	2.9047380000	-0.5172670000	1.1172040000
C	4.6374720000	0.0769080000	1.1883040000
H	5.0582270000	0.1583570000	0.1846430000
H	4.6793760000	1.0575720000	1.6662870000
H	5.2474050000	-0.6194720000	1.7682850000
C	2.4140640000	-0.7345030000	2.8699560000
H	3.1782880000	-1.3040600000	3.4032340000
H	2.3018050000	0.2354710000	3.3575480000
H	1.4680180000	-1.2714340000	2.9355500000
C	0.7671580000	1.5885610000	-1.5717670000
O	0.1358230000	2.1053090000	-2.3910250000
C	-2.2983120000	-3.3629650000	-0.6364650000
H	-3.1509380000	-3.4391650000	0.0409060000
H	-2.5596410000	-3.8302620000	-1.5880750000
H	-1.4625890000	-3.9045640000	-0.1913870000
C	-1.5872180000	0.7891100000	2.3498190000
O	-1.6167560000	1.4781730000	3.2536720000
H	0.0997670000	0.1077680000	0.4391000000
C	1.2864110000	1.9516590000	1.0173500000
O	1.1965660000	2.7468860000	1.8195250000
Co	1.3947290000	0.6570520000	-0.2261670000
Co	-1.5379100000	-0.2745670000	0.9274600000
C	2.8966060000	3.3423470000	-1.5412000000
C	2.7385660000	1.8340240000	-1.6558410000
H	2.1131510000	3.8827210000	-2.0748080000
H	2.7501240000	1.4865430000	-2.6871030000
H	3.5307460000	1.3114460000	-1.1241480000
H	2.9116110000	3.6865200000	-0.5053710000
H	3.8508900000	3.6330140000	-1.9916830000
C	-1.1544910000	-1.6890090000	1.9044870000
O	-0.9696340000	-2.6148430000	2.5462650000

TS(Co_2*D:Co_2*E')

Frequency: −264.81 cm^{-1}

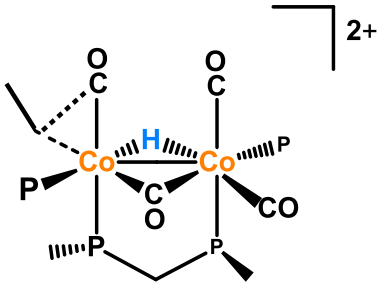

(For clarity P chelate ligands are removed.)

P	3.3511100000	-0.7179680000	-0.3676370000
P	1.5631920000	1.8301320000	-0.0279710000
C	3.6644090000	0.7174710000	-1.4943480000
H	4.7227130000	0.7476260000	-1.7667420000
H	3.0982940000	0.5266510000	-2.4091020000
C	3.2285770000	2.0262550000	-0.8291880000
H	3.2020930000	2.8531720000	-1.5428950000
H	3.9250870000	2.3137060000	-0.0366930000
C	3.6355540000	-2.2101520000	-1.3844010000
H	2.8758930000	-2.2804110000	-2.1626750000
H	4.6221800000	-2.1520980000	-1.8497070000
H	3.5981260000	-3.1054760000	-0.7615730000
C	4.7033560000	-0.7120080000	0.8698450000
H	4.5880360000	-1.5635460000	1.5437050000
H	5.6715860000	-0.7940400000	0.3705790000
H	4.6872310000	0.2004500000	1.4676850000
C	0.3220490000	2.4624040000	-1.2515920000
H	0.2860240000	3.5541040000	-1.2066760000
H	0.6757060000	2.1842870000	-2.2482810000
P	-1.3630700000	1.7069600000	-1.0689750000
C	-2.1909390000	2.1081220000	-2.6561780000
H	-2.1444460000	3.1782760000	-2.8668400000
H	-1.7142090000	1.5624060000	-3.4730210000
H	-3.2381990000	1.8041340000	-2.6056010000
C	-2.2631550000	2.6957130000	0.2210030000
H	-1.5619280000	2.9296660000	1.0257890000
H	-2.6105600000	3.6462210000	-0.1915230000
C	-3.4353810000	1.8620420000	0.7595810000
H	-4.2103930000	1.7477090000	-0.0037750000
H	-3.9040130000	2.3508740000	1.6174430000
P	-2.8692210000	0.1503680000	1.2242920000
C	-4.4068090000	-0.8181750000	1.4601640000
H	-4.9713740000	-0.8859300000	0.5313550000
H	-4.1566480000	-1.8286840000	1.7880090000
H	-5.0298840000	-0.3452360000	2.2222730000
C	-2.2248390000	0.3173850000	2.9365330000
H	-3.0103840000	0.6811490000	3.6021710000

H	-1.8890040000	-0.6576970000	3.2947980000
H	-1.3818170000	1.0076420000	2.9718930000
C	1.5589620000	3.0668030000	1.3262430000
H	2.3410940000	2.8283140000	2.0488320000
H	1.7500920000	4.0642860000	0.9240590000
H	0.6028870000	3.0756680000	1.8503910000
C	1.1615530000	-2.1542070000	0.8359290000
O	1.1257160000	-3.2636330000	1.0517680000
Co	1.2651210000	-0.3785340000	0.5405250000
Co	-1.2663380000	-0.4575510000	-0.3397240000
H	-4.4525070000	-1.2315010000	-1.6018350000
C	0.3170160000	-0.6586430000	-1.2648050000
O	0.7632790000	-0.8309130000	-2.3336120000
C	-1.7416260000	-2.1429240000	-0.1929150000
O	-1.9674420000	-3.2011880000	0.2219110000
H	-0.2959090000	-0.0977790000	0.8982330000
C	-2.3413240000	-1.6971360000	-1.9036950000
C	-3.8190580000	-2.0521450000	-1.9425290000
H	-2.1452430000	-0.7701540000	-2.4376170000
H	-4.0986070000	-2.2664900000	-2.9784220000
H	-4.0461030000	-2.9421870000	-1.3541650000
H	-1.7120460000	-2.4553870000	-2.3693000000
C	1.5720080000	-0.0027180000	2.3314430000
O	1.7392980000	0.2086900000	3.4306120000

TS(Co_2G:Co_2H)

Frequency: −90.68 cm^{-1}

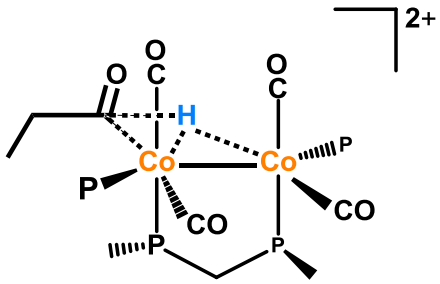

(For clarity P chelate ligands are removed.)

P	-3.6452450000	1.4566490000	-0.0663070000
P	-2.3627670000	-1.2525340000	-0.8335220000
C	-3.8816530000	0.8754200000	-1.8122940000
H	-4.8337240000	1.2340140000	-2.2116720000
H	-3.0853100000	1.3322980000	-2.4067930000
C	-3.7960850000	-0.6520940000	-1.8610650000
H	-3.7151510000	-1.0247940000	-2.8851560000
H	-4.6924540000	-1.1036900000	-1.4273990000
C	-3.4110970000	3.2674720000	-0.2178800000
H	-2.4537990000	3.4585060000	-0.7040890000
H	-4.2182690000	3.7146580000	-0.8017370000
H	-3.3992140000	3.7255420000	0.7727360000

C	-5.2759730000	1.2496030000	0.7459750000
H	-5.2234930000	1.6320010000	1.7671110000
H	-6.0531910000	1.7919580000	0.2029520000
H	-5.5385270000	0.1922630000	0.7994300000
C	-0.9753610000	-1.3990230000	-2.0602470000
H	-1.2154480000	-2.1834060000	-2.7852160000
H	-0.9503290000	-0.4474070000	-2.5988780000
P	0.7605410000	-1.6434400000	-1.4341360000
C	1.6937040000	-1.6448580000	-3.0222360000
H	1.3199830000	-2.4183640000	-3.6968030000
H	1.5972820000	-0.6698730000	-3.5024060000
H	2.7525100000	-1.8193130000	-2.8279960000
C	0.8883590000	-3.4047930000	-0.8526120000
H	0.1264620000	-3.5647710000	-0.0865810000
H	0.6928610000	-4.1062130000	-1.6678430000
C	2.2859350000	-3.6124780000	-0.2492850000
H	3.0409860000	-3.6652810000	-1.0380060000
H	2.3380120000	-4.5531130000	0.3038610000
P	2.7444360000	-2.1811200000	0.8635080000
C	4.5795580000	-2.2230420000	0.8910640000
H	4.9731650000	-1.9619160000	-0.0925790000
H	4.9526940000	-1.4978540000	1.6164880000
H	4.9420120000	-3.2151370000	1.1688050000
C	2.2611040000	-2.7155550000	2.5543520000
H	2.7635700000	-3.6496040000	2.8156350000
H	2.5517410000	-1.9451580000	3.2710640000
H	1.1823320000	-2.8527610000	2.6224740000
C	3.3517960000	3.4549170000	-1.1437100000
O	3.8036250000	2.7896740000	-1.9297500000
C	-2.8500970000	-2.9720810000	-0.4223480000
H	-3.7408270000	-2.9332270000	0.2076030000
H	-3.0802630000	-3.5369550000	-1.3283290000
H	-2.0722060000	-3.4903090000	0.1364210000
C	-1.9557440000	1.3136680000	2.2166600000
O	-1.9609700000	2.0261760000	3.1050460000
H	1.3002270000	2.0933700000	-0.9611090000
C	2.8639430000	0.7896690000	0.7454910000
O	3.6320720000	1.6290940000	0.9747300000
Co	1.7200220000	-0.2990270000	0.0892800000
Co	-1.9547180000	0.2184990000	0.8282280000
C	4.1847930000	5.5369770000	-0.1120270000
C	3.0215150000	4.5064060000	-0.2159740000
H	5.0908190000	5.0654020000	0.2659100000
H	2.8121090000	4.0176010000	0.7412070000
H	2.0911370000	4.9588680000	-0.5813950000
H	4.3835340000	6.0111280000	-1.0722730000
H	3.8614910000	6.2988820000	0.5980710000
C	-1.3695060000	-1.1022700000	1.7981270000
O	-1.1041510000	-2.0066470000	2.4539270000
C	0.7427620000	1.1997470000	-0.4936080000
O	-0.4663420000	1.4101380000	-0.3864080000

Bimetallic cobalt catalyzed aldehyde-water shift catalysis

TS(Co_I:Co_K)

Frequency: –1547.6 cm^{-1}

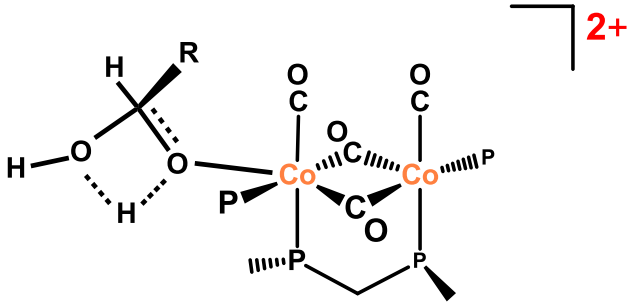

(For clarity P chelate ligands are removed.)

P	-2.5259210000	-2.3769710000	0.2251160000
P	-0.6012640000	-0.5928390000	1.9003220000
C	-2.1594940000	-2.8709000000	1.9758850000
H	-3.0017090000	-3.4349650000	2.3845280000
H	-1.3004460000	-3.5469730000	1.9510770000
C	-1.8585190000	-1.6169770000	2.8032300000
H	-1.5015950000	-1.8652340000	3.8055730000
H	-2.7538400000	-0.9998570000	2.9198610000
C	-2.4371090000	-3.9181470000	-0.7555070000
H	-1.4000800000	-4.2388640000	-0.8475910000
H	-3.0214940000	-4.7002400000	-0.2657690000
H	-2.8460120000	-3.7494840000	-1.7534810000
C	-4.3146190000	-1.9579620000	0.2458870000
H	-4.6307420000	-1.5835690000	-0.7288470000
H	-4.8957810000	-2.8520200000	0.4823600000
H	-4.5236260000	-1.1995720000	1.0017980000
C	1.0133840000	-1.3628370000	2.3808000000
H	1.2730400000	-1.0943420000	3.4078500000
H	0.9010430000	-2.4485000000	2.3396380000
P	2.3516930000	-0.8880800000	1.1805400000
C	3.4641590000	-2.3408310000	1.1151210000
H	3.8119780000	-2.6180440000	2.1125530000
H	2.9319550000	-3.1804640000	0.6651230000
H	4.3158610000	-2.0899790000	0.4777320000
C	3.3498930000	0.4565650000	1.9723490000
H	2.6801190000	1.1253840000	2.5188680000
H	4.0551680000	0.0284610000	2.6896000000
C	4.0797790000	1.2058840000	0.8499290000
H	4.8423010000	0.5731160000	0.3899510000
H	4.5682700000	2.1107780000	1.2198830000
P	2.8852040000	1.6437680000	-0.5018470000
C	3.9379700000	2.0083690000	-1.9563280000
H	4.5473550000	1.1322400000	-2.1809730000

H	3.3162600000	2.2543490000	-2.8190200000
H	4.5921610000	2.8563890000	-1.7417310000
C	2.2001290000	3.2736020000	-0.0104160000
H	2.9968880000	4.0209800000	-0.0442380000
H	1.4126990000	3.5753470000	-0.7006460000
H	1.8049820000	3.2358040000	1.0065340000
C	0.2774460000	0.9672900000	-1.4191380000
O	-0.1904280000	1.8516840000	-2.0025730000
C	0.4234140000	-1.7449000000	-0.6373630000
O	0.5970850000	-2.9101990000	-0.6345420000
C	-0.6208510000	1.0459780000	2.6971310000
H	-1.5328750000	1.5582560000	2.3935400000
H	-0.5935430000	0.9356040000	3.7838050000
H	0.2411080000	1.6320230000	2.3823730000
Co	-1.1035600000	-0.6648210000	-0.3360440000
Co	1.4727180000	-0.1541070000	-0.7709030000
C	-1.6817170000	-0.8539470000	-2.0411740000
O	-2.0875120000	-0.9848390000	-3.0908700000
C	2.3684690000	-0.8388240000	-2.1740300000
O	2.9329600000	-1.2674870000	-3.0660480000
O	-2.4992320000	0.9214040000	0.0893500000
C	-2.9850220000	1.9378060000	-0.7481810000
H	-2.5391100000	1.9528770000	-1.7416380000
C	-3.1103350000	3.3086350000	-0.1182470000
H	-3.7920050000	3.9065320000	-0.7309760000
H	-3.5779820000	3.1876840000	0.8649010000
O	-6.4562860000	2.8025200000	-0.6196630000
H	-7.0074040000	2.9609960000	-1.3944160000
H	-6.9807060000	3.0520750000	0.1486730000
O	-4.3457130000	1.2809830000	-0.8859790000
H	-5.1486840000	1.8553480000	-0.6974250000
H	-3.7872930000	0.6589660000	-0.0754390000
O	1.8360860000	3.1940700000	3.4146950000
H	1.1677050000	3.7146030000	3.8740940000
H	2.6709890000	3.5907220000	3.6882350000
O	5.5256940000	-1.0563230000	-1.3196750000
H	6.4861220000	-1.1078160000	-1.2527960000
H	5.3085880000	-1.5692170000	-2.1068770000
C	-1.7665030000	4.0301980000	0.0149510000
H	-1.3138330000	4.2072700000	-0.9625120000
H	-1.9084280000	4.9982030000	0.4982210000
H	-1.0644160000	3.4495190000	0.6162880000

TS(Co_L:Co_M)

Frequency: –336.54 cm^{-1}

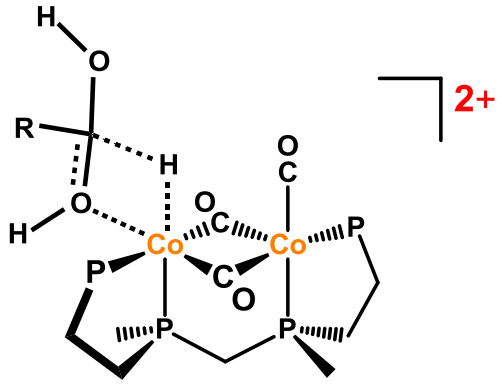

(For clarity P chelate ligands are removed.)

P	3.0342030000	1.3906250000	-0.6602270000
P	0.3236930000	2.4861830000	0.3670040000
C	2.5418600000	3.1055200000	-1.1831400000
H	3.4275650000	3.7242880000	-1.3483490000
H	2.0363340000	2.9994510000	-2.1474580000
C	1.6032910000	3.7323590000	-0.1447470000
H	1.1306960000	4.6427370000	-0.5205110000
H	2.1530050000	4.0079930000	0.7597250000
C	3.8434120000	0.6825010000	-2.1386840000
H	3.0986360000	0.5338220000	-2.9214120000
H	4.6180540000	1.3633550000	-2.4992080000
H	4.2912570000	-0.2791670000	-1.8936910000
C	4.3804780000	1.6365390000	0.5662970000
H	4.7864990000	0.6719170000	0.8768700000
H	5.1847080000	2.2322970000	0.1279140000
H	4.0033140000	2.1521230000	1.4511920000
C	-1.1451320000	2.7881280000	-0.7234050000
H	-1.7188010000	3.6527990000	-0.3808650000
H	-0.7666000000	3.0132600000	-1.7236820000
P	-2.2192670000	1.2713920000	-0.8752910000
C	-2.9179570000	1.4010230000	-2.5639970000
H	-3.4028970000	2.3689790000	-2.7102690000
H	-2.1139320000	1.2826260000	-3.2926560000
H	-3.6403840000	0.5946030000	-2.7121140000
C	-3.6594330000	1.4952630000	0.2649830000
H	-3.2877730000	1.8486190000	1.2301510000
H	-4.3572360000	2.2384120000	-0.1297460000
C	-4.3299000000	0.1231770000	0.4153430000
H	-4.8006900000	-0.1836520000	-0.5215540000
H	-5.0988150000	0.1356630000	1.1915400000
P	-3.0691070000	-1.1866320000	0.8179570000
C	-3.8542780000	-2.7516850000	0.2800640000
H	-4.0590120000	-2.7018580000	-0.7906390000
H	-3.1993300000	-3.5974880000	0.4954910000

H	-4.7945350000	-2.8934520000	0.8181550000
C	-3.0594120000	-1.2870770000	2.6485480000
H	-4.0276070000	-1.6589230000	2.9920170000
H	-2.2784540000	-1.9681170000	2.9878430000
H	-2.8871880000	-0.2975500000	3.0752900000
C	-0.2136540000	-0.5373690000	1.3006520000
O	0.0693030000	-0.7049200000	2.4165330000
C	0.2308330000	0.0386660000	-1.4287730000
O	0.4499300000	0.2047190000	-2.5698110000
C	-0.1896170000	2.9997530000	2.0476550000
H	0.6324790000	2.8220020000	2.7443210000
H	-0.4275520000	4.0666950000	2.0554710000
H	-1.0632130000	2.4442450000	2.3920930000
Co	1.1741250000	0.4010440000	0.0919630000
Co	-1.1340840000	-0.6286260000	-0.2384910000
C	-1.0195050000	-2.1807420000	-1.0640210000
O	-0.8074270000	-3.1938790000	-1.5677810000
O	3.9452860000	-2.1066480000	-0.3667280000
C	2.6862470000	-2.4423320000	-0.3711340000
H	1.9529580000	-0.9900470000	0.0105430000
C	2.0792940000	-3.2721390000	0.7386510000
H	0.9944500000	-3.1721820000	0.6816010000
H	2.3163890000	-4.3082190000	0.4589080000
O	5.6245320000	-1.6393880000	1.5983860000
H	6.5273540000	-1.7877390000	1.2910160000
H	5.6542710000	-1.7064590000	2.5593700000
O	2.2600090000	-2.6200800000	-1.6067780000
H	1.3704260000	-3.0055090000	-1.6300130000
H	4.3861110000	-2.0406670000	0.5209660000
O	-2.8580990000	1.9457970000	3.7531010000
H	-2.4091230000	1.7858780000	4.5910850000
H	-3.6576680000	2.4258680000	3.9977790000
O	-4.7128120000	-1.4786310000	-2.7487550000
H	-5.6496710000	-1.5454430000	-2.9677090000
H	-4.2640470000	-1.9031130000	-3.4888900000
C	2.5825120000	-2.9852430000	2.1505530000
H	2.4266580000	-1.9417030000	2.4289640000
H	2.0309590000	-3.6014980000	2.8611710000
H	3.6384660000	-3.2374900000	2.2594840000

Appendix 5 – $Si_5O_{16}\tilde{H}_{12}$ Cluster geometry in Å

Si	0.39221095	-0.03543176	0.05250489
O	1.80641918	-0.77521497	0.03083506
O	0.11442704	0.58372974	-1.40835065
O	0.43329849	1.14856662	1.13436654
O	-0.78612236	-1.05242084	0.46010557
Si	2.29588684	-2.33661876	0.24409997
Si	-0.59982064	1.80266507	-2.23308277
Si	0.34312850	2.42943860	2.11196954
Si	-2.04085654	-1.87020620	-0.21097811
O	2.30009761	-2.51114198	1.92497222
O	1.33366440	-3.40293144	-0.59881184
O	3.87900065	-2.53963593	-0.30965559
H	2.70404213	-3.28465360	2.41334564
H	0.34094817	-3.40039204	-0.71926113
H	4.07567371	-2.94004598	-1.20463687
O	-0.55735642	3.24403271	-1.41826939
O	-2.17076839	1.17392378	-2.51521853
O	0.03259483	2.03256523	-3.77389560
H	-0.51732211	3.44341018	-0.43916476
H	-2.76974293	1.54390341	-3.22539074
H	0.69984036	2.74264443	-3.99877542
O	-0.68717913	2.28778142	3.42334432
O	1.85026020	2.85468925	2.71719749
O	-0.36249213	3.63603523	1.12801832
H	-0.42455275	1.95121633	4.32764036
H	2.73086988	2.75778665	2.25336941
H	-0.78386532	4.45758924	1.51206733
O	-3.08779838	-2.51061246	0.94111731
O	-2.91670902	-0.95523054	-1.27656949
O	-1.24797830	-3.22733021	-0.89119877
H	-3.95258790	-2.07564465	1.19199993
H	-2.66075458	-0.14754288	-1.80772669
H	-1.74183970	-4.01726835	-1.25465253

Appendix 6 – Letter of Permission

Re: Permission to publish in a dissertation

Gustavo Scuseria, JCTC <scuseria-office@jctc.acs.org>

Fri 11/13/2015 10:10 AM

Inbox

To: Sayakkarage Fernando <rfema7@lsu.edu>;

Hello,

Yes, you have permission to do this.

Gustavo E. Scuseria, Editor
Journal of Chemical Theory and Computation

On 11/12/2015 9:40 PM, Sayakkarage Fernando wrote:

> Dear Prof. Scuseria
>
> I am the primary author of the following open-access paper:
> http://pubs.acs.org/doi/abs/10.1021/ct500943m
>
> "X-ray Absorption in Insulators with Non-Hermitian Real-Time Time Dependent Density Functional Theory"
> Ranelka G. Fernando, Mary C. Balhoff, and Kenneth Lopata
> DOI: 10.1021/ct500943m
> J. Chem. Theory Comput. 2015, 11, 646−654
>
> I want to use this material in my dissertation and I would like to obtain written permission to do so.
>
> Thank you,
>
> Best Regards,
> Ranelka Fernando

--

Professor Gustavo E. Scuseria, Editor

Vita

Sayakkarage Ranelka Geethmi Fernando was born in Colombo, Sri Lanka to Rohan Fernando and Indra Fernando. She received her Bachelor of Science in Chemistry from the University of Colombo in August 2010. She then worked as a chemistry demonstrator at the University of Colombo. She was accepted to Graduate School Doctoral Program at Louisiana State University in the Department of Chemistry in fall 2011, where she is currently a doctoral candidate in chemistry working under the direction of Prof. George Stanley. Her graduate dissertation work is on computational studies on bimetallic catalysis and X-ray absorption spectroscopy.